Towards In-Process Robotic Ultrasonic Weld Geometry Estimation and Lack of Sidewall Fusion Monitoring

Angelos Dimakos

Department of Electronic and Electrical Engineering

University of Strathclyde

A thesis submitted for the degree of

Doctor of Philosophy

April 2026

Copyright

This thesis is the result of the author’s original research. It has been composed by the author and has not been previously submitted for examination which has led to the award of a degree.

Signed:

Date: 09/03/2026

Acknowledgements

Initially, I would like to thank Charles MacLeod, Nina Sweeney, Ehsan Mohseni and Harris Loukas for the supervision and reviewing of my work, and the fundamental work they did, enabling me to work on this domain. I could not have had a more multi-talented, helpful and supportive team, and I genuinely appreciated the opportunity to work with them. My main supervisor in particular is someone without whom I would not have the journey, and experiences I had. Additionally, I would like to thank my family (Rengina, Dimitrios, Foteini) for the support throughout my studies. They were my anchor throughout my PhD and its many up and downs, and I could not have performed to the same level throughout it without them. Furthermore, I would like to thank my fellow lab members (Sam, Brandon, Chris, Calum, James, Ewan) for both the technical support with the experiments, as well as providing some levity in this part of my academic journey. I would also like to thank James Sibson from Babcock International Group and Tony Burnett from Cavendish Nuclear for engaging with my work and the opportunity to work on this. I would also like to thank the FUSE CDT for giving me the opportunity to work at the cutting edge of robotic ultrasonic inspection for welding.

Abstract

Robotic arc welding is central to the automation of modern manufacturing, yet the integration of volumetric quality assurance directly into the manufacturing workflow remains an open challenge. This thesis presents four distinct contributions for robotic phased array ultrasonic inspection that enables lack of sidewall fusion (LOSWF) monitoring and continuous weld bevel geometry estimation during and after deposition.

Four interconnected contributions are established. First, it is demonstrated for the first time that LOSWF can be detected in real time using ultrasonics during active Gas Tungsten Arc Welding as B-Scan signal dropout: proper sidewall fusion causes longitudinal wave absorption into the melt, while LOSWF maintains signal stability, providing a binary, physically interpretable proxy for joint integrity, as shown in Chapter 4. Second, a comprehensive experimental framework is presented to characterise and reduce robot-induced measurement error across a range of robotic parameters; roll, lateral offset, and coupling force; identifying a critical transition zone that governs the optimal selection between linear and sector scan modalities, as described in Chapter 5. Third, a low-latency signal and image processing pipeline is introduced in Chapter 6, combining Area Under Curve (AUC)-based sparsification with Graphics Processing Unit (GPU) accelerated Histogram of Oriented Gradients (HOG) estimation to achieve Full Matrix Capture data compression exceeding 88% while extracting bevel orientation to within 0.4° in under 250 ms. Finally, a machine learning

pipeline is presented in Chapter 7, employing data augmentation; using Gaussian Process Regression (GPR) to augment scarce training data and a stacked ensemble of Support Vector Machine and polynomial regressor for inference; that achieves bevel length estimation within 1.2 mm, consistent with ISO 13920 weld preparation tolerances. Together, these contributions demonstrate that high-resolution volumetric ultrasonic data can be compressed, processed, and interpreted within the latency constraints of industrial robotic path planning. This work establishes a foundation for closed-loop, self-correcting robotic welding systems capable of providing real-time quality assurance in safety-critical applications such as shipbuilding and nuclear fabrication.

Table of Contents

List of Figures

List of Tables

1. Introduction

This chapter introduces the wider context of automated manufacturing and quality assurance with the wider UK industry. It presents the research goals, contributions and structure of this thesis. Finally, it provides an overview of the scientific and professional outcomes of this research.

1.1 Industrial Motivation

The UK is ranked 11th in the world for manufacturing output, with a sector contributing roughly £211 billion annually and 42% of total exports [1], with steel manufacturing exports accounting for 6% of that. Welding is a critical process within steel manufacturing, to create continuous mechanical bonds between different materials. However, there is significant delay in the adoption of automation across the different sectors, placing it in 24th place in terms of robot density, far behind the other G7 nations [2]. This is due to a variety of factors, such as fragmented support, skills gap and risk aversion. This delay affects the development of advanced manufacturing capabilities. In order to address these barriers to adoption, the British Government is committed to reducing outdated regulations and invest £52 million for new hubs to facilitate business adoption [3]. This action would address the 58,000 vacancies in UK manufacturing, boosting the local economy and improving supply chain resilience [4].

Ongoing investments of over £210 million from Babcock International Group at Rosyth for the manufacturing of five Type 31 frigates [5], and up to £300 million in shipbuilding facilities at Govan from BAE Systems, with the creation of over 1,700 jobs in Scotland, improving automation capabilities for the manufacturing of Type 26 frigates [6]. This is in response to global conflicts around the world driving additional investment, with the need for the development of sovereign capabilities [7]. Furthermore, external investment in automated manufacturing of wind turbines [8] indicates significant interest in extending these capabilities to renewable energy, aiming for net zero emissions by 2050 [9]. For shipbuilding applications, and renewable energy infrastructure, automated welding and quality assurance processes remain a critical process to enhance throughput, repeatability, and adherence to strict standards.

Automated arc welding is central to the automated manufacturing use cases, with a critical need for increase in productivity. The rising skill gap of up to 35,000 positions by 2027 [10] necessitates the rapid adoption and integration of robotic solutions to reduce risk and onboarding times [11]. As such, an increase in robot installations of up to 51% was observed across the UK according to the International Federation of Robotics in 2023 [12]. Robotic welding has been recognised as one of the most widely spread industrial applications [13].

Due to increased complexity and throughput demands, intelligence is integrated into robotic welding systems, to self-diagnose and control the path planning and welding parameters [14]. While vision-based methods are well established, there has been increased interest in the integration of ultrasonic imaging at the point of manufacture, in order to enable full volumetric coverage during deposition [15]. This is driven by a need to reduce rework and excavation for repair works, for large structures, aiming for a 55% decrease in weld process time [16].

For ultrasonic imaging to enable accurate automated inspection and autonomous welding control, some crucial steps need to be taken. This includes the extension of current automated inspection capabilities to detect defects during welding at the point of acquisition. Furthermore, the quantification of error is crucial to enable reliable and accurate inspection using articulated robots. Additionally, data compression and rapid inference of geometric features of weld joints is imperative for real-time control and adaptation of inspection.

1.2 Research Goals

The overarching goal of this thesis is to establish the feasibility of in-process LOSWF monitoring, and address challenges regarding measurement reliability, data management, and geometry extraction for automated deployment. In particular:

a) Establish a baseline of current in-process weld monitoring and seam tracking techniques to isolate the technical barriers preventing real-time, volumetric quality control.
b) Compare existing ultrasonic data compression methodologies to identify limitations that inhibit automated industrial deployment.

c) Validate the physics-based relationship between phased-array ultrasonic signals and face fusion to enable real-time LOSWF monitoring during active TIG welding.
d) Quantify and decouple robot-induced effects from ultrasonic measurement to enable accurate robotic volumetric metrology for multi-pass weld geometry.
e) Design a hybrid CPU-GPU processing and machine learning pipeline capable of compressing volumetric data and inferring weld geometries at the point of acquisition.

1.3 Contributions to Knowledge

The research presented in this thesis has resulted in several distinct contributions to the fields of robotic welding monitoring, ultrasonic Non-Destructive Evaluation (NDE), and applied machine learning. These contributions address the technical barriers preventing the integration of volumetric sensing into autonomous manufacturing workflows.

a) The first major contribution is the experimental validation of real-time LOSWF monitoring during active TIG welding using phased array ultrasonics, as shown in Chapter 4. This work established, for the first time, that the transient signal loss and recovery patterns observed in B-Scan visualisations correspond directly with the physics of the molten pool and material solidification. A 45^{o} linear scan can reliably distinguish between proper fusion (signal absorption) and lack of fusion (signal stability), this research provides a binary detection proxy that is essential for developing real-time, feedback-driven quality control systems.

b) Secondly, this thesis contributes an experimental and analytical framework for the quantification of robot-induced error during the inspection of multi-layered bevel geometries, as shown in Chapter 5. By isolating the effects of robotic pose; specifically roll, lateral offset, and coupling force; from the ultrasonic measurement, the research identified a critical transition zone at 9.62 mm. This finding led to the development of a robotic parameter prioritisation hierarchy, defining the specific mechanical conditions required to maintain sub-millimetre accuracy for different joint depths. This contribution effectively transforms the robotic manipulator from a passive delivery tool into an active metrological instrument.

c) The third contribution is the design and implementation of a modular signal- and image- processing pipeline for the rapid reduction of FMC data, as shown in Chapter 6. Utilising an AUC-based sparsification method on the CPU and a GPU-accelerated HOG algorithm, the framework achieved data compression rates exceeding 88%. This pipeline allows for the extraction of bevel orientation within 0.4° in under 250 ms, proving that high-resolution volumetric imaging can be integrated into high-speed robotic scanning without the latency bottlenecks associated with traditional TFM reconstruction.

d) Finally, this work contributes a machine learning framework for the continuous regression of weld bevel geometry directly from compressed ultrasonic features, as shown in Chapter 7. By leveraging a data augmentation approach; using GPR to augment training data and a stacked ensemble of SVM and polynomial regressors; the system achieved bevel length estimation within 1.2 mm. This contribution demonstrates that geometric features can be inferred with high precision even in low-data industrial regimes, providing a pathway for real-time weld fit up and adaptive process control.

1.4 Thesis Structure

The thesis is structured as follows:

Chapter 2 presents the relevant theory for this body of work, including fundamental ultrasonic wave physics and definition of LOSWF in the context of welding, ultrasonic modalities and machine learning fundamentals. A comparison of different sensing modalities is presented, with emphasis into the benefits of ultrasonic imaging for monitoring and geometry measurement.

Chapter 3 describes the automated welding and inspection system, to facilitate the data acquisition throughout this thesis. It includes a comprehensive description of the robotic systems, ultrasonic data acquisition, welding equipment, monitoring, and thermal management.

Chapter 4 presents, for the first time, the monitoring of LOSWF during welding during ultrasonic imaging. It establishes a baseline for lack of fusion, based on the creation of artificial defects, and the sensitivity of the robotic inspection system for the detection of LOSWF at both room temperatures, and during welding.

Chapter 5 presents an experimental and analytical framework to characterise the robot-induced error during measurement of a machined sample, used as a surrogate of a welded joint. Then, the optimal selected robotic parameters are used for a welded sample and compared against the ground truth created using automated laser scanning.

Chapter 6 introduces a two-stage signal and image processing pipeline, to compress raw Full Matrix Capture (FMC) data during robotic inspection, and extract the geometric orientation for the surrogate. Then, the performance is validated using a mock narrow gap sample, proving generalisability.

Chapter 7 expands upon the work in the previous chapter, establishing a machine-learning framework addressing data scarcity and sparsity, for the continuous regression of weld bevel geometry, directly at the point of acquisition.

Chapter 8 serves as a conclusion of the main findings and limitation of this thesis and discusses potential future research directions in adaptive inspection and welding control.

1.5 Lead Author Publications Arising from this Thesis

1.5.1 Journal Papers

1. Chapter 4 Contribution: Dimakos, A., Sweeney, N. E., Loukas, C., Thompson, C. D., Serjeant, S., MacLeod, C. N., Mohseni, E., Lines, D., & Sibson, J. (2025). Evaluation of signal disturbance and recovery in phased array ultrasonic inspection during welding. Welding in the World. Advance online publication. https://doi.org/10.1007/s40194-025-02256-3
2. Chapter 6 Contribution: Dimakos, A., Sweeney, N. E., Loukas, C., Nicolson, E., MacLeod, C. N., Mohseni, E., Lines, D., & Sibson, J. (2026). Ultrasonic phased array measurement & compression for in-process weld bevel estimation. Ultrasonics, 164, Article 108025. Advance online publication. https://doi.org/10.1016/j.ultras.2026.108025
3. Chapter 5 Contribution: Dimakos, A., Thompson D. Christopher, Sweeney, N. E., Loukas, C., MacLeod, C. N., Mohseni, E., Lines, D., & Sibson, J., Vithanage, R.K.W. (2026). Error Characterization of Robotic Phased Array Ultrasonic System for 15.8 Carbon Steel Joint. Under preparation
4. Chapter 7 Contribution: Dimakos, A., Tunukovic, V., Mohseni, E., Sweeney, N. E., Nicolson, E., MacLeod, C. N., Mohseni, E., Lines, D., & Sibson, J. Machine Learning for Robotic Ultrasonic Automated Bevel Length Estimation Of 16 mm S275 90° Weld Joint Surrogate. Under Preparation.

1.5.2 Conference Presentations

1. Chapter 5-6 Contribution: Dimakos, A., Sweeney, N., Loukas, C., Nicolson, E., MacLeod, C. N., Mohseni, E., & Lines, D. (2025). Automated weld bevel detection and characterization via ultrasonic imaging with novel data compression. Abstract from The 78th IIW Annual Assembly and International Conference, Genoa, Italy.

2. Chapter 4-7 Contribution: Dimakos, A., Nicolson E., Thompson, C., Serjeant, S., Tunukovic, V., Sweeney, N., Loukas, C., MacLeod, C., Mohseni, E., Lines, D., Sibson, J. (2026). High-Fidelity Data Reduction and Feature Extraction for Real-Time Robotic Ultrasonic Geometry Estimation in Nuclear Manufacturing. Abstract from Postdocs in Nuclear Energy 2026, Glasgow, United Kingdom.

1.5.3 Professional Recognition

1. Invited Technical expert – UK Government Office for Science (DSIT), Robotics Capabilities Workshop, January 2026.
2. Chartered Engineer (CEng MIMechE) – UK Engineering Council, Insitution of Mechanical Engineers: professional registration granted on the basis of research conducted during this PhD, certifying engineering competence to UK-SPEC standards.
3. Presenter – Institution of Mechanical Engineers: Making Glasgow a Smart and Sustainable City, June 2025

2. Background

2.1 Arc Welding Processes and Defect Formation

Multi-pass arc welding forms the manufacturing foundation for a broad class of thick-section components, encompassing pressure vessels, nuclear reactor internals, shipbuilding assemblies, and offshore infrastructure. Processes such as Gas Metal Arc Welding (GMAW), Gas Tungsten Arc Welding (GTAW), and Plasma Arc Welding (PAW) are employed to deposit sequential weld beads within pre-machined joint groove preparations; typically V-groove, U-groove, or narrow-gap geometries depending on material thickness and application [17], [18]. A simple representation of the different processes is presented in Figure 1. Gas Metal Arc Welding can be used for materials where productivity is the main driver, for less sensitive materials. It is often used for thicker sections, and to ensure higher productivity. The electrode is consumable and is deposited into the molten material. On the other hand, Plasma Arc Welding (PAW) and Gas Tungsten Arc Welding (GTAW) are often used for materials with high quality demands, such as titanium alloys, however the productivity is lower. Here, the electrode is non consumable, and only inert gases can be used, such as helium and argon.

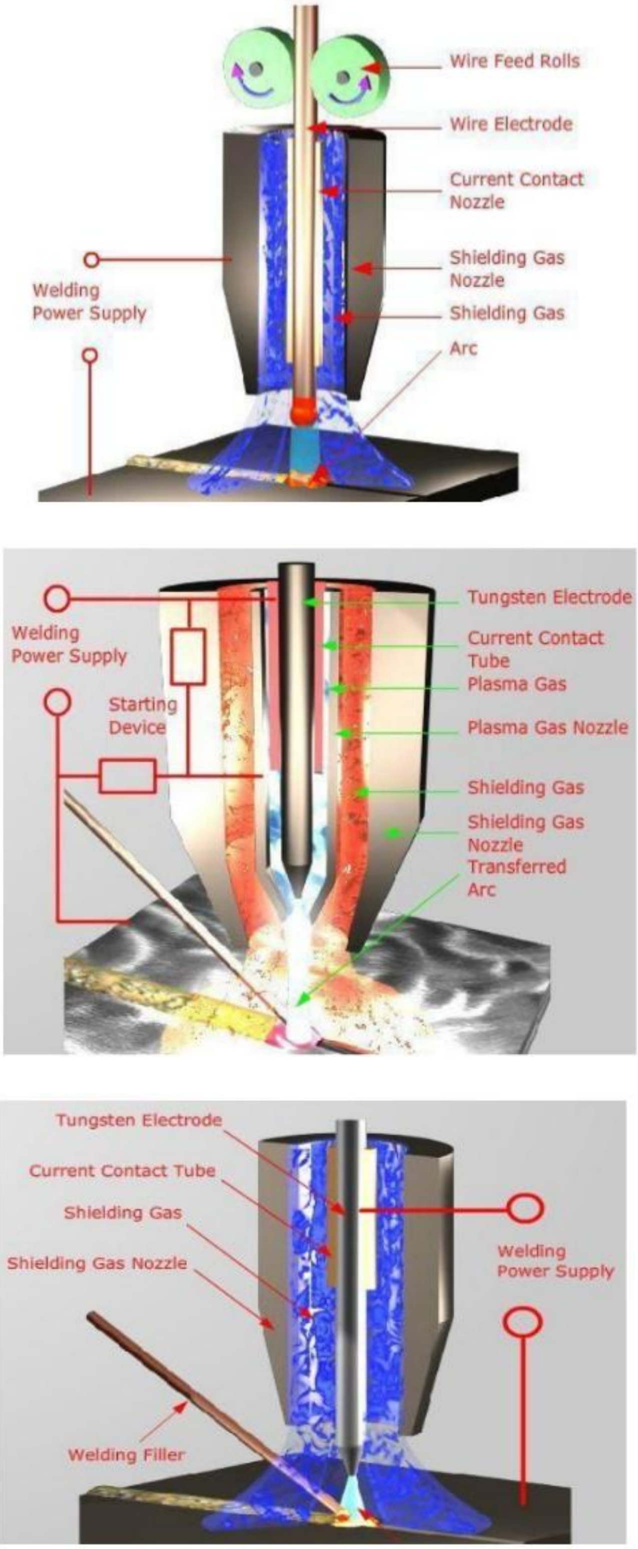

Figure 1. GMAW (upper), PAW (middle) and GTAW (bottom) schematic representations [19]

In each case, the parent material is prepared with a bevel angle that defines the fusion faces against which successive weld passes must bond. For thick-section components (above 30 mm thickness) requiring tens of passes, controlling the geometry and structural integrity of each deposited layer is critical to the structural performance of the final assembly, to be considered fit for service. Geometric control is achieved through thermal management to minimize effect of heat distortion, and optimisation of bead geometry, to optimise number of passes, as shown in previous work [20].

Each successive weld pass imposes a thermal cycle on the underlying material, producing metallurgical transformations including normalisation, grain refinement, and tempering of the heat-affected zone (HAZ) [17]. The heat input per pass (H) governs both the microstructural evolution and the susceptibility of the joint to defect formation, and is characterised by the expression:

$$H = \frac{\eta EI}{v} \qquad 1$$

Where η is the thermal efficiency, E (V) is the arc voltage, I (A) is the welding current, and v is the travel speed (TS) (m/min) [17]. Insufficient heat input restricts the ability of the molten pool to wet and fuse to the surrounding parent material, whilst excessive heat input promotes hot cracking, distortion, and adverse HAZ microstructures. Achieving the correct balance across every pass in a multi-pass sequence is therefore a central process control challenge, particularly as joint geometry evolves and access to the previous fusion faces becomes increasingly restricted with each deposited layer.

Among the defect modes that arise from multi-pass welding, LOSWF, as shown in Figure 2, represents one of the most critical quality concerns for thick-section bevel joints. LOSWF is classified under reference number 4011 in International Organisation for Standardisation (ISO) 6520:2007 [21] within Group 4 (Lack of Fusion and Penetration), and occurs when deposited weld metal fails to achieve full metallurgical bonding with the parent metal bevel face. Several mechanisms promote LOSWF formation: insufficient arc energy directed at the sidewall, improper torch or electrode angle diverting the arc away from the fusion face, the weld pool running ahead of the arc, surface contamination by oxides or mill scale, and narrow-gap configurations, which leads to restricted arc access that severely limits heat deposition at the bevel [22], [23]. In narrow-gap joints specifically, the steep bevel geometry makes LOSWF the dominant defect concern throughout the deposition sequence [22].

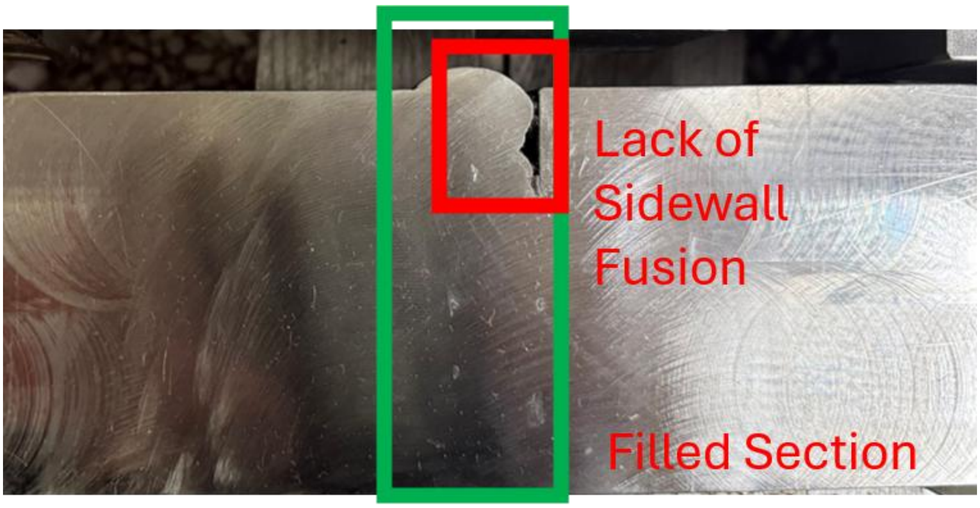

Figure 2. Indicative LOSWF defect.

The industrial criticality of LOSWF arises from its morphology. Unlike volumetric defects such as porosity and inclusions, LOSWF presents as a planar, crack-like discontinuity oriented along the original bevel surface. Under BS7910:2019 [24], which is used to assess acceptability of flaws in metallic structures, LOSWF is assessed using fracture mechanics in the same manner as a crack, with the potential to act as a fatigue initiation site under cyclic loading or a stress corrosion cracking precursor in aggressive service environments. Acceptance criteria are defined across quality levels in BS EN ISO 5817:2023 [25], which defines quality acceptance levels for steel, nickel and titanium and their alloys. Three morphological types have been described in the literature [23]: pure lack of fusion (where an oxide film separates the faces, producing a brazed-type interface largely undetectable by Non Destructive Testing (NDT)); open lack of fusion (where the faces separate under solidification contraction, producing a detectable void of the order of hundredths of a millimetre); and lack of fusion with non-metallic inclusions. Of these, the open and pure lack of fusion are the primary targets for ultrasonic detection, while the lack of fusion with-non metallic inclusions can

Conventional radiographic testing (RT) is substantially limited for LOSWF detection because the planar defect orientation renders it nearly invisible to X-rays unless the beam direction is precisely perpendicular to the defect; a condition rarely achieved in practice for bevel-oriented defects [23]. This limitation, combined with the volumetric nature of multi-pass weld cross-sections and the need for real-time detection during deposition, drives the requirement for an ultrasonic inspection approach capable of targeting the bevel fusion faces directly.

2.2 Non-Destructive Evaluation Modalities for Weld Inspection

NDT of weld integrity encompasses a range of sensing modalities, each offering distinct capabilities and limitations with respect to defect sensitivity, penetration depth, spatial resolution, and suitability for in-process deployment. This section reviews the principal approaches and motivates the selection of phased array ultrasonics as the modality of choice for the work presented in this thesis.

Visual testing (VT) is the most fundamental inspection method and is required as a prerequisite before all other NDE techniques under standards such as American Welding Society (AWS) D1.1 [26]. It is effective for detecting surface discontinuities including external cracks, undercut, incomplete fill, and surface-breaking porosity, but it is intrinsically incapable of evaluating subsurface or interpass defects. Its sensitivity is operator-dependent and provides no volumetric information regarding the through-thickness integrity of the joint.

Thermal and infrared imaging offers non-contact, real-time monitoring of the weld thermal field. Sreedhar et al. [27] demonstrated online defect detection during TIG welding by analysing infrared images taken offset from the arc, detecting porosity with results comparable to post-weld radiography, Similarly, Venkatraman et al [28] confirmed that IR thermography can estimate weld penetration during active deposition.

However, thermal imaging is fundamentally limited in penetration depth; sensitivity diminishes rapidly beyond a few millimetres in metallic structures; making it unsuitable for detecting LOSWF in thick-section components where fusion faces may lie tens of millimetres from the surface. Arc radiation also introduces significant interference requiring careful optical filtering and spatial offset of the measurement zone.

Acoustic emission (AE) monitoring provides real-time, in-situ detection of stress waves generated by cracking, solidification, and phase transformations during and after welding. ASTM E749 [29] standardises AE monitoring during continuous welding, and Droubi et al. [30] demonstrated that AE signal parameters can be influenced by defect presence in carbon steel welds. However, AE offers poor spatial resolution; defect localisation relies on triangulation from multiple sensors, which yields only approximate source locations; and is highly susceptible to electromagnetic noise from the welding arc [31]. Critically, AE cannot characterise defect size, shape, or orientation, limiting its role to screening rather than definitive volumetric characterisation [32].

Radiographic Testing (RT) is one of the most widely established volumetric inspection methods for weld quality certification, employing X-ray or gamma-ray radiation to produce two-dimensional images of internal weld structure in accordance with BS EN ISO 17636-1 [33], which is the international standard covering film techniques for industrial X-ray radiography of fusion-welded joints. The technique detects volumetric discontinuities such as porosity, slag inclusions, and incomplete penetration through differential radiation absorption, and has been extensively applied across pressure vessels, ship building, and nuclear fabrication sectors. Shaloo et al. [34] identified RT as one of the volumetric NDE modalities for fusion welding, noting its broad industrial adoption and its ability to provide a permanent image record suitable for post-inspection review. However, RT is fundamentally limited in its sensitivity to planar defects such as LOSWF; detection is highly dependent on the angular alignment between the radiation beam and the defect plane, and a bevel-oriented discontinuity presents minimal differential absorption unless the beam is directed along the defect face [35]. This orientation dependency, combined with the requirement for bilateral access, the use of ionising radiation requiring controlled exclusion zones, and the inherent inability to deploy the technique in-process during active deposition, renders RT unsuitable for the real-time, single sided volumetric monitoring of multi-pass bevel weld joints as pursued in this thesis.

Eddy Current Testing (ECT) operates by inducing oscillating electromagnetic fields in electrically conductive materials and monitoring the perturbation of coil impedance caused by near-surface discontinuities, surface-breaking cracks, and conductivity variations. Eddy Current Array (ECA) technology extends this principle through the multiplexing of multiple coil elements, enabling rapid C-scan imaging of surface and near-surface defect distributions without mechanical raster scanning. Foster et al. [36] demonstrated the robotic deployment of a flexible ECA system for the automated inspection of stress corrosion cracking on nuclear stainless steel canisters, achieving repeatable impedance imaging through force-torque controlled lift-off compensation and real-time data logging at latencies below 7 ms. Tunukovic et al. [37] further demonstrated simultaneous ECA and ultrasonic acquisition for a Wire Arc Additive Manufacturing component, confirming that ECA provides complementary surface sensitivity to the volumetric coverage of ultrasonic methods. However, the fundamental skin-depth limitation of eddy current inspection confines detectable sensitivity to within a few millimetres of the inspection surface, with penetration depth inversely related to both inspection frequency and material conductivity [38].This constraint renders ECA inherently incapable of detecting subsurface planar defects such as LOSWF located at bevel fusion faces tens of millimetres from the scanning surface, precluding its use as a standalone volumetric inspection modality for the carbon steel joints examined in this thesis.

Ultrasonic testing is uniquely suited to volumetric in-process inspection because it provides full through-thickness penetration, high sensitivity to planar defects, and the ability to accurately localise and size discontinuities in three dimensions. Planar defects oriented perpendicular to the ultrasonic beam produce strong reflections that are readily distinguishable from the surrounding material for isotropic materials, whereas the same defects would be largely invisible to radiographic methods. Single-sided access, the absence of ionising radiation, direct depth measurement, and the potential for real-time imaging make ultrasonics particularly compatible with integration into automated and robotic welding systems. Chauveau [39] provides a comprehensive review of NDT and process monitoring techniques available to welding and additive manufacturing, concluding that ultrasonic methods offer the broadest combination of volumetric sensitivity and real-time capability. Shaloo et al. [34] similarly reviewed NDE techniques for fusion welding across all principal modalities, affirming that multiple complementary methods are required for comprehensive monitoring but that ultrasonics provides the most complete volumetric coverage of any single approach.

The specific capability of phased-array ultrasonic imaging for in-process weld pool monitoring was demonstrated by Sweeney et al. [40], who showed that ultrasonic signals acquired during multi-pass GTAW deposition contain information about the melting and solidification transitions of the weld pool and can detect defects such as lack of root penetration in real time. The feasibility of the in-process ultrasonic monitoring approach was established in [40] and pursued throughout this thesis, in the context of LOSWF.

2.3 Ultrasonic Wave Physics

2.3.1 Wave Modes and Propagation Velocities

Ultrasonic waves are mechanical disturbances that propagate through elastic media by the periodic transfer of kinetic and potential energy between neighbouring material elements. In a homogeneous, linearly elastic, isotropic solid, the motion of every material point is governed by the Navier equation, derived by combining Newton's second law with the constitutive relations of linear elasticity [41]:

$$(\lambda + \mu)\nabla(\nabla \cdot \mathrm{u}) + \mu \nabla^2 u = \rho \frac{\partial^2 u}{\partial t^2} \qquad 2$$

Where u (mm) is the particle displacement vector, ρ (g/mm^3) is the material density, and λ an μ are the first and second Lamé elastic constants respectively, related to the more familiar engineering constants by:

$$\lambda = \frac{Ev}{(1-v)(1-2v)} \quad (3)$$

$$\mu = \frac{E}{2(1+v)} \quad (4)$$

Where E is Young's modulus and v is Poisson's ratio. Applying the Helmholtz decomposition; expressing u as the sum of an irrotational scalar potential φ and a solenoidal vector potential ψ ($F = -\nabla\varphi + \nabla\psi$); decouples this single vector into two independent wave equations. This decoupling reveals that elastic solids support exactly two classes of bulk wave, each governed by its own characteristic propagation speed [41], [42].

Longitudinal (compressional, or L-) waves are associated with the scalar potential φ and involve particle displacement parallel to the direction of propagation, producing alternating zones of compression and rarefaction. Their phase velocity is:

$$c_L = \sqrt{\frac{\lambda + 2\mu}{\rho}} = \sqrt{\frac{E(1-v)}{\rho(1+v)(1-2v)}} \quad (5)$$

Transverse (shear, or T-) waves are associated with the vector potential ψ and involve particle displacement perpendicular to the propagation direction, with no associated volumetric change. Because they require shear stress for their existence, they cannot propagate in fluids or gases, which are incapable of sustaining shear deformation. Their phase velocity is:

$$c_S = \sqrt{\frac{\mu}{\rho}} = \sqrt{\frac{E}{2\rho(1+v)}} \qquad 6$$

For structural carbon steel (E= 207 GPa, v = 0.29, ρ = 7850 kg/m^3, these expressions yield c_L= 5920m/s and c_s=3200m/s. The velocity ratio:

$$\frac{c_S}{c_L} = \sqrt{\frac{1-2v}{2(1-v)}} = 0.54 \qquad 7$$

Is a function of Poisson's ratio alone for any isotropic elastic solid and holds approximately constant across the range of structural steels encountered in weld inspection. The acoustic wavelength $\lambda = \frac{c}{f}$ directly governs spatial resolution: at 5 MHz centre frequency used throughout this thesis, the longitudinal and shear wavelengths are approximately 1.18 mm and 0.65 mm respectively. These dimensions set the fundamental diffraction limit on the smallest detectable feature and on the lateral and axial resolution.

Shear waves are further subdivided by polarisation into vertically polarised Shear Vertical (SV) waves, in which particle motion lies in the vertical plane containing the propagation direction and the surface normal, and horizontally polarised Shear Horizontal (SH) waves, in which particle motion is perpendicular to this plane. SH waves do not couple to other wave modes at smooth planar interfaces under the conditions of in-plane incidence that govern standard phased array operation and are therefore of limited practical relevance in the probe configurations used in this thesis. SV waves, by contrast, participate in mode conversion at the wedge-specimen interface and are the dominant shear mode exploited in angle-beam inspection of bevel weld fusion faces. The movement of the particles for different waves is presented in Figure 3, according to [43].

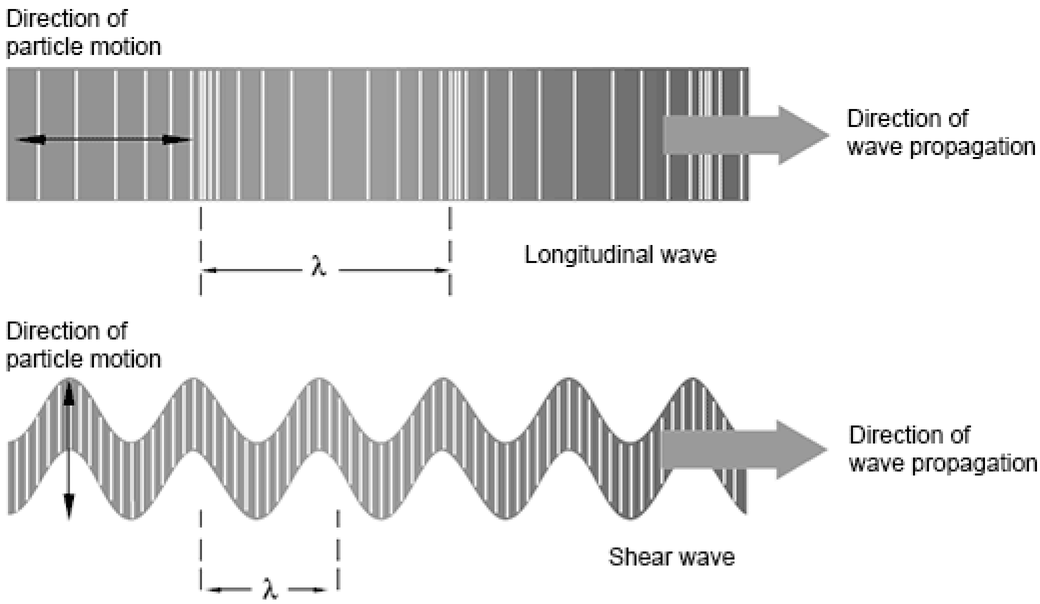

Figure 3. Particle movement for longitudinal (upper) and shear (lower) waves relative to wave propagation direction [43].

2.3.2 Acoustic Impedance and Energy Partitioning at Interfaces

The specific acoustic impedance $Z=\rho c$ (units of Pa s/m, commonly expressed in MRayl, where 1 MRayl = 10^6 Pa s/m) is the fundamental material property governing the partitioning of acoustic boundaries between dissimilar media [41], [42]. For a plane wave at normal incidence on a planar interface separating media of impedances Z_1 and Z_2, application of the boundary conditions of continuity of normal stress and particle velocity yields the pressure reflection and transmission coefficients:

$$R_p = \frac{Z_2 - Z_1}{Z_2 + Z_1} \quad (8)$$

$$T_p = \frac{2Z_2}{Z_2 + Z_1} \quad (9)$$

The corresponding energy (intensity) reflection and transmission coefficients are:

$$R_I = R_p^2 \quad (10)$$

$$T_I = \frac{4Z_1 Z_2}{(Z_1 + Z_2)^2} \quad (11)$$

Respectively, which satisfy the condition of preservation of energy $R_I + T_I = 1$. At a steel-air interface (Z_{steel} = 46.3 MRayl, Z_{air} = 0.0004 MRayl), R_I = 0.9999; essentially no acoustic energy crosses the interface, confirming that air-gapped reflectors such as open LOSWF defects behave as near-total reflectors and that couplant is often essential at any solid-solid inspection interface. This physical behaviour directly underpins the detectability of lack-of-fusion defects by ultrasonic methods: the air-filled void presents an acoustic impedance discontinuity of approximately 10^5:1 relative to steel, producing a reflection coefficient indistinguishable from unity for practical purposes. Oxide-bonded (brazed-type) LOSWF, in which the faces remain in contact separated only by an oxide film, presents a far smaller impedance contrast and may be effectively invisible to any ultrasonic technique irrespective of imaging algorithm; a fundamental physical limitation acknowledged in Section 2.1.

2.3.3 Snell's Law, Critical Angles, and Mode Conversion

When a plane wave is incident obliquely on a planar interface between two elastic media, boundary conditions always require continuity of traction and displacement across the interface for all positions satisfying these conditions simultaneously for the incident, reflected, and transmitted wave fields leads to Snell's law of refraction and mode conversion [41], [42].

$$\frac{sin\theta_i}{c_i} = \frac{sin\theta_{rL}}{c_{1L}} = \frac{sin\theta_{tL}}{c_{2L}} = \frac{sin\theta_{tS}}{c_{2S}} \qquad 12$$

Where θ_i is the angle of the incident wave to the interface normal, θ_{rL} is the angle of the specularly reflected wave, θ_{tL} and θ_{tS} are the angles of the refracted longitudinal and shear waves in the second medium, and c_i, c_{1L}, $c_{2L,}$ c_{2S} are the respective wave speeds.

This configuration is of particular importance for the inspection geometry addressed in this thesis. LOSWF defects are oriented along the bevel fusion face, which is nominally inclined at the groove angle relative to the scanning surface. Directing shear waves toward the fusion face at or near normal incidence maximises the specular reflection from the defect, providing the highest possible Signal-to-Noise Ratio (SNR) for detection.

2.3.4 Attenuation in Polycrystalline Metals

The amplitude of an ultrasonic wave decays exponentially with propagation distance as energy is removed from the coherent beam by absorption and scattering: $A(x) = A_0 \exp(-ax)$, where α (db/mm or Np/m) is the total attenuation coefficient. Absorption; the irreversible conversion of acoustic energy to heat through thermoelastic coupling, dislocation damping, and viscoelastic mechanism; is approximately linear in frequency and is generally the subordinate mechanism in metals at NDE frequencies [41]. Scattering from grain boundaries, inclusions, and micro-structural heterogeneities is typically the dominant attenuation mechanism in polycrystalline materials and exhibits a more complex frequency and microstructure dependence.

Stanke and Kino [44] developed the unified theory for elastic wave scattering in polycrystalline metals, identifying three scattering regimes according to the dimensionless wavenumber-grain size product *kd*, where $k = 2\pi f/c$ the angular wavenumber, *f*: frequency (Hz), *c*: propagation speed (m/s), *d* (µm): is the mean grain diameter. In the Rayleigh regime (*kd*<<1, grain much smaller than wavelength), scattering losses scale as $\alpha_s \propto d^3 f^4$, exhibiting strong frequency dependence characteristic of small-obstacle scattering. In the stochastic regime (*kd*=1, grain size comparable to wavelength), the dependence softens to $\alpha_s \propto df^2$, the regime most relevant to multi-pass weld inspection at typical NDE frequencies where grain dimensions of 0.3-1.0 mm approach the wavelength at 2-5 MHz. In the geometric regime (*kd*>>1, grain much larger than wavelength), scattering becomes frequency-independent and scales as $\alpha_s \propto 1/d$. For the carbon steel welds inspected in this thesis, measured scattering attenuation in the weld metal ranges from approximately 0.2 to 1.5 db/cm depending on the propagation direction relative to the grain axis, the local heat input history, and the inspection frequency [45]. Consequently, selection an inspection frequency requires balancing this grain-induced attenuation against spatial resolution, While higher frequencies (>5 MHz) improve flaw sensitivity the $\alpha_s \propto df^2$ scaling severely limits penetration in thick-multi pass joints. Conversely, lowering the frequency below 2 MHz reduces scattering but increases beam divergence ($sin\gamma = \frac{1.22v}{Df}$), where γ(°): half-angle beam divergence, v(m/s): acoustic velocity, D(mm); transducer element diameter, f(Hz): frequency, which degrades lateral resolution and introduce geometric clutter. The 5 MHz utilized in this study thus represents an optimization, minimizing scattering losses while maintaining sufficient resolution.

The practical consequences of attenuation for in-process inspection are significant. For thick-section welds where fusion faces may lie 20-60 mm from the scanning surface, cumulative one-way attenuation losses of 10-30 dB constraining the minimum detectable reflector amplitude at depth and set a lower bound on the required transmit voltage and receiver gain. Frequency-dependent attenuation causes progressive downshift of the received pulse centre frequency with increasing propagation depth, since higher-frequency spectral components are attenuated more rapidly than lower-frequency ones. This pulse stretching degrades axial resolution for deep reflectors. Additionally, the same grain boundary network that attenuates the coherent beam generates backscattered noise that occupies the same temporal window as defect echoes from the inspection zone, degrading the SNR and complicating automated detection. These considerations motivate the signal processing approaches in Section 2.4.4.

2.4 Phased Array Ultrasonics and Full Matrix Capture

2.4.1 Phased Array Beam Steering and Focusing

A phased array ultrasonic transducer consists of N piezoelectric elements that can be pulsed with computer-controlled time delays, typically arranged in a linear configuration with element pitch d (mm). By applying independently controlled time delays to each element during transmission, the superposition of emitted wavefronts produces constructive interference at a desired location in the inspection volume, enabling electronic beam steering and focusing without mechanical probe movement [46], [47]. For a linear array steering the beam to angle θ from normal incidence, the required time delay for the n-th element is, as shown in equation 13:

$$\Delta t_m = \frac{n \cdot d \cdot \sin(\theta)}{c} \qquad 13$$

Where c (m/s) is the acoustic wave velocity in the coupling medium and inspection material. Focusing at a specific point required delays that account for the full Euclidean propagation distance from each element to the focal point, and can be applied simultaneously during both transmission and reception to maximise lateral resolution at the target depth [48]. This electronic control of beam geometry provides significant advantages over conventional single-element transducers. A single phased array probe can steer, focus a range of beam angles within the same acquisition sequence and create sector scans, as shown in Figure 4; a capability exploited in this thesis through linear and sectorial scans; thereby interrogating fusion faces across a range of lengths without mechanical repositioning.

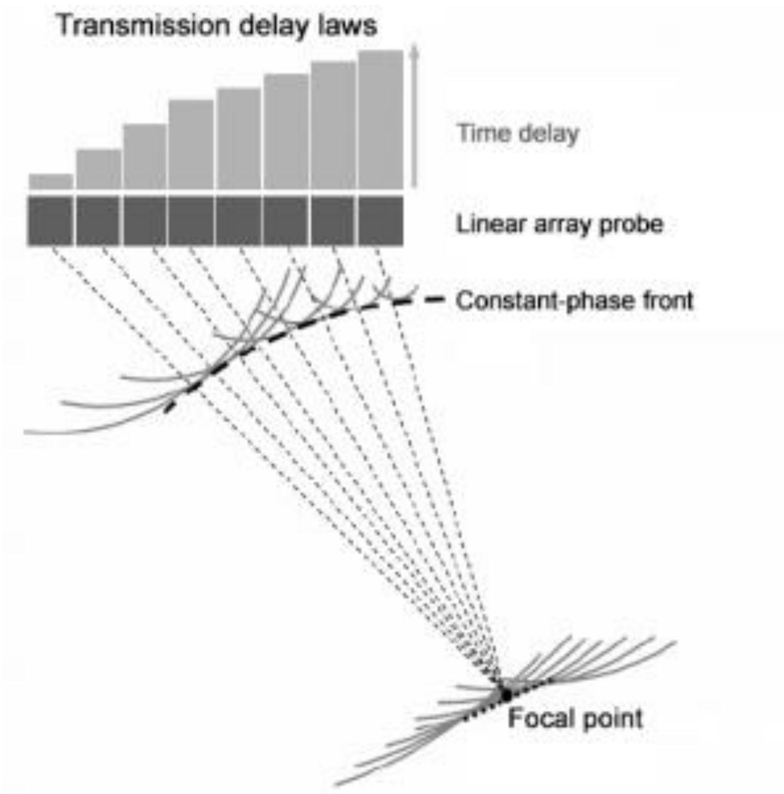

Figure 4. Fundamental principle of PAUT array. Adapted from [49].

Different modalities can be used for ultrasound testing, depending on the application, sample geometry and requirements. Those include amplitude scans (A-Scan), Total Focusing Method (TFM) images and sector scans (S-Scan) and can be acquired using either a single element transducer, or an array of elements. The modalities for a single element transducer can be found in Figure 5. An A-Scan, also known as an amplitude scan, is the representation of the signal acquired from a source location, while B-Scans and C-Scans compile these individual signals along defined spatial axes: a B-Scan aggregates A-Scans along a linear path to generate a cross-sectional view, whereas a C-Scan maps them over a two-dimension grid with an overhead view. The main difference between B-Scans and C-Scans is the direction of wave propagation, where for B-Scans it is vertical to the surface of the sample, while for C-Scans it is parallel.

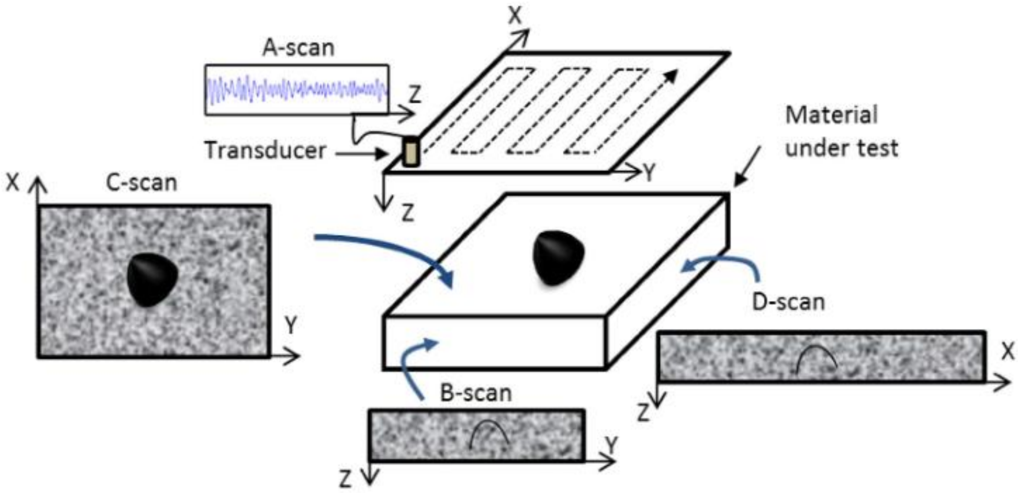

Figure 5. Principal mode representations for multi element transducer. Reproduced with permission from Springer Science Business Media New York [50]

2.4.2 Full Matrix Capture

FMC is a data acquisition strategy in which each of the N array elements transmits individually while all N elements receive simultaneously, with this procedure repeated for every element in sequence. The result is an N x N matrix of time domain A-scan signals, where entry (Tx, Rx) represents the waveform transmitted by element Tx and received by element Rx. For a 64-element array, this yields 4,096 individual A-scans, each capturing a unique transmit-receive path through inspection volume.

Holmes, Drinkwater, and Wilcox [51] introduced and formalised FMC together with a set of post-processing algorithms for image reconstruction, representing the foundational contribution to this area of the field. FMC's defining advantage over conventional phased array acquisition is that the complete dataset is recorded prior to any beam-forming, preserving all acoustic information captured by the array. This enables retrospective application of any imaging algorithm, beam angle, or wave mode without re-acquiring data, and supports post-hoc optimisation of image parameters. A framework for the compression and geometry inference based on the raw data is presented in Chapters 6 and 7.

2.4.3 The Total Focusing Method

TFM is the primary image reconstruction algorithm applied to FMC data throughout this thesis. TFM is a delay-and-sum algorithm that synthetically focuses the array at every pixel in a defined region of interest (ROI), producing an image in which every point is reconstructed at the diffraction-limited resolution of the full array aperture [51]. The image intensity at pixel position P = (x, z) is computed by coherently summing all N x N transmit-receive contributions, as shown in 14, in the formulation of [22] :

$$I_{TFM}(x_i,z_j) = \frac{1}{n}\sum_{tx=1}^{Ntx}\sum_{rx=1}^{Nrx} \hat{u}_{tx,rx}\left(\tau_{tx}(x_i,z_j) + \tau_{rx}(x_i,z_j)\right) \tag{14}$$

Where (x_i,z_j) are the point coordinates, Ntx, Nrx the number of transmitting and reception elements respectively, $\hat{u}_{tx,rx}$ the Hilbert transform of the dataset, and $\tau_{tx}(x_i,z_j)$, $\tau_{rx}(x_i,z_j)$ (µs) the transmission and reception Time of Flights (TOF) respectively.

TFM can be extended to multi-mode imaging by incorporating wave mode conversion, allowing different combinations of longitudinal (L) and transverse (T) wave paths; such as direct LL, half-skip TT, or mode converted TL-TT; to be reconstructed from the same FMC dataset [52]. These modes occur due to non-normal incidence of ultrasonic waves with defects, and specific converted and unconverted modes are selected for the calculation the time-of-flight map and TFM reconstruction, in order to accurately characterise near-vertical defects.

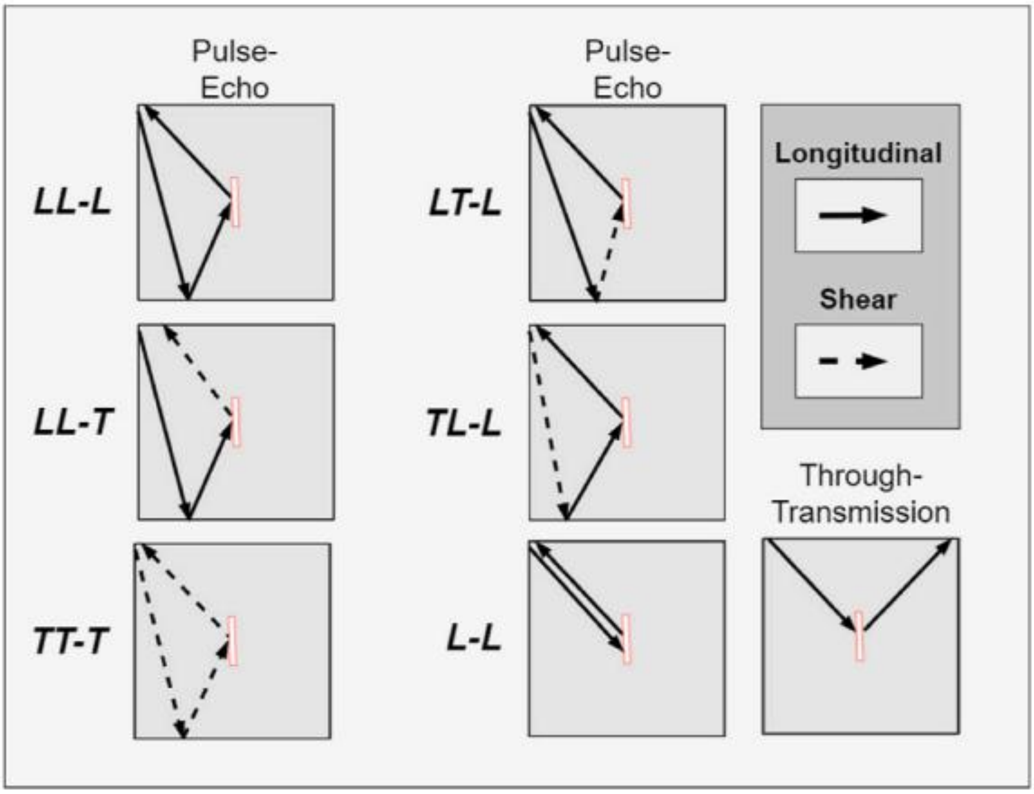

Figure 6. TFM multiple modes. Adapted from [53]

This is particularly valuable for weld inspection where near-vertical fusion face defects may respond differently to different insonification paths. The wavenumber algorithm developed by Hunter et al. [54] provides a computationally efficient Fourier-domain alternative to time-domain TFM for applications where acquisition speed is the primary constraint.

2.4.4 Signal Processing Foundations for FMC-TFM

2.4.4.1 Ultrasonic RF Signals

Raw FMC A-Scans are narrowband radiofrequency (RF) signals: oscillatory waveforms centred at the transducer centre frequency whose amplitude envelope encodes the reflectivity of the inspection volume as a function of round-trip propagation time. The oscillatory character arises because the transducer excitation pulse; typically a short voltage spike or toneburst; excites the piezoelectric element into a waveform that rises, oscillates for several cycles at the resonant frequency, and decays as the mechanical vibration dissipates. The number of oscillation cycles in the pulse, inversely related to the fractional bandwidth, determines the axial resolution of the system: a broader bandwidth yields a shorter pulse, whilst a narrower bandwidth implies a more elongated pulse that fails to resolve closely spaced reflectors in depth.

The bipolar, oscillatory character of RF signals creates an immediate practical problem for image reconstruction. When TOF delay-and-sum is applied to raw RF A-scans, adjacent pixels in the reconstructed image receive contributions from successive positive and negative half-cycles of the signal, causing the image intensity to oscillate at the spatial period of the acoustic wavelength. A reflector at a given depth appears not as a single bright pixel but as an alternating pattern of positive and negative fringes at the carrier wavelength scale. This fringe structure obscures the underlying reflectivity map, complicates the extraction of defect position and amplitude, and prevents straightforward comparison of intensities across the image. The established solution is to process each A-scan through the analytic signal formalism prior to TFM reconstruction, replacing the real RF signal with its complex envelope [47].

2.4.4.2 The Hilbert Transform and the Analytic Signal

For a real-valued signal u(t) the Hilbert transform is defined as the convolution of u(t) with the function 1/(πt), expressed as a Cauchy principal value integral (p.v.) to handle the singularity at t=0 [55] for integration variable τ:

$$\hat{u}(t) = \mathcal{H}u(t) = \frac{1}{\pi} p.v. \int_{-\infty}^{+\infty} \frac{x(\tau)}{t-\tau} d\tau \tag{15}$$

In the frequency domain, the effect of this operation is that the Hilbert transform applies a -90° phase shift to every spectral component of x(t), without altering any amplitude. Formally, if $U(f) = \mathcal{F}\{u(t)\}$ is the Fourier transform of x(t), then the Fourier transform of $\hat{u}(t)$ is $\hat{U}(f) = -j \cdot sgn(f) \cdot U(f)$ where sgn(f) is the signum function, equal to +1 for positive frequencies and -1 for negative frequencies. The Hilbert transform is therefore an ideal all-pass phase filter: it modifies only the phase spectrum of the signal, leaving the magnitude spectrum entirely unchanged. This property is significant because it guarantees that no frequency information is discarded by the Hilbert operation, which matters when the received signal bandwidth is already reduced by frequency-dependent attenuation in the weld metal.

The analytic signal z(t) is the complex-valued function formed by taking x(t) as the real part and its Hilbert transform $\hat{u}(t)$ as the imaginary part [55]:

$$z(t) = u(t) + j\hat{u}(t) = A(t)e^{j\varphi(t)} \tag{16}$$

The polar decomposition of z(t) yields three physically meaningful quantities. The instantaneous envelope $A(t) = |z(t)| = \sqrt{u^2(t) + \hat{u}^2(t)}$ is a smooth, non-negative function that tracks the amplitude of the oscillatory carrier and represents the reflectivity information encoded in the pulse. The instantaneous phase $\varphi(t) = \arctan\left(\frac{\hat{u}(t)}{u(t)}\right)$ describes the carrier phase at each moment in time. The instantaneous frequency $f_i(t) = \frac{1}{2\pi} \cdot \frac{d\varphi}{dt}$ provides a local estimate of the signal frequency, useful for detecting frequency downshift caused by depth dependent attenuation. In the frequency domain the spectrum of z(t) is one-sided: $Z(f) = 2U(f)$ for f>0 and $Z(f) = 0$ for f<0, confirming that the analytic signal retains only the positive-frequency content of x(t), with doubled amplitude to preserve energy.

In practice, the analytic signal is not computed via direct numerical integration of the Hilbert transform definition, which would be computationally prohibitive for large FMC datasets. Instead, the efficient Fast Fourier Transform (FFT)-based algorithm of Marple [56] is universally employed for signal reconstruction: the discrete Fourier transform *U[k]* of each scan *u[n]* is computed: the negative-frequency bins ($k>N/2$) are zeroed; the positive-frequency bins ($0<k<N/2$) are doubled; the DC ($k=0$) and Nyquist ($k=N/2$)

components are left unchanged; and the inverse FFT is applied to recover *z[n]*. This procedure is *O(N logN)* in computational cost and is numerically exact to within floating-point round-off, making it the standard implementation in FMC-TFM processing pipelines.

2.4.5 Conventional Crack Sizing Methods in Ultrasonic NDE

Accurate through-wall sizing of planar defects is a prerequisite for fitness-for-purpose assessment under BS 7910:2019 [24], which employs fracture mechanics to determine whether a detected flaw is acceptable under the applied stress state and fatigue loading conditions. For LOSWF specifically, the through-wall height is the dominant parameter in fracture mechanics assessments, since it governs the stress intensity factor at the crack tip and therefore the remaining fatigue life and critical flaw size. Three established ultrasonic sizing methodologies have been historically applied to planar weld defects: the amplitude drop method, time-of-flight diffraction (TOFD), and tip diffraction within phased array and TFM configurations. Understanding the physical basis, accuracy, and limitations of each contextualises the approach adopted in this thesis and motivates the machine learning sizing framework developed in Chapter 7.

2.4.5.1 The -6 db Amplitude Drop Method

The -6 dB drop method is the most widely applied amplitude-based sizing technique in conventional and phased array ultrasonic inspection [57]. Its operating principle is straightforward: the boundary of a defect is defined as the probe position; or in TFM and Phased Array Ultrasonic Testing (PAUT) images, the pixel location; at which the echo amplitude falls to half (-6.02 db) of the maximum recorded value, as shown in Figure 7. The physical justification for this criterion is that, for a plane wave beam incident on a flat, specularly reflecting surface that is large compared to the beam width, the amplitude at -6 db point corresponds approximately to the edge of the beam footprint coinciding with the physical edge of the reflector. When half the beam energy insonifies the reflector and half passes beyond it, the coherent reflected amplitude is reduced by half, providing a geometrically motivated definition of defect extent.

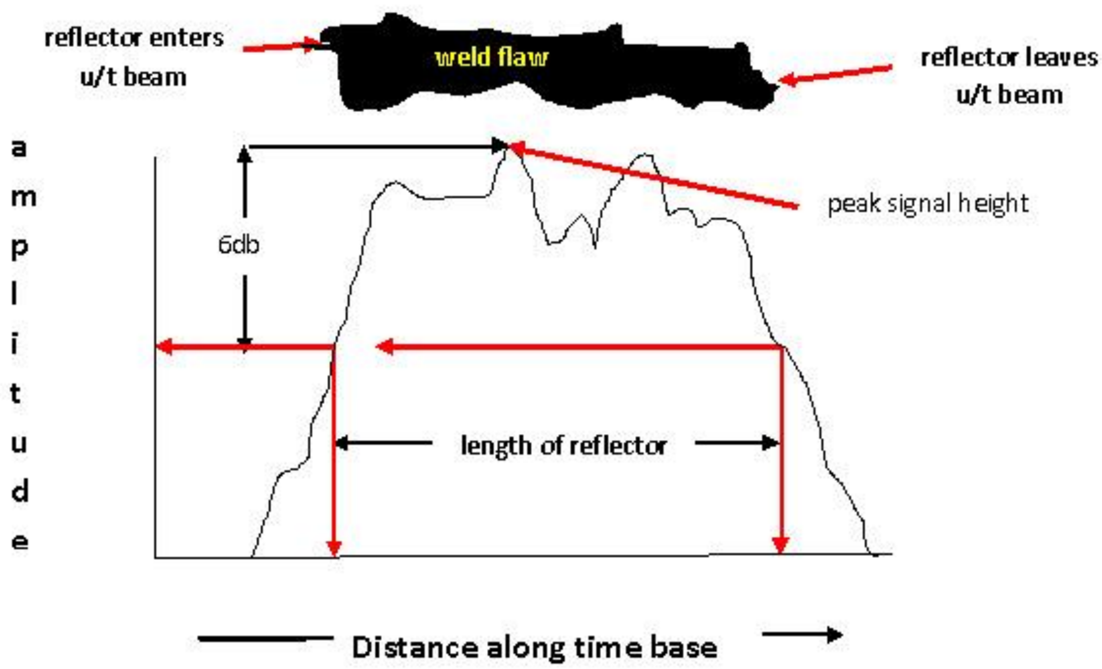

Figure 7. Schematic of 6dB reflector sizing. Adapted from [58]

In TFM images, the -6 db method is applied by thresholding the reconstructed intensity map at half the peak pixel value and measuring the spatial extent of the thresholded region in the through-wall direction. The spatial resolution of TFM; which synthetically focuses at every pixel using the full array aperture; is substantially superior to conventional single-element or sectorial scan methods, and the -6 db sizing uncertainty achievable with TFM on idealised reflectors can be as low as ± 0.5 mm under controlled conditions [47]. Acceptance criteria for PAUT amplitude-based sizing, including the minimum detectable signal and the amplitude threshold for reporting, are codified in BS EN ISO 19825 [59].

Despite its widespread use, the method is subject to well-documented systematic limitations that are particularly problematic in the context of LOSWF sizing. The assumption that defect size exceeds beam width is frequently violated for smaller defects heights. When the defect is smaller than the beam, the -6 db boundaries are determined by the beam dimensions rather than the defect extent, leading to systematic oversizing at small defects heights that paradoxically reverse to undersizing at larger heights as the specular reflection geometry changes. LOSWF presents a further fundamental difficulty: the defect is oriented along the bevel fusion face, and the amplitude of the specular reflection is acutely sensitive to the angular relationship between the beam and the defect normal. Small angular deviations; arising from bevel angle variation, surface tilt, or probe positioning uncertainty; alter the peak amplitude and consequently shift the -6 db boundary, introducing a dependence of the measured size on inspection geometry as true defect extent. The practical consequence is that amplitude-based sizing of LOSWF by the -6 dB method carries uncertainties that are difficult to bound without detailed knowledge of the defect morphology and orientation. Recent advancements explore methods to address fundamental sizing limitations by initially localising defects and then optimizing transmission and reception using a sliding window to exclude receivers with minimal defect information for nickel based alloys [60], which present challenges due to their coarse grain structure. Additionally, by combining TFM with probabilistic models [61] , with sizing errors reduced to 0.13mm for a nickel-based alloy.

2.4.5.2 Tip Diffraction in Phased Array and TFM Configurations

Time-of-Flight diffraction was introduced by Silk and Liddington [62] in the 1970s as a fundamentally orientation-insensitive alternative to amplitude-based sizing. The technique exploits the Huygens wavelet re-radiation that occurs at any geometric discontinuity in the elastic medium, including crack tips: when an elastic wave encounters the terminus of a crack, it re-radiates energy omnidirectionally as a point-like source, regardless of the orientation of the crack face relative to the incident wave. The amplitude of the tip-diffracted signal is lower than that of the specular reflection; typically by 15-25 db for through-thickness cracks; but its arrival time is uniquely determined by the geometry of the crack tip location rather than by the crack face orientation, making TOFD inherently more robust to tilt and surface roughness than amplitude methods.

In the standard two-probe pitch-catch configuration, a transmitter and receiver are positioned symmetrically about the weld centreline, separate by a distance 2S, where S (mm): distance between transducer index point and centreline, chosen to optimise the signal geometry for the expected defect depth range. Four characteristic signals are recorded, as shown in Figure 8: the lateral wave, a head wave that travels just below the scanning surface at the longitudinal wave velocity and serves as a precise time reference; the upper tip diffraction signal from the tip of the crack closest to the scanning surface; the lower tip diffraction signal from the far tip; and the back-wall reflection. For a defect whose upper and lower tip arrival time are t_{upper} and t_{lower} respectively, the depths of the two tips below the scanning surface are computed as [63]:

$$d = \sqrt{\left(\frac{c_L \cdot t}{2}\right)^2 - \frac{S^2}{2^2}} \quad (17)$$

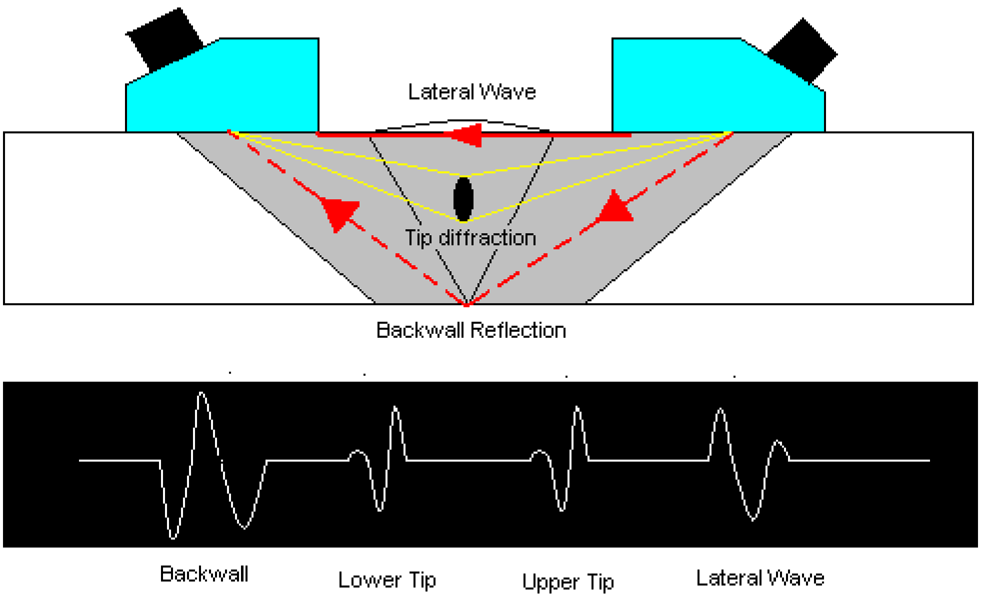

Figure 8. TOFD setup with 4 distinct indications: backwall, lower tip, upper tip and lateral wave. By [64] under CC BY-SA 3.0.

And the through-wall height of the defect is $L = d_{lower} - d_{upper}$,derived directly from the time separation between the two tip signals. Because this calculation depends only on timing and geometry, and not on the amplitude of the diffracted signals, TOFD achieves through-wall sizing accuracy of typically ±1-2 mm under favourable conditions [65]. TOFD procedure requirements and acceptance levels for weld inspection are governed by BS EN ISO 10863 [66] and BS EN ISO 15626 [67] respectively. The main practical limitation is the requirement for a dedicated two-probe pitch catch arrangement that is not compatible with a single-probe robotic configuration employed in this thesis, where only one probe face is available for both transmission and reception at any given scan position.

The same diffraction physics that underpins TOFD operates in pulse-echo phased array and TFM configurations, producing a satellite pulse or tip-diffracted signal alongside the dominant specular reflection from the crack face [68]. In an angle-beam configuration, insonification of a planar defect at or near the specular angle produces both a strong face reflection and weaker diffracted signals from the upper and lower tips, arriving at times corresponding to the additional path length from the array to each tip rather than to the face centroid. In multi-mode TFM images, where the N^2 A-scans provide contributions from all transmit-receive path geometries simultaneously, coherent summation significantly enhances the visibility of tip-diffracted signals relative to single-element methods: contributions from all transmit-receive paths that geometrically intersect the crack tip location sum constructively at that pixel, whereas the specular reflection energy; which requires near-normal incidence on the crack face; is distributed over a narrower range of paths and appears as a spatially distinct indication from the tip signals [51].

In practice, upper and lower tip signals appear as distinct indications in TFM images, spatially offset in depth from the specular reflection by the distance from the centre of the defect face to the respective tip. Their through-wall separation provides a direct measurement of defect height that is independent of the amplitude of the specular echo and therefore substantially less sensitive to defect orientation than the -6db method. BS EN ISO 19285 [59] explicitly requires that where diffracted signals are observable in phased array data, they shall be used to determine defect height in preference to amplitude-based measurements; a recognition that tip diffraction provides superior sizing accuracy for planar defects. The multi-mode capability of FMC/TFM is particularly valuable for this application: Zhang et al. [52] demonstrated that TT mode (shear-shear, half-skip geometry) provides substantially improved sensitivity to upper tip diffraction signals from near-vertical planar defects compared to LL mode, owing to the more favourable insonification geometry for the diffraction wavelet. Current development include crack sizing for complex joint using a sparse representation framework [69] and the use of generative adversarial networks for data augmentation [70], indicating a shift towards imaging of more challenging geometries and addressing data scarcity for static inspection.

2.4.5.3 Limitations of Conventional Methods and the Motivation for Machine Learning Sizing

Each of the three methods described above has limitations that are compounded in the specific inspection environment targeted by this thesis. Amplitude-based sizing is unreliable for near-vertical LOSWF due to specular orientation sensitivity and its dependence on beam width relative to defect height. TOFD requires a dedicated two-probe configuration or a split crystal single probe with both transmission and reception incompatible with a single crystal robotic probe deployment, and its near-surface dead zone prevents sizing of defects in the latest passes close to the weld cap. Tip diffraction in TFM provides the most physically robust sizing information, but the required SNR for reliable tip signal detection is challenging to achieve consistently in the presence of arc-induced noise and the evolving, coarse grained microstructure of freshly deposited weld metal. In the context of this thesis, FMC-TFM with 6 dB amplitude drop method was selected to minimize the complexity of robotic deployment by using a single array wedge, in order to isolate the results from measurement errors due to tandem robotic inspection synchronization for two inspection robots, thus eliminating the applicability of TOFD as viable sizing method. Furthermore, FMC was selected as a main modality, due to the capability for post processing imaging with different methods, enabling future work in evaluating the results presented here for different imaging modalities.

FMC/TFM datasets are, by construction, the most information-rich ultrasonic measurement possible with a given array: the complete N^2 transmit-receive matrix captures all acoustic paths through the inspection volume simultaneously, encoding specular, diffracted, and mode-converted contributions across every transmit-receive combination. Machine learning regression models that operate on features extracted from TFM images or raw RF data are not constrained to exploit a single amplitude threshold or a single pair of tip arrival times; they can in principle retain information from across the full image; including the relative positions and amplitudes of specular and diffracted indications, image texture, and multi-mode contrast; to produce a sizing estimate that is more robust and more accurate than any single conventional method. Recent work has demonstrated that data-driven models trained on simulated and experimental TFM images can achieve sizing accuracy competitive with conventional methods for controlled defect geometries [71], [72], motivating the Machine Learning (ML)-based bevel length estimation framework developed in Chapter 7.

2.5 Robotic Ultrasonic Inspection Systems

2.5.1 Deployment of Articulated Robots for PAUT

Six-degree-of-freedom (6-DOF) industrial articulated robots have increasingly become one of the preferred manipulation platforms for automated PAUT inspection of complex weld geometries, offering flexibility in probe positioning, scanning path programmability, and the ability to maintain a consistent probe-to-surface relationship across curved or irregular joint profiles [73]. Compared to gantry or fixed-axis scanner systems, articulated robots enable access to confined joint configurations and can be integrated directly into welding cells to enable interpass or in-process inspection without moving the component [74].

The University of Strathclyde Centre for Ultrasonic Engineering (CUE) has established the principal body of work in robotic PAUT for in-process weld inspection. Vasilev et al. [74] demonstrated a dual-robot system; one robot welding, one inspecting; using full external positional control via KUKA Robot Sensor Interface (RSI), achieving post-weld, interpass, and live-arc inspection capabilities with a 5 MHz 64-element phased array on high-temperature wedges. Javadi et al. [75] further demonstrated continuous 96-hour robotic hydrogen crack monitoring, revealing that hydrogen-induced cracking initiated 43 minutes after weld completion and continued propagating for up to 24 hours; a finding that underscores the necessity of continuous rather than single point post-weld inspection. The University of Bristol has established an automated inspection system for fastener holes [76] and the Pipebots consortium for the development of miniature robots and acoustic sensors for in-pipe [77] and sewer pipe [78] inspection. However, these are mostly limited to mobile robotics and assembly operation at room temperatures, limiting applicability to the harsh environment of in-process welding monitoring.

2.5.2 Source of Positional and Angular Error

Despite their operational flexibility, articulated robots introduce systematic positional and angular errors that must be characterised and managed when used as precision PAUT manipulators. Industrial robots are specified by manufacturers in terms of their ability to repeat specified commands, rather than follow specified trajectories. Absolute accuracy for trajectory tracking is typically 10-20 times worse than repeatability: a robot with 0.06 mm repeatability may exhibit 1-3 mm absolute positional accuracy across its workspace [79], [80].

The principal sources of this discrepancy are well established in the literature. Geometric kinematic model errors; deviations in link lengths, joint offsets, and axis alignments from their nominal values; account for approximately 95% of absolute inaccuracy and are addressed by kinematic calibration against external metrology references such as laser trackers [79]. Joint gear backlash [81] and elastostatic compliance calibration errors [82] contribute additional uncertainty, compounded through six joints. Thermal drift arising from environmental and self-heating temperature changes degrades accuracy over extended operation periods. Tool Centre Point (TCP) calibration error, reference frame transformations, and end-effector alignment further contribute to the total uncertainty budget [80].

Morozov et al. [80] characterised a KUKA KR5 arc HW robot for NDT applications per ISO 9238:1998, reporting approximately 1 mm pose inaccuracy, 4.5 mm path inaccuracy at full scanning speed, and up to 14° orientation inaccuracy at worst-case configurations. These figures have direct consequences for ultrasonic measurement quality: probe positional error alters the beam entry point and refraction geometry within the component, whilst angular misalignment from surface normals degrades coupling efficiency and shifts reconstructed image. Probe misalignment exceeding approximately 12.5° from surface normal can render inspection results unreliable [83].

Accurate characterisation of robot-induced error is therefore a prerequisite for reliable and accurate automated PAUT inspection. It enables the derivation of measurement uncertainty budgets, informs the selection of optimal scan parameters, and supports the development of compensation strategies including cross-correlation position correction, force-torque sensor feedback for angular alignment, and kinematic calibration protocols [79], [80]. This characterisation forms the central contribution of Chapter 5.

2.5.3 High-temperature Inspection Challenges

Deployment of ultrasonic probes near an active welding arc introduces additional challenges beyond positional accuracy. Temperature-dependent changes in acoustic velocity (approximately 1 mm/s per °C in steel) alter the beam geometry and refraction angles assumed during image reconstruction if not compensated. Standard phased array wedge materials, such as Rexolite and ULTEM, are rated to approximately 100 [84] and 150 °C respectively, limiting their applicability during active welding at temperatures of several hundred degrees. A comparison of their properties is presented in Table 1, based on available datasheets for Ultem [85] and Rexolite [86].

Physical and Acoustical Property	Rexolite	Ultem
Longitudinal Acoustic Velocity	2340 m/s	2470 m/s
Acoustic Impedance	2.44×10^6 kg/m^2-s	3.13×10^6 kg/m^2-s
Density	1.05 g/cm^3	1.27 g/cm^3
Operating Temperature Range	-60°C to 100°C	-60°C to 100°C
Attenuation	0.15 dB/mm	0.5 dB/mm

Table 1. Physical properties of Rexolite and Ultem.

Vithanage et al. [87] addressed this through development of a PAUT roller probe operating at temperatures up to 350 °C, using 55° transverse waves and a dry-coupling roller probe; enabling continuous rotation scanning suitable for robotic interpass and in-process inspection without liquid couplant at the surface of the sample. Electromagnetic interference from the welding arc further degrades signal-to-noise ratio and required careful shielding and signal gating to isolate ultrasonic reflections from arc-induced noise.

2.6 Machine Learning Fundamentals for Regression

Previously, the NDE modalities, UT imaging methods, physics of LOSWF generation and wave propagation, and error sources of robotic inspection were discussed. To facilitate complete geometric characterisation, supervised learning is used to enable continuous geometric regression using the raw RF data from FMC at the point of acquisition. In this section, the theoretical foundations of the Machine Learning (ML) algorithms used in this thesis are briefly described. These include Gradient Boosted Trees (GBT), Gaussian Process Regression (GPR), and Support Vector Machine Regression (SVR) to address the issue of data scarcity in NDE problems.

2.6.1 Supervised Regression

Supervised regression algorithms learn a mapping from input features $\boldsymbol{x}$ to a continuous-valued output y from a labelled training dataset $\{x_i, y_i\}$. The goal is to predict continuous numerical values based on input features. The expected generalisation error decomposes into bias (systematic error from model assumptions), variance (sensitivity to fluctuations in the training data), and irreducible noise; the classical bias-variance trade-off that governs model complexity selection [88]. Regularisation methods constrain model flexibility to reduce variance at the cost of controlled bias, and are fundamental to achieving good generalisation from limited experimental data [89].

In the context of this thesis, regression is applied to predict a continuous geometric quantity; bevel length; from ultrasonic feature vectors extracted from FMC/TFM data. The practical constraints of the problem; limited numbers of continuous measurements, measurement noise, and the need for sub-second inference during robotic scanning; motivate the use of ensemble and kernel-based methods rather than deep neural network approaches, which typically require large training datasets.

2.6.2 Ensemble Methods: Random Forests and Gradient Boosting

Ensemble learning combines the predictions of multiple base models to improve generalisation beyond any individual learner, exploiting the principle that diverse models make uncorrelated errors whose average is more accurate than any single component.

Random Forests [90] construct an ensemble of multiple decision tree regressors, each trained on a bootstrap sample of the training data with a randomly selected subset of features considered at each split. This double randomisation; in data sampling and feature selection; reduces correlation between trees and thereby lowers ensemble variance. The final prediction averages across all trees.

Gradient Boosting [91] takes a complementary sequential approach: each new weak learner is fitted to the residuals of the current ensemble, with the update scaled by a learning rate to prevent overfitting. XGBoost [92] extends this framework with a regularised objective function incorporating both L1 and L2 penalty terms and a second-order Taylor expansion of the loss, providing efficient training and strong generalisation on tabular feature datasets. Both ensemble approaches are well suited to the small-to-medium dataset sizes characteristic of experimental NDT programmes and are robust to correlated input features. This is a common property of ultrasonic signal descriptors derived from the same underlying waveform. The difference in training between random forests, using parallel training, and gradient boosted trees, using sequential training, is presented in Figure 9.

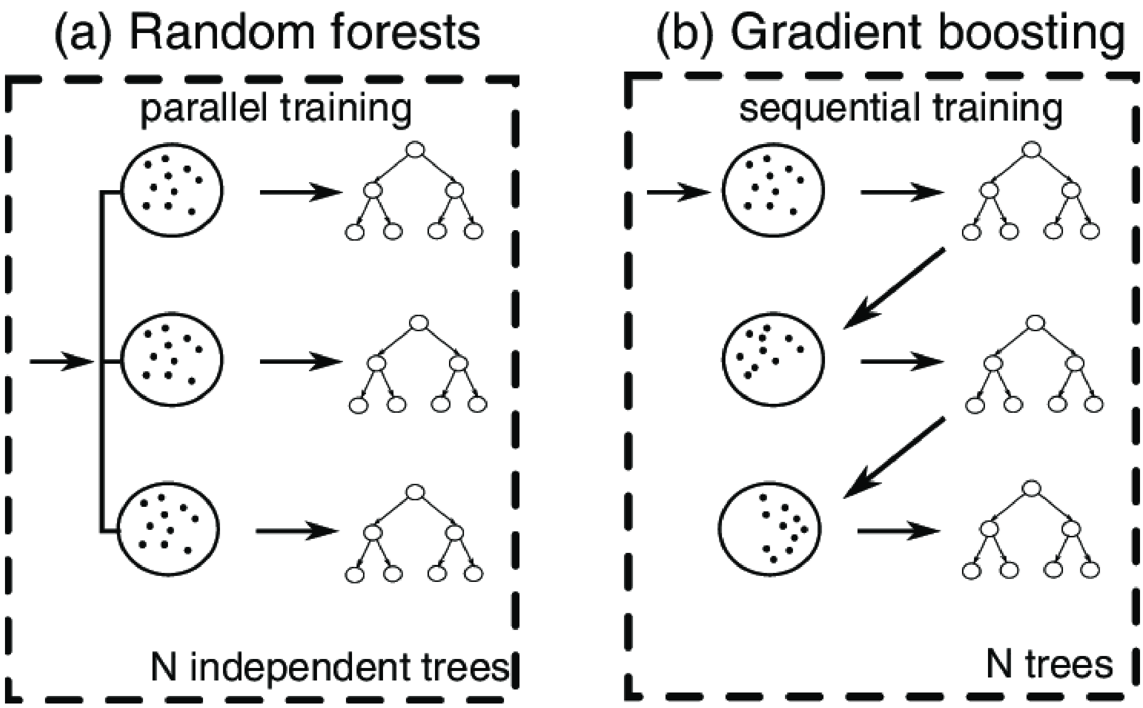

Figure 9. Comparison between random forest and gradient boosting training. Adapted from [93].

2.6.3 Support Vector Regression

Support Vector Machines were originally introduced by Cortes and Vapnik [94] as maximum-margin classifiers: given a labelled dataset, an SVM finds the hyperplane that separates classes with the largest possible margin, thereby maximising generalisation to unseen data. The extension to regression (Support Vector Regression (SVR)) was formalised by Smola and Scholkopf [95] and operates by fitting a function within an ε-insensitive tube around the training data, penalising only predictions that deviate from the target by more than ε. This formulation encourages a sparse solution in which only the training points lying outside the tube (the support vectors) influence the final model.

For non-linear regression problems, SVR employs the kernel trick: rather than explicitly mapping inputs into a high-dimensional feature space, a kernel function $k(x_i, x_j)$ implicitly computes the inner product between mapped feature vectors, enabling the algorithm to fit complex non-linear functions without prohibitive computational cost. Common kernel choices include the radial basis function (RBF) kernel, which measures similarity as a function of Euclidean distance in input space, and polynomial kernels. Hyperparameters (the regularisation parameter C, the tube width ε, and kernel parameters) are selected by cross-validation. A schematic of the tube fitting used in SVRs is presented in Figure 10, where a function f(x) is fitted against the data points with absolute distance equal or below the tube width.

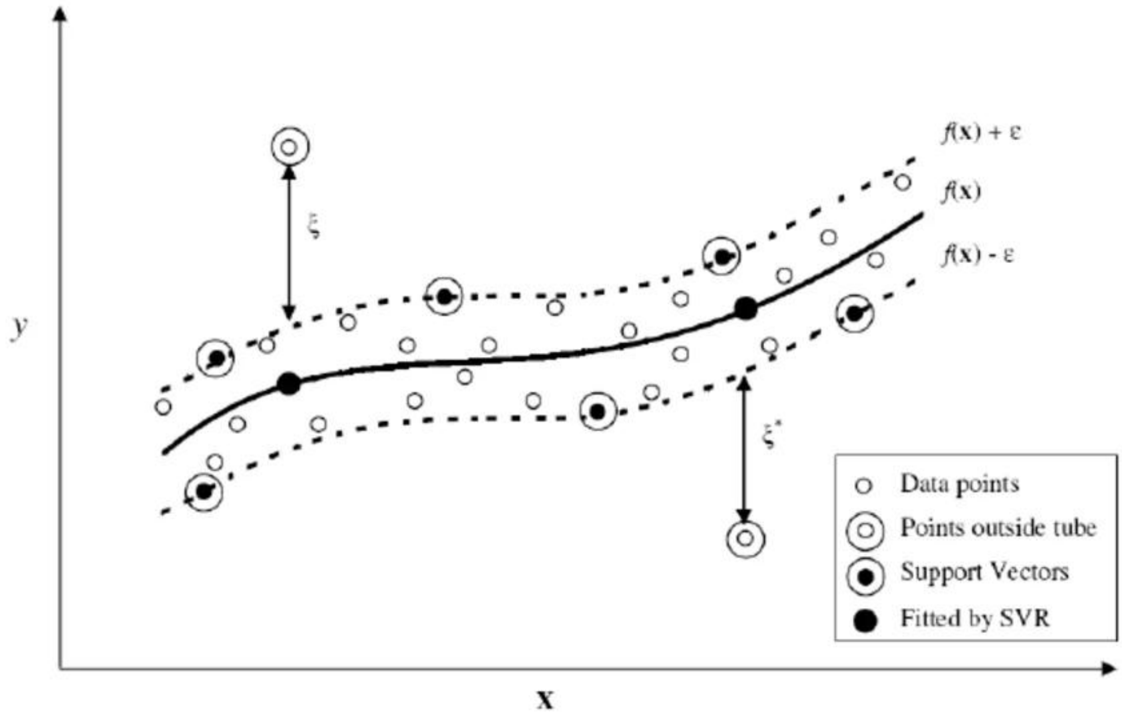

Figure 10. Support Vector Regression with ε-sensitive function. Adapted from [96].

SVR is particularly well suited to small datasets with high-dimensional feature spaces, where its margin-based objective provides strong regularisation. In Chapter 7, SVR forms one component of a stacked regression ensemble, contributing predictions that are combined with those of polynomial regressors under an ML framework.

2.6.4 Gaussian Process Regression

Gaussian Process Regression (GPR) is a non-parametric, probabilistic approach to regression that models the unknown function as drawn from a Gaussian process prior [97]. Rather than learning a fixed set of parameters, GPR uses all training observation to produce a posterior distribution over functions consistent with the data, yielding both a point prediction and a principled uncertainty estimate at every input location. The covariance structure of the process is governed by a kernel function (commonly the squared exponential or Matern family) whose hyper-parameters are optimised by maximising the log marginal likelihood of the training data. A simplified schematic for the estimation of the distribution in GPR, while accounting for uncertainty, is presented in Figure 11.

The uncertainty quantification property distinguishes GPR from deterministic regressors and is its primary motivation for use in this thesis. In Chapter 7, GPR is employed not as a primary regression method but as a data augmentation tool: a GPR model is fitted to the available experimental feature-geometry pairs, and synthetic training examples are drawn from the posterior predictive distribution. This expands the effective training set in a statistically principled manner, addressing the data scarcity inherent to experimental NDT programmes without introducing arbitrary assumptions about the underlying data distribution.

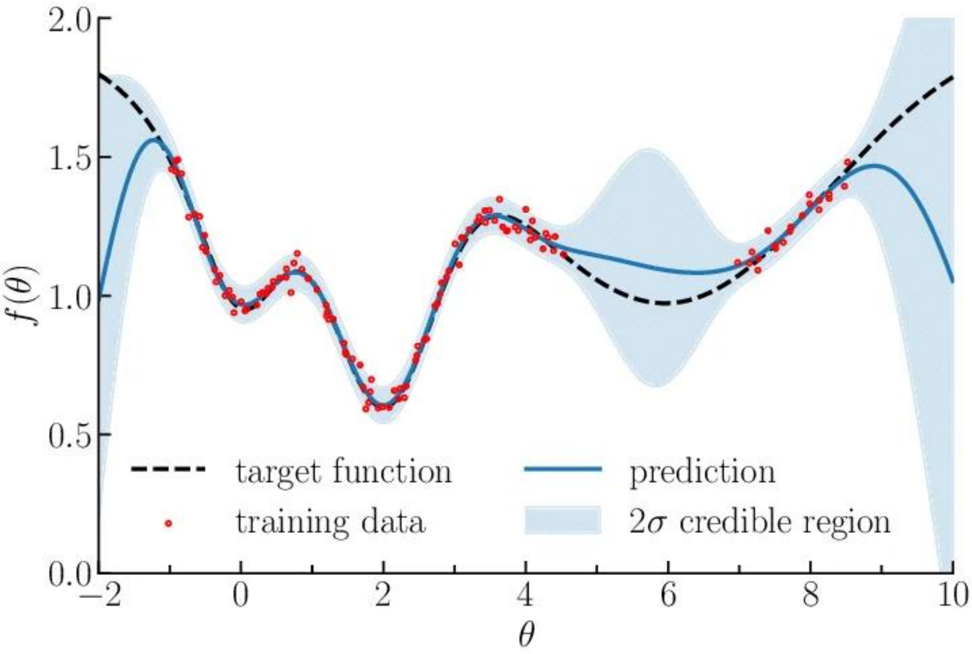

Figure 11. Illustration of GPR in one dimension. Adapted from [98]

2.6.5 Linear Regression Methods: OLS, Ridge, and Lasso

The simplest parametric approach to supervised regression assumes a linear relationship between input features and the target variable. Ordinary Least Squares (OLS) regression estimates model coefficients by minimizing the sum of squared residuals between predicted and observed outputs [99]. While OLS is computationally efficient and yields unbiased estimates under standards assumptions, it offer no regularisation and is therefore susceptible to high variance when features are correlated or the training set is small relative to the feature dimensionality.

Ridge regression [100] addresses this limitation by augmenting the OLS objective with an L2 penalty term proportional to the squared magnitude of the coefficients. This shrinks all coefficients continuously towards zero, reducing variance at the cost of a small, controlled increase in bias. Crucially, Ridge retains all input features in the model, making it well suited to problems where many features contribute weakly but collectively to the prediction.

The Least Absolute Shrinkage and Selection Operator (LASSO) [101] instead applies an L1 penalty on the absolute magnitude of the coefficients. The geometric properties of the L1 constraint induce exact sparsity: coefficients of uninformative features are driven to precisely zero, yielding simultaneous regularisation and automatic feature selection. This property is particularly advantageous in high-dimensional feature spaces where interpretability and parsimony are desirable.

2.7 Summary

This chapter has presented the foundational knowledge regarding the thesis chapters. Initially, a brief introduction of welding processes and the mechanism and distinctions of LOSWF were detailed. Then, different NDE methods and their limitations were highlighted, as well as the advantages of ultrasonic imaging. This was followed by the fundamental wave propagation physics, including wave modes, Snell's law for oblique incidence, acoustic impedance and attenuation. The beam forming capabilities and the focusing capabilities of FMC/TFM modality, as well as applied signal processing were presented. The error sources of robotic ultrasonic inspection, as well as a brief overview of ML algorithms that will be used are presented, as direct background to Chapters 5 and 7.

The remainder of this thesis will use the background presented here for the following identified gaps, which will be addressed in the following chapters:

a) in-process LOSWF monitoring using ultrasonic imaging, addressed in Chapter 4
b) characterisation of error for robotic ultrasonic inspection and interaction of robot positioning with ultrasonic coverage, addressed in Chapter 5
c) lightweight data management and orientation extraction for FMC data to enable in-process, multi-modal inspection, addressed in Chapter 6
d) geometry sizing using ultrasonic imaging, while circumventing traditional limitation of amplitude and TOFD methods, addressed in Chapter 7.

3. Experimental Infrastructure and System Integration

This chapter introduces the integrated robotic welding and inspection platform used throughout this thesis. The system architecture combines automated arc welding, robotic phased array ultrasonic imaging, and multi-modal data acquisition into a unified cell, enabling both in-process monitoring and offline inspection of LOSWF experiments. All experimental work presented in Chapters 4 through 7 was conducted using the infrastructure described here, with chapter-specific configurations noted in the respective methodology sections. The main contribution of this chapter is the miniaturisation of existing software within a compact workspace of 1500 x 1000 mm, based on previous work [74].

3.1 Overview of the Robotic Cell

The experimental platform is centred on a dual-robot cell configured for simultaneous or sequential tandem welding and ultrasonic inspection. The cell integrates two KUKA KR10 R1100 [102] industrial manipulators, an arc welding subsystem, a phased array ultrasonic acquisition unit, and a suite of ancillary sensors including a force-torque sensor and a camera for weld pool monitoring. A Proportional-Integral-Derivative (PID)-based force control loop maintains a set probe coupling force throughout scanning, ensuring repeatable dry-coupled contact conditions without the need for liquid couplant at the sample surface. Figure 12 provides an overview of the cell, showing the spatial arrangement of the inspection and welding robots with preheating equipment on the Siegmund welding table.

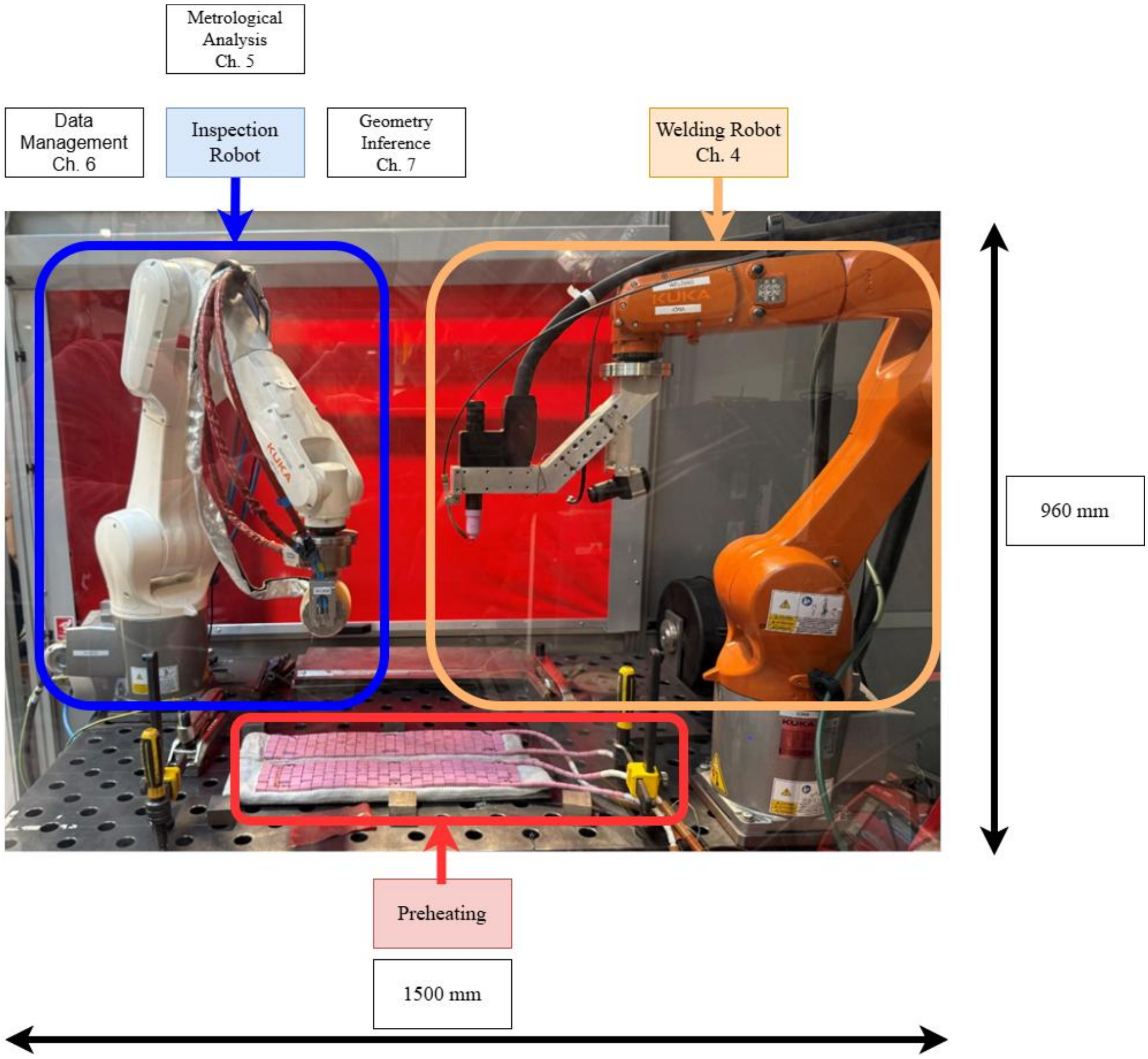

Figure 12. Overview of the dual-robot welding and inspection cell at CUE, University of Strathclyde. The white KUKA KR10 inspection robot (blue boundary, left) carries the RollerProbe end-effector, while the orange KUKA KR10 welding robot (orange boundary, right) carries the GTAW torch assembly. Preheating blankets on the Siegmund welding table are visible in the foreground.

The integrated control architecture is shown in Figure 13. Both subsystems are coordinated through a central laptop running LabView. The welding subsystem is orchestrated via a National Instruments Compact RIO real-time controller, which sequences process parameters and issues motion commands to the welding robot over the KUKA RSI [103]. The inspection subsystem operates through the PEAK-NDT LTPA [104] acquisition unit, which triggers the acquisition from the laptop and returns ultrasonic data. A welding camera mounted on the torch assembly provides continuous video feed for weld pool monitoring, and force feedback from the ATI force-torque sensor is used with PID control for the inspection robot controller to regulate probe coupling force. Two calibrations were conducted: static, to ensure consistent response from known reflectors, and dynamic using a block with embedded defects, to ensure coupling and tire condition.

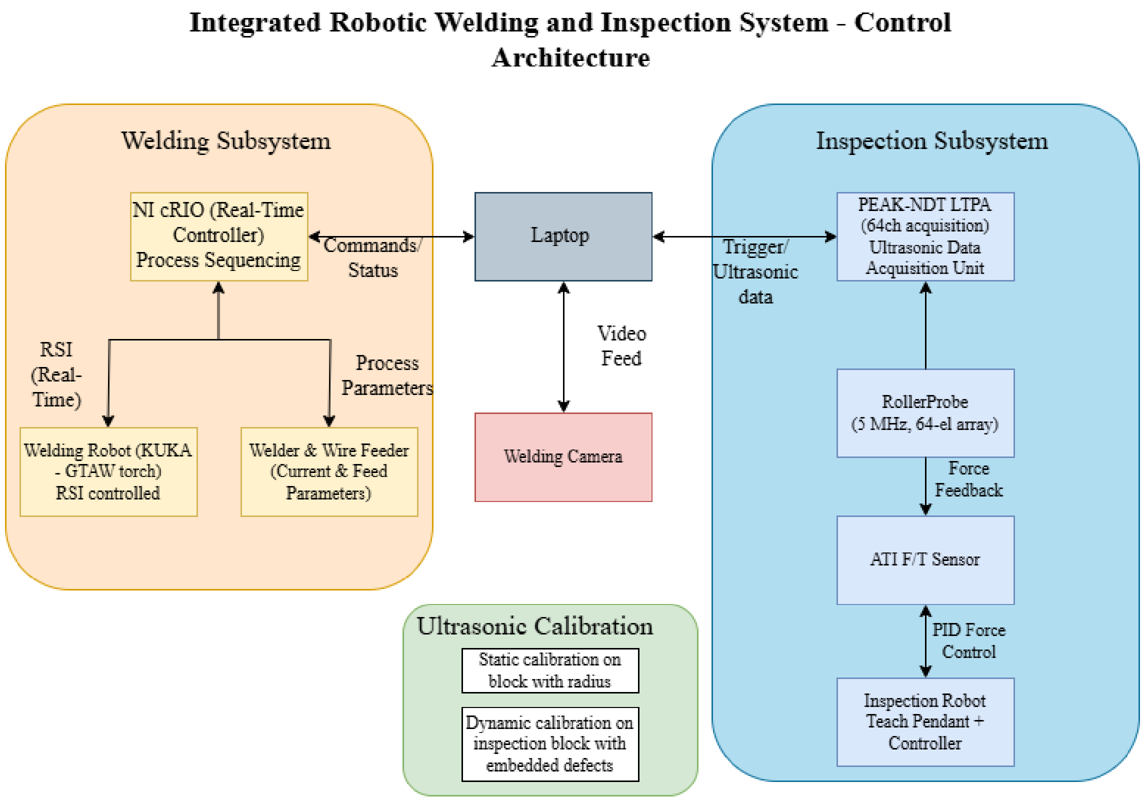

Figure 13. Control architecture of the integrated robotic welding and inspection system. The central laptop coordinates both subsystems: the welding subsystem (left, orange) via the NI cRIO real-time controller and RSI link to the KUKA welding robot; and the inspection subsystem (right, blue) via trigger signals to the PEAK-NDT LTPA

acquisition unit. Force feedback from the ATI F/T sensor closes the PID loop at the inspection robot programmed with a teach-pendant.

The architecture supports three distinct operational modes used across this thesis: (i) post-weld robotic inspection at room temperature (Chapter 4 and 5); (ii) in-process monitoring with a statically mounted wedge probe during active welding (Chapter 4); and (iii) dynamic robotic FMC scanning for geometry estimation and machine learning inference (Chapters 6 and 7). The modular nature of the cell allows the welding and inspection robots to operate independently or in a tandem configuration with zero separation between torch and probe.

3.2 Robotic Manipulators

Two six-degree-of-freedom KUKA KR10 (6-DOF) industrial articulated robots are deployed within the cell. These have a maximum payload of 10 kg, a maximum reach of 1101 mm, and a weight of approximately 56.5 kg [105]. The primary inspection manipulator is a KUKA KR10 R1100, which carries the phased array RollerProbe end-effector and force-torque sensor assembly. The KR10 executes preprogrammed scanning paths over test specimens. The complete inspection end-effector stack; composed of the KUKA KR10 arm, ATI force-torque sensor, RollerProbe, and PEAK LTPA acquisition unit; is shown in Figure 14.

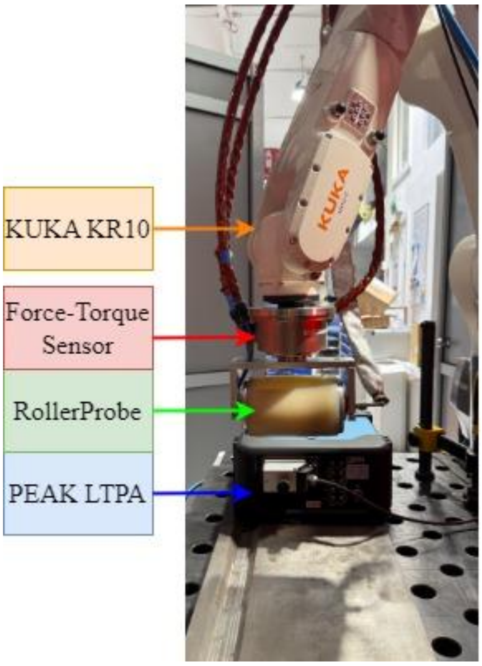

Figure 14. KUKA KR10 inspection manipulator with the complete end-effector assembly. From top to bottom: the KUKA KR10 arm, ATI force-torque sensor (red), RollerProbe phased array transducer (green), and PEAK-NDT LTPA acquisition unit (blue).

The welding manipulator is also a KUKA KR10, which carries a bespoke torch assembly, which is composed of a wire feeding nozzle, a non-consumable tungsten electrode, and a welding camera, as shown in Figure 15. The GTAW welding robot is externally controlled using a bespoke LabView virtual instrument, and the motion commands are issued through the KUKA RSI.

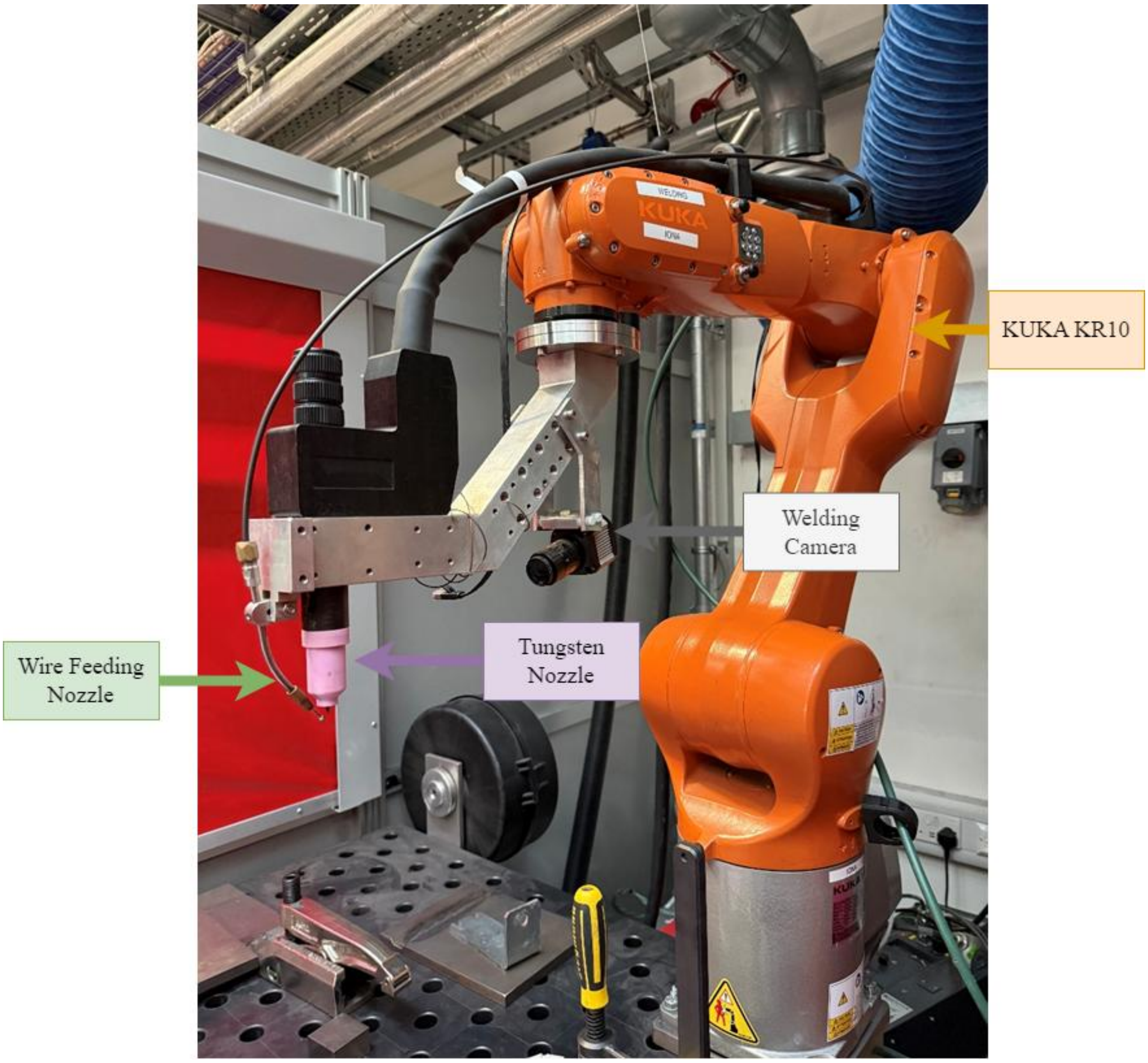

Figure 15. KUKA KR10 welding manipulator with bespoke GTAW torch assembly. The wire feeding nozzle (green arrow), non-consumable tungsten electrode nozzle (purple arrow), and welding camera (gray box) are identified.

A third manipulator, external to the welding cell, is the KUKA KR210 R2700, used exclusively for laser scanning metrology during ground truth acquisition. A MicroEpsilon scanCONTROL 2910-100 laser profilometer is mounted as its end-effector, and the system is positioned to scan test specimens, as shown in Figure 16. The larger payload and reach of the KR210 provide the stability necessary for precise surface profile measurements over extended scan lengths.

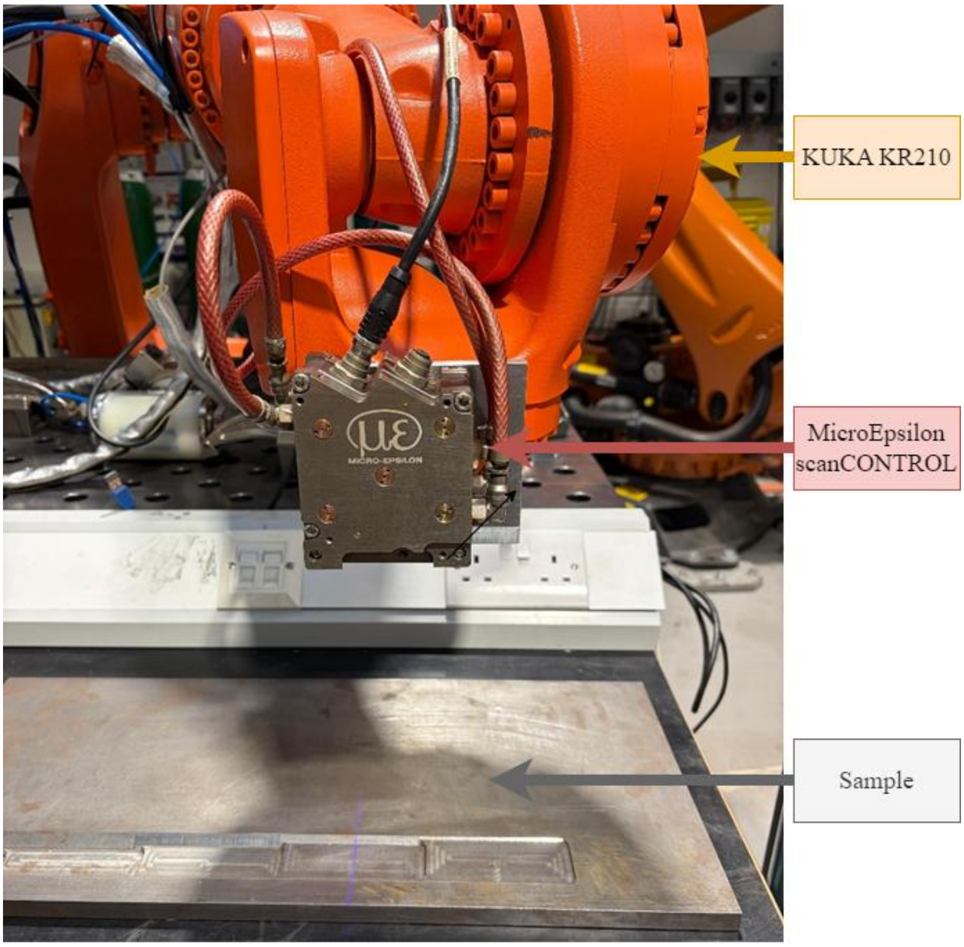

Figure 16. KUKA KR210 R2700 laser metrology robot with MicroEpsilon scanCONTROL 2910-100 laser profilometer mounted as its end-effector. The robot is shown positioned above a carbon steel sample on the table for ground truth profile acquisition, as used in Chapter 5.

The metrological performance of the inspection robot is characterised in detail in Chapter 5. In summary, robot-induced metrological error arises from a combination of errors inherent to robotic manipulators, such as link deflection and gear backlash, as well as suboptimal selection of ultrasonic inspection modality for geometry characterisation, where linear scans provide higher accuracy for larger geometries. These errors are not treated as noise but are systematically quantified using residual analysis and regression analysis of robot and ultrasonic features, enabling the robot to function as a metrological instrument rather than a passive probe carrier.

3.3 Welding Equipment and Process Configuration

Arc welding deposition is performed using a GTAW torch mounted on a dedicated robotic arm configured for depositing on S275 carbon steel plate specimens, described in Section 3.2. The welding system supports programmable torch path deviation, enabling the deliberate creation of LOSWF defects by laterally offsetting the arc from the bevel face during deposition. This capability is exploited in Chapter 4 for controlled sensitivity studies. The welding power source is a Jäckle 350AC welder. Wire feeding is managed by a dedicated wire feeder unit, and filler material is supplied from an ER70S 1.2 mm wire spool. These components are shown in Figure 17.

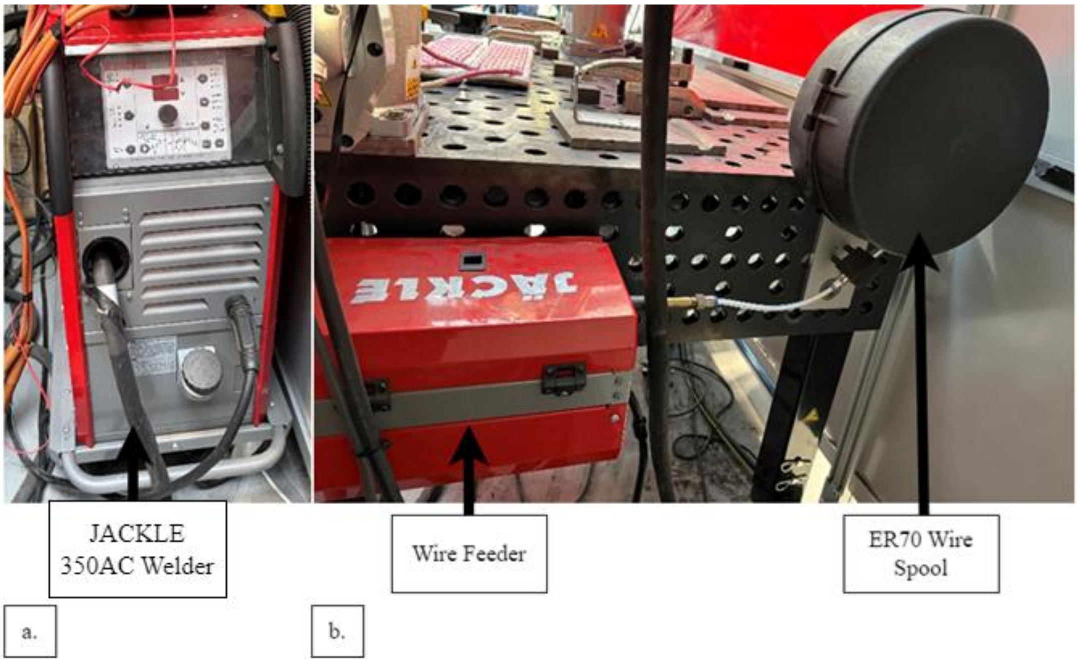

Figure 17. Welding equipment assembly: (a) JACKLE 350AC welder; (b) Wire feeder unit (left) and ER70S 1.2 mm filler wire spool (right), positioned adjacent to the robotic cell.

3.4 Phased Array Ultrasonic System

3.4.1 Acquisition Hardware

Ultrasonic data acquisition is performed using a PEAK-NDT LTPA system with 64 independent transmission-reception channels, shown in Figure 18. The standard acquisition parameters used throughout this thesis are: centre frequency of 5 MHz, 64 elements, element pitch of 0.5 mm, array elevation of 10 mm, pulse repetition frequency (PRF) of 2.1 kHz, excitation voltage of 200 V, and sampling frequency of 100 MHz.

The PRF value was selected to minimize interference from robotic motors, the excitation was selected due to loss of acoustic energy at the roller probe tire, and the array characteristics were selected in order to compatibility with the mechanical assembly of the roller probe, and ensure minimization of the effect of temperature gradient on the attenuation. Gate and gain setting are configured per-experiment as detailed in the respective chapter methodology section, reflecting the selected modality. The gain was selected per modality, as a gain of 70 dB was needed for FMC data acquisition due to single element transmission, and for sector scans due to deviation of extreme angles (30° and 60°) from nominal geometry (45°). Linear scans required the least amount of gain (40-50 dB), due to matching between transmission angle (45°) and nominal geometry (45°). For in-process experimentation, it was determined through experimental trials that linear scans with increased gain (70 dB) to account for change in attenuation due to thermal gradient were sufficient, as shown in Chapter 4.

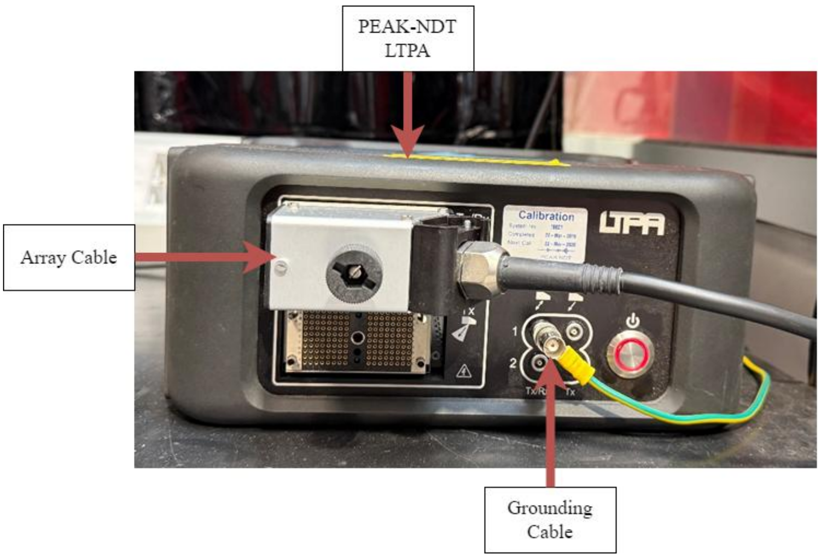

Figure 18. Front view of PEAK-NDT 64-channel phased array acquisition unit. The array cable connector (left) is connected with the array embedded in the RollerProbe transducer, while the grounding cable (bottom) provides electromagnetic shielding.

3.4.2 The RollerProbe End-Effector

Robotic ultrasonic scanning is performed using a custom phased array RollerProbe, developed at the University of Strathclyde [87]. The RollerProbe integrates a 5 MHz, 64-element piezoelectric array within a mechanical housing that couples ultrasonically to the specimen surface through a specialised polymer roller tyre, enabling dry-coupled contact inspection, as shown in Figure 19a. The internal wedge geometry produces a shear wave refraction angle of 55° into the material, with an array incidence angle of 38.3° relative to the wedge face, as shown in Figure 19b. These angles were selected, to minimize mode conversion of acoustic waves during the transition to the sample. This configuration supports high-temperature inspection capability up to 350°C, making it suitable for interpass and near-arc deployment.

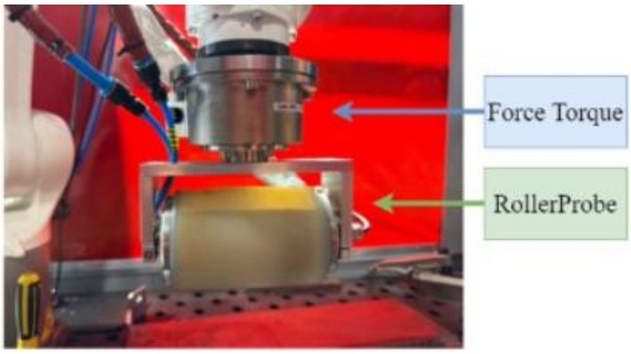

a

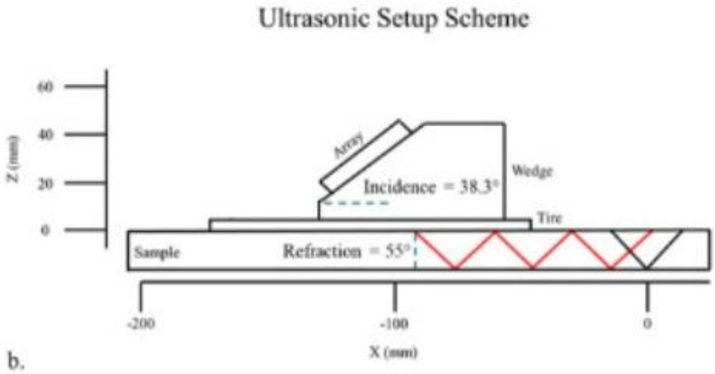

b.

Figure 19. (a) RollerProbe end-effector mounted on the KUKA KR10 inspection robot, with the ATI force-torque sensor (blue box) visible above and the RollerProbe with polymer tyre (green box). (b) Schematic of the ultrasonic setup, showing the wedge geometry, array incidence angle of 38.3º relative to the wedge face, and resulting shear wave refraction angle of 55º propagating into sample.

Consistent coupling during dynamic scanning is maintained by a Delta IP65 SI-165-15 ATI force-torque sensor mounted between the robot flange and the RollerProbe assembly. A PID control loop used force feedback to regulate the downward contact force, with a nominal set-point of 125 N unless otherwise specified. The sensor has a vertical force capacity of 495 N and a resolution of 1/16 N. This arrangement eliminates the variability in coupling associated with manual probe handling.

3.5 Test Specimens

3.5.1 Machined Surrogate Sample

The primary test specimen used in Chapters 5,6, and 7 is a precision-machined carbon steel plate (600 mm x 250 mm x 15.8 mm) fabricated from S275 bright steel, as shown in Figure 20a. The specimen incorporates five distinct stepped bevel levels that replicate the progressive joint fill sequence of a multi-pass 90° V-groove weld from the root pass to cap pass, following the weld geometry established in prior work [40]. The five bevel lengths; 16.69 mm, 13.15 mm, 9.62 mm, 6.08 mm, and 2.39 mm; correspond to decreasing weld fill at depths of 11.80, 9.30, 6.80, 4.30, and 1.69 mm respectively, as shown in Figure 20b.

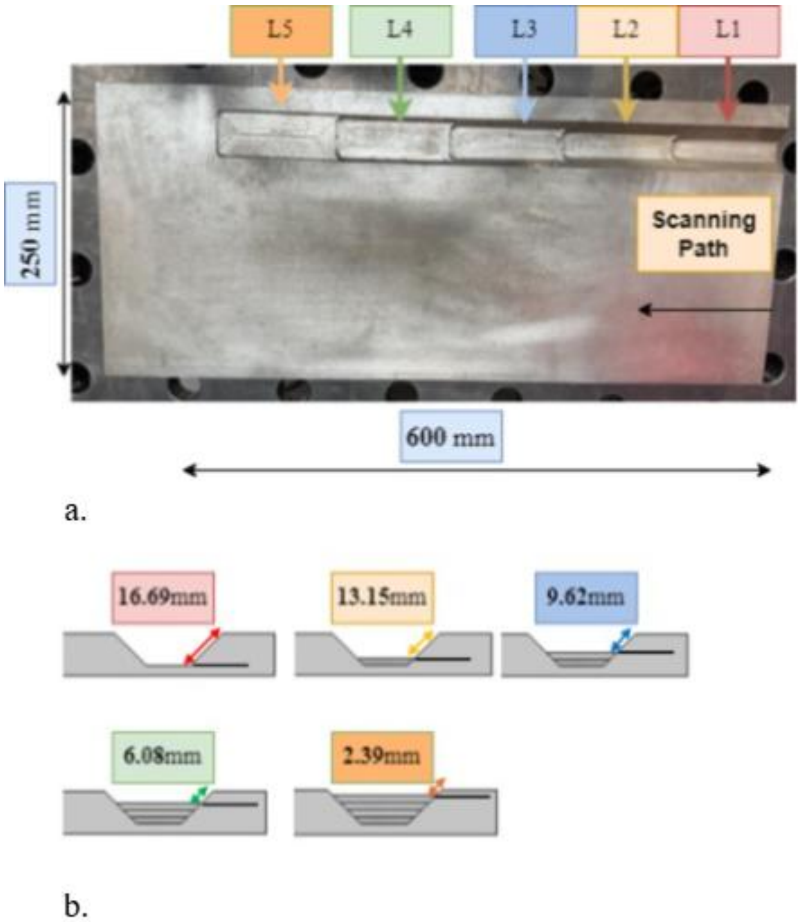

Figure 20. Precision-machined carbon steel surrogate specimen (600 mm x 250 mm x 15.8 mm). (a) Photograph showing the five stepped bevel levels L1-L5 machined into the plate and the robotic scanning path direction. (b) Cross-sectional schematic of each step, illustrating the five bevel lengths (16.69 mm, 13.15 mm, 9.62 mm, 6.08 mm, and 2.39 mm) corresponding to progressive weld fill from root to cap pass.

The stepped geometry was selected to function as a deterministic surrogate for LOSWF geometries, decoupling robot-induced positioning errors from the stochastic thermal and metallurgical variability inherent to active welding. By replicating the geometric boundary of real fusion faces in a precision machined artifact, the specimen enables a controlled and repeatable uncertainty analysis applicable to a broader class of contact-based robotic inspection systems.

3.6 Computational Infrastructure

Signal processing and machine learning pipelines are implemented in MATLAB and executed on a Dell Precision 5570 laptop with the following specifications: Intel Core i7-12800H (14 cores, 4.8 GHz), NVIDIA RTX A2000 GPU (8 GB, GDDR6), and 32 GB DDR5 Random Access Memory (RAM) (4800 MHz). The two-stage processing pipeline; (Central Processing Unit) CPU-based FMC compression followed by GPU-accelerated bevel orientation estimation; is described in detail in Chapter 6, with the machine learning extension for continuous bevel length regression in Chapter 7. Per-frame execution times of approximately 150 ms (compression) and 100 ms (orientation estimation) were achieved on this hardware, supporting real-time operation during robotic scanning at 4 frames per second. It should be noted that MATLAB was selected to maintain consistency with the existing imaging codebase, and ensure maintainability.

3.7 Summary

This chapter has described the integrated robotic welding and inspection platform that underpins all experimental work in this thesis. The cell combines an inspection robot carrying a custom RollerProbe end-effector and a force-torque feedback control, a PEAK-NDT LTPA acquisition, a GTAW welding robot with a welding camera, and external cooling for the RollerProbe into a unified infrastructure for in-process and offline weld quality assurance. The modular architecture supports static in-process monitoring, dynamic robotic scanning, and dual-robot tandem operation. Chapters 4 through 7 each draw on this infrastructure with experiment-specific configurations. For external metrology and ground truth validation, a laser profilometer mounted on a robot was used, as will be discussed in Chapter 5.

4. Evaluation of Signal Disturbance and Recovery in Phased Array Ultrasonic Inspection During Welding

4.1 Introduction

The evolution toward intelligent manufacturing systems has positioned welding automation as a cornerstone of Industry 4.0 transformation, where real-time quality assurance becomes essential for autonomous production environments. Modern manufacturing demands have driven the integration of cyber-physical systems that bridge physical welding processes with digital intelligence, enabling immediate process adjustments based on quality feedback. However, the transition from post-process inspection to in-process monitoring presents significant technical challenges, particularly for detecting critical defects that compromise structural integrity during fabrication.

Welding remains a fundamental joining technique in the fabrication of large-scale infrastructure such as pipelines, pressure vessels, offshore platforms, and modular structural assemblies. The long-term reliability and load-bearing capacity of these structures hinge on the integrity of their welded joints. Among the various defect modes encountered in multi-pass welding, LOSWF represents one of the most critical quality concerns due to its potential to weaken interlayer bonding, resulting in premature failure under cyclic loading or stress corrosion conditions [53], [106]. LOSWF typically manifests in narrow-groove geometries where accessibility is restricted, and poor arc control or surface contamination may cause incomplete melting of the sidewall [106]. The economic impact of undetected defects is substantial—with welding representing up to 40% of total fabrication costs and defect-related repairs costing 2-3 times the original fabrication expense. Therefore, there is urgent industrial need for real-time quality assurance systems [107], [108].

Despite decades of advancement in NDT, traditional inspection methods such as VT, and RT are inherently limited in their ability to detect interpass and subsurface defects like LOSWF during active welding. Visual inspection remains surface-dependent and incapable of identifying flaws buried within multilayer welds [34], [39]. Radiographic techniques, although suitable for planar flaw detection, struggle with fusion-type defects due to their limited volumetric sensitivity and orientation dependence [109]. These limitations create a critical gap between manufacturing requirements and quality assurance capabilities, often delaying defect discovery until post-weld inspection when repair costs escalate dramatically [110].

The convergence of intelligent manufacturing paradigms with advanced sensing technologies has created unprecedented opportunities for embedded quality assurance systems. For multi-pass welding operations, in-process detection of interpass flaws like LOSWF becomes particularly critical before subsequent layers obscure the defects [87], [111]. Automated and robotic welding systems further necessitate embedded inspection methods that provide timely feedback to prevent defect propagation and enable adaptive process control [111]. Phased Array Ultrasonics offers unique advantages for this application through its volumetric imaging capability, electronic beam steering, and high spatial resolution [112]. However, deployment of ultrasonic imaging for real-time weld monitoring remains technically challenging due to thermal gradients, electromagnetic interference, and probe coupling instability in high-temperature welding environments [113], [114].

Recent research efforts have focused on advancing process-integrated NDT through controlled creation and detection of artificial defects to evaluate phased array system sensitivity under realistic welding conditions. These artificial flaws are commonly embedded within calibration blocks or fabricated in mock-up welds to simulate interpass conditions and benchmark detectability thresholds [115], [116]. Such experimental approaches enable systematic evaluation of probe configurations and acoustic response characteristics under known defect scenarios [117], [118]. Parallel investigations explore the effects of probe positioning, wedge design, and thermal interference on signal integrity during live welding, often utilizing B-scan imaging to visualize signal damping and recovery behaviour [40], [119].

Phased array imaging utilizes multiple transducer elements that can be excited in programmed sequences (focal laws) to synthesize ultrasonic beams. Unlike conventional single-element probes, phased arrays can perform linear scans, where the active aperture is electronically stepped across the array, enabling coverage of a large inspection surface without mechanical probe movement. In weld fusion inspection, this approach is particularly effective when the expected defect location and orientation are known a priori [120]. In this study, a 45° linear scan was employed to insonify the sidewall region with reduced gain requirements due to incidence with the 45° bevel to maximise amplitude, ensuring reliable detection of lack-of-sidewall-fusion defects while maintaining sensitivity under high-temperature welding conditions.

In previous studies, [74], [121], the capability for PAUT monitoring in both welding and human-robot interaction for additively manufactured components was established. Recent studies (2024-2025) have advanced multi-sensor frameworks for real-time weld quality monitoring by integrating vision, thermal, acoustic, and electrical sensing with deep learning and attention-based models. For instance, He et al. [122] implemented an open-source, multi-robot directed energy deposition framework incorporating in-process thermal imaging, laser scanning, acoustic, and electrical sensors for adaptive process control and post-printing metrology. While ultrasonic testing was referenced for geometry evaluation and NDE, it remained confined to post-pass inspection rather than arc-on sensing. Beyond welding, Mohamed et al. [123] demonstrated ultrasonic-driven adaptive control in robotic plasma cutting, where real-time ultrasonic thickness sensing informed bevel geometry and cutting parameters. However, the sensing occurred prior to or between cuts rather than during an active fusion process, distinguishing it from true arc-on ultrasonic monitoring. Despite these advances, subsurface defect detection remains limited to inspection stages removed from area of dynamic welding conditions. Ultrasonic testing continues to be applied post-pass, inter-pass, and during welding for solidified material, with notable exceptions [40]. This absence underscores a critical research gap —the integration of ultrasonic imaging into arc-on approaches for real-time detection of LOSWF and similar fusion defects.

This study presents a novel integrated approach combining real-time phased array ultrasonic monitoring with systematic artificial defect validation to advance in-process LOSWF detection capabilities. First, a static wedge probe was positioned ahead of the welding torch enables real-time B-scan visualization of sidewall fusion during active welding. This approach captures transient signal loss and recovery patterns that correlate directly with weld pool interference and material solidification, providing an immediate proxy for fusion quality assessment. Second, controlled sensitivity studies using artificially introduced LOSWF defects was conducted in conjunction with a robotic RollerProbe inspection to establish detection thresholds and validate signal interpretation under realistic multi-pass geometries. The integration of real-time monitoring with confirmatory post-process validation represents a significant advancement toward fully autonomous welding quality assurance systems. This is the first systematic integration of real-time interpass PAUT monitoring with artificial LOSWF calibration protocols, establishing foundational capabilities for embedded inspection in intelligent welding manufacturing workflows.

4.2 Welding Parameter Trials

Initial trials consisted of bead-on-plate welding to identify process parameters that produced consistent weld morphology and favourable penetration characteristics. The goal was to obtain tall, uniform beads with minimal ripple effect, enabling reliable sidewall inspection and deliberate defect generation. A range of Travel Speeds (TSs) and wire feed rates were explored, as shown in Table 2, and visual inspection was used to identify stable operating conditions, as shown in Figure 21. The optimized parameters were subsequently used both to induce artificial LOSWF and to conduct in-process monitoring trials under consistent welding conditions. After establishing stable welding parameters, controlled defects are introduced to validate the sensitivity of the system offline and during welding. Programmed torch deviation was used to generate reproducible LOSWF flaws, enabling direct assessment of detection sensitivity and correlation between signal response and fusion integrity.

Parameters	**Units**	**Process Values**
Wire Feed Speed (WFS)	mm/min	[456, 563, 670, 777, 884]
Travel Speed (TS)	mm/min	[95, 111, 127]
Current (Curr)	A	[166, 182, 198]

Table 2. Process parameters for bead-on-plate experimentation

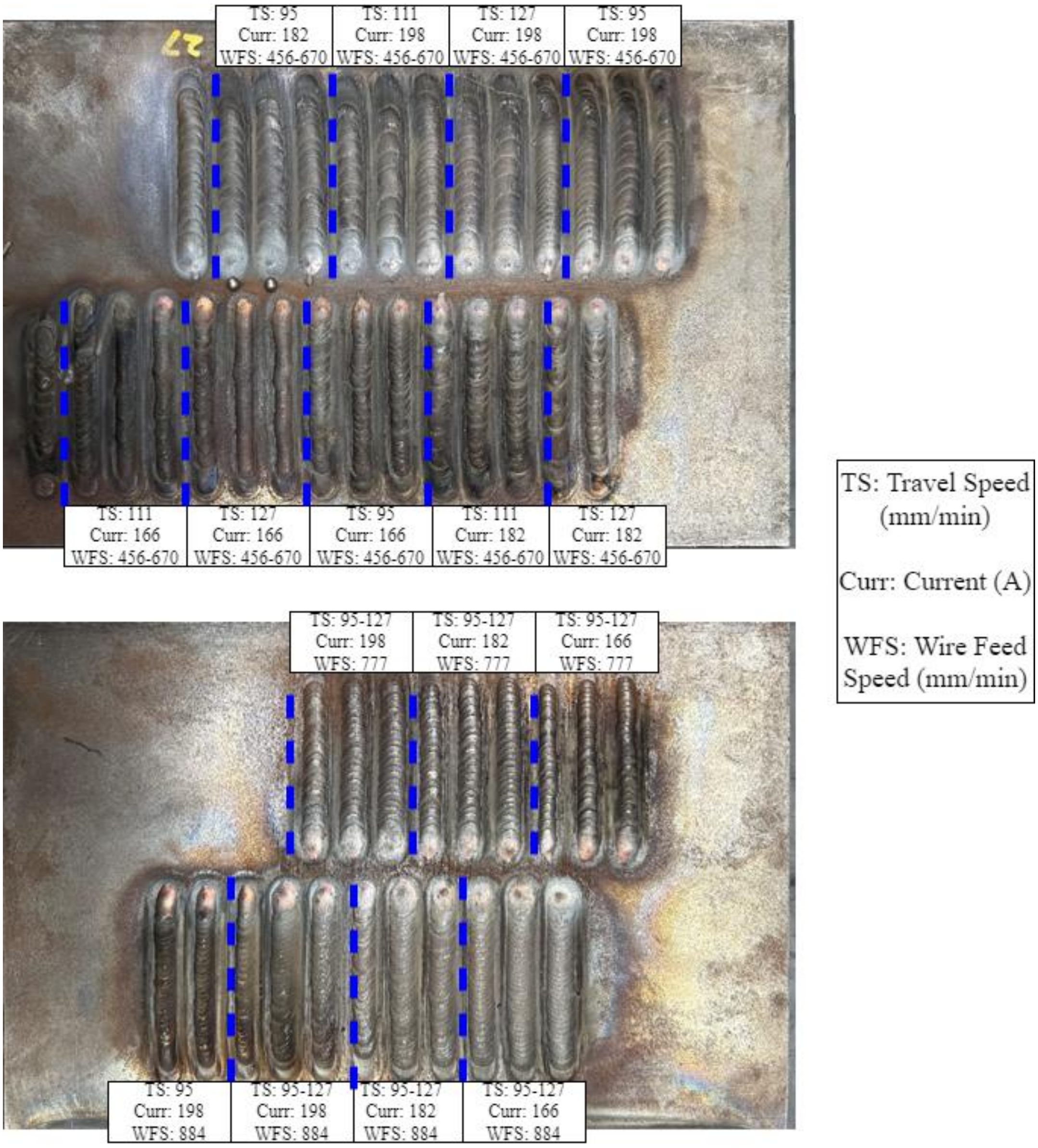

Figure 21. Bead-on-plate weld matrix used for process parameter tuning. Welds were deposited on S275 steel using varying heat inputs to evaluate bead shape and sidewall engagement.

as shown in Figure 22b, where the live weld pool visibly deviates from its nominal path, as shown in Figure 22a. A sinusoidal weaving path was applied using a weaving frequency of 0.3 Hz and an amplitude of 2.2 mm, which determined the lateral oscillation rate and maximum deviation of the torch from the weld centerline. This motion facilitated uniform heat distribution and consistent bead formation across the joint width. The procedure was carried out under process conditions previously optimized for stable penetration, ensuring that the observed defects were exclusively due to geometric mispositioning rather than erratic process variables. Two disturbances of 8 mm and one of 10 mm were introduced to analyse the sensitivity of ultrasonic imaging to LOSWF detection, measuring the distance between the middle of the weaving motion and the bottom corner as shown in Figure 22c.

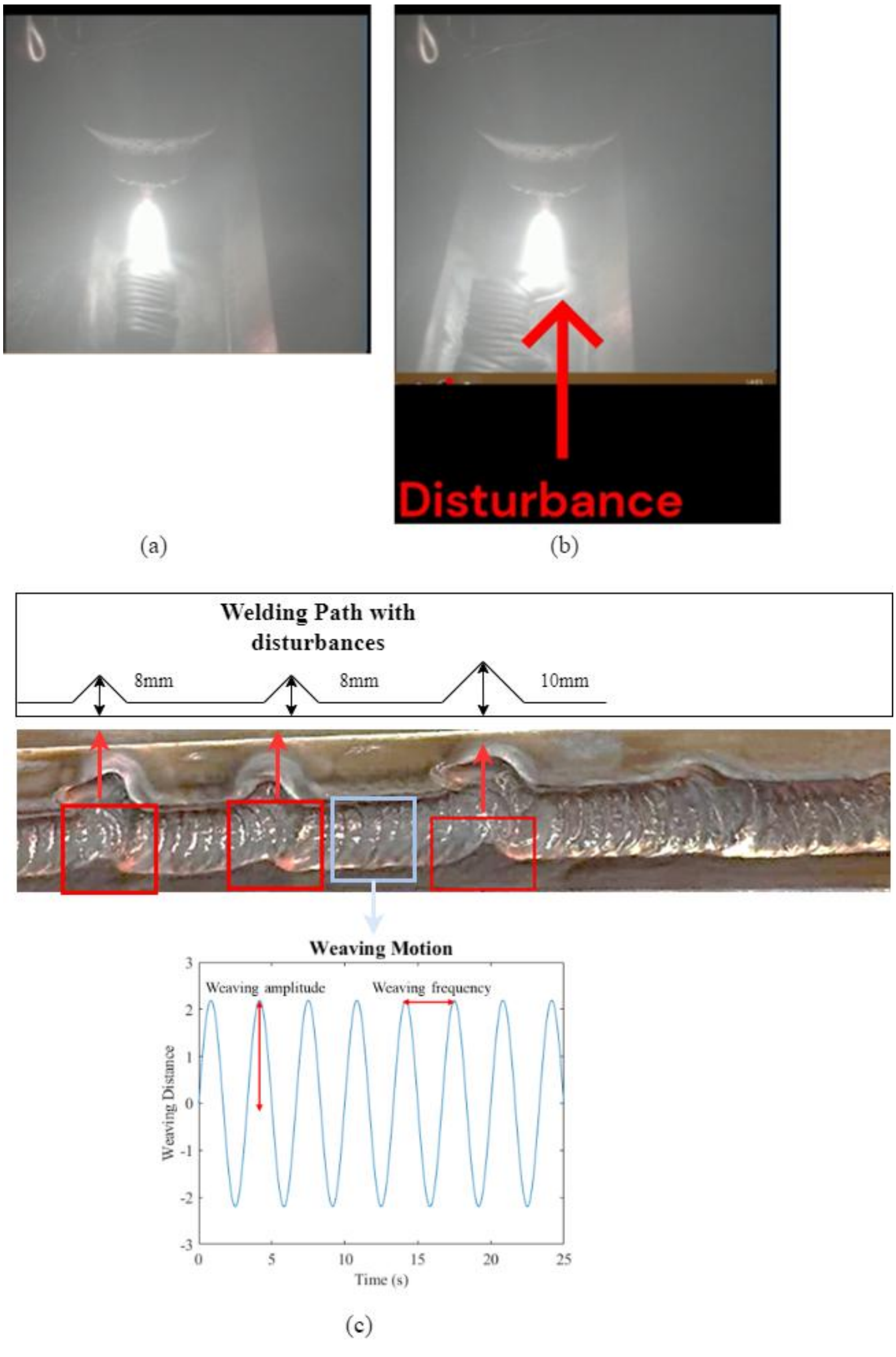

Figure 22. Illustration of welding disturbances and weaving motion during LOSWF generation. (a) Normal welding condition. (b) Welding under a disturbance showing visible path deviation. (c) Welding path schematic with disturbances of 8 mm and 10 mm.

4.4 Automated LOSWF & Post-Process Ultrasonic Detection

To verify the above LOSWF generation strategy, automated ultrasonic inspection was conducted after weld completion and at room temperature using a RollerProbe affixed to a 6-axis robotic arm. The RollerProbe was programmed to follow a single longitudinal path, offset by 40 mm from the plate edge to align the inspection line directly over the upper bevel corner—matching the location of the expected sidewall fusion defects, as shown in Figure 23a. A constant force-torque feedback loop with 125N of force ensured uniform coupling throughout the pass. Data was collected using B-Scans, enabling reconstruction of high-resolution C-scans. A gain of 35 dB, a subaperture of 8 elements, and single element spacing, and an inspection angle of 45° was used. Furthermore, a sampling rate of 100MHz, a voltage of 200V and a gate of 2000 to 4508 samples (40 to 90μs) was used. As shown in Figure 23b, zones corresponding to intentionally induced LOSWF defects showed echo amplitude size increase for -80 mm,-50 mm and-20 mm, validating the probe's sensitivity under static, room-temperature conditions. For cross validation, the sample was then scanned using a Micro-Epsilon Scan-Control 2910-100/B to establish a ground truth for ultrasonic sensitivity, as shown in Figure 23d. The minimum height was measured in a range of -12 mm to -4 mm, with a spatial resolution of 0.08 mm in the Y direction (welding direction), 0.03 mm in the X direction (bead width) and 0.01 mm in the Z direction (bead height), in order to establish the ground truth for disturbance depth relative to the base plate.

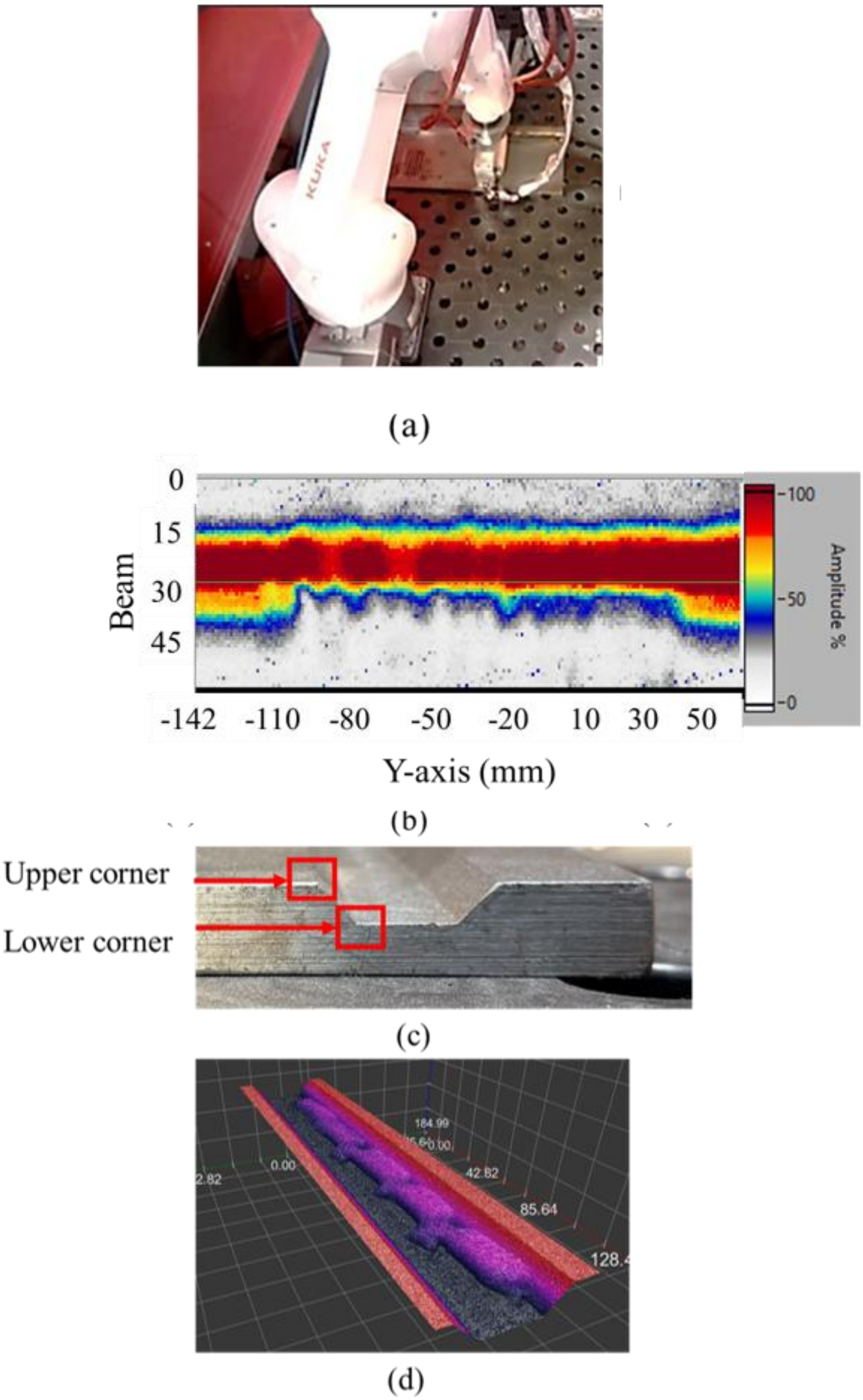

Figure 23. Post-weld robotic inspection using the roller-probe. (a) Live image during scanning. (b)Corresponding C-scan showing amplitude drop near weld centerline due to artificial sidewall fusion defect, (c) Bevel corner definition. (d) P.C. reconstruction

4.5 Automated Real-Time LOSWF Generation & Ultrasonic Detection

To then investigate the real-time ultrasonic detection of LOSWF during weld deposition, a single-pass weld was deposited while in-process ultrasonic inspection was was simultaneously performed. A 5 MHz, 64-element phased array probe was used, coupled to a high-temperature wedge designed to transmit ultrasonic waves at a nominal refracted angle of 55° into the material. In order to monitor the LOSWF, the 6dB drop method was used on the C-Scan to determine the position of the upper and lower bevel corner. The wedge was positioned with the front face 20 mm from the upper bevel corner. A steering angle of 45 degree, with longitudinal transmission mode, was selected to monitor the melt pool with a gain of 35dB, subaperture of 8 elements, single element spacing. Furthermore, a sampling rate of 100MHz, a voltage of 200V, a gate from 1800 to 2600 samples (36μs to 52μs), and no focusing was used. This configuration enabled real-time B-scan acquisition during welding (Figure 24b). The torch followed a 50 mm linear path without any deliberate deviation, ensuring stable thermal and geometric conditions, as shown in Figure 24a. The wedge was positioned in the middle of the bead, pointing to an index of 25mm to ensure even heat distribution at the start and end of the weld. Then, a trapezoidal disturbance was created, as shown in Figure 24c, to simulate LOSWF during welding. A distance of 5mm was selected between the edge of the bead and the bottom corner, in order to ensure full coverage of the bevel. This test served as a baseline to assess signal quality, interference effects, and the feasibility of live defect detection during robotic welding.

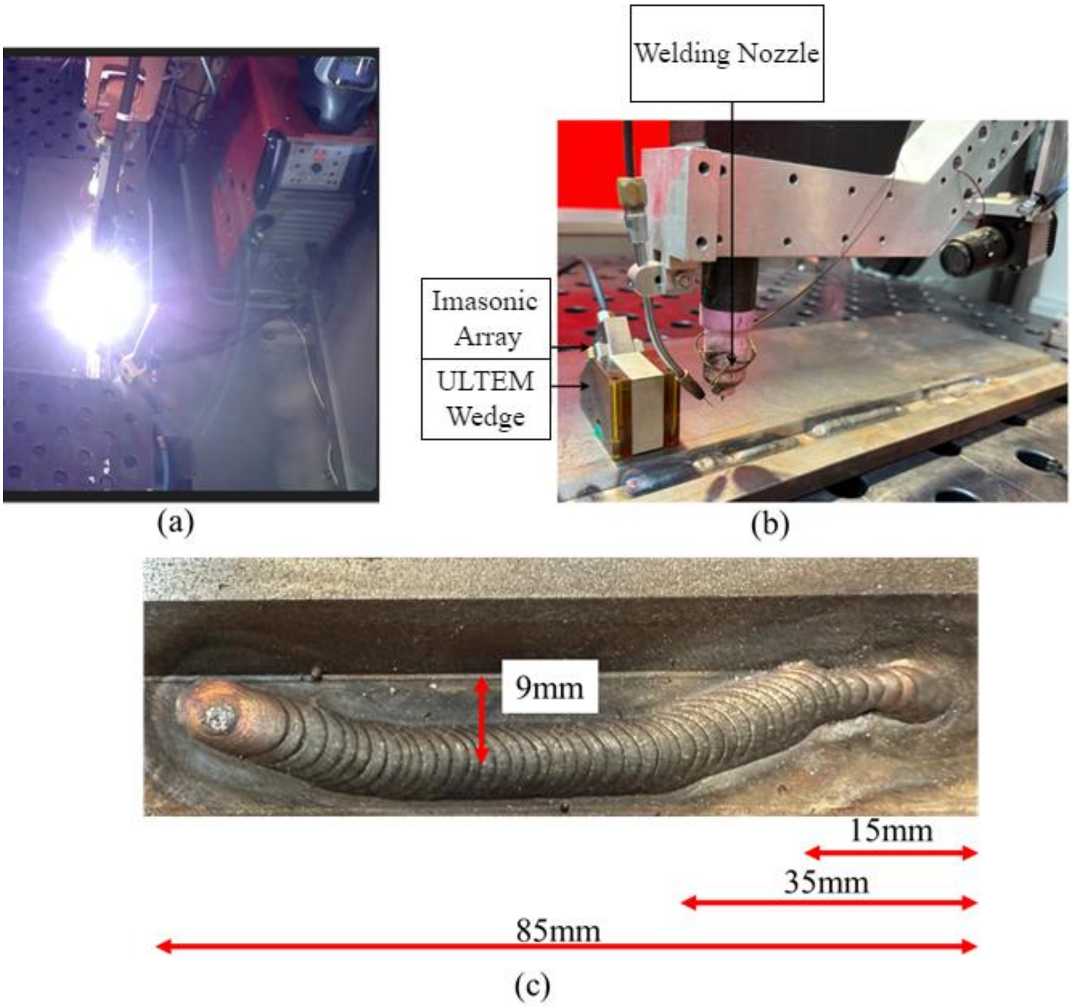

Figure 24. Composite view of in-process phased array experimental setup. (a) Robot-mounted TIG welding torch depositing a single bead during live ultrasonic acquisition. (b) Stationary ULTEM wedge housing a 5 MHz 64-element Imasonic probe positioned 20 mm. (c) In-process experiment with defect generation

4.6 Automated Real-Time LOSWF Ultrasonic Detection

To ensure that the selected welding conditions produced predictable and reproducible bead morphology, linear Least Absolute Shrinkage and Selection Operator (LASSO) regression was performed on the bead-on-plate trials across a range of travel speeds and wire feed rates. LASSO relies on L1 regularization for shrinkage of specific parameters [101], and was used in order to handle multicollinearity of polynomial terms, as quadratic and cubic expansions of process parameters were used. It was selected to retain only the subset of features with the highest predictive capability, while shrinking the coefficient of parameter combinations with minimal impact. Figure 25 shows the relationship between actual and predicted values from the regression models of weld width (Figure 25a) and cross-sectional area (Figure 25b). The width and height were manually measured using a vernier caliper across 5 different points of the bead to calculate the average, and the cross section area was calculated by considering the height and width, and calculating the elliptical area defined by them. The points were selected in increments of 15mm, to fully characterize dimensional deviation, starting 5mm after the start of the weld. Strong linear trends were observed across the full range of experimental conditions (7–11 mm in height, 30–80 mm^2 in cross-section), with strong statistical fits of 87.4% and 81.3% for width and cross section respectively, validating that weld geometry was a consistent function of input parameters on the deployed system. It should be noted that only R^2 was selected as a metric, as the goal was to find optimal fit and optimize to a single set of parameters, rather than evaluate the overall performance and measurement error. These results confirm that bead dimensions—particularly sidewall engagement—could be systematically manipulated and reproduced during both flaw induction and in-process inspection trials. The optimal selected parameters are 198A, 95 mm/min and wire feed speed of 884 mm/min for a bead height of 2.4mm, and width of 11.05mm. These parameters were selected based on visual evaluation of bead morphology to maintain process consistency and achieve an appropriate bead height, ensuring a detectable resolution above 2.0 mm for ultrasonic inspection and ensure sufficient bevel wetting. This was used as the basis for single bead geometry optimization for the process parameters, which were used for in-process experimentation and room temperature sensitivity analysis.

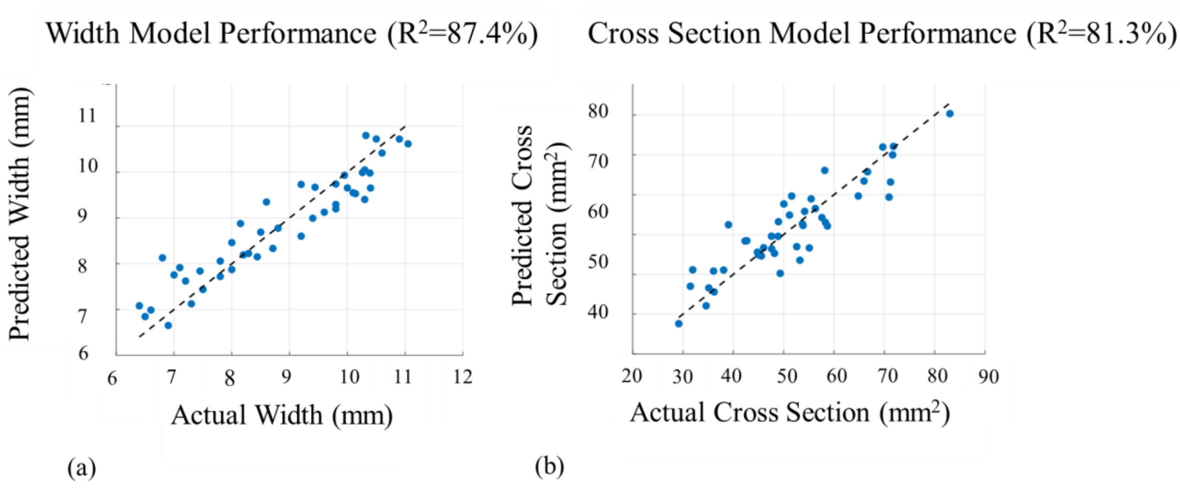

Figure 25. (a) Predicted versus actual weld bead width for bead-on-plate trials. (b) Predicted versus actual weld cross-sectional area for bead-on-plate trials.

To assess the detectability of artificial LOSWF defects, deliberate torch deviation was employed to locally shift the arc away from the fusion face during deposition. As shown in the image (Figure 26c), the resulting bead exhibited visible underfill and inconsistent wetting near the sidewall, confirming successful defect induction. A corresponding plot of bevel length across the weld (Figure 26a) shows a clear negative spike in profile deviation at the same Y-position, verifying that the defect was also geometrically distinct. Depending on the lateral offset, the disturbance depth changes from 2 to 4 mm, with the same disturbance of 8 mm producing differing depths due to proximity and effect of thermal gradient. Critically, phased array C-scan data (Figure 26b) captured a pronounced increase in echo size at this location, with echo intensity markedly increased in the affected region. While smaller disturbances were less clearly distinguishable due to background variation and bead irregularity, the most severe defect produced a detectable ultrasonic signature aligned with visual and geometric cues. These results confirm that phased array ultrasonics can reliably detect sidewall fusion defects of sufficient size, highlighting the value of geometric-acoustic correlation in weld monitoring and inspection. The x-axis was initialized at -100 mm in order to account for the initial period of time required for the tire coupling with the sample surface.

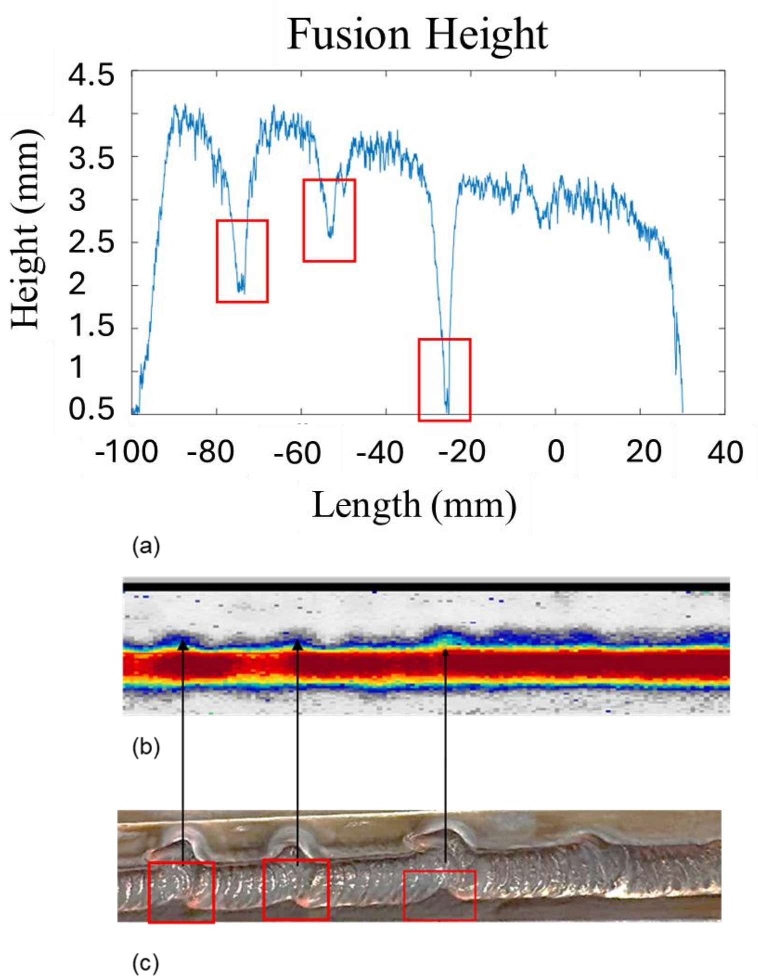

Figure 26. Composite defect validation from the disturbance experiment. (a) Extracted bevel length trace from laser scan, showing changes in height corresponding to disturbance. (b) Corresponding C-scan amplitude map from phased array data showing signal attenuation near the weld centerline with the defect zone. (c) Surface macrograph with visible fusion defects (highlighted in red box).

To evaluate the feasibility of real-time ultrasonic feedback during deposition, a static wedge configuration was employed with the phased array probe positioned ahead of the weld torch path. While artificial lack-of-sidewall-fusion (LOSWF) defects were introduced under controlled bead-on-plate conditions, their acoustic and geometric responses closely mimic those reported in real-world fusion flaws. Artificial LOSWF defects are widely used in weld qualification and ultrasonic validation studies as reliable surrogates for service-induced flaws, since their geometric and acoustic responses closely replicate those of real defects [124], [125], [126]. Nonetheless, extrapolating to complex multi-pass welds requires caution, as thermal gradients, constraint effects, and process variability may alter defect signatures. These experiments therefore establish a foundational validation framework, with ongoing work aimed at extending applicability to production-scale welding scenarios. B-scan images acquired during single-pass GTAW revealed distinct signal behaviour in two stages for both experimental scenarios. For the lack of disturbance, before the arc arrived, as shown in Figure 27a, we observed clear echoes from the bevel sidewall, indicating strong coupling and material response. Smaller echoes surrounding the main indication correspond to scattered or mode-converted reflections at the bevel interface, confirming proper beam engagement during skip inspection. However, when the arc passed directly in front of the wedge, as shown in Figure 27b, the ultrasonic longitudinal signals were absorbed into the molten pool. In contrast, when the experiment is repeated, as shown in Figure 27c, but including an artificial LOSWF disturbance directly in front of the wedge, the signal is still apparent when the torch approaches the middle of the wedge as the wave does not enter the molten pool, as shown in Figure 27d. Understanding this behaviour is essential for developing closed-loop welding inspection systems that must interpret ultrasonic data in near real-time during material deposition. Notably, the temporary signal loss during proper fusion—caused by phase mixing—provides a reliable indicator of bonding integrity. Experimental results demonstrate that in-process fusion face monitoring is feasible and presents a binary detection problem: the ultrasonic longitudinal wave is absorbed by the molten pool in fused joints, while it is not in lack of fusion cases. This finding opens a promising pathway for real-time, feedback-driven welding quality control.

4.7 Conclusion

This work demonstrates a novel approach for real-time detection of LOSWF using Phased Array Ultrasonics integrated with automated welding systems. By deploying Phased Array Ultrasonics during the welding process, we achieved real-time B-scan monitoring which revealed characteristic signal dropout and recovery patterns correlating with fusion quality. This transient behaviour from 60% normalized amplitude to 0% for proper fusion provides an immediate proxy for sidewall fusion status during active welding. An important limitation of this work is the difficulty in extracting quantitative information from the fusion face during welding, which constrains the design of more advanced control algorithms. As observed in Figure 7, thermal gradients can further narrow the monitoring window due to signal degradation. Additionally, in complex multi-pass welds, elevated interpass temperatures, variable geometries, and arc-induced noise may degrade signal stability and introduce ambiguity in distinguishing genuine fusion loss from transient acoustic fluctuations. To enable robust fusion-face control near the melt pool, integration with complementary sensing—

such as visual feedback or melt pool width monitoring as demonstrated in prior work [40] as well as positional feedback and thermal compensation —will be essential.

Controlled experiments with artificially induced LOSWF defects validated detection sensitivity and established baseline characterization metrics, while thermal disturbance trials quantified signal behaviour under realistic welding conditions. The results demonstrate that ultrasonic signals remain interpretable, enabling rapid evaluation of fusion integrity at the point of deposition using signal amplitude as the main criteria.

These findings enable direct integration of ultrasonic imaging into intelligent welding manufacturing systems, supporting both predictive defect identification and real-time quality confirmation. This embedded NDT approach addresses key Industry 4.0 requirements for autonomous quality assurance, reducing post-process inspection burden while enhancing manufacturing reliability in safety-critical applications.

Future work will focus on fully autonomous tandem robotic systems combining real-time welding with trailing PAUT inspection. Key challenges include maintaining signal integrity under challenging interference and developing adaptive control algorithms that respond to ultrasonic feedback. This represents a critical step toward fully closed-loop intelligent welding systems where quality monitoring drives real-time process adaptation, establishing the foundation for next-generation automated manufacturing platforms.

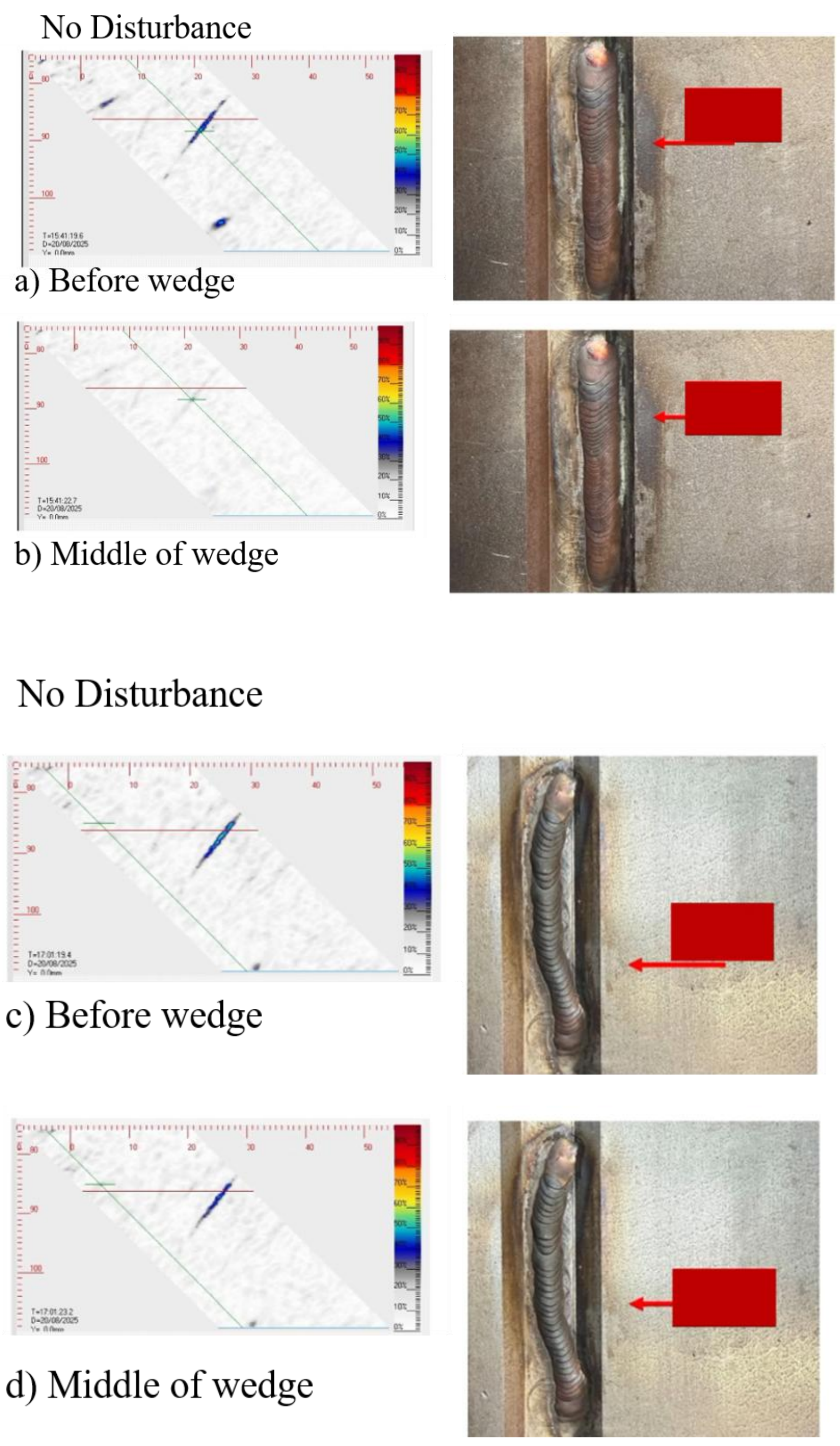

Figure 27. B-scan sequence during in-process welding with a static wedge for no disturbance: (a) clear signal before arc arrival; (b) signal loss as arc passes probe, and for disturbance: (c) clear signal before arc arrival and (d) signal stability as arc passes probe.

5. Error Characterization of Robotic Phased Array Ultrasonic Systems for 15.8 mm Carbon Steel Joint

5.1 Introduction

PAUT inspection systems have emerged as a leading modality for volumetric, non-optical inspection in industrial settings, offering advantages in resolution, speed, and adaptability where conventional methods often face limitations due to surface irregularities or restricted access [127]. With growing demand for automation of inspection for large load bearing components [128], robotic phased array ultrasonic inspection system deployment has gained traction across nuclear, aerospace, and pipeline sectors, enhancing inspection coverage and operational consistency [87]. However, while robotic systems can assist manual operators, they introduce new uncertainty on measurement repeatability originating from deviations in tool pose and coupling force; which can adversely affect the metrological reliability of weld assessment [129], [130].

Recent efforts in automated ultrasonic imaging have emphasized weld defect detection and image segmentation using machine learning and robotic probes [131], with systems increasingly integrating aerial or platform-based robotics to inspect complex geometries and leveraging deep learning to enhance flaw characterization. Additionally, recent work has highlighted the potential for autonomous path planning using ultrasonic data for positioning feedback [132]. Yet, few studies explicitly examine how robot-induced positional uncertainty affects quantitative measurements such as bevel length or weld geometry dimensions. While ultrasonic field modelling and beam propagation are well characterized under idealized conditions [133], these models often overlook parametric disturbances intrinsic to real-world robotic platforms.

In response, new research has begun addressing robotic pose localization and force feedback [134], [135], [136], leveraging sensor fusion and real-time feedback for improved repeatability. Simultaneously, Uncertainty Quantification (UQ), the science of measuring, analysing, and reducing the unknowns in computational models, has matured within robotics and instrumentation domains, where it is employed for safety assurance, pose estimation, and probabilistic planning [137], [138], [139], [140]. Despite this, contact-based ultrasonic inspections, especially those involving multi-modal scans or layered geometries, remain underexplored in terms of spatially varying uncertainty and its implications on scan configuration.

Recent investigations have demonstrated the potential of machine learning for UQ in ultrasonic applications [141], [142], [143], [144], including crack characterization, guided wave modelling, and sensitivity analysis. These works highlight the growing importance of incorporating UQ directly into NDT workflows, both to improve interpretability and to enable adaptive inspection strategies. Nevertheless, practical integration of these methods into field-deployed robotic phased array ultrasonic inspection systems remains limited. Recent work in cladding inspection using the PAUT Roller Probe [145] illustrated the ability for imaging internal defects in complex surfaces that arise from overlapping beads. However, a key limitation was the lack of adaptability due to the rigid structure. Hence, the ability to compensate using robotic motion is crucial.

This Chapter addresses that gap by introducing a systematic experimental framework that quantifies how robot pose (roll, lateral translation) and coupling force affect phased array ultrasonic inspection measurement accuracy. To ensure the generalizability of these findings to industrial weld inspection, a multi-layered machined specimen is utilized as a deterministic surrogate for LOSWF geometries. As established in prior work on in-process monitoring [146], the acoustic signature of LOSWF is fundamentally characterized by specific amplitude attenuation and time-of-flight shifts. By replicating these geometric boundary conditions in a precision-machined artifact, this study decouples robot-induced positioning errors from the stochastic thermal and metallurgical noise inherent to active welding. This isolation validates the use of ultrasonic data as a realistic proxy for defect characterization, enabling a rigorous uncertainty analysis that is applicable to the broader class of contact-based robotic inspection systems.

Using a RollerProbe end-effector mounted on a 6-degree of freedom manipulator, two scan modalities are evaluated; linear and sector; and error patterns are analysed using Ordinary Least Square (OLS) regression and residual-based uncertainty estimation, by evaluating the uncertainty of regression models using the forecast errors. Layer-specific error metrics and uncertainty bounds are computed to provide actionable insight for scan planning under mechanical uncertainty. The results provide a data-driven foundation toward quantitative and qualitative understanding for the decoupling of positioning from ultrasonic measurement error for V-joints of 90 degrees for 15.8 mm thick parent material using S275 steel for structural applications.

This Chapter makes the following contributions:

1. A physics-based calibration methodology that quantifies robot induced UT error coupling across layered geometries, replacing conventional single-point geometric correction approaches.
2. A comparative analysis of sector and linear scans, revealing their geometry-dependent performance regimes.
3. The quantification of the geometrical point at which the acoustic physics change for inspection of 15.8 mm thick plates.
4. Quantification of robot-induced measurement variability distinct from systematic sensor bias, validating the framework's ability to isolate controllable error sources.

5.2 Methodology

Unlike conventional PAUT calibration which validates system performance against a single reference geometry, this Chapter introduces a multi-regime residual-based analysis to quantify measurement error in automated ultrasonic imaging for plates of 15.8 mm thickness, as shown in Figure 28. This thickness was selected, due to its widespread use in welding of columns in the welding of intersecting structures, which is common in shipbuilding. Initially, different focal laws are used to acquire different representations of the reference geometry [147]. Then, the ultrasonic data and robotic experimental parameters are collected for offline processing. Afterwards, OLS regression modeling is used to evaluate the effect of ultrasonic imaging modality and robotic features on measurement accuracy. Finally, the parameter influence, layer lengthwise error and contribution of ultrasonic imaging modality and robotic parameters are evaluated.

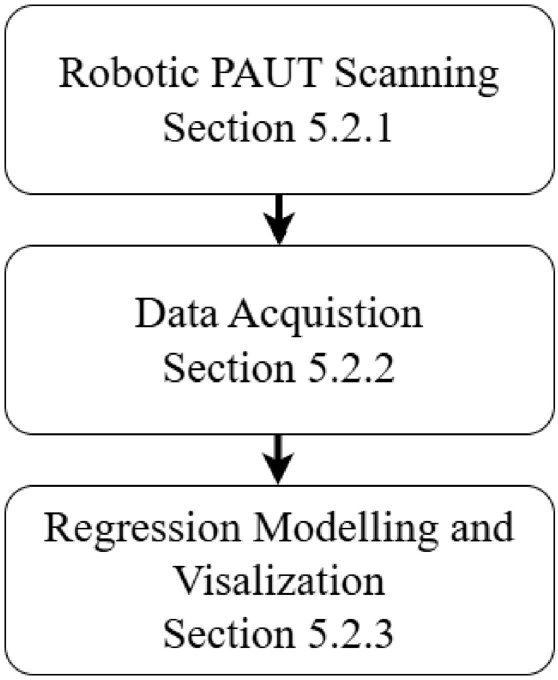

Figure 28. Overview of methodology.

5.2.1 Experimental Setup

The inspection process begins with the deployment of a robotic phased array ultrasonic inspection system using a robotic manipulator equipped with a force-torque sensor and a custom-designed PAUT RollerProbe [87], as shown in Figure 29. The custom sensor is composed of a mechanical assembly for automated delivery, an ultrasonics array, a wedge with a refraction angle of 55 degrees, and a specialized polymer tire to enable high-temperature, continuous inspection. The array has 0.5 mm element size, 64 elements, 10 mm elevation and a central frequency of 5 MHz, and incident angle of 38 degrees with the wedge. The robotic system ensures consistent coupling and stable scanning force throughout the inspection procedure. A PEAK NDT LTPA with 64 phased array channels is used for data acquisition. The robot traverses a pre-defined linear scanning path over the test specimen (600.00 × 250.00 x 15.80 mm), as shown in Figure 30a, which contains multiple simulated bevel features, as illustrated in Figure 29b. A 16 mm thick carbon steel specimen was fabricated to simulate realistic multipass weld conditions across diverse bevel configurations, as shown in Figure 30a. The sample incorporates an industry-standard bevel angle and represents the complete joint filling sequence from initial root pass through final cap pass, following the weld geometry specifications detailed in previous work [40], in Appendix Part B. As illustrated in Figure 30b, the specimen features five distinct stepped levels with decreasing bevel lengths of 16.69 mm, 13.15 mm, 9.62 mm, 6.08 mm, and 2.39 mm, corresponding to different weld pass stages in a typical multipass welding sequence. The indexing of layers in the subsequent study is L1 for the biggest layer, and L5 for the smallest, with intermediate steps corresponding to L2 through L5 respectively. The layer heights and depths are presented in Table 3, including machining inaccuracy of 0.1 mm.

Table 3. Machined sample geometry; ground truth measurements

Index	Depth (mm)	Length (mm)
1	11.80±0.1	16.69±0.1
2	9.30±0.1	13.15±0.1
3	6.80±0.1	9.62±0.1
4	4.30±0.1	6.08±0.1
5	1.69±0.1	2.39±0.1

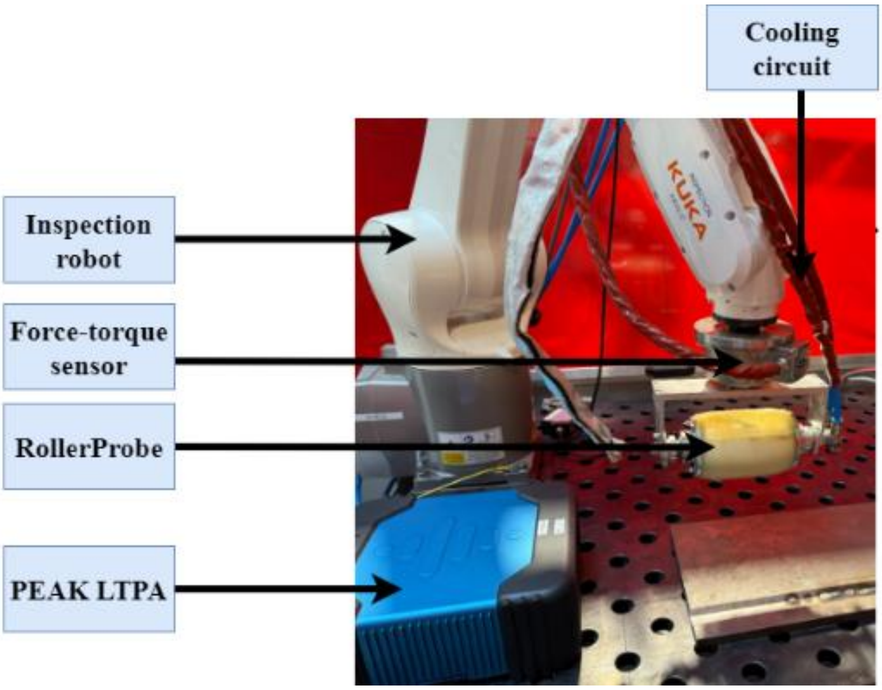

Figure 29. Robotic inspection setup used for data acquisition, featuring a KUKA KR10 manipulator with a custom Roller Probe, force-torque sensor, and PEAK LTPA FMC system.

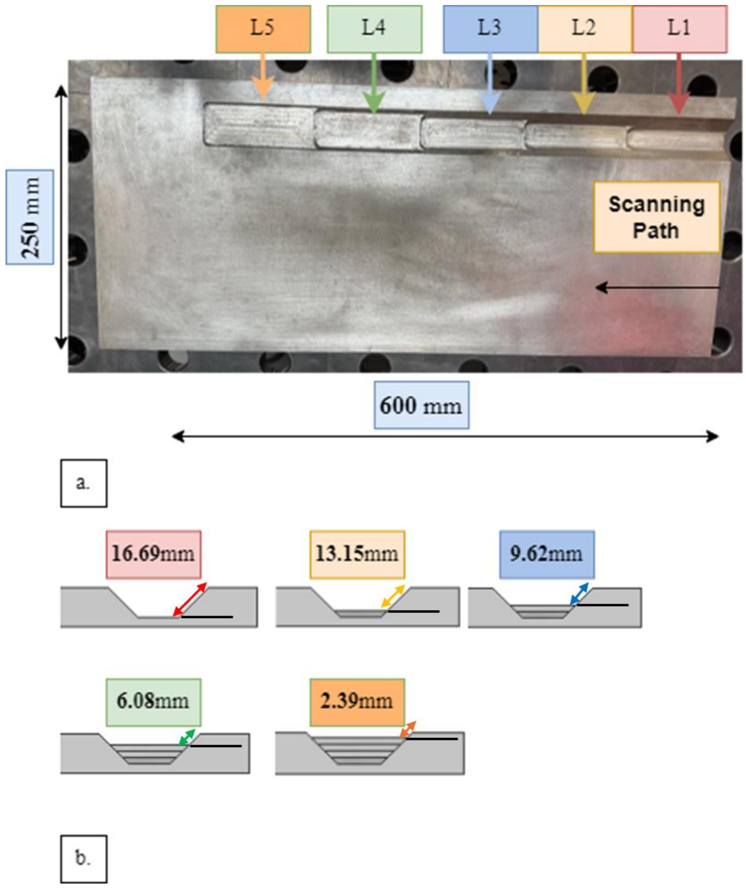

Figure 30. Machined reference geometry designed to isolate robotic positioning effects. (a) The robotic scanning trajectory executed over the precision-machined stepped bevel, serving as a metrological ground truth to decouple measurement error from weld manufacting variability. (b) Cross-sectional dimensions of the five distinct layers (L1-L5) used to benchmark linear and sector scan performance under controlled pose variations.

Measuring accuracy in this study is influenced by three main categories of error: ultrasonic measurement uncertainty, robot-induced error during dynamic motion, and manufacturing tolerances of the test sample (Table 4).

Error Source	**Measured Property**	**Nominal Value**	**Uncertainty**
Grain structure of metal sample	Steel shear wave speed	3250 m/s	±3.48 m/s
Robotic manipulator	Coupling force	125 N	±0.06 N
Robotic manipulator	Height	0 mm	±0.1 mm for coupling, ±0.06 mm for laser scanning
Robot Manipulator	Angular Error	0 º	0.0035º
Metal plate	Bevel length (measured from laser)	16.69, 13.15, 9.62, 6.08, 1.69 mm	±0.21 mm, ±0.21 mm, ±0.03 mm, ±0.08 mm, ±0.20 mm

Table 4. Uncertainty sources for quantification of robot induced error

Measurement error for the variation in shear wave speed for steel was determined using a rexolite wedge with carbon steel material, a sector range of 40° to 70 with a radius of 100 mm, and calculating the difference in TOF for the first and second reflection, as shown in Figure 31b, for a calibration block according to [148]. For the robotic system, additional errors originate from the TCP calibration errors reported by the robot controller and the resolution limit of the Delta SI-165-15 force–torque sensor [149].

Finally, the machining accuracy was measured using a MicroEpsilon scanCONTROL 2910-100 laser scanner [150] mounted on a KR 210 R2700 robot with a repeatability of ±0.6 mm [28], as shown in Figure 31a. It should be noted that the laser measurement error is a combination of robotic vibrations during movement, surface preparations and manufacturing imperfections. Five cloud points were averaged, down sampled and linearly interpolated, as shown in Figure 31c. Then a spline was fitted each 0.1 mm with a smoothing parameter of 0.9. The spline normals were calculated, using angle deviation to segment the bevel end-points. Finally, the Euclidean distance was calculated.

5.2.2 Data Acquisition

In ultrasonic testing (UT), linear and sector scans are two phased array scanning techniques used to visualize internal structures and detect flaws within materials. A linear scan moves the ultrasonic beam along a straight path at a constant angle, providing uniform depth coverage and is particularly suited for detecting defects perpendicular to the inspection surface. In contrast, a sector scan (or S-scan) sweeps the beam across a range of angles from a fixed probe position, enabling the detection of flaws at varying orientations and enhancing coverage of complex geometries. In this study, a gain of 36 dB, a sub aperture of 8 elements, a time gate from 40 μs τo 90 μs, an exit angle of 45° and an intra-beam spacing of one element were used for linear scans. This scan is shown in Figure 32b.

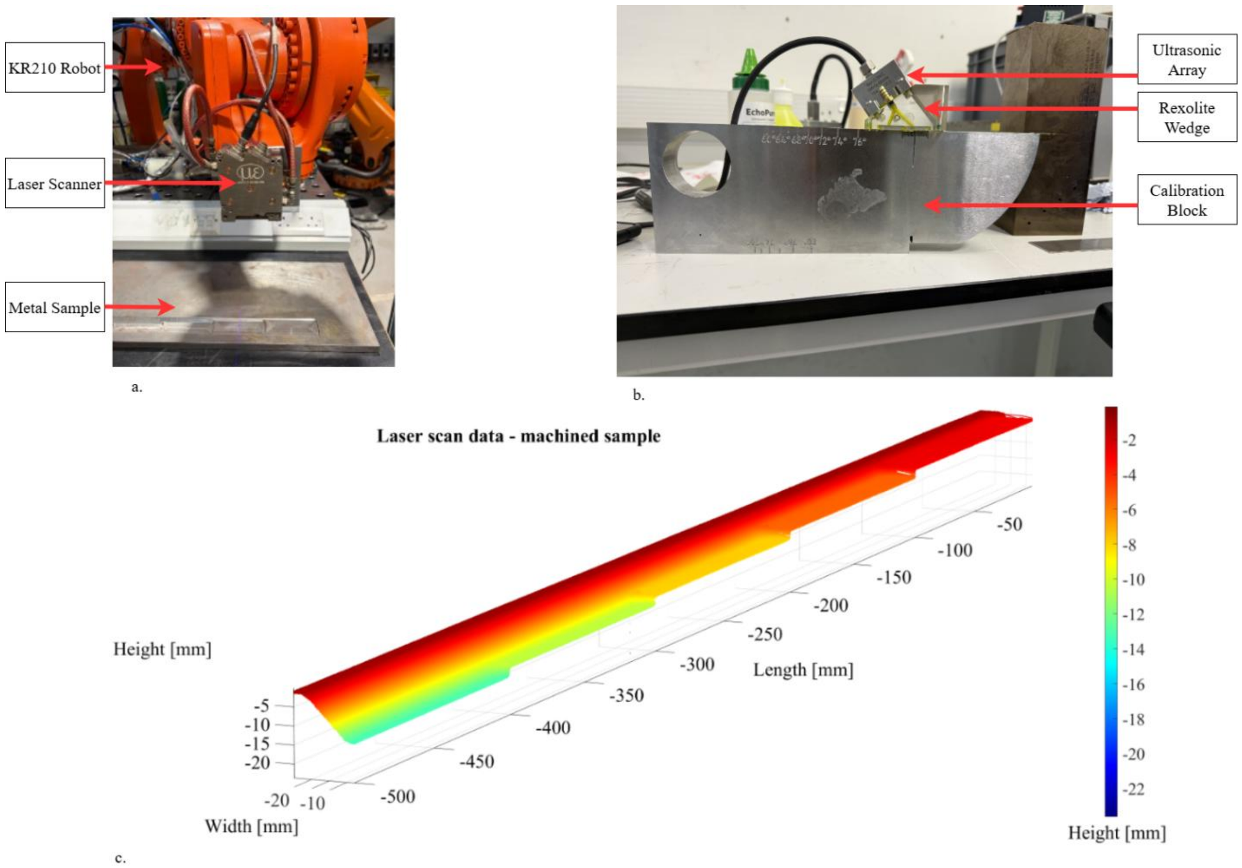

Figure 31. Measurement uncertainty measurements. (a) Laser scanner mounted on KR90 robot. (b) Experimental setup for measurement of sh ear wave speed variation. (c) Interpolated cloud point for measurement of bevel length.

Sector scans were performed using a gain of 70 dB, a time gate of 40 μs to 66 μs and a sector range of 30°–60°. This scan is shown in Figure 32a. For the linear scans, these parameters were selected to ensure an appropriate resolution of 0.5mm for bevel measurement while minimizing signal saturation using a lower gain, while for the sector scans the range was selected to include the natural bevel angle of 45° at the centre, and maximize the amplitude response there. For both methods, a Pulse Repetition Frequency of 2.1 kHz, a sampling rate of 100MHz and a voltage of 200V were used. These gain settings were selected to maintain 80% of the maximum amplitude for the biggest bevel, ensuring accurate measurements on non-saturated signals. This approach, as described in [148]., allows for optimized flaw detection and signal clarity across both scanning modes, enhancing the reliability of the inspection process

Parameter sweeps of coupling force, offset and roll, as shown in Figure 33, were used to determine the systematic effect of robot parameters and ultrasonic modality on the bevel measurement accuracy. These are correlated with the robot manipulator and force torque errors presented in Table 4. It should be noted that the angular error was estimated based on the assumption that there is a linear relation with scanning speed, using errors from the literature [151]. A full factorial Design of Experiments (DoE) [27] was generated to evaluate the effect of all combinations of experimental parameters on measurement accuracy, with 27 different experiments conducted for linear and sector scans, for a total of 54 different experiments. The roll range was 179.5°–180.5°, with a 0.5° increment, the offset range was ±2 mm, with 2 mm increment, and the coupling force range was

100-150 N downforce, with a 25 N increment. The scanning speed was fixed at 2 mm/s. The coupling force is applied in the Z downward direction, X is the direction parallel to the centre of the RollerProbe, and roll is defined the rotation about X. Finally, the offset is in Y axis which is perpendicular to the scanning direction.

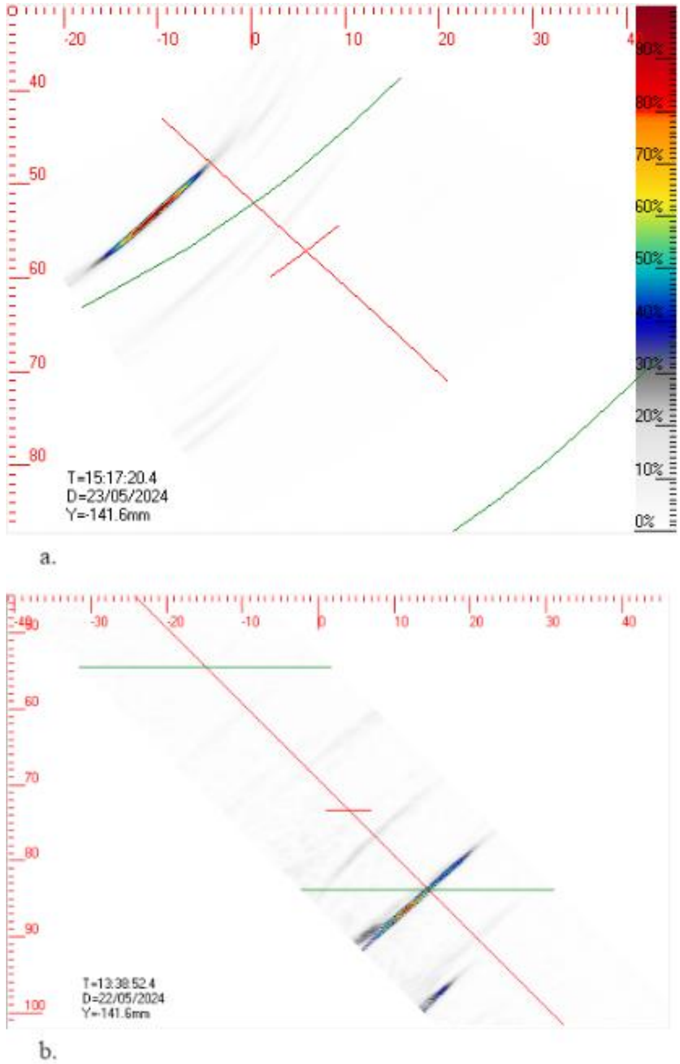

Figure 32. Representative PAUT images showing (a) a sector scan performed at 30°–60° with a 70 dB gain, and (b) a linear scan using an 8-element sub aperture, 1-element spacing, and 52 dB gain.

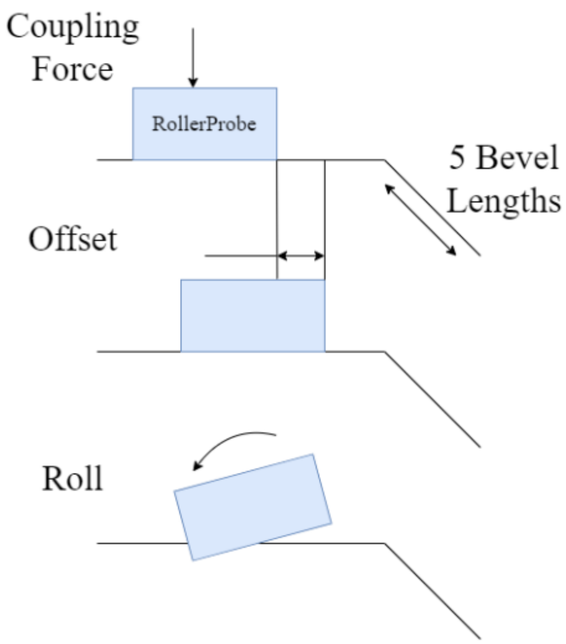

Figure 33. Robotic parameter sweeps (coupling force, offset, roll) to evaluate effect of robot pose on measurement accuracy.

5.2.3 Regression Modeling and Reporting

Following the robotic parameter sweep, the data is processed, and visualized, as shown in Figure 34 for the analysis pipeline. Initially, the appropriate dataset is selected through a simple user interface, for downstream analysis. The data is composed of bevel lengths extracted from C-Scans using the 6 dB drop method in .txt format, and the ultrasonic data in Multi-frame Full Matrix Capture (MFMC) format [152] is processed to extract the maximum amplitude and TOF. For each experiment, the dataset is composed of 5 layers, 18 measurements for each layer, 5 mean and standard deviation values. The total dataset is composed of 675 unique datapoints for each modality. Then, this data is aggregated to a single data structure. The five features (roll, offset, coupling force, maximum amplitude, and TOF) are extracted. These terms were empirically selected to validate the significance of robotic pose on the measurement accuracy.

Then, ordinary least square regression is used to fit 135 samples against the respective bevel lengths for each layer, creating five layer specific models. Stored metrics include the coefficients that minimize overfitting, the coefficient of determination (R^2), the Root Mean Square Error (RMSE), the bias from nominal, the residuals from the ground truth, and the standard deviation of the residuals. These metrics were selected in order to fully isolate systematic error from random noise, and enable downstream residual analysis. For model validation, 100-fold bootstrap resampling is used to evaluate the performance. Model evaluation was based on predictive accuracy metrics, permutation testing, linear regression coefficient trends and uncertainty was quantified using residual distributions with $\pm 2\sigma$ Type A confidence intervals (CIs). Finally, the uncertainty is calculated by finding the linear trend of the residuals, subtracting it from the to find the type B uncertainty, followed by component and coefficient estimation based on the trained regression models, and subsequently the visualization using residual-based uncertainty analysis.

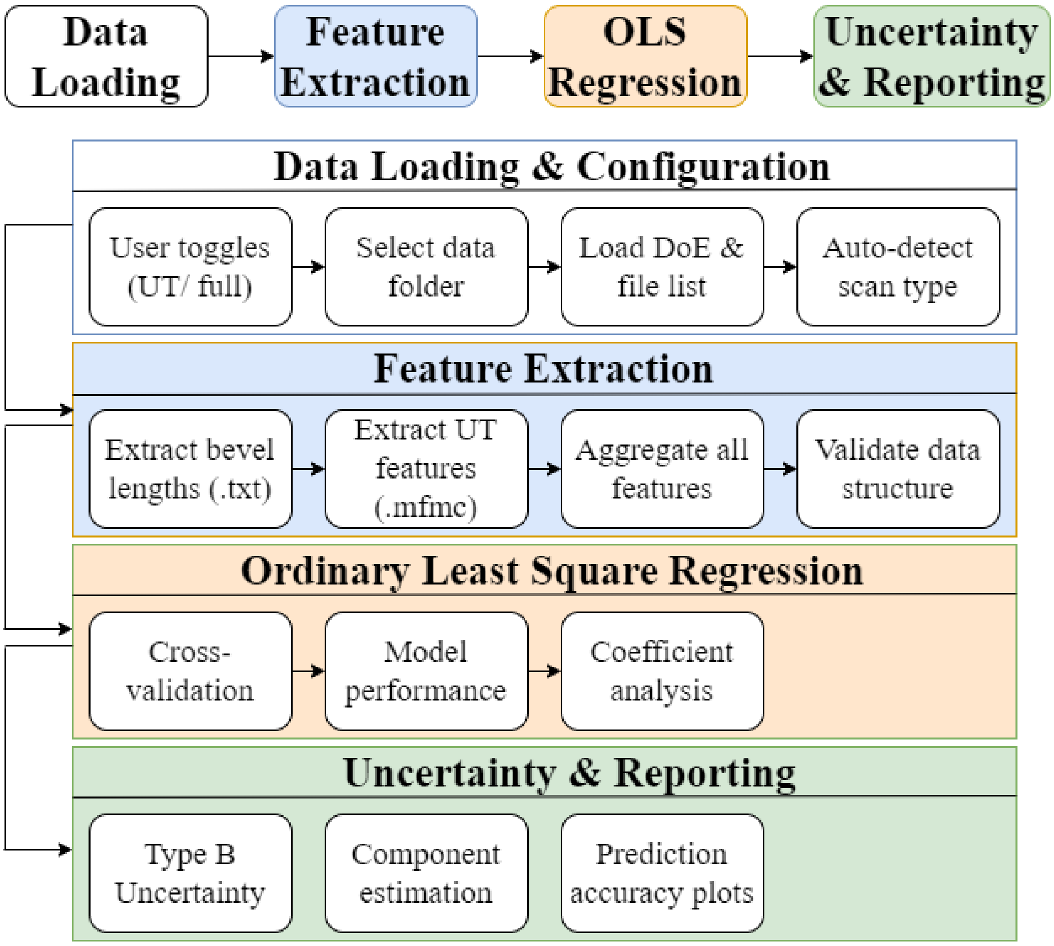

Figure 34. Analysis pipeline.

5.3 Results & Discussion

The following analysis demonstrates fundamental limitations of conventional calibration approaches, which assume measurement error is geometry independent is only performed using sector scans and single element scanning, without consideration for planar defect size [153], [154]. To evaluate the effect of scanning modality on measurement performance, both model fit quality and measurement precision were assessed across different bevel geometries.

5.3.1. Regression Accuracy and Model Fit

The regression analysis in Figure 35 highlights distinct performance trade-offs between the scanning modalities, as well as the transitionary nature of Layer 3. The confidence bands were calculated by repeatedly training the models with bootstrapping, repeatedly drawing from the same samples, in order to evaluate the average performance and stability. In the linear scan layout, Layer 1 predictions are more spread out, yet it remains the layer closest to the nominal value in terms of bias. Conversely, Layer 2 tracks closely to the nominal trendline, whereas Layer 3 demonstrates a systematic tendency to overpredict the bevel length. The sector scans are generally able to better model relationship between robotic parameters, ultrasonic features and geometry, with higher R^2 values and a smaller overall bias compared to the linear models. Statistical robustness is confirmed via permutation tests, which reveal a statistically significant relationship between the input features and bevel length ($p=0.010$). Additionally, the proximity to 1 in overfitting ratio, as shown in Table 5, illustrated minimal difference between training and validation RMSE. It should be noted that for each modality, only the ratio for the layers with optimal performance is reported. Furthermore, the coefficient stability analysis and Variance Inflation Factor (VIF) calculations indicate minimal multicollinearity and highly stable features, as shown in Figure 36. Coefficient stability was performed to analyse zero crossing and sign flip of coefficients, while VIF of the coefficients was performed to determine parameter independency. It can be observed that for both linear and sector scans, the features are independent, due to low VIF factors below 2 for the transitional layer 2, and zero crossing occurring for roll and offset for linear scans, with small confidence bands, indicating the small effect relative to ultrasonic features.

Layer	Linear Scan – Overfitting Ratio	Sector Scan - Overfitting Ratio
L1	1.04	Not Applicable (N/A)
L2	1.04	N/A
L3	1.11	1.07
L4	N/A	1.06
L5	N/A	1.04

Table 5. RMSE overfitting ratio for linear and sector scans.

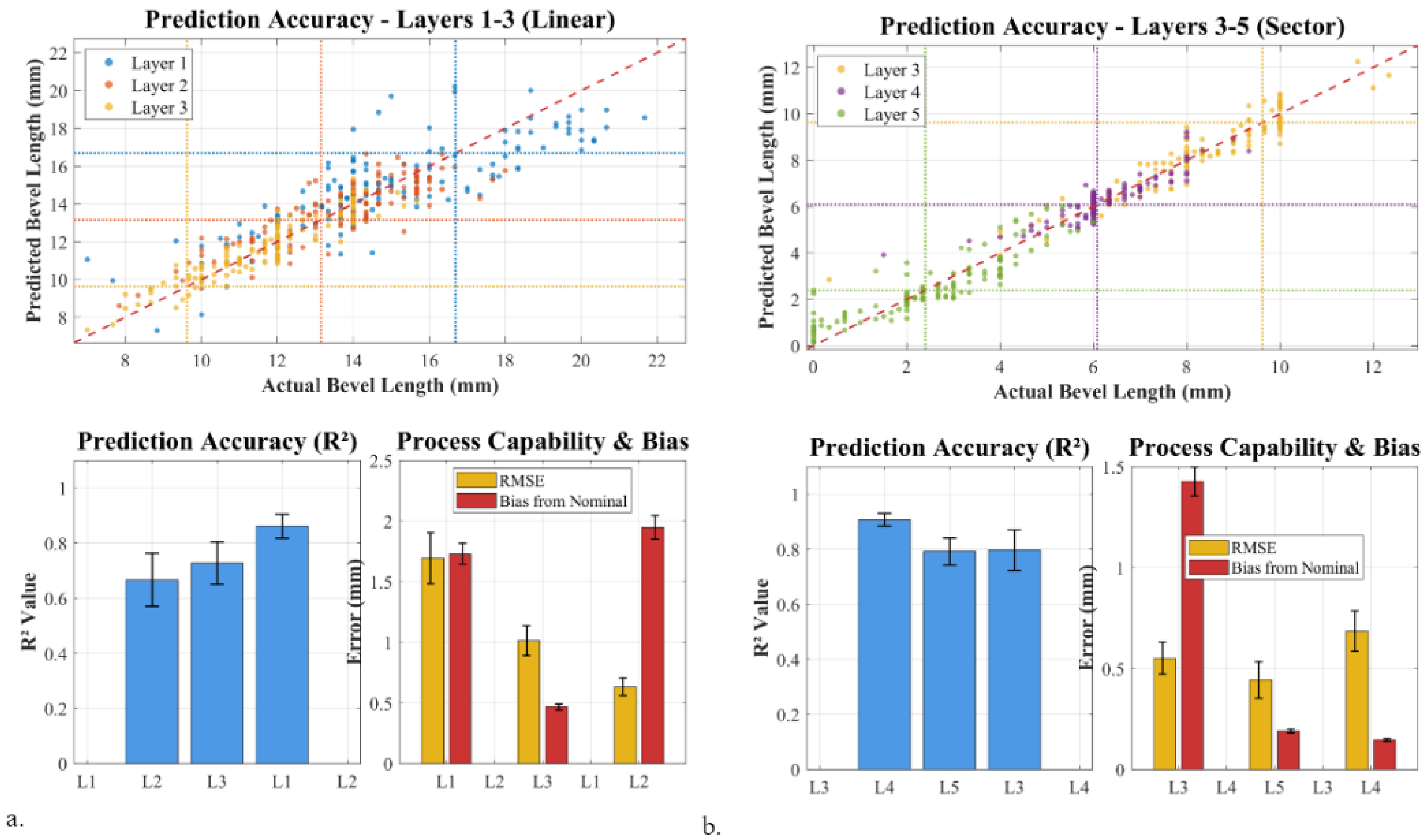

Figure 35. Regression performance. (a) Linear scan prediction accuracy (top) and error metrics (bottom), showing wider spread for Laye r 1 and systematic overprediction for Layer 3, with corresponding RMSE and bias values with bootstrapped CIs. (b) Sector scan prediction accuracy (top) and error metrics (bottom), demonstrating superior fit for deeper Layers 4 and 5. And reduced bias compared to linear scans.

5.3.2. Scan Modality Performance

The deviation analysis with ±2σ Type B CIs confirms the complementary performance characteristics observed in the model fit quality assessment. For linear scans (Figure 37), measurement precision is optimal for wider bevels, with Layers 1-3 demonstrating tight clustering around the nominal value) and narrow CIs. Layer 1 shows the largest spread (±4 mm) but maintains reasonable centering, while Layers 2-3 exhibit improved precision with deviations typically within ±2 mm. However, measurement performance deteriorates significantly for narrower bevels in Layers 4-5, where systematic bias becomes evident with predominantly positive deviations (overestimation) in Layer 5 and increased scatter extending beyond the CIs.

Conversely, sector scans (Figure 38) demonstrate superior measurement precision for narrower bevels. Layers 4-5 show well-centered distributions around the nominal value with deviations predominantly within ±2 mm and tight confidence. Layer 3 represents a transition zone with moderate performance, while Layers 1-2 exhibit systematic underestimation with negative deviations extending to -8 mm and -6 mm respectively, indicating significant measurement bias for wider bevels.

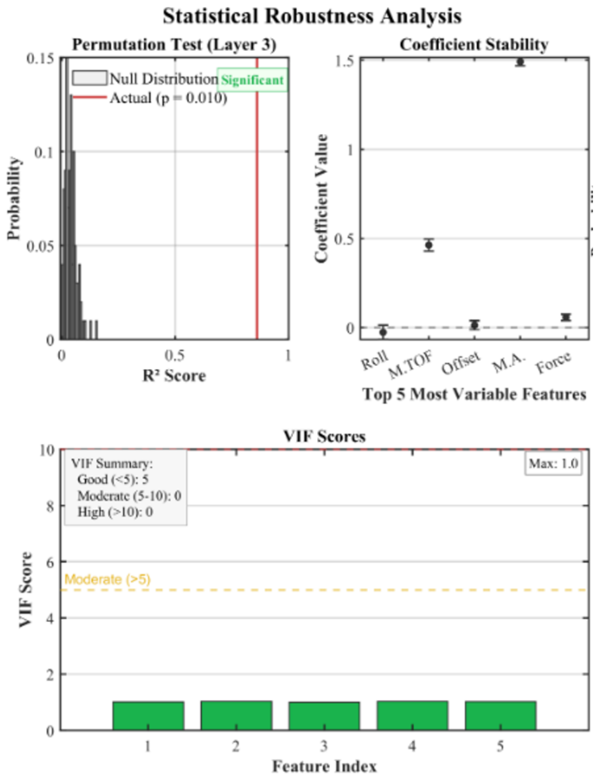

a.

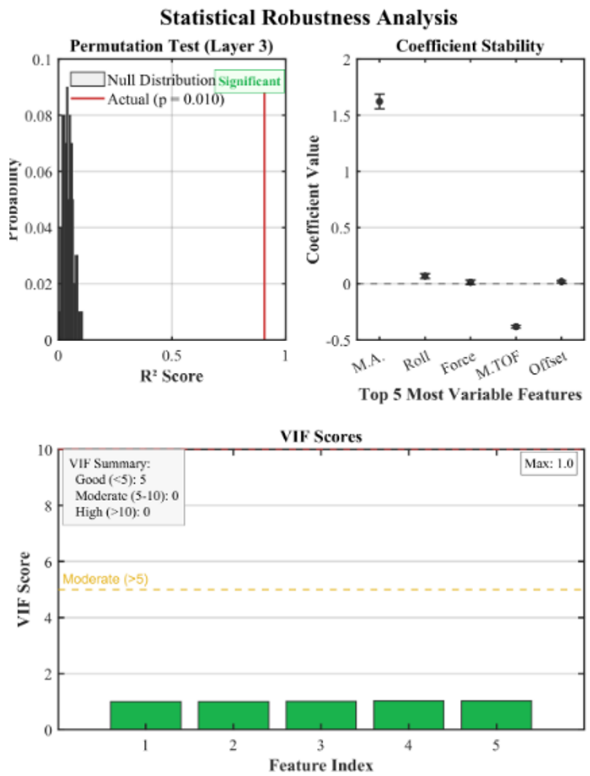

b.

Figure 36. Statistical validation analysis for ultrasonic scan modalities (a) Linear scan statistical robustness metrics, including permutation testing (p = 0.010) confirming significance, coefficient stability analysis and VIF scores indicating minimal collinearity.

The CI analysis reveals that linear scans maintain measurement within ±2σ bounds for Layers 1-3 but exceed acceptable limits for narrower geometries. Sector scans show the inverse pattern, with reliable measurements for Layers 3-5 but poor performance for wider bevels. This precision analysis validates the geometry-dependent scanning modality selection strategy, where the transition point occurs around layer 3 (9.62 mm nominal bevel length).

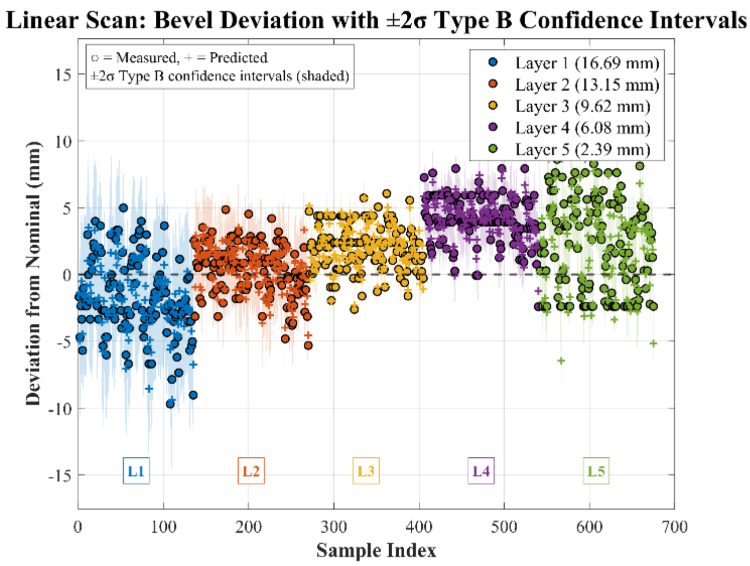

Figure 37. Residual distribution for linear scans.

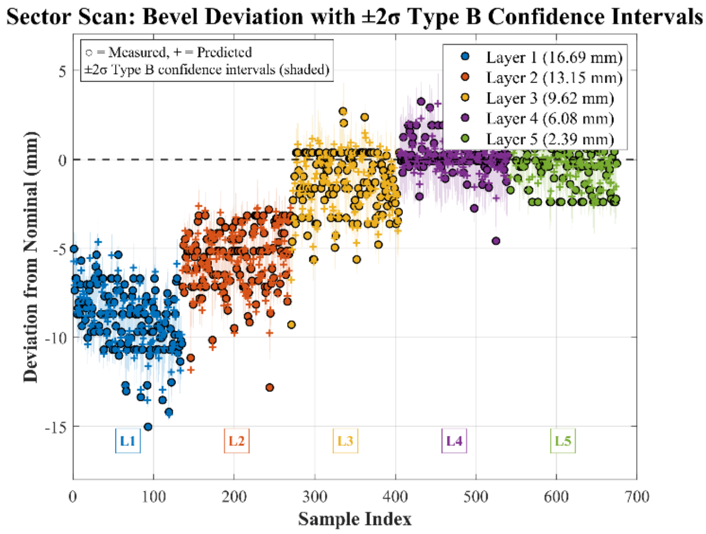

Figure 38. Residual distribution for sector scans.

The differences between scanning modalities can be attributed to fundamental differences in beam coverage and acoustic energy distribution, as defined by [127]. For linear scans, the consistent beam path and uniform incident angles provide optimal acoustic coupling for wider bevels where the surface area allows uniform energy distribution across multiple sub apertures. However, for narrower bevels, the acoustic energy rapidly disperses at the sharp corners, leading to signal degradation and corner reflection artifacts that cause the observed overestimation bias in layers 4-5, as shown in Figure 37.

Sector scans utilize a range of incident angles (30° to 60°) which creates more complex beam coverage patterns. For narrower bevels, this angular diversity compensates for the limited surface area by providing multiple acoustic paths to the bevel edges, improving signal-to-noise ratio, and reducing corner effects. However, for wider bevels, the large angular deviation from the nominal 45° orientation, particularly at the sector range limits, results in reduced acoustic energy coupling at the upper bevel corners, leading to the systematic underestimation observed in layers 1-2, as shown in Figure 38.

This result demonstrates that robotic positioning errors do not simply translate to geometric measurement offsets. Instead, pose perturbations interact with the acoustic field in modality-dependent ways: a ±0.5° roll error shifts a linear scan's fixed 45° beam uniformly off the bevel normal, creating saturation-limited overestimation, whereas the same roll error redistributes energy across the sector scan's 30°-60° angular range through differential beam steering, producing amplitude-weighted averaging effects. This non-geometric coupling proves that robot error compensation cannot be treated as a purely kinematic problem. Each ultrasonic modality transforms identical positioning perturbations into distinct error signatures, necessitating physics-aware calibration models rather than universal geometric correction factors. The focal law selection strategy thus becomes critical: linear scans maximize energy efficiency through consistent beam geometry for larger targets, while sector scans leverage angular diversity to overcome the acoustic challenges presented by smaller geometric features.

5.3.3. Feature Importance

The feature importance analysis for linear scans (Figure 39) reveals that each bevel layer exhibits unique behavior driven by distinct dominant factors. Mean Amplitude (M.A.) response remains a predictor with strong positive effect across the three layers, aligning with the physical intuition that larger amounts of energy are reflected from larger reflectors. In addition, force and roll maintain the same negative sign for the first two layers, indicating that excessive tire compression and misalignment can lead to underestimation of bevel geometry. It should be noted that for the third layer, measurement accuracy is dominated by ultrasonic features with higher time-of-flight leading to overestimation.

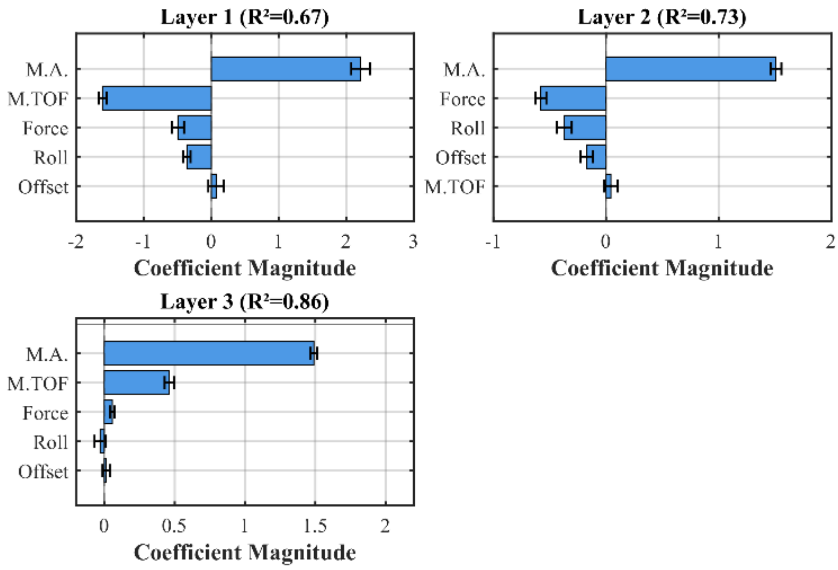

Figure 39. Linear regression coefficients for linear scans across Layers 1–3. The charts display the five influential coefficients affecting measurement accuracy, with error bars indicating stability across cross-validation.

The resulting equations are 20, 19 and 20 for layers 1, 2 and 3 respectively:

$$L_1 = 14.9617 + 0.0737Offset - 0.3617Roll - 0.4925Force + 2.2131MeanAmp - 1.6062MeanTOF \quad 18$$

$$L_2 = 13.6160 - 0.17080Offset - 0.3701Roll - 0.5787Force + 1.5092MeanAmp + 0.0435MeanTOF \quad 19$$

$$L_3 = 11.5667 + 0.0136Offset - 0.0284Roll + 0.0567Force + 1.4891MeanAmp + 0.4619MeanTOF \quad 20$$

,where L1, L2, L3 (mm): respective bevel lengths, and Offset (mm): standardized offset, Roll (°): standardized roll, Force (N): standardized force, MeanAmp: standardized mean amplitude and MeanTOF (us): standardized mean time-of-flight.

The feature importance analysis for sector scans (Figure 40) highlights distinct behavioural shifts as the bevel geometry deepens. The third layer is primarily driven by the ultrasonic features, consistent with the linear scan. The main difference is the adversarial relationship between amplitude and time-of-flight, highlighting that a shorter acoustic path can lead to less attenuation, and higher amplitude response. For the fourth and fifth layers, force and roll remain the dominant parameters, with diminishing effect compared to linear scans. This occurs due to the increased complexity of the ultrasonic coverage patterns, which reduces reliance on robotic pose, position and coupling. Furthermore, as opposed to linear scans, force and roll have an adversarial effect, highlighting that torque optimisation is critical to maintain consistent tire deformation. Additionally, the explained variance is, on average, higher for sector scans, highlighting the complexity of bevel geometry measure for lengths above 9.62 mm.

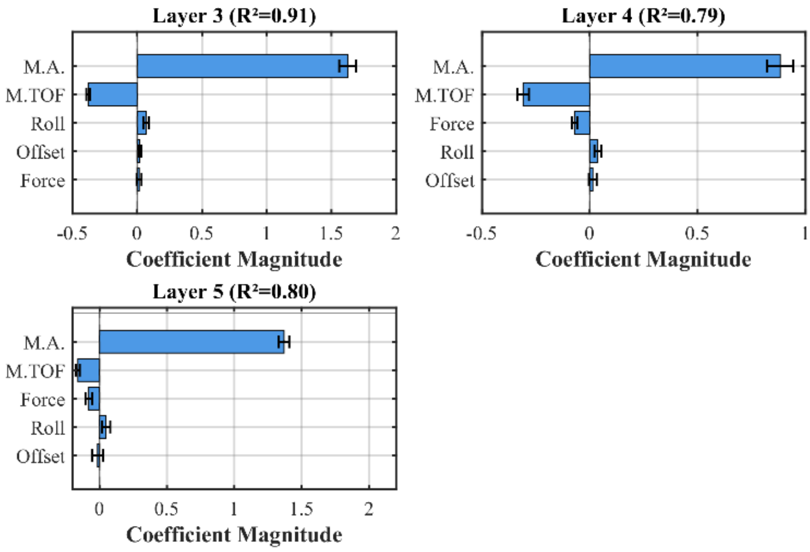

Figure 40. Sector regression coefficients across Layers 3–5. The charts display the top five influential coefficients affecting measurement accuracy for deep bevel layers.

The resulting equations are 21, 22, 23 for layers 3, 4 and 5 respectively:

$$L_3 = 8.1938 + 0.0192Offset + 0.0698Roll + 0.0143Force + 1.6248MeanAmp - 0.3799MeanTOF \tag{21}$$

$$L_4 = 6.2691 + 0.0136Offset + 0.0372Roll - 0.0696Force + 0.8823MeanAmp \pm 0.3094MeanTOF \tag{22}$$

$$L_5 = 2.5358 - 0.0150Offset + 0.0490Roll - 0.0803Force + 1.3680MeanAmp - 0.1613MeanTOF \tag{23}$$

,where L3, L4, L5 (mm): respective bevel lengths, and Offset (mm): standardized offset, Roll (°): standardized roll, Force (N): standardized force, MeanAmp: standardized mean amplitude and MeanTOF (us): standardized mean time-of-flight.

The sign reversal in force-roll interaction between linear and sector scans reveals a fundamental difference in error coupling mechanics. For linear scans, force and roll errors compound multiplicatively - increased tire compression under angular misalignment creates a geometric path shortening effect that drives systematic underestimation. In contrast, sector scans exhibit error compensation: the angular diversity of the beam sweep means that roll-induced coupling asymmetry redistributes acoustic energy across the 30°-60° range, while increased normal force homogenizes contact across this angular range, creating an adversarial interaction. This compensation mechanism explains why sector scans maintain sub-millimeter accuracy in narrow bevels despite pose variations - the modality inherently trades off mechanical perturbations against each other rather than allowing them to accumulate.

Layer 3 exhibits a distinctive error signature characterized by systematic bias (1.7-1.8 mm) exceeding random error (RMSE 0.7-0.8 mm) for both scanning modalities - a 2.4× bias-to-RMSE ratio compared to <1.5× for all other layers, as shown in Figure 35. This bias-dominated behavior, coupled with the simultaneous dependence on Force, Offset, and Roll parameters shown in Figure 39 and Figure 40, confirms Layer 3 as a critical sensitivity regime where small robotic perturbations amplify through coupled error pathways rather than independent random noise.

To bridge the gap between statistical characterization and practical robotic deployment, the dominant error sources identified via linear regression were synthesized into a parameter prioritization hierarchy. Table 6 serves as a deterministic look-up guide for adaptive scan planning, defining the critical robotic parameters required to maintain sub-millimeter accuracy across the full range of bevel feature lengths (2 mm to 16.69

mm). The optimal parameters were determined by selecting the set of parameters that minimize error against the nominal values for each layer.

Layer	Bevel Length (mm)	Optimal Modality	Optimal Parameters (Force, Angle, Offset)
L1	16.69	Linear	125N, -0.5°, 0 mm
L2	13.15	Linear	125N, -0.5°, 0 mm
L3	9.62	Transition	100N, 0.0 °, -2 mm
L4	6.08	Sector	100N, 0.0 °, -2 mm
L5	2.39	Sector	100N, 0.0 °, -2 mm

Table 6. Robotic parameter optimization hierarchy.

The observed transition in error mechanisms between layers can be hypothesized to be attributed to geometry-dependent acoustic interference effects at the bevel-substrate interface. For narrow bevels (Layers 4-5), the decreased length leads to a reduced acoustic region where corner-trapped scattered signal interacts with Rayleigh waves propagating along the bevel face. As the volume of the joint surrogate increases, higher amounts of acoustic energy are absorbed. This interaction between absorption, and destructive interference of surface and scattered signal is highly sensitive to beam incidence angle, explaining why robotic pose parameters become the dominant error source in these geometries.

5.3.4. Measurement Precision and CIs

The RMSE breakdown results demonstrate the significant improvement achieved by incorporating robotic motion parameters alongside traditional UT features in measurement accuracy prediction. For linear scans, as shown in Figure 41a, the inclusion of robotic parameters (full model including both robotic parameters and ultrasonic features presented in Sections 5.3.1 to 5.3.3, blue bars) consistently reduces measurement error compared to UT-only predictions (grey bars) across all bevel layers. The effect was evaluated by comparing regression models that included robotic parameters against models using only UT features in this section, by removing the ultrasonic features and retraining models from Section 5.3.1. to 5.3.3. The improvement is most pronounced for Layers 1-2, where linear scans achieve RMSE values below 1.8 mm, supporting the conclusion that linear scanning is optimal for these wide layers.

Sector scans, as observed in Figure 41b, show less pronounced improvements over the 6 dB drop sizing method, with similar performance between full and UT-only model due to diminishing effect of robotic positioning. This superior performance in narrower layers confirms that sector scanning is the preferred method for these geometries, due to the beam diversity advantages discussed in the feature importance analysis. Layer 3 represents a transition zone where both scanning modes achieve similar performance levels, making it a practical decision point between methodologies. The ability to predict measurement accuracy based on robotic motion parameters enables real-time quality assessment and adaptive scanning protocols, representing a significant advancement in automated ultrasonic inspection capabilities.

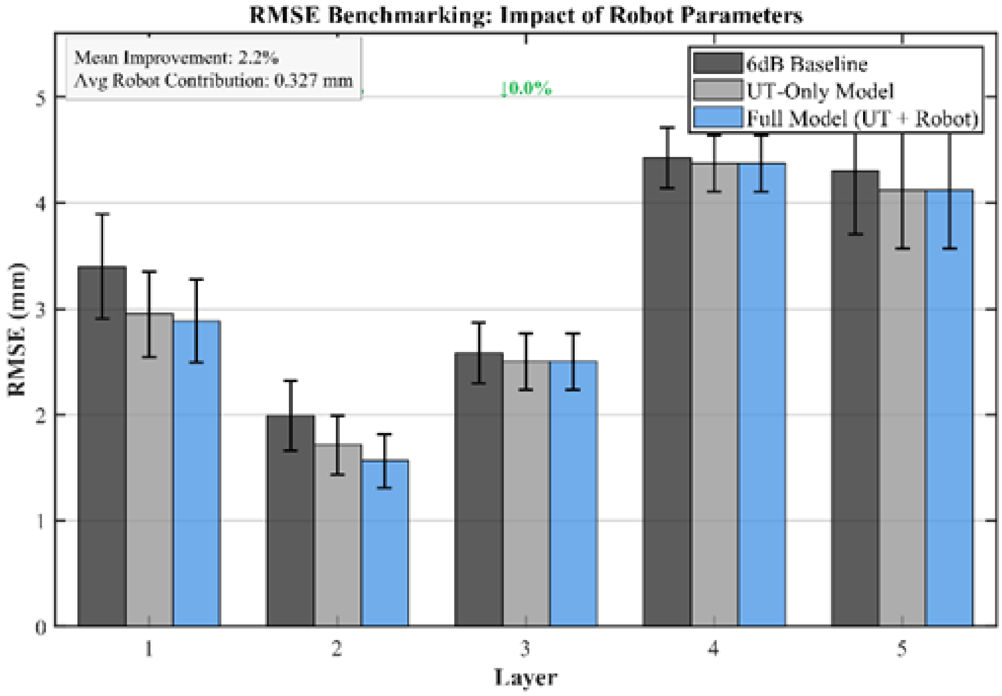

a.

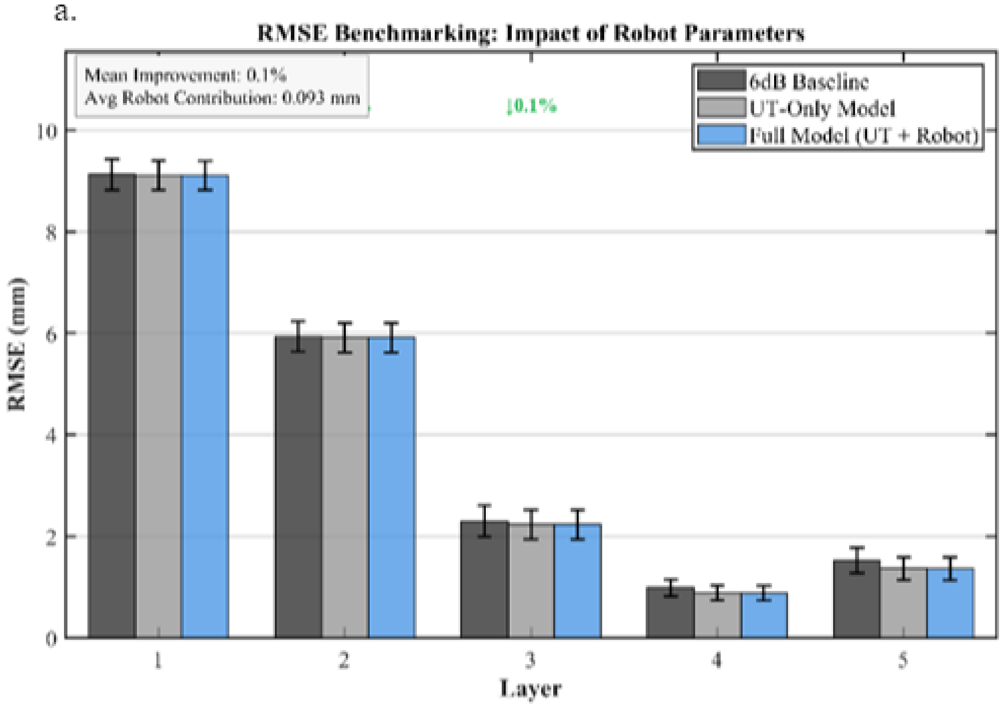

b.

Figure 41. RMSE benchmarking analysis demonstrating the impact of robotic parameter fusion. (a) Linear scan performance showing consistent error reduction when integrating robotic motion features (Full Model) compared to ultrasonics-only predictions (UT-Only), achieving optimal accuracy (mm) in shallow Layers 1–2. (b) Sector scan performance revealing similarly low measurement error for deep layers, revealing relative independence from robotic parameters.

5.3.5. Welded Sample Validation

To validate the efficacy of different modalities and optimal modalities, validation was conducted on a welded staircase sample with distinct welded steps, as shown in Figure 42a. Laser scanning was conducted to determine the bevel length, as shown in Figure 42c, which was then compared with the different modalities with the optimal robotic parameters for the linear (125 N, -0.5°, 0 mm) and sector scan (100 N, 0.0°, -2 mm) and a gain of 65 db. As shown in Figure 42b., the linear modality follows the general trend of the ground truth, with approximately 1.0 mm of overestimation on average for the initial unfilled section. For the second and third layers, the linear scan is more accurate, with the sector producing more unstable measurements for the second layer, and consistent underestimation of up to 2.0 mm for the third layer. For the fifth layer, the sector scan provides a relative increase in accuracy, with a consistent underestimation of 2.0 mm and more stable values. Finally, for the fourth layer, both modalities underperform in terms of accuracy, with the measurement error of linear scan increasing by more than 3.0 mm, and the sector scan having a gradual decrease before stabilizing in the fifth layer. The underestimation for the fourth and fifth layers is consistent with the fact that due to weaving, the measured bevel length for UT will be smaller, due to direct reflection for the 45° unfilled section, and diminishing acoustic energy at the welded toe due to the varying fusion face, as shown in Figure 42

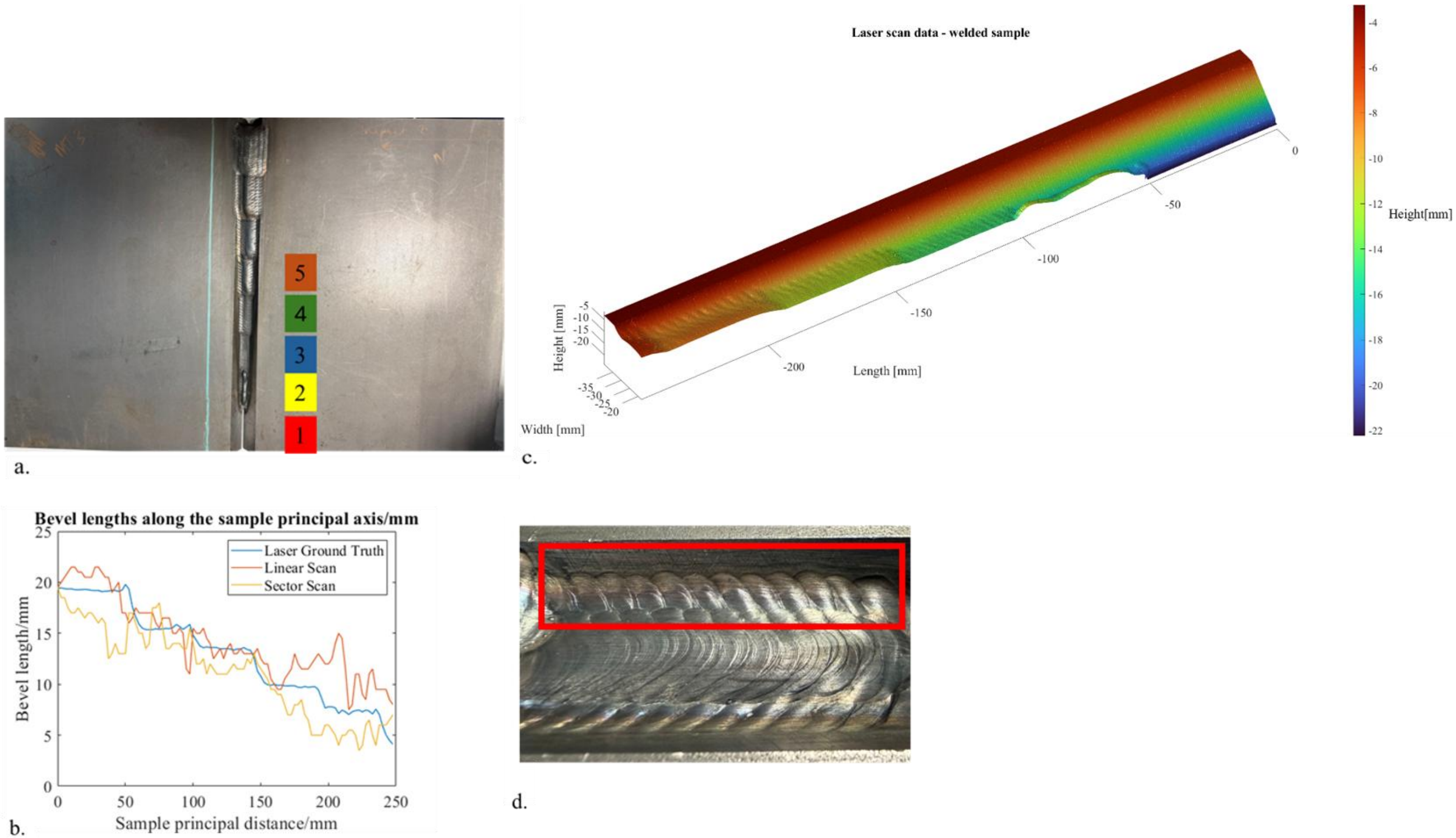

Figure 42. External validation of robotic parameter selection using a welded staircase sample. (a) Overhead view of welded sample. (b) Bevel length comparison between laser ground truth and UT modalities. (c) Interpolated laser cloud point of stepped sidewall. (d) Zoomed view of fifth layer

5.4 Conclusion

This work establishes a calibration framework for quantifying geometry characterization error in robotic contact-based inspection for 90 degree V joints for 15.8 mm thick S275 plates, contributing directly to the development of autonomous systems capable of adapting to geometric variation; a critical requirement for intelligent manufacturing. By isolating the effects of robotic positioning, the regression modeling reveals a fundamental operational dichotomy that was previously uncharacterized: linear scans maximize energy efficiency for wide geometries but suffer from saturation sensitivity, whereas sector scans leverage angular diversity to maintain precision in narrow features. The third layer is identified not merely as a middle ground, but as a critical "transition zone" where dominant robotic parameters and optimal modality change.

Although a single artifact was used, its stepped geometry forces the inspection system through five distinct acoustic regimes, effectively creating a multi-scenario benchmark. The analysis confirms that error mechanisms shift fundamentally with depth: the deepest layer is governed by coupling and positioning, while the second shifts to a saturation-limited regime driven by energy density. This progression proves that the experiment isolates a continuous spectrum of physical boundary conditions, validating system adaptability across diverse industrial scenarios rather than merely repeating a single thickness measurement.

By synthesizing these behaviours into a parameter prioritization hierarchy (Table 6), this framework moves beyond trial-and-error configuration, providing a deterministic guide for scan planning. The demonstrated ability to enhance prediction reliability by integrating robotic motion parameters effectively transforms the robot from a passive probe carrier into an active metrological instrument. This fusion capability lays the foundation for next-generation adaptive inspection platforms that can autonomously reconfigure scan strategies in real-time based on the geometric reality of the workpiece, by establishing a calibration framework that treats geometry, modality, and robotic parameters as coupled variables rather than independent error sources.

6. Ultrasonic Phased Array Measurement & Compression for In-Process Weld Bevel Estimation

6.1. Introduction

Measurement of bevel length and angle is a key measurement parameter in robotic welding applications, deterring optimum torch position and angle. Incorrect welding bevel angles can lead to serious fabrication issues, particularly in fit-up, distortion, and reference alignment. A mismatch in bevel angles complicates proper fit-up, resulting in gaps that demand excessive filler metal and may cause weld defects. Larger bevel angles tend to increase transverse and longitudinal shrinkage, contributing significantly to angular distortion, which compromises dimensional accuracy and structural integrity [155]. Distortions caused by asymmetric heat input during welding also impair geometric referencing, leading to challenges in maintaining tolerances in large structures [156].

Robotic welding inspection systems have traditionally relied on active vision-based techniques such as structured light, stereo triangulation, and infrared or laser sensors for seam tracking and feature detection. While effective in controlled environments, these approaches degrade significantly under arc light saturation, fume interference, surface fouling, shiny metallic surfaces and variable emissivity [157], [158], [159]. Moreover, the reflective artifacts and tight alignment requirements of laser-based methods limit their utility in unstructured or dynamic scanning conditions, as opposed to volumetric reconstruction using ultrasonic imaging [160], [161], [162].

Ultrasonic techniques are widely valued for their ability to provide volumetric inspection—detecting flaws not just at the surface, but deep within the weld structure. A key advantage over optical or infrared methods is their insensitivity to surface conditions such as roughness, reflectivity, or emissivity, which often impair other modalities. Ultrasonic transducers, especially those based on piezoelectric polymers, have demonstrated robust performance in varied and harsh environments, including those with high humidity, temperature shifts, or fume-laden atmospheres [163]. These attributes make ultrasonics particularly suited for weld inspection in industrial settings, where consistent imaging and flaw detection must be maintained despite environmental variability.

Phased array ultrasonics is a cornerstone of NDE, particularly in industrial environments where visual inspection fails due to occlusions, poor lighting, or surface contamination. When augmented with FMC, phased array ultrasonics offers unparalleled volumetric imaging resolution by recording all transmit–receive combinations within an array and post-processing then using methods such as TFM [164], [165]. However, the widespread adoption of FMC-TFM pipelines is constrained by practical limitations and requirements such as high-dimensional data and significant computational resources [166], [167], [168]. These challenges are especially problematic for robotically deployed applications where travel speed is often a key driver and metric [169].

TFM-based imaging can provide sub-millimetre precision but often incurs delays of several seconds per frame—rendering it unsuitable for in-process robotic control or closed-loop inspection [166], [167], [168]. In response, recent research has proposed strategies to reduce FMC data load, including compressive sensing, sparsely designed transducer arrays, and numerical modelling optimizations [168], [170]. While these methods have achieved compression rates upwards of 80% [171], they typically rely on offline reconstruction and remain poorly integrated with real-time robotic systems. High-throughput acquisition systems also face trade-offs between flexibility and interpretability, particularly in embedded contexts, such as robotic deployment of PAUT [172].

Despite these efforts, a significant gap remains in the field of ultrasonic driven robotic welding as no existing framework performs both real-time bevel geometry estimation and task-specific FMC compression in a way that is compatible with robotic ultrasonic scanning. This dual challenge—balancing computational efficiency with geometric accuracy—represents a critical barrier to deploying PAUT systems for dynamic, in-process inspection.

This work addresses that gap by presenting a lightweight, unified ultrasonic signal processing pipeline tailored for ultrasonic driven robotic welding applications. The core contributions are as follows. First, a GPU-accelerated Histogram of Oriented Gradients (HOG) algorithm for bevel orientation estimation is proposed, capable of sub-second execution (<100 ms) with angular precision of ±0.4°, significantly outperforming prior edge detection or optical flow-based methods. Second, an adaptive FMC compression scheme based on numerical integration and Area Under the Curve (AUC)-thresholding is introduced, which unlike prior compressive sensing strategies, emphasizes interpretability and task relevance, while maintaining low execution times (<250 ms) for conventional V-grooves. Third, we demonstrate the generality of the framework by validating across geometric extremes: from 16 mm thick V-grooves to 120 mm thick narrow gap mock samples using both robotic inspection using pulse-echo configuration for V-grooves and manual dual tandem configurations for thick sample. Together, these contributions represent the first demonstration of a modular and real-time-capable FMC processing pipeline that performs geometry inference and data sparsification in tandem. Its low-latency design and interpretable architecture demonstrate strong feasibility for future deployment in embedded, closed-loop robotic welding platforms.

6.2. Related Work

Post-FMC imaging algorithms such as TFM come at the cost of data scale: FMC acquisitions grow quadratically with array size, creating bandwidth and memory bottlenecks that hinder their use in time-sensitive robotic applications [166], [173]. Furthermore, human operation can induce additional errors during NDE [174], specifically regarding wedge positioning. Robotically enabled ultrasonic inspection scanning can mitigate this through precise, repeatable motion for complex parts [175] and human-robot collaboration [173]. To mitigate the FMC data burden during NDE and potentially enable integration with automation, various signal compression techniques have been proposed. Classical approaches include wavelet transforms, and sub-band coding, which achieve high compression ratios but often introduce latency or suffer from interpretability issues [176], [177]. More recent work has explored deep learning–based encoders and generative models, such as autoencoders and Generative Adversarial Networks (GANs) , to achieve compression ratios upwards of 90% [178], [179]. While effective in reducing dimensionality, these models are typically trained offline and are not readily suited for edge deployment or real-time feedback control.

Compressive sensing frameworks offer an attractive alternative by exploiting the sparsity of ultrasonic signals. Several studies have demonstrated 60–80% data reduction using sparsely sampled arrays combined with signal recovery models [168], [171], [180]. The integration of these two capabilities would enable closed-loop robotic control, real-time weld monitoring, and data-efficient inspection pipelines. The current work addresses this void by proposing a GPU-accelerated, threshold-based signal processing pipeline validated within realistic robotic welding environments.

A comparative summary of existing compression approaches is presented in Table 7. Across the spectrum, none of the reviewed techniques simultaneously support geometric feature inference and data compression in a real-time-capable, robot-integrated framework. This motivates the current work: a unified, lightweight pipeline that enables both ultrasonic feature extraction and FMC sparsification, validated under realistic robotic scanning conditions. In the context of time reversal imaging, partial real time capabilities correspond to the need for a static setup in order to enable reconstruction of the signal without lateral defocusing.

Method	Compression Ratio (%)	Reconstruction Accuracy / Peak SNR	Real-Time Capable	Ref. No.
Discrete Wavelet Transform (DWT)	~80–90%	PSNR: 36–39 dB	✗	[176], [177]
3D Wavelet + DWT + Fourier	~95%	PSNR: ≥27 dB	✗	[181]
Wavelet + ML (Fast Chirplet)	95%+	High fidelity, parametric	✗	[182]
Autoencoders + GANs	80–98%	High visual fidelity	✗	[178], [179]
Compressive Sensing	60–80%	<1 mm error typical	✗	[168], [171], [180]
Time-Reversal Imaging	N/A	Comparable to TFM	Partial	[183]
Proposed Method (Threshold + HOG)	>88%	<2 mm length error, <0.4° orientation error	✓	—

Table 7. Literature review of existing compression method.

6.3. Methodology

This study presents a robust, multi-stage pipeline for automated ultrasonic inspection and bevel orientation estimation using a combination of robotic FMC scanning, AUC-based data compression, and HOG-based orientation analysis, as shown in Figure 43. The methodology comprises three primary stages: robotic scanning and data acquisition, AUC-based data sparsification and reconstruction, and orientation estimation via gradient feature analysis.

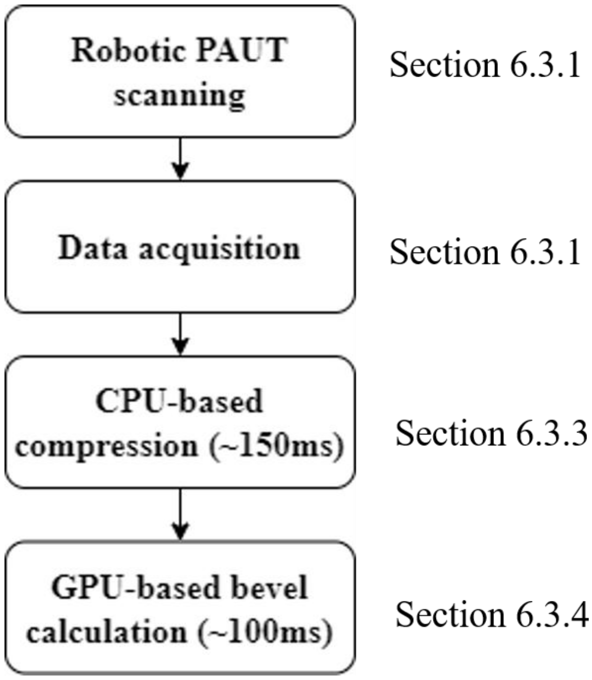

Figure 43. Overview of methodology. Initially, PAUT is robotically deployed to acquire ultrasonic data. Then, the data is compressed and orientation is extracted.

6.3.1 Experimental Setup and Data Acquisition

The inspection process begins with a robotically deployed ultrasonic system equipped with a force-torque sensor and a custom-designed RollerProbe [87], as shown in Figure 44a. The robotic system ensures consistent coupling and stable scanning force throughout the inspection procedure. The robot traverses a pre-defined linear scanning path over the test specimen (600 mm × 250 mm), which contains multiple machined bevels, as shown in Figure 44b. The 16 mm thick carbon steel sample was manufactured to represent a wide range of bevel lengths, at industry representative angles, across the full joint fill cycle from root pass to cap pass, as shown in the weld geometry of [184]. The geometry of the specimen is presented in Figure 44c, with heights of 11.8, 9.3, 6.8, 4.3 and 1.69 mm, to simulate the different layers of that multipass weld.

A scanning speed of 2 mm/s, a coupling force of 125 N, and an acquisition time of 0.5 frames per second were used with a gain of 90 decibels. During scanning, FMC data is acquired at each position. The data processing pipeline initiates a two-part processing sequence comprising CPU-based data compression (approximately 150 ms) and GPU-accelerated bevel orientation estimation (approximately 100 ms), ensuring near real-time execution.

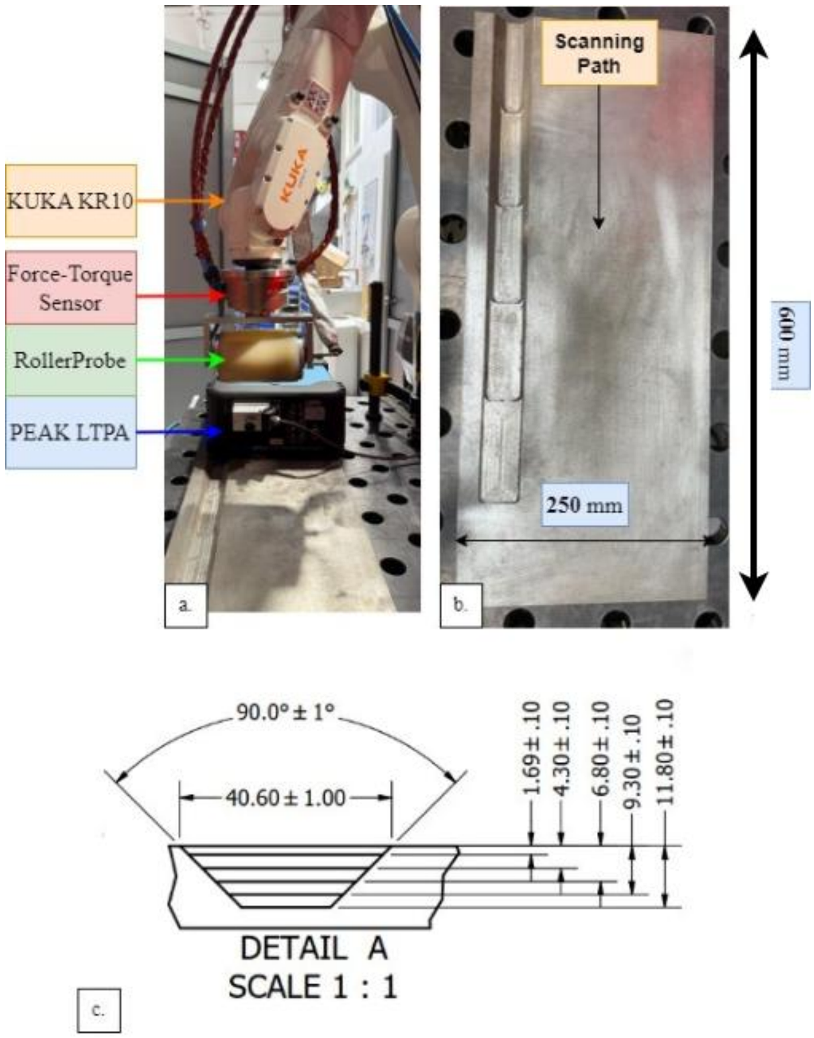

Figure 44. (a) Robotic inspection setup used for data acquisition, featuring a KUKA KR10 manipulator with a custom RollerProbe, force-torque sensor, and PEAK LTPA FMC system. (b) Scanning performed along a predefined linear trajectory over simulated weld bevels. (c) Cross section of sample geometry

For the phased array, a central frequency of 5 MHz, 64 elements, and a pitch of 0.5 mm were used. Additionally, a Pulse Repetition frequency of 2.1 kHz, a voltage of 200 V, and a gate of 60 μs to 120 μs with a sampling frequency of 100 MHz were used for the array, leading to a frame size of 6000x4096. As shown in Figure 19b, 3 shear full skips were used for transmission and reception, leading to an acoustic path of 67.0mm.

6.3.2 Calibration

The measurement accuracy in this study is influenced by three main categories of error: ultrasonic measurement uncertainty, robot-induced error during dynamic motion, and manufacturing tolerances of the test sample (Table 8). The measurement error for the variation in shear wave speed for steel was determined using a wedge with the same material, refraction angle, incidence angle and acoustic path, and conducting thickness measurement using a linear scan with a sub aperture of 8 elements, gain of 70 dB, voltage of 150 V for a sample with thickness of 120 mm, and a gate of 60 to 95 μs, as shown in Figure 45. Then, the variation in the TOF was evaluated to extract the aggregate measurement error, composed of both error due to microstructure variation, as well as manufacturing imperfections in the ultrasonic wedge. For the robotic system, additional errors originate from TCP height variations reported by the robot controller and the resolution limit of the Delta SI-165-15 force–torque sensor [149]. Finally, the sample was machine to an ±0.1 mm accuracy.

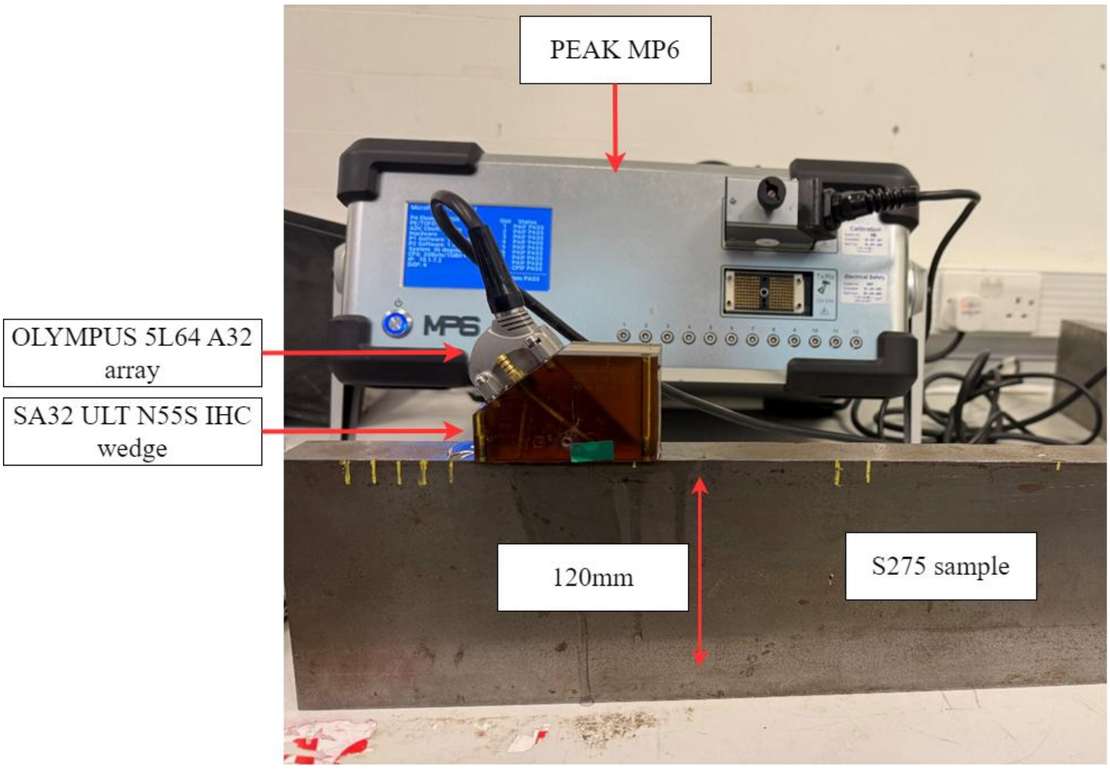

Figure 45. Experimental setup for measurement of shear wave speed variation.

Uncertainty Source	Measured Property	Nominal Value	Error
Steel sample	Steel shear wave speed	3260 m/s	5.9 m/s
Robotic manipulator	Coupling force	125 N	1/16 N
Robotic manipulator	Height	0 mm	±0.1 mm
Metal plate	Bevel length	11.8, 9.3, 6.8, 4.3 and 1.69 mm	±0.1 mm

Table 8. Sources of uncertainty for current study

6.3.3 Compression

Following data acquisition, the raw FMC data undergoes compression through an AUC-based numerical integration and sparsification procedure, as shown in Figure 46. The first phase, numerical integration, involves computing the absolute values of FMC signals, followed by averaging across transmit-receive pairs, as shown in equation 24.

$$\bar{F}(i,t) = \frac{\sum_{j=1}^{64} |f(t,j)|}{64} \tag{24}$$

where $f(t,j)$: ultrasonic amplitude scan, $\bar{F}(i,t)$: average of absolute value per transmission, t: time index, $t \in \{1, 2, \ldots, 6000\}$, j: reception element, $j \in \{1, 2, \ldots, 64\}$, and i: transmission element, $i \in \{1, 2, \ldots, 64\}$.

Variable windowing is then applied to adapt the temporal resolution based on signal characteristics. The windowed signals are integrated to compute local AUC values, which represent the spatial energy distribution of the ultrasonic responses, as shown in equation 25:

$$A(i,n) = \int_{t+(n-1)\cdot w_s}^{t+n\cdot w_s} \bar{F}(i,t)dt \tag{25}$$

, where $A(i,n)$: AUC per transmission and window index, n: window index where n is in range (1 to 6000/w_s), with 6000 being the number of time samples and w_s: window size.

In the sparsification phase, statistical features of the AUC map are used to define adaptive thresholds that suppress low-energy or irrelevant signal regions by subtracting the scaled standard deviation from the average AUC over the whole aperture. Low-AUC regions are discarded, and only significant transmission pairs with strong acoustic responses are retained, as shown in equation 26:

$$A(i,w) = \begin{cases} A, A \geq T \\ A, A < T \end{cases} \qquad (26)$$

where T: statistical threshold based on integral of amplitude.

These are used to construct a sparse matrix representation of the acoustic scene.

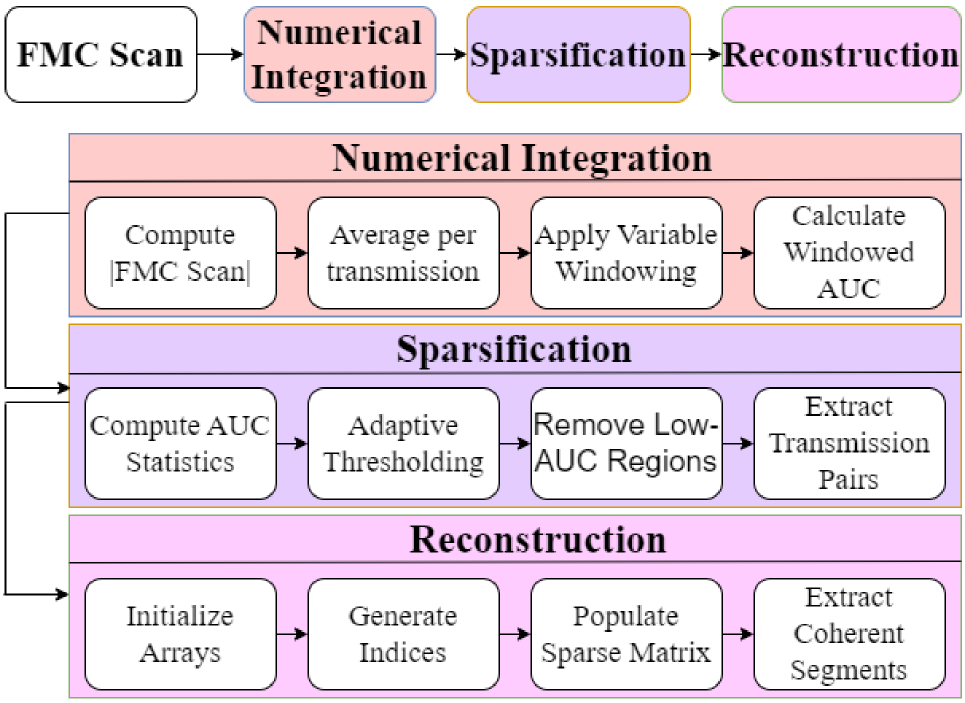

Figure 46. In the AUC-based sparsification process, raw FMC data is first used to compute the indices of windows with high acoustic energy. These indices are then used to remove low-energy regions based on the threshold, resulting in a sparsified signal matrix that preserves the most informative components.

The reconstruction step initializes sparse arrays and regenerates the data indices of retained signals. These indices are used to populate a sparse matrix while maintaining spatial coherence. Subsequently, the data is segmented into coherent signal regions for downstream analysis. This results in a highly compressed and information-rich representation of the original ultrasonic scan, optimized for rapid interpretation and feature extraction.

6.3.4 Bevel Orientation Extraction

HOG is a feature descriptor used to identify objects by analysing the distribution of edge direction and intensity [185]. In this Chapter, bevel orientation estimation is performed using a pipeline based on HOG applied to the reconstructed B-scan images, as depicted in Figure 47. The approach was methodologically inspired by previous work [186], which utilized HOG descriptors for automatic rebar detection in ground penetrating radar images of deteriorated concrete bridge decks. The process begins with log-scaling to enhance signal contrast, followed by thresholding to suppress low-value noise. Peak bin ratio filtering is then applied to isolate dominant reflections, and high-noise regions are excluded. The HOG feature computation uses Sobel operators, a common computer vision filter for edge detection, to compute image gradients, as shown in equations 27 and 28, followed by calculating the gradient magnitude and angle at each pixel, as shown in equations 29 and 30. The equations are as follows:

$$G_h(t, j) = I(t, j + 1) - I(t, j - 1) \tag{27}$$

$$G_v(t, j) = I(t + 1, j) - I(t - 1, j) \quad 28$$

$$M(t, j) = \sqrt{G_h^2(t, j) + G_h^2(t, j)} \quad 29$$

$$\theta(t, j) = \arctan\left(\frac{G_v(t, j)}{G_h(t, j)}\right) \quad 30$$

where G_h: horizontal gradient, G_v: vertical gradient, M: magnitude and θ: angle.

Finally, a sliding window approach is employed to extract local HOG features across the B-scan. Histogram averaging is used to determine the dominant gradient orientation within each window, which corresponds to the local bevel angle. This orientation output provides a precise and computationally efficient estimate of the weld bevel geometry.

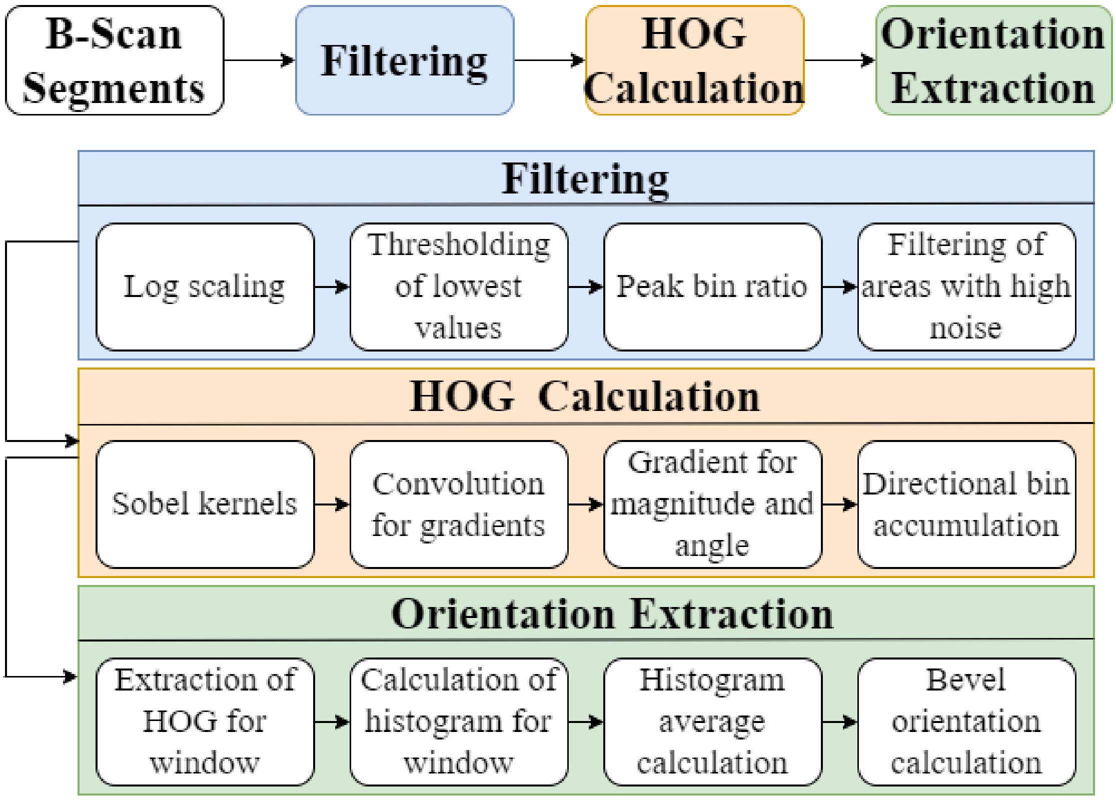

Figure 47. Bevel orientation estimation using HOG involves log-scaling the B-scan image, applying noise suppression with peak filtering, extracting HOG descriptors across localized windows, and estimating the dominant orientation from aggregated gradient histograms.

6.3.5 Evaluation

To evaluate the performance of the proposed ultrasonic inspection and bevel orientation estimation pipeline, three key quantitative metrics were employed: orientation accuracy, length estimation, and execution time. Orientation was measured in degrees (°) and compared against ground truth bevel angles obtained from both the CAD design and manufactured reference, enabling the assessment of angular deviation in the estimated bevel orientation across multiple scan frames. The nominal value of the bevel orientation is the result of the subtraction between the natural exit angle of the wedge (55°), and the bevel orientation (45°) for the A-Scans. Length estimation, expressed in millimetres (mm), was used to quantify the spatial extent of detected bevel features along the scan path, validated against known physical dimensions of the machined test specimens. The length was calculated using the 6 dB drop method on the final TFM images, as described in Section 2.4.5.1. Execution time was recorded in seconds (s) to benchmark the computational efficiency of the system, with CPU-based AUC compression and GPU-accelerated orientation estimation stages evaluated independently. The execution time was measured using timing functions from Matrix Laboratory (MATLAB), for the compression (numerical integration and sparsification), and bevel orientation (filtering, HOG calculation, orientation extraction). The computer specifications are presented in Table 9 which establish a reference for execution timing.

Specification	**Component**
Central processing unit	I7-12800H (14 cores, 4.8 GHz)
Graphics processing unit	Nvidia RTX A2000 (8GB GDDR6)
Random Access Memory	32 GB (DDR5, 4800 MHz)

Table 9. Laptop specifications.

Metrics were selected from literature to quantitively evaluate the performance of the proposed method, in addition to the bevel length and orientation. These include the array index performance (API) [187], sparseness [188], and percent residual difference (PRD) [171]. These metrics were selected to evaluate the difference in signal reconstruction, the image lateral resolution and the overall sparseness for the resultant FMC array using the proposed method. The definitions for API, sparseness and PRD are presented in equations (31), (32) and (33) respectively.

$$P = A_{ampl}/\lambda^2 \tag{31}$$

$$PRD = \sqrt{\frac{\sum_{n=1}^{N}(x_n - \hat{x}_n)^2}{\sum_{n=1}^{N}(x_n)^2}} \cdot 100 \tag{32}$$

$$\text{Sparseness} = \frac{\sqrt{N} - \|X\|_1/\|X\|_2}{\sqrt{N} - 1} \tag{33}$$

where P: API, A_{ampl}: area where amplitude of point scatterer is greater, λ: wavelength, x_n: original signal, $\hat{x}_n$: reconstructed signal, N: signal length, and X: reconstructed signal.

Data were collected continuously during dynamic scan passes with the robotic system acquiring FMC data in motion, enabling frame-by-frame evaluation under realistic inspection conditions. To assess performance systematically, 15 frames were extracted at 20 mm intervals from the initial dataset of 86 frames. For each frame, a grid search with 15 different permutations of algorithmic parameters were performed over window sizes ranging from 32 to 288 samples (in 64-sample steps).

This approach captured the system's response across varying sparsification settings and noise conditions. Frames exceeding a 220-sample window consistently lost structural detail, prompting a focus on smaller window sizes for reliable evaluation. This combination of dynamic acquisition, parameter sweeps, and automated geometric inference enabled a robust, high-throughput pipeline suitable for real-world weld characterization in NDE applications.

6.4 Results

Following the methodology outlined above, the proposed ultrasonic inspection and bevel orientation pipeline was evaluated across multiple metrics: data sparsification effectiveness, geometric inference accuracy, and computational performance. These results demonstrate not only the feasibility of the system for real-time application but also its consistency and reliability for different algorithmic permutations.

The segmentation and reconstruction fidelity of the pipeline were initially assessed by comparing the original and segmented FMC frames. As illustrated in Figure 48a, the original frame retains full transmission information, resulting in a high-resolution TFM image (where the bevel reflection is clearly defined, as shown in Figure 48b. The segmented frame in Figure 48c, which retains only high-AUC transmission pairs, shows a drastically reduced number of active signal paths. Nevertheless, the reconstructed TFM image in Figure 48d remains visually consistent with the original, confirming that critical structural features are preserved despite substantial data reduction. This aligns with sparsification strategies seen in compressed sensing NDT [171], but goes further by incorporating a grid search of AUC thresholds, to find an optimal combination of algorithmic parameters tailored to ultrasonic energy distributions, rather than fixed sparsity patterns.

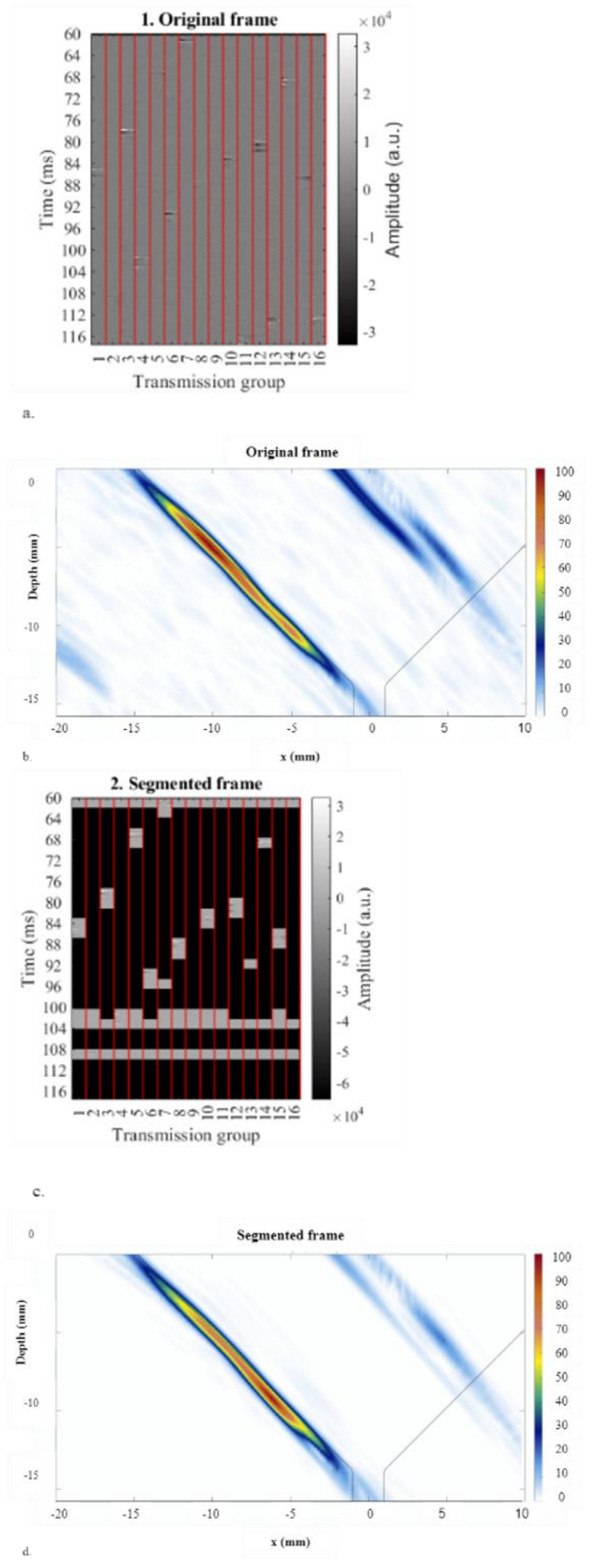

Figure 48. TFM image reconstruction comparison: (a) full FMC dataset and (b) corresponding TFM image; (c) sparsified dataset using AUC-thresholded pairs and (d) resulting TFM reconstruction. Structural integrity preserved despite significant data reduction.

A quantitative analysis of the proposed method is presented in Figure 49 for the original frame, as shown in Figure 49a. As a baseline, shown in Figure 49b, a homogenous sparse array with a skip step of 3 was created in post-processing, by removing corresponding transmissions and receptions. This is in line with current compressive sensing methods, where the main methods of sparsification include array layout [189] and signal [171] sparsification. The proposed method configurations achieve compression ratios exceeding 89% while maintaining superior image quality compared to using a sparse array layout. High PRD values (80-83%) reflect high modification of the original data, demonstrating the reconstruction algorithm's ability to preserve diagnostic image quality (SNR, bevel length, and low artifact levels) despite significant raw channel data compression. Here, it should be noted that reconstruction accuracy is higher, relative to using a sparse array layout. The window size 160 in the configuration shown in Figure 49d achieves the best performance with 37.4 dB SNR, an increase of 8.8dB and lower API than the original image, matching and improving the original full-aperture result while using a fraction of the data.

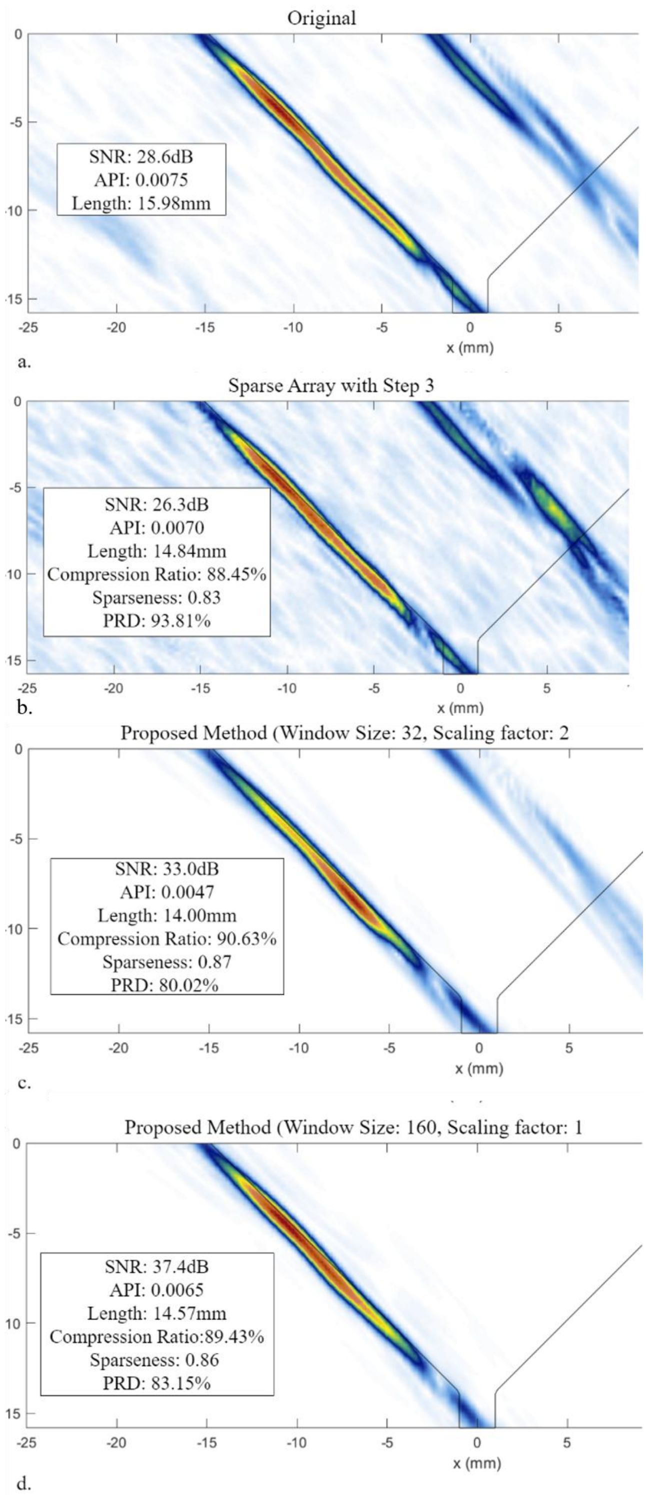

Figure 49. Comparison of ultrasonic imaging reconstruction methods for a side-drilled hole phantom. (a) Original full-aperture image using all array elements (baseline). (b) Sparse array reconstruction using every 3rd element without compression. (c) Proposed compressed sensing method with window size 32 and scaling factor 2. (d) Proposed compressed sensing method with window size 160 and scaling factor 1.

The next step in the methodological pipeline is orientation estimation, which relies on the accuracy of the compression. In Figure 50a, the first step is construction of a tall array of the segmented B-scans, while Figure 50b demonstrates suppression of robotic interference and background noise. HOG analysis in Figure 50c reveals dominant directional gradients, which differs based on the prominence of either structural echoes or robot interference. The reported angle of 0.12 rad (equivalent to 6.84°) reflects the orientation relative to the vertical scanning axis, not the absolute bevel geometry. Given the system's natural probe exit angle of 55° and an expected bevel angle of 45°, the resulting signal orientation is expected to fall in the ~10° range. The deviation is attributed to localized actuation noise and interference, which can introduce gradient components typically around 7°, thus biasing the averaged estimate in local regions. This highlights a current limitation of the AUC thresholding strategy: while it effectively reduces low-energy clutter, it can over-preserve noise-dominated regions under high actuation or poor coupling. This is in part circumvented through averaging of the regions, but future work will explore adaptive thresholding and structural filtering to better isolate acoustic features.

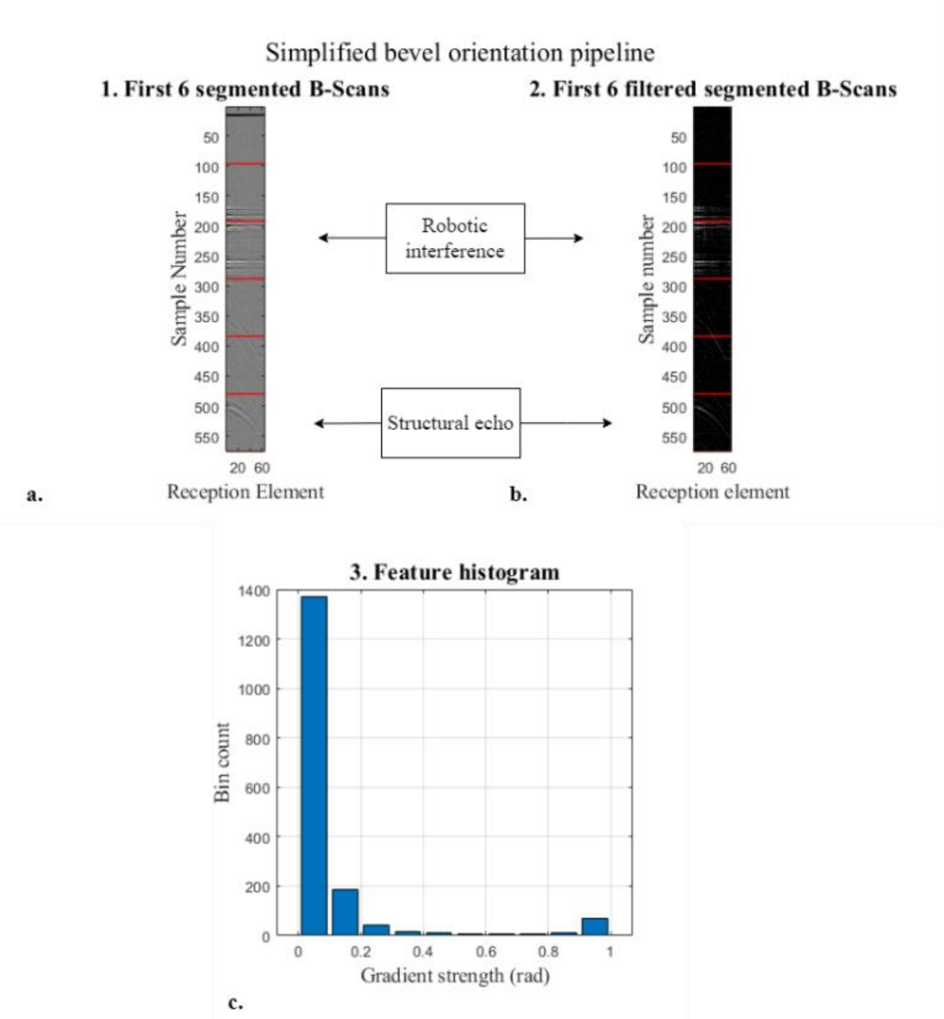

Figure 50. Gradient analysis in bevel orientation estimation: (a) segmented B-scan image; (b) interference suppression (c) histogram of gradient orientations highlighting dominant directional bias.

To evaluate spatial consistency, bevel lengths were extracted across sequential frames using the proposed pipeline. Figure 51 presents a boxplot illustrating per-frame variability, with most values ranging from 12–16 mm, closely aligning with the larger machined bevel dimensions. These metrics were computed across a grid of window sizes and statistical thresholds to assess robustness under variable sparsification conditions. Window sizes beyond 220 samples consistently led to image degradation dominated by robotic interference, prompting us to restrict analysis to sub-220 sample ranges. The resulting narrow interquartile spread across frames indicates a stable and repeatable system response. In contrast to earlier robotic phased array ultrasonic inspection systems such as [190], our approach preserves spatial coherence of structural features under efficient compression, effectively maintaining the bevel echo, where previous methods did not address this challenge.

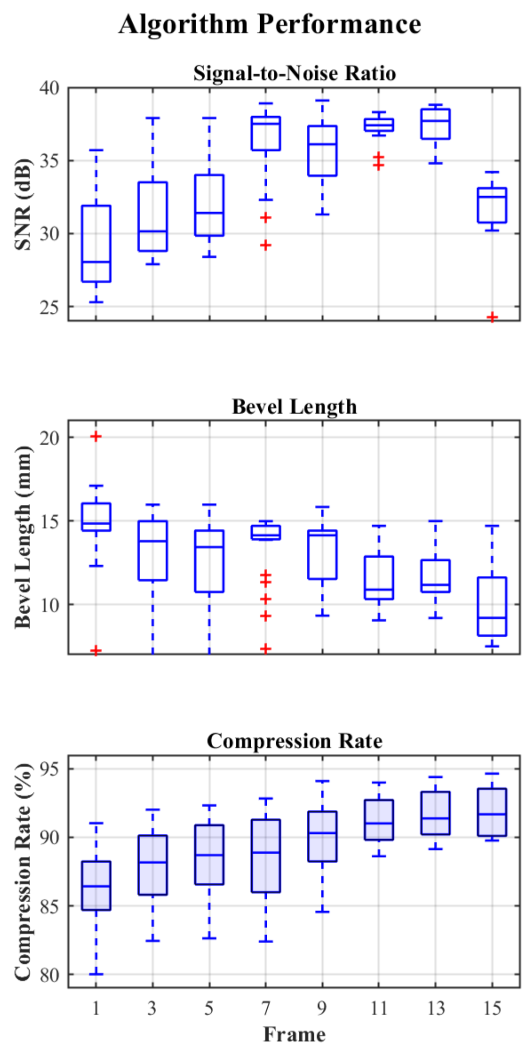

Figure 51. Boxplot of bevel length estimates across 15 sequential scan frames. Most values fall within 12–16 mm, consistent with known geometry. Variability in later frames attributed to boundary signal fading and occlusion.

More specifically, frame-wise results track closely with physical bevels across Layers 1–3. Frame 1 (Layer 1) shows near-exact alignment (~16 mm), while Frames 3, 5, and 7 (Layer 2) centre around 13–14 mm—matching the known 13.15 mm length. Frames 9, 11, and 13 (Layer 3) remain within 1–1.5 mm of the 9.62 mm ground truth. The only notable deviation occurs at Frame 15 (Layer 4), which overestimates the 6.08 mm feature as ~10 mm . This discrepancy stems from limitations in TFM resolution and shallow-depth SNR rather than from the compression itself. The pipeline preserves geometric fidelity up to the limits imposed by the underlying imaging method. An additional crucial cause is the very long acoustic path, which can lead to mode conversions and spreading of acoustic energy, as discussed in prior work [191].

The geometric inference accuracy was further quantified by analyzing the absolute error of signal fidelity and shape estimation. As shown in Figure 52, the signal-to-noise ratio (SNR) error remains predominantly within 0–4 dB, indicating minimal degradation due to compression. Bevel length errors are centered around ±2.0 mm, while bevel orientation errors mostly lie within ±0.4°, with very few outliers. This is significant when contrasted with earlier work such as [164], where bevel features in narrow-gap welds were difficult to resolve without full-resolution FMC data. Here, similar resolution is achieved with substantially fewer data points.

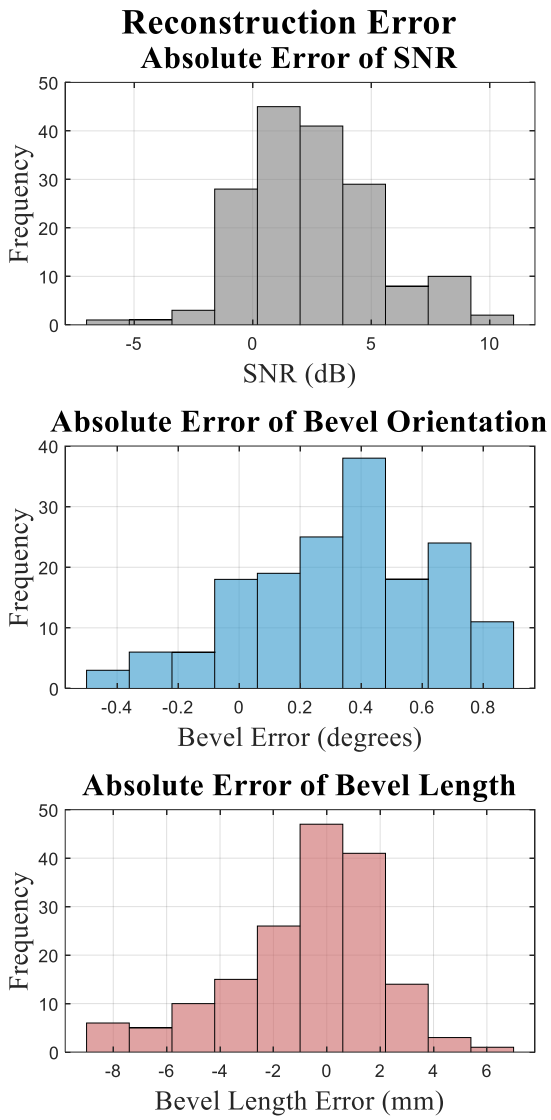

Figure 52. Quantitative analysis of geometric inference errors: (a) SNR deviation, (b) bevel length error, and (c) orientation error across test frames. Compression-induced distortions remain within acceptable thresholds (<4 dB, <2.0 mm, ±0.4°).

Notably, algorithmic parameters—including AUC thresholds, HOG window sizes, and gradient binning—were empirically selected to reflect typical energy distributions and feature prominence observed in ultrasonic B-scans. A comprehensive sensitivity analysis of these parameters is beyond the scope of this study but remains a critical dimension for future work.

The real-time capability of the system was evaluated through detailed time performance metrics, summarized in Figure 53. The CPU-based AUC compression consistently executes within 150 ms per frame, while the GPU-based bevel orientation estimation completes under 100 ms. This sub-second performance supports practical deployment for in-process inspection. Comparable systems in the literature, such as the framework proposed by [171] employ full FMC-TFM imaging pipelines but encounter significant computational burdens, with frame reconstruction times often exceeding 1 second. This makes them impractical for dynamic robotic integration without introducing latency bottlenecks or post-processing delays.

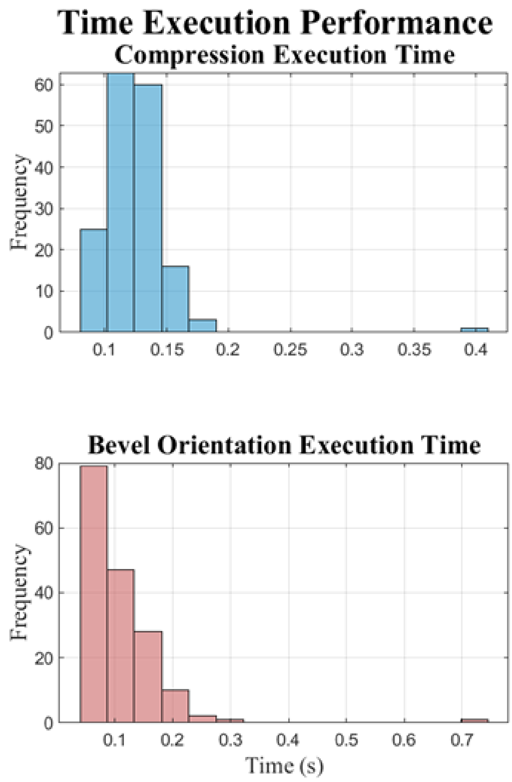

Figure 53. Execution time performance across processing modules. CPU-based AUC compression remains within 150 ms per frame; GPU-based orientation estimation executes under 100 ms—supporting real-time operation.

Following the aggregate execution time for compression and orientation extraction, a detailed breakdown is presented in Figure 54. For frames 2-9, the compression execution time remains consistent at approximately 50 ms per stage (totaling ~150 ms) across different geometries, with each of the three stages—integration, sparsification, and reconstruction—contributing roughly equal proportions. In contrast, the orientation extraction time is dependent on the extracted bevel length, with filtering and HOG calculations requiring the majority of the computation time, which remains consistently below 100 ms for frames 2-9. The notably slower execution time in frame 1 is attributed to startup overhead required for GPU initialization in the bevel orientation extraction pipeline.

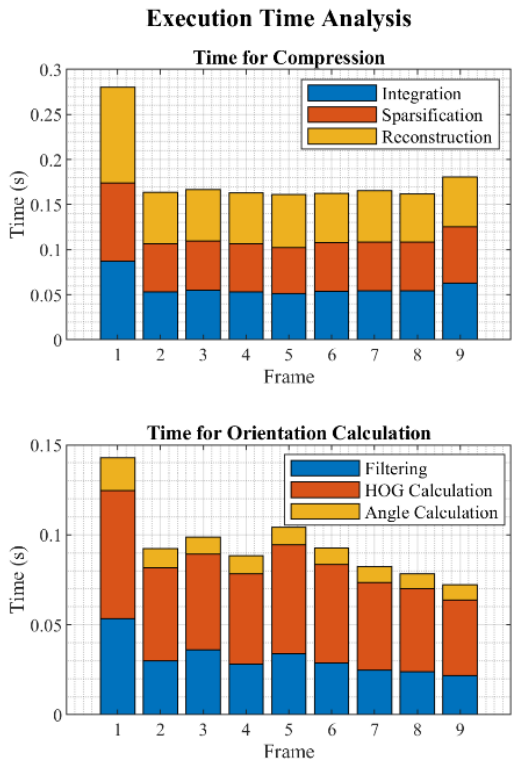

Figure 54. Execution time analysis for compression and orientation calculation pipelines for V-groove. Stacked bars show the breakdown of computational costs across nine frames.

6.5. Narrow Gap Validation

In order to evaluate the generality of the method across both geometry detection and internal planar flaw detection, the compression methodology presented in this work was validated by experimentally replicating the previous study by Nicolson et al. [53] for data acquisition, which employed a dual-tandem phased array configuration for imaging near-vertical defects in mock narrow-gap welds. Figure 55 illustrates the experimental setup showing a 120 mm thick carbon steel sample containing an Electrical Discharge Machining (EDM) notch (height = 5.0 mm, width = 1.0 mm, orientation = 2°) positioned at 60mm depth, with probes separated by 243.0 mm. This configuration is presented here to provide context for the ultrasonic data utilized in our compression analysis. The dual-tandem arrangement employed 5 MHz, 64-element Imasonic arrays with 60° refraction angle Rexolite wedges, optimized for simultaneous longitudinal and shear wave transmission. This original experimental framework provides a robust foundation for evaluating our compression technique, as the full matrix capture data encompasses multiple imaging modes (L-L, LL-L, LL-T, LT-L, TL-L, TT-T) across both pulse-echo and through-transmission views, offering diverse ultrasonic signatures against which to assess compression fidelity. In this study, LL-T was used from the left wedge.

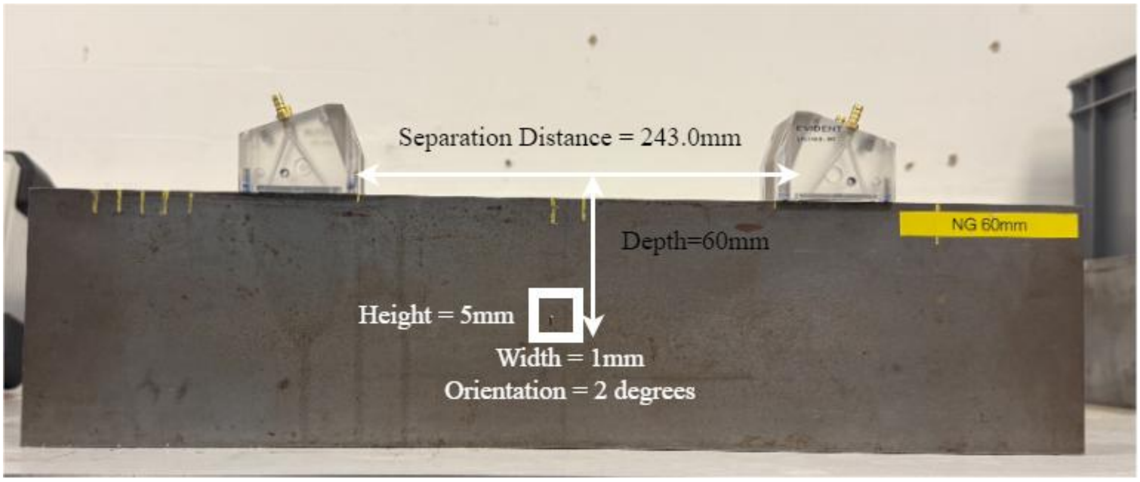

Figure 55. Dual-tandem phased array wedge configuration from Nicolson et al. [53]. Mock narrow-gap sample (120mm thick carbon steel) with 5mm × 1mm EDM notch at 60mm depth, oriented 2° from vertical. Probe centre spacing: 243.0mm.

Figure 56 evaluates the compression framework's performance using TFM reconstructions of a 60mm deep defect in a mock narrow gap sample, where image (a) serves as the uncompressed baseline (SNR: 30.7 dB, length: 15.2mm) against which compressed configurations (b) and (c) are compared. Despite substantial data reduction at 93.3% and 67.08% compression rates, the reconstructed images maintain a robust SNR of 26.8 dB, representing a modest 3.9 dB degradation that remains well within industrial detection limits. Critically, defect characterization remains highly accurate across compression levels, with measured orientations of 2.99° and 2.92° closely matching the true 2° notch angle. It is important to clarify that while the physical EDM notch height is 5mm, the baseline ultrasonic reconstruction measures 15.2mm; this discrepancy is an inherent limitation of single-mode imaging for this geometry, as discussed in previous work [40]. The consistency between baseline and compressed lengths (18.0 mm and 17.8 mm) confirms that the sparse representation framework preserves the essential acoustic signature. Parametric variation demonstrates a clear trade-off, where tripling the window size from 32 to 96 samples reduces the PRD (64.59% to 50.99%) at the cost of reduced compression aggressiveness. It should be noted that for accurate bevel orientation, the number of bins during computation of HOG was increased from 16 to 128, for each bin to encapsulate 180/128=1.4°.

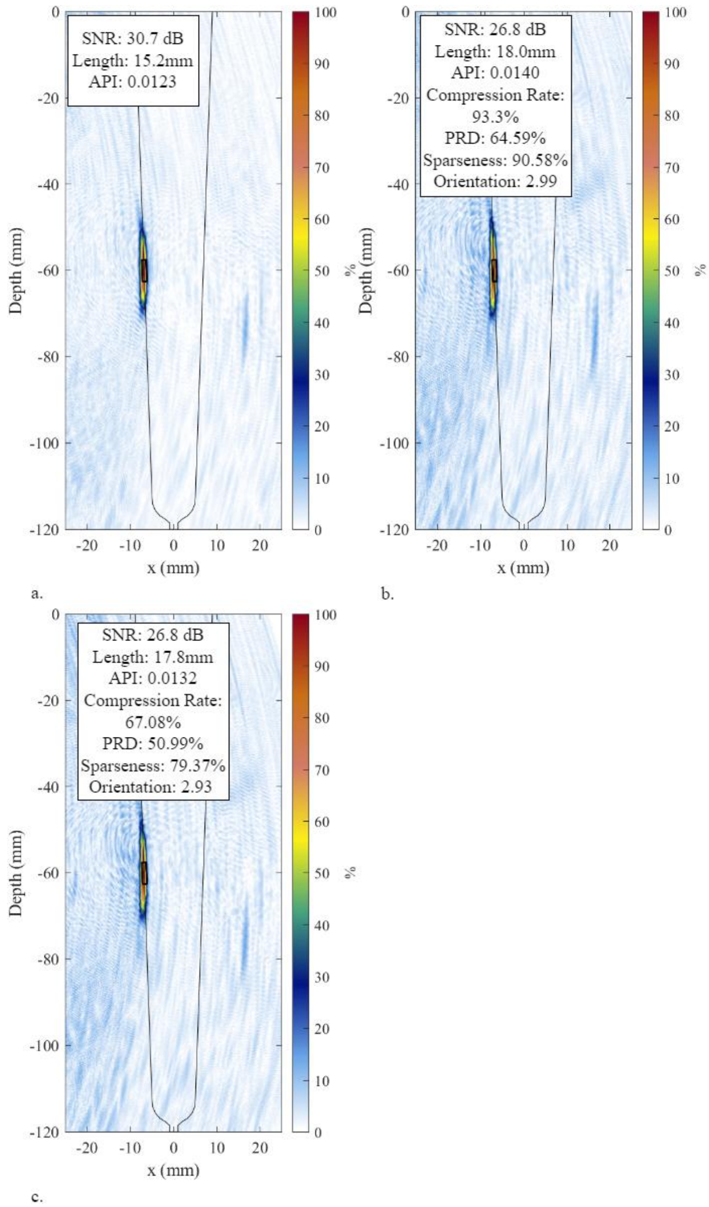

Figure 56. TFM image quality comparison across compression levels for 60mm depth defect. (a) Uncompressed baseline: SNR 30.7 dB, length 15.2mm, API 0.0123. (b) 93.3% compression: SNR 26.8 dB, orientation 2.99°, sparseness 90.58%, PRD 64.59% for window size of 32 samples, and scaling factor of 2. (c) 67.08% compression: SNR 26.8 dB, orientation 2.93°, sparseness 79.37%, PRD 50.99% for window size sample of 96 and scaling factor of 2. Compressed images maintain defect detectability and geometric accuracy despite significant data reduction.

The computational performance of the proposed compression framework is characterized in Figure 57 for the mock narrow gap geometry, which presents timing analysis for both data compression and defect orientation calculation processes. The compression workflow, comprising integration, sparsification, and reconstruction stages, maintains total execution times below 1.1 seconds per frame, with each component contributing approximately equal computational load. Orientation calculation, encompassing filtering, HOG computation, and angle extraction, completes within 0.6 seconds per frame. The temporal consistency across three sequential frames demonstrates stable algorithmic performance independent of defect depth or imaging complexity. Importantly, these timing characteristics reflect processing of the complete dual-tandem dataset—encompassing four distinct views (left pulse-echo, right pulse-echo, left through-transmission, right through-transmission)—indicating that the compression methodology maintains practical feasibility even when handling the increased data volume inherent to dual-probe configurations. The increase in execution time relative to V-grooves is expected, due to an increase in the number of bins to account for near-vertical nature of defect.

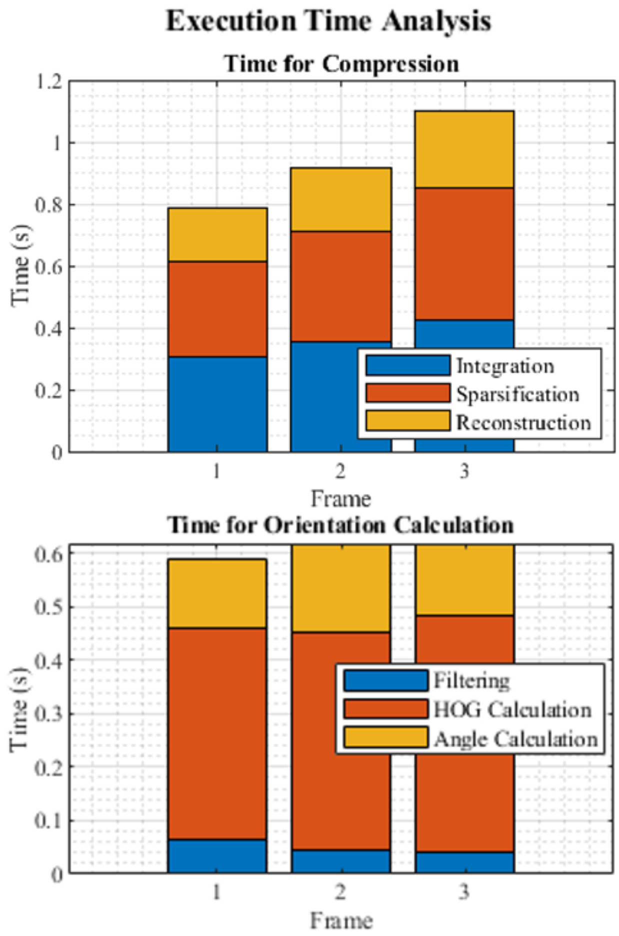

Figure 57. Execution time analysis for compression and orientation calculation pipelines for near-vertical defects. Stacked bars show the breakdown of computational costs across nine frames.

Comparative analysis across the narrow-gap and V-groove geometries reveals the compression framework's robust performance despite fundamentally different inspection scenarios and parameter configurations. Table 4 summarizes key performance metrics across both geometries with various compression parameters. The mock narrow-gap geometry (near-vertical 2° defect) maintained consistent SNR of 26.8 dB across two compression levels (93.3% and 67.08%) achieved through window size variation (32 vs. 96 samples), demonstrating stable noise floor characteristics despite aggressive data reduction. The V-groove geometry (90° bevel, conventional defect orientations) exhibited remarkable SNR enhancement (4.4-8.8 dB above baseline) at comparable compression rates (89.43-90.63%), suggesting geometry-dependent noise characteristics that the sparse representation framework effectively suppresses. As expected, due to an increase in the amount of data for compression 24.576e6 to 65.536e6 datapoints, the execution time increases approximately proportionally from 0.15s to 0.9s for the compression, with a larger increase from 0.1s to 0.6s due to increased number of bins. The characterisation accuracy of the defect for narrow gap and geometry for V-groove was preserved: orientation measurements in narrow-gap configurations exhibited <1° error (2.99° and 2.92° vs. true 2°), while length measurements in both geometries maintained <12% deviation from baseline. The parametric flexibility demonstrated through window size (32-160 samples) and scaling factor (1-2) variations enables optimization for specific inspection scenarios: narrow-gap configurations may prioritize maximum compression (window 32, scaling 2 → 93.3%) to minimize data storage for long-duration in-process monitoring, while V-groove configurations could exploit SNR enhancement capabilities (window 160, scaling 1 → +8.8 dB SNR) to improve detection sensitivity in high-noise environments. This validated adaptability across geometrically disparate weld configurations—spanning the practical extremes from near-vertical narrow-gap to conventional open V-groove geometries—directly addresses concerns regarding method generality and establishes applicability across the spectrum of thick-section industrial welding practices.

Geometry	Parameters	Compression Rate	SNR Baseline (dB)	SNR Compressed (dB)	Length-Baseline (mm)	Length-Compressed (mm)
Narrow Gap	Window Size: 32 Scaling Factor: 2	93.3%	30.7	26.8	15.2	18
V-Groove	Window Size: 160 Scaling Factor: 1	89.43%	28.6 dB	37.4	15.98	14.97

Table 10. Comparative analysis between narrow gap and V-groove geometry for compression algorithm.

6.6. Discussion

The bevel orientation estimation pipeline presented in this work leverages HOG, traditionally a computer vision technique, to extract dominant edge directions from segmented ultrasonic B-scans. Unlike classical methods in weld feature detection, such as template matching, corner detection, or rule-based tracking ([157], [158], [159])—the HOG-based approach offers several key advantages: it is non-parametric, highly parallelizable, and naturally suited to orientation-dominant features such as bevel edges. Furthermore, its integration with GPU-accelerated computation enables frame-level estimation in under 250 ms, making it considerably faster than edge-deconvolution methods or optical flow-based trackers commonly used in robotic seam tracking ([157],

[158], [159]). The resulting orientation errors (within ±0.4°) validate both the stability and the repeatability of this approach across dynamic scan sequences.

Building on this efficient geometric inference, the proposed adaptive AUC sparsification method addresses the parallel challenge of FMC data management. It introduces a compression scheme that significantly reduces the data burden without compromising the interpretability of ultrasonic features. Unlike methods that apply fixed sparsity patterns [168], [171], [180] our approach uses an AUC-based grid search to find optimal threshold and window size according to the signal's energy profile. This context-aware strategy aligns with recent developments in sparse deconvolution [162] but is tailored specifically for weld bevel characterization. More importantly, the trade-off we observe is not just numerical—such as maintaining SNR errors below 4 dB and bevel length errors under 2.0 mm—but also structural. As seen in Figure 5, even with substantial data reduction, the reconstructed TFM images retain key geometric features, supporting the integrity of the bevel representation. This reflects a shift from compression for the sake of efficiency to compression that is purpose-built for preserving diagnostic relevance.

To contextualize this approach, it is instructive to compare it directly with existing ultrasonic compression techniques. Classical DWT-based methods ([176], [177]) achieve high Peak SNR values (36–39 dB) and up to 90% compression but operate entirely offline and lack task specificity. Deep learning–based approaches such as autoencoders and GANs ([178], [179]) offer compression ratios up to 98%, yet they sacrifice interpretability and require extensive training. Compressive sensing methods ([168], [171], [182]) provide strong geometric accuracy (<1 mm error) but often depend on iterative solvers and sparse hardware configurations not standardized in industrial practice. Although time-reversal imaging [183] matches TFM in theoretical fidelity, its algorithmic complexity limits it to mostly experimental use. In contrast, this method achieves >88% compression with <2 mm bevel error in under 250 ms per frame for V-groove and >60% with <3mm defect measurement error in under 1500ms for near planar defects in thick samples, offering a practical and lightweight alternative for weld characterization during robotic FMC scanning.

This compression–inference pipeline enables sub-second performance across the pipeline, achieved through a hybrid CPU-GPU architecture. Unlike full-resolution FMC-TFM pipelines that routinely exceed 1 second per frame, our approach operates within the latency envelope needed for responsive robotic systems. As a result, it enables data-driven weld feature tracking in dynamic scanning conditions where full-resolution imaging is computationally prohibitive. Furthermore, the compactness of the processing stack supports deployment on portable edge platforms, such as embedded GPUs or mobile robotic crawlers, where compute resources are limited. This modular architecture also lays the foundation for future closed-loop robotic systems, where real-time feedback on weld geometry can inform adaptive transducer alignment or trajectory correction.

Despite these promising results, the pipeline has several limitations. First, it is currently implemented in MATLAB, which, while flexible for prototyping, is not optimized for real-time deployment in embedded or industrial platforms. Although the execution time remains sub-second, integration into high-frequency scanning systems (>100 Hz) may require further optimization. Second, the system operates in a feed-forward mode and does not yet incorporate closed-loop feedback based on in-situ weld feature recognition. This limits its application to fully adaptive or autonomous robotic workflows. Finally, while tested under pose variation and coupling uncertainty, the method's robustness against severe surface contamination, interference from various welding processes, and extreme geometric irregularities has not been fully characterized.

While the proposed methodology demonstrates high fidelity across different geometries of 10° defect orientation and 90° bevel angle, and 15.8 and 120mm thickness, certain limitations remain. Specifically, the selection of the window size, number of bins for HOG computation and scaling factor is currently semi-empirical; while the algorithm is adaptable, future work will focus on automated parameter optimization to further enhance user-independence. Additionally, while this study validated the approach on single-V using a robotic manipulator and narrow-gap geometries conducting manual inspection, complex profiles such as Double-V grooves—which introduce multiple internal reflections— may require further separation of echoes based on amplitude level, to distinguish between robotic noise, reflections at the root and structural echoes. Finally, due to the mismatch between the length of the wedge (56mm) and the bevel geometry for narrow gap geometries (upwards of 120 mm), which approximately equal the thickness of the sample, changes in lateral offset will be required to monitor the relevant, filled area of the weld.

Looking ahead, several pathways can extend the capabilities of this framework. Future work will focus on integrating the system into a fully in-process inspection loop, where bevel estimation continuously informs robotic path planning. This live feedback could also serve as a valuable tool to validate the algorithm’s performance under challenging conditions particularly for non-uniform reflections from unmachined, rough-welded faces, or at elevated temperatures during pre-heating. These scenarios introduce distortions in the structural echo, making bevel orientation estimation more difficult. Addressing such conditions will be critical for advancing the systems deployment in real-world industrial settings. To further improve efficiency, interpretable machine learning could be using, enabling additional flexibility without sacrificing interpretability [192]. Integration of ML-based feature recognition could further enable inspection of multi-pass welds and complex geometries. Additionally, efforts will also explore fusing ultrasonic data with structured light or stereo-vision methods, enabling sensor redundancy and improved robustness under poor coupling or low-SNR scenarios. Finally, porting the pipeline to C++/ Compute Unified Device Architecture (CUDA) or Python/Torch will be critical for deployment on edge platforms like NVIDIA Jetson, ultimately enabling scalable, intelligent ultrasonic inspection in production settings.

6.7. Conclusion

This Chapter presents a real-time compression algorithm for ultrasonic measurement of weld bevel orientation in robotic welding applications. Through the integration of a GPU-accelerated orientation estimator and an adaptive compression strategy, the system achieves efficient, interpretable ultrasonic signal processing suitable for deployment in embedded or edge computing environments.

The proposed approach was validated with a robotic inspection platform under realistic conditions, demonstrating reliable geometric inference, data reduction, and rapid execution. By pairing real-time data acquisition with offline processing tuned for low-latency execution, the framework bridges the gap between high-throughput ultrasonic imaging and responsive robotic control.

This work contributes toward the development of adaptive, closed-loop ultrasonic-driven robotic welding systems by offering a modular, deployable solution for in-process weld optimisation. Future developments will focus on live feedback integration, hardware deployment, and extending the framework to more complex geometries and inspection scenarios, enabling intelligent automation in manufacturing quality assurance.

7. Machine Learning for Robotic Ultrasonic Automated Bevel Length Estimation

7.1 Introduction

Robotic welding has transformed modern fabrication through its ability to deliver consistent weld quality, improved throughput, and reduced operator variability. Studies have demonstrated that adaptive robotic welding systems can significantly enhance productivity and repeatability when integrated with intelligent sensing and process feedback systems [193],[194]. Sensor-enabled robotic systems that bridge NDE and welding automation were demonstrated in [195], where cost-function-driven adaptive welding framework demonstrated how real-time data can be used to optimize welding passes and deposition parameters.

However, the actual welding seam may vary due to factors such as thermal deformation, bevel preparation, detection error and positioning error. Therefore, it is essential to realize real-time weld seam tracking in robotic welding [196]. Additionally, the algorithm selection is crucial to capture weld geometry deviation. As shown in the work of [197], a typical system for guidance of the robot consists of an articulated arm, a control cabinet, a depth camera and/ or a laser vision sensor, and the joint geometry, as shown in Figure 58.

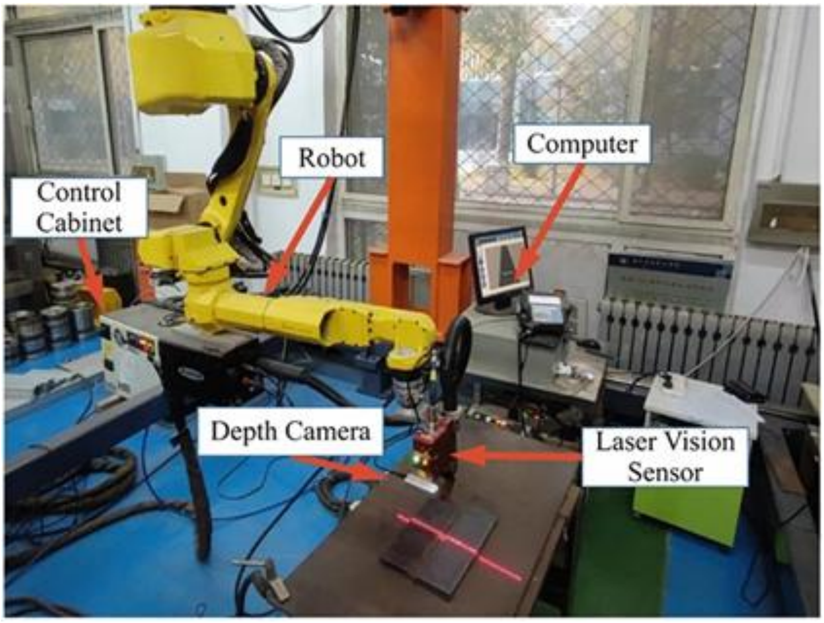

Figure 58. Robotic welding guidance system with vision. Adapted from previous work [197].

Different applications of weld seam trajectory and path planning can be found in Table 11. Welding in large structures is characterized by the large variety of joints, in terms of orientation, materials, and joint configurations. Butt welds join two pieces on the same plane edge-to-edge; laps join overlapping pieces; and fillet welds fill the corner intersection of two perpendicular or angled pieces. The ability to sense the welding geometry and generate the appropriate path and welding sequence parameter is crucial, to ensure defect free welds, while eliminating sudden accelerations, singularities and collision. However, it should be noted that these methods rely on visual feedback, where material brightness, arc spatter and lack of visual access can affect the efficacy of these methods, needing more advanced, Deep learning (DL)-enabled image processing.

Weld seam trajectory	Weld joints	References
Straight line weld	Butt joint	[198], [199], [200], [201], [202]
	Fillet joint	[203]
Plane curve weld	Butt joint	[204], [205]
	Fillet joint	[204]
Space curve weld	Butt joint	[206]
	Lap joint	[207]

Table 11. Weld seam trajectories applications for different weld joint configurations.

Volumetric, sub-surface characterisation of the bevel geometry using ultrasonic sensing could enable monitoring of the deviation of thicker welds during welding. Recent work by [123] introduced ultrasonic-driven adaptive control for robotic plasma arc cutting, showcasing how in-situ sensing can actively compensate for bevel deviations in real time. Using ultrasonic imaging for geometric compensation is also directly applicable to automated welding. Similarly, previous work has shown the value of sensor-enabled multi-robot inspection systems capable of online ultrasonic data acquisition and feedback during fabrication [74], [208]. Building upon these efforts, integrating real-time ultrasonic bevel estimation (such as the ML approach proposed in this Chapter) offers a promising path to achieve true online monitoring and adaptive correction of welding parameters. This fusion of geometric intelligence and robotic control closes the gap between inspection and process actuation, advancing toward fully autonomous, reliable and accurate manufacturing workflows.

In practice, two major limitations constrain the adoption of ML-driven NDE systems:

1. Lack of interpretability, where the decision making process cannot be easily understood or audited by human inspectors [209], [210];
2. Limited research in geometry estimation of welds using volumetric imaging for visually non-accessible areas using ML.

In recent years, robotic automation and advanced ultrasonic techniques have gained traction for in-process monitoring and post-weld inspection of large components [110], [211]. FMC/TFM imaging could enable rapid scanning with consistent quality, improved repeatability, encoded traceable inspection results often combined with digital twins and better coverage compared to traditional single element [212] and array [213] probe-based approaches. However, while majorly utilised for defect detection and characterisation, the potential of this data-rich inspection modality remains underutilised for geometric estimation tasks such as bevel length measurement, especially during early fit-up stages.

Additionally, interpretation remains the rate-limiting step, constrained by both computational and epistemic challenges. While robotic automation unlocks high scanning speeds, data analysis and interpretation still heavily relies on manual operation which hampers full automation realisation, is time-consuming, subjective, and error-prone [214], [215] . While ML and DL methods have demonstrated success in defect classification and segmentation tasks [216], [217], [218], their application remains limited to defect sizing, instead of joint geometry measurement [219], [220], [221], [222], [223]. Furthermore, generally, these methods rely on image reconstruction after static data acquisition, instead of raw data processing. A summary is provided in Table 12.

Ref.	Input	Model Architecture	Dataset Size	Length Error	Crack Length	Experimental Setup	Modality
[219]	3400x1	Convolutional Neural Network [224]	1200 simulated and 21 physical	0.08 mm	2-4 mm	Static single-element transducer	Amplitude scan
[220]	32x32x4	VGG-19 [225] base	16875 simulated and 1485 experimental	0.592 mm	0.2 to 5 simulated, 1 to 5 mm experimental	Static phased array	2 plane wave image with 2 modalities
[221]	9x128x128	Deep convolutional neural network	8850 simulated	0.23 mm	2 to 12 mm	Static phased array	Multi-modal TFM
This work	6000x4096	GBT feature selection, GPR augmentation, stacked polynomial and SVM	393 augmented experimental and 100 augmented	1.2 mm	6.08 mm to 16.69 mm (bevel)	Robotic phased array	Full Matrix Capture Data

Table 12. Literature review on crack sizing using ultrasonics and learning algorithms

.

In addition to the lack of transparency, quadratic data increase, depending on the array size, also presents a unique challenge. For automated inspection of large structures, multiple meters of joints need to be scanned. While FMC data can be post-processed for advanced multi-modal imaging of different geometries [22], the inherent multi-dimensionality can lead to data explosion. In previous work, compressive sensing has been employed as a technique to limit the amount of acquired data, by optimising the transmitting and reception apertures, to decrease the number of transmission elements [168], [171], [180]. This leads to the selection of an optimal sparse element matrix, as specific elements are not utilised. These methods rely on iterative element selection, image quality optimisation, and prior domain knowledge, thereby limiting their adaptability to novel geometries. Consequently, such approaches often prove inflexible, as capturing unfamiliar geometries would necessitate the integration of additional sensing elements, making optimisation prohibitive.

To address these gaps, the research presented in this chapter presents a machine learning pipeline for automated bevel length estimation using robotised ultrasonic inspection data acquired via PAUT and FMC. This study builds upon a previously validated ultrasonic data compression and orientation extraction framework in Chapter 6 [226], which established a fast and accurate representation of FMC data for weld monitoring. While that work addressed data efficiency and signal fidelity, the present research focuses on a distinct problem: the inference of geometric weld length using ML models. The proposed approach advances beyond prior classification-oriented ultrasonic ML frameworks by introducing a fully structured regression architecture for continuous, real-time bevel length estimation.

Here, three primary contributions are offered in the field of automated NDE. First, a novel ML regression pipeline is established, tailored for the continuous estimation of bevel lengths during robotic ultrasonic inspections. To address the inherent challenges of sparse and skewed industrial datasets, a robust learning architecture was developed; this framework employs a GPR geometry balanced augmentation strategy to ensure reliable generalisation across four distinct bevel geometries. Finally, the work demonstrates a real-time inference capability that eliminates the computational overhead of traditional imaging techniques, allowing for direct length prediction at the point of data acquisition.

By enabling high-accuracy, bevel length estimation in the presence of measurement noise using ultrasonic data for a 16mm, 90° joint configuration, geometry imbalance, and limited training data, the proposed system could support improved weld fit-up control, reduced distortion, and enhanced end-to-end process traceability in large-scale fabrication workflows. This chapter is organized as follows. is organized as follows. In Section 7.2, the software and hardware methodology for this setup is described. In Section 7.3, the results are presented for geometry estimation. In Section 7.4, discussion is conducted based on these results, and in Section 7.5, the conclusions of this study are presented.

7.2. Methodology

7.2.1 Experimental Setup

The system configuration, as presented in Figure 59, was described in Chapter 3. Furthermore, the machined experimental setup functioning as a surrogate of a 16 mm V-groove joint was described in Section 3.5.1. Finally, the ultrasonic setup with the setup of the wedge and the array, as well as the acoustic path, is described in Section 3.4.2.

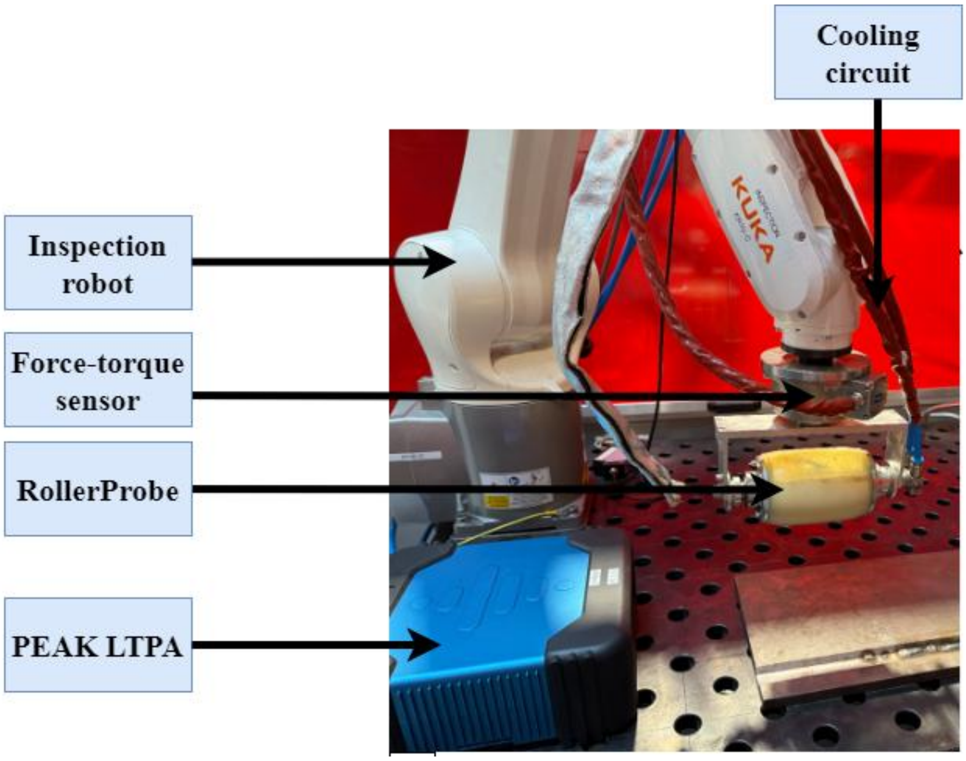

Figure 59. Robotic inspection setup used for data acquisition, featuring a KUKA KR10 manipulator with a custom ultrasonic RollerProbe, force-torque sensor, and PEAK LTPA ultrasonic controller.

7.2.4. Signal processing and Machine Learning Pipeline

The overall workflow adopted in this study is presented in Figure 60, which integrates feature engineering, data preprocessing, and downstream learning pipelines. The feature engineering stage captures algorithmic parameters, compression statistics, bevel orientation metrics, and sparsification-based descriptors. These features are then passed into the data augmentation stage, where the most important features are selected, and underrepresented areas are augmented. The final learning employs the creation of a meta learner, aggregating measurement errors of a Support Vector Machine (SVM) and a third order polynomial, in order to capture both global trends, as well as local non-linearities and feature interactions. Together, this provides a rigorous framework for assessing continuous performance of the engineered features for geometrical estimation based on sparsification pattern in addition to raw signal statistics.

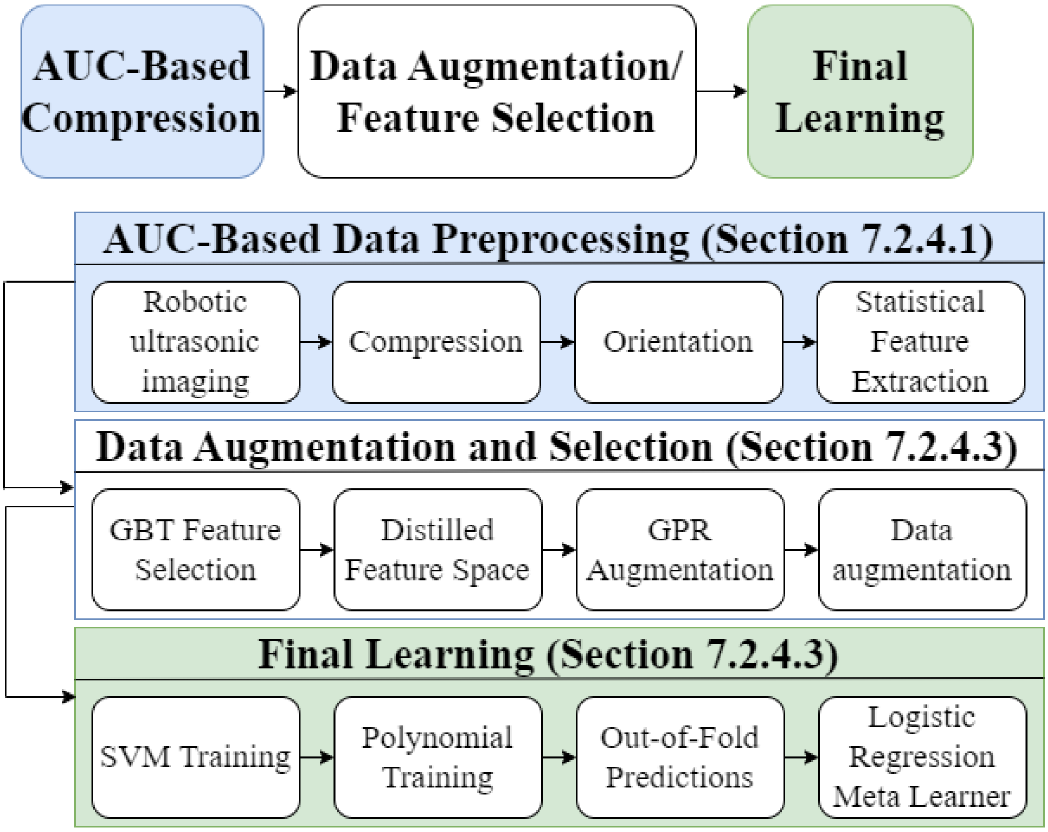

Figure 60. Full machine learning pipeline for bevel length estimation. The workflow integrates AUC-based compression, data augmentation and final learning.

7.2.4.1. Preprocessing

The preprocessing and feature extraction relies on the data compression and orientation extraction proposed in Chapter 6. Figure 61 summarises the main stages. The robotic inspection acquires raw ultrasonic frames that are first processed on the CPU to extract compact descriptors from the time domain. The proposed compression algorithm segmented each frame according to a preselected window and scaling factor using numerical integration. Then, statistical features related to the distribution in both the time and aperture domain are extracted from the compressed data. Additionally, individual window metrics are calculated. The compressed representation is then transferred to the GPU, where orientation features are extracted using a HOG approach. This hybrid CPU-GPU implementation enables efficient bevel-angle estimation with an average orientation error below 0.4 degrees, while maintaining per-frame processing times below 150 ms. Finally, the orientation and execution time to extract it are calculated.

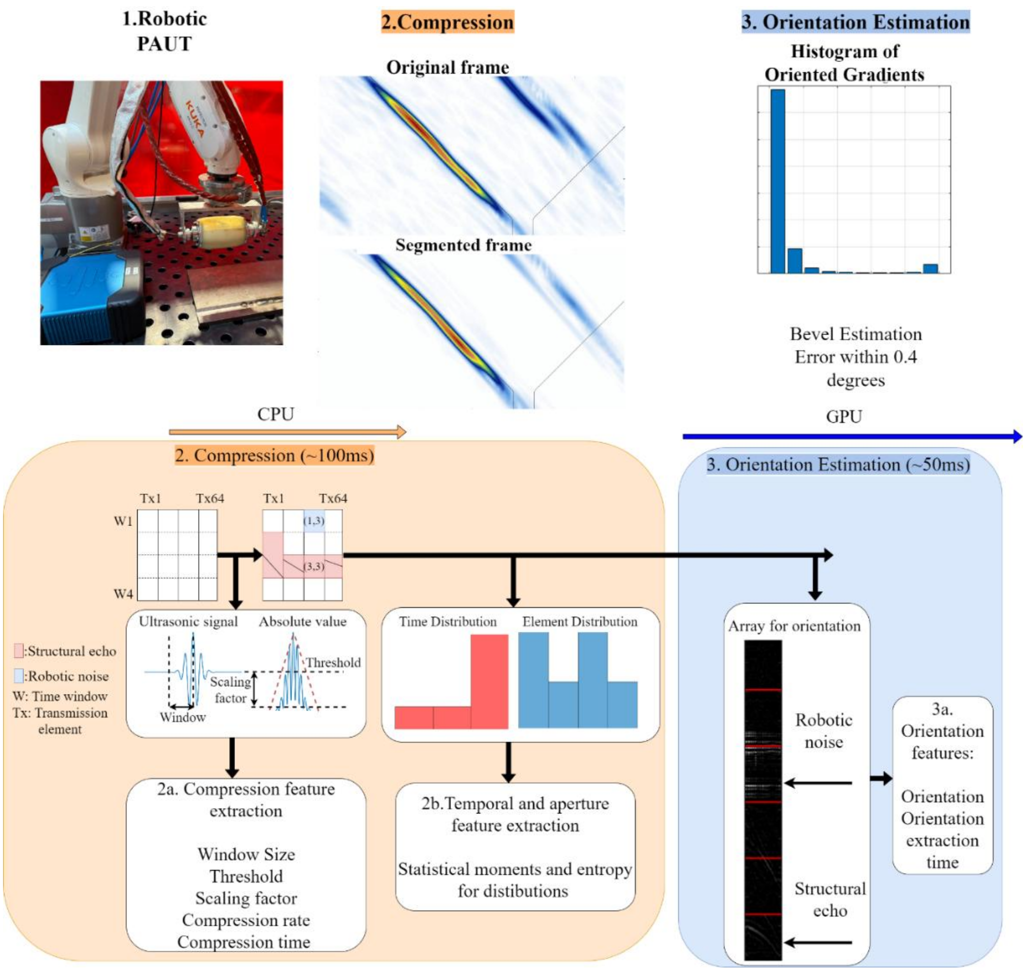

Figure 61. Overview of PAUT compression and orientation-estimation pipeline. (1) Robotic PAUT acquired ultrasonic frames through a force-controlled automated inspection system. (2) On the CPU, the proposed compression algorithm segments and encodes each frame by extracting time- and element-domain distributions, with adjustable window size, threshold and scaling factor parameters (~ 100 ms). (3) On the GPU, orientation features

are derived from the compressed time-domain array using a HOG, enabling bevel-angle estimation with 0.4 ° at ~ 100 ms per frame.

However, excessive compression discards not only redundant signal paths but also structural information critical to geometric inference. As illustrated in Figure 62, compression parameters of a window size of 96 and a statistical scaling factor of 2 preserves the dominant bevel echo and yields reconstructions, whereas overly aggressive thresholds, such as a window size of 160 samples and a statistical scaling factor of -2, suppress coherent energy and produce noise-dominated artefacts. This highlights the importance of balancing data reduction with feature integrity: compression is valuable only insofar as it retains diagnostic content. The framework developed in this work explicitly addresses this trade-off by constraining sparsification to ranges where structural fidelity is maintained, ensuring that compression operates as an enabler of efficient inspection rather than a source of degradation.

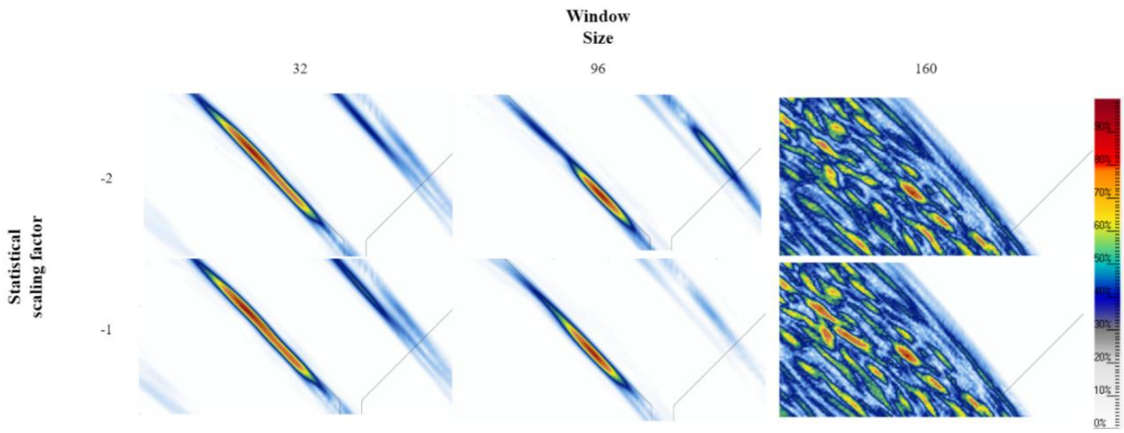

Figure 62. TFM images of bevel geometry with different compression parameters (Statistical scaling factor, window size). These are different reconstructions of the same initial data with changing algorithmic parameters.

To ensure minimal overfitting for subsequent feature engineering and model training, sufficient variance in the data is essential, as shown in the distributions of the 393-sample dataset in Figure 51. Signal-to-noise ratio (SNR) values (top panel) remain largely within 25–40 dB, reflecting consistent acquisition quality while capturing variability due to geometry, coupling and scanning conditions, as well as reconstruction. The distribution of bevel length measurements (middle panel) spans 7–18 mm, consistent with the stepped specimen geometry and confirming that compressed data preserved sensitivity to geometric variation. Compression rates (bottom panel) consistently exceed 80%, with most samples approaching 90–95%, demonstrating that significant data reduction was achieved while retaining essential structural features. These distributions highlight both the robustness of the augmented dataset and the stability of the compression pipeline across a representative range of conditions, as well as meaningful variance due to algorithmic permutations.

7.2.4.2 Feature engineering

The features extracted in this work are not just direct measurements from ultrasonic signals but statistical descriptors of the compression and sparsification process itself, as shown in Table 13. In addition to treating raw A-scans or B-scans as fixed data sources, the proposed framework evaluates how information is retained, suppressed, or reorganised during adaptive reduction. This feature space transformation, from signal values to compression behaviour, creates features such as mean AUC, entropy, or deviation The result is a feature set that can be rapidly computed, compressing the initial array into a compact set of descriptors.

Feature Group	Individual Feature and Statistical Moment
Compression /orientation metrics	Bevel orientation, bevel orientation extraction time
	Compression rate, Compression execution time
Statistical threshold	Deviation scaling factor, window size
AUC metrics	Mean, deviation
Time distribution	Mean, variance, skewness, entropy
Element distribution	Mean, variance, skewness, entropy
Mean of B-Scan	Mean, variance, range
Variance of B-Scan	Mean, variance, range
Skewness of B-Scan	Mean, variance, range
Kurtosis of B-Scan	Mean, variance, range
Minimum of B-Scan	Mean, variance, range
Maximum of B-Scan	Mean, variance, range

Table 13. List of engineered features used for bevel classification and regression. Features span eight categories: compression/orientation metrics, statistical thresholds, AUC metrics, domain-specific entropy/variance descriptors across time and aperture, and statistical moments of raw B-Scans.

7.2.4.3. Machine Learning Framework

The ML pipeline, as proposed in Figure 63, is structured to mitigate the challenges inherent in low-sample data regimes (e.g., 33 features for approximately 400 samples), where the large number of features for small datasets [227] threatens generalisation capability. The hyperparameter tuning of the models on the initial fold, is presented in Table 14. The process begins with tree-based feature selection utilizing Gradient Boosted Trees (GBT) [91], which acts as an initial feature selection step by identifying the most predictive features that capture non-linearity and interaction effects, thereby reducing the feature space and minimizing the risk of overfitting noisy dimensions. A GBT model was selected instead of an RF model to reduce bias and prevent underfitting due to non-linear nature of the features. Feature importance ranking was performed on the complete dataset using GBT. Model training for final feature selection and model evaluation were performed using 5-fold validation, with all model parameters trained and selected exclusively on training folds. Feature stability was verified by computing fold-specific ranking, Following this, Gaussian Process Regression (GPR) is employed for measurement smoothing and data augmentation, using Sampling Minority Oversampling Technique (SMOTE)[228] to randomly create linear interpolation of features in underrepresented areas and fitting a probabilistic, smooth surrogate that is trained on the original data, to generate augmented training samples using model interpolation. This is a modification to the Synthetic Minority Over-sampling technique for ReGressioN [229], in order to circumvent the linear assumption that is made for samples in close proximity. To prevent data leakage, each augmented pair has a unique cluster identification and excluded from validation, to eliminate the chances of affecting the final model evaluation. The augmented data and selected features are then used for the final model. The Stacked Model Training utilised a third order polynomial regressor to capture low-frequency, baseline global trends and a Support Vector Machine (SVM) to address high-frequency, local interactions, ensuring robust bevel length prediction.

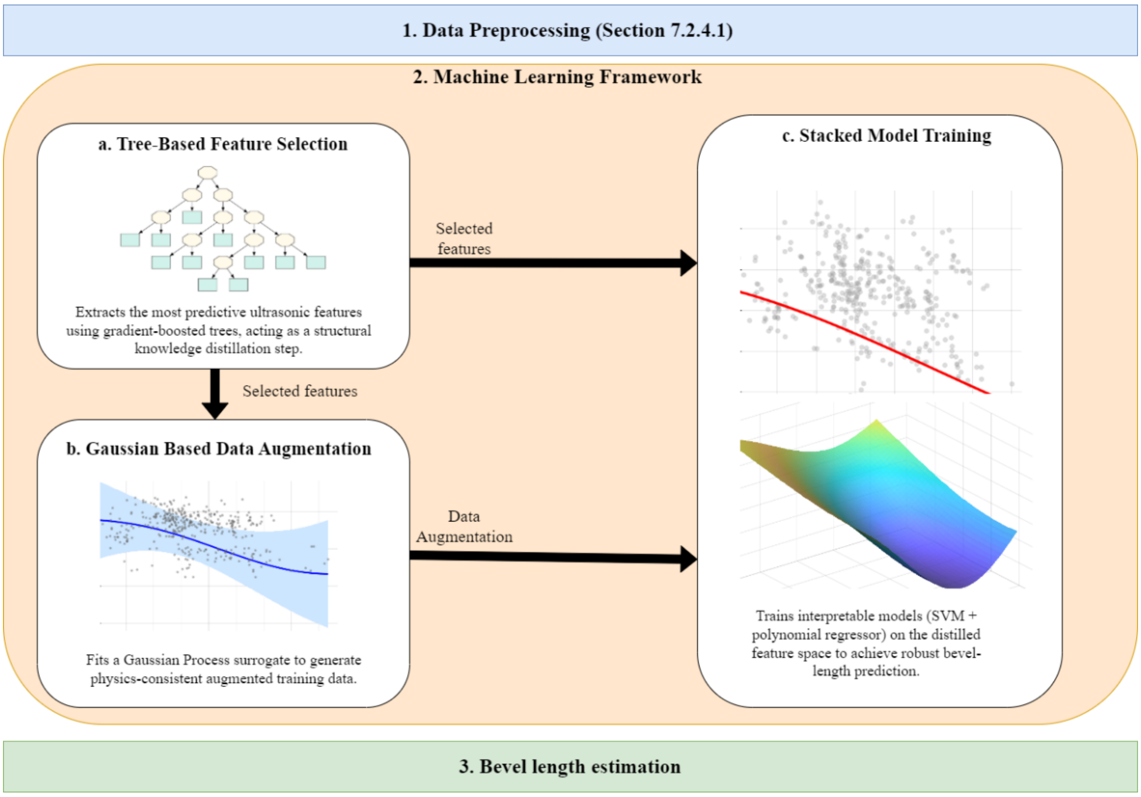

Figure 63. Overview of the Machine Learning Framework for Estimating Bevel Length from Compressed Phased Array Ultrasonic Features. The pipeline begins with (a) feature selection using gradient-boosted trees and (b) data augmentation/denoising via Gaussian Process synthetic data generation. The features and augmented data are the used for (d) Stacked Model Training (SVM + polynomial regressor) to achieve robust prediction of the bevel length at the point of acquisition.

Model	Parameters	Values	Hyperparameter Iteration Loops	Hyperparameter Value
Boosted Tree	Boost cycles	[1, 75]	10	71
	Learn rate	[0.005, 0.05]		0.05
SVM	Box Constraint	[1e-3, 10]	30	10.7393,
	Kernel Scale	[1e-2, 10]		2.7779,
	Epsilon	[0.3, 0.6]		0.3041
	Kernel	Radial Basis Function		N/A
GPR	Kernel Function	Squared Exponential	N/A	N/A
	Sigma	0.5		N/A

Table 14. Hyperparameter ranges used for regression models for framework. SVMs and GBT were optimized using Bayesian optimization, empirically determining range to reduce overfit. For GPR, the parameters were empirically selected to reduce target variance elimination.

7.2.4.4. Machine Learning Evaluation metrics

For regression, performance was evaluated using the coefficient of determination (R^2), adjusted coefficient of determination (Adj- R^2) as the measure of fit quality, supplemented by RMSE to capture magnitude, as shown in equations 34 and 35:

$$R^2 = 1 - \frac{\Sigma\,(y_i - \hat{y}_i)^2}{\Sigma\,(y_i - \bar{y})^2} \tag{34}$$

$$RMSE = \sqrt{\frac{1}{N} \cdot \sum_{i=1}^{N} (y_i - \hat{y}_i)^2} \tag{35}$$

$$AdjR^2 = 1 - \frac{(1 - R^2)(n - k - 1)}{n - 1} \qquad 36$$

Where n: observations, k: predictors, y_i: measured values, $\hat{y}_i$: predicted values, and $\bar{y}$: mean of observed values and N: sample number. This reporting ensured that both explained variance and absolute predictive deviation were considered. Furthermore, the adjusted R^2 was used to accurately weight the effect of the reduced number of features during the initial stage.

7.3. Results

7.3.1 Feature Selection & Stability

To address the high dimensionality of the compressed ultrasonic feature space relative to the available sample size (N=393), a GBT analysis was performed to identify the most predictive signal descriptors. Figure 64a illustrates the hierarchical decision path of a representative learner (Learner 5), identifying MaxAUC, StdAUC and compression time (ComprTime) as primary splitting criteria. The feature importance analysis (Figure 64b) confirms empirically, based on the available data, that MaxAUC, StdAUC and MeanStdUT are the dominant predictors, indicating that the maximum energy amplitude and its standard deviation and the standard deviation of the ultrasonic time-trace are the strongest proxies for bevel geometry. As shown in Figure 64c, the stability analysis reveals a critical threshold at k^*=12 features. While adding features up to this point improves the Cross-Validated Adjusted R^2 up to 0.65, retaining more than 12 features introduces noise, causing a degradation in model stability and predictive performance . Consequently, the subsequent feature selection utilised only this optimal 12-feature subset. Cross-validation across folds, as shown in Table 15, 80% average feature overlap is achieved, with 7 out of 12 features (58%) appearing in all folds. These core features; MaxAUC, StdAUC, MeanStdUT, TimeStd, ScalFact, MinStdUT, and WinSize; represent descriptors of signal energy, variance, and compression parameters. The remaining features showed expected variability, with 1 features appearing in 4/5 folds, 1 in 3/5, 1 in 2/5 and only 2 features showing low consistency, indicating they capture marginal signal at the boundary of statistical significance. It should be noted that model performance was validated using fold-specific rankings, while the final features were derived from global importance analysis.

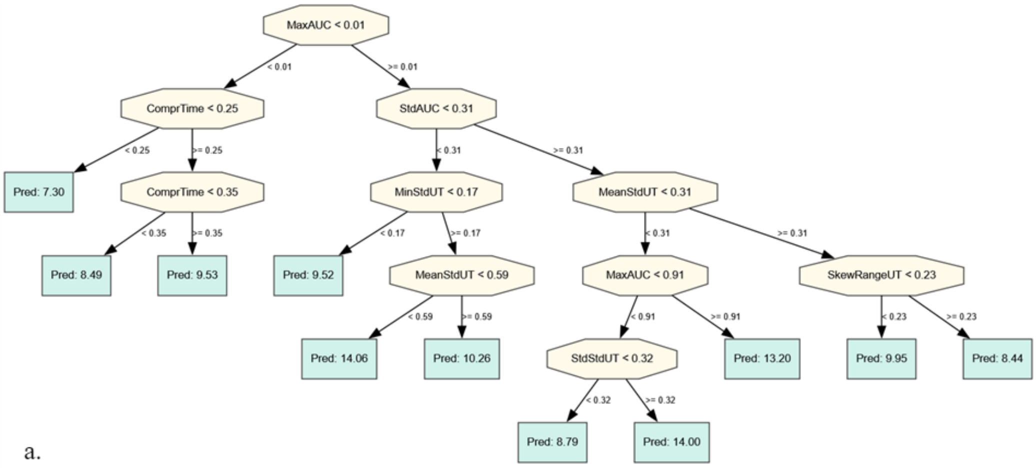

a.

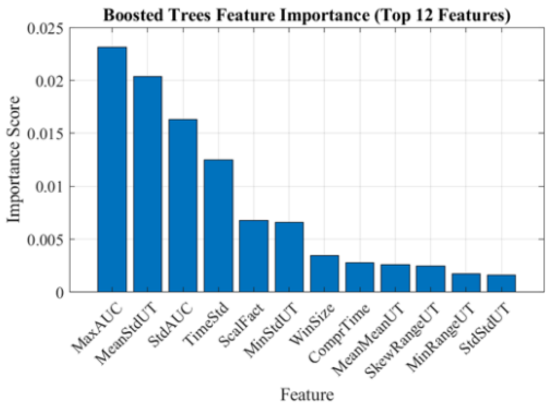

b.

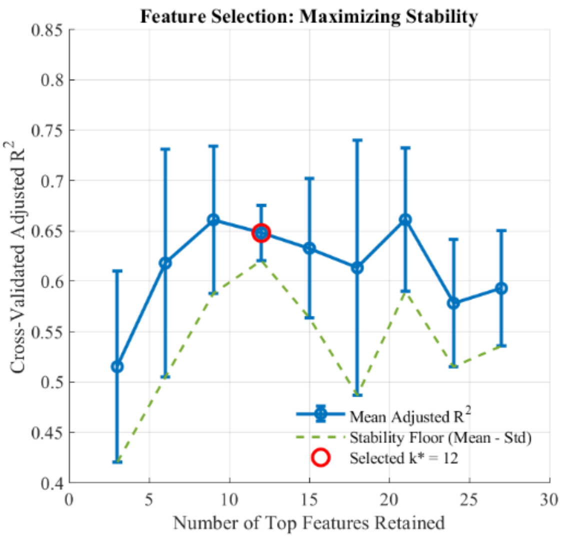

c.

Figure 64. GBT analysis for feature selection prior to data augmentation. (a) Representative structure of a single regression tree (Learner 5), illustrating the hierarchical decision path. (b) The ranking of the top 12 features based on Importance Score, heavily weighted towards MaxAUC and MeanStdUT. (c) Feature subset selection based on cross-validated adjusted R^2, identifying the optimal stability point at k=12 features, after which model performance degrades.*

Feature	Fold Appearances	Stability (%)
MaxAUC	5/5	100
MeanStdUT	5/5	100
StdAUC	5/5	100
TimeStd	5/5	100
ScalFact	5/5	100
MinStdUT	5/5	100
WinSize	5/5	100
SkewRangeUT	4/5	80
ComprTime	3/5	60
MeanMeanUT	2/5	40
MinRangeUT	1/5	20
StdStdUT	1/5	20

Table 15. Feature stability across cross-validation folds.

7.3.2. Efficacy of Data Augmentation

The impact of using GPR to generate artificial targets using oversampling in minority regions prior to training the stacked model is analysed in Figure 65. Figure 65a contrasts the probability density of the target bevel lengths. The linear interpolation method (dashed red line), based in SMOTE [228], results in a jagged, multi-modal distribution. In contrast, the GPR distillation (solid blue line) produces a smoother, continuous distribution. This improvement in target quality translates directly to model performance. The feature selection strategy also correlates directly to model performance. Using the 12 features of the GBT feature selection leads to better performance than 50-fold resampling and consensus ranking of 16 features for the

LASSO model (RMSE = 1.396 mm vs RMSE = 1.159 mm). Figure 65c demonstrates that augmenting data from the GPR to the SVM component of the stacked model yields a modest but important improvement in predictive accuracy (RMSE decreases from 1.20 to 1.16 mm) and explained variance (R^2 increases from 0.715 to 0.75). More critically, the reduction in error bars indicates enhanced model stability across the validation folds.

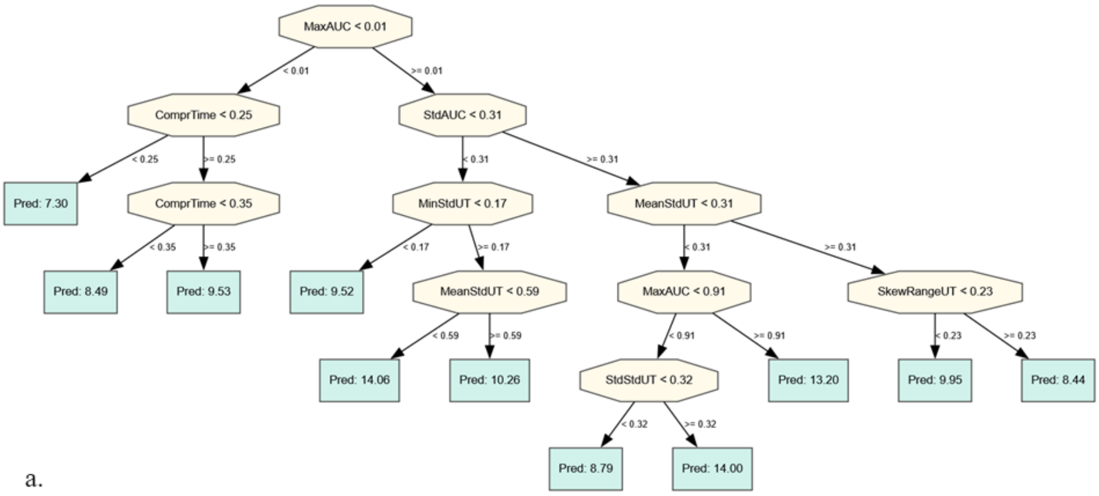

a.

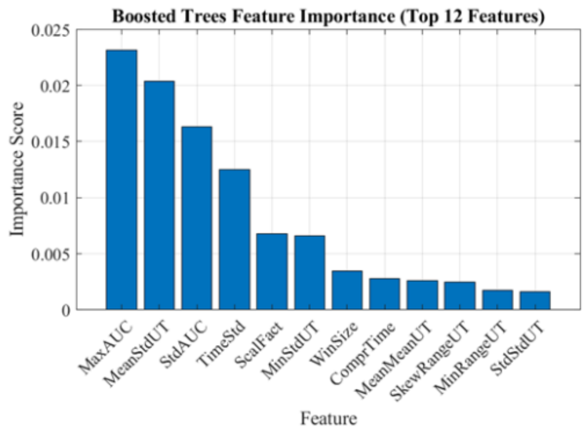

b.

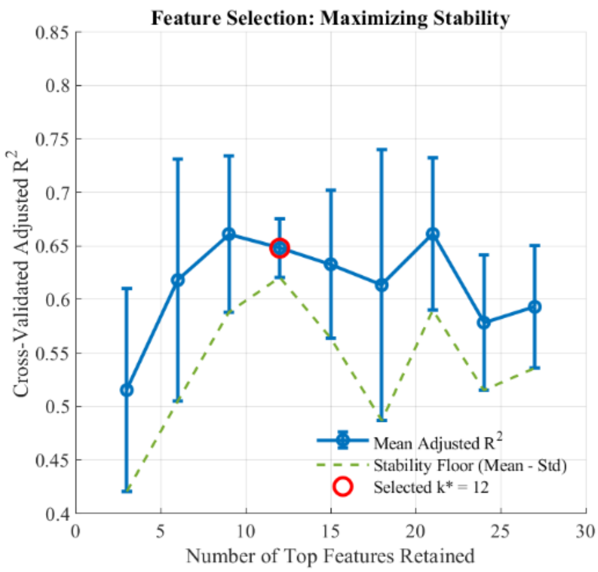

c.

Figure 65. Analysis of oversampling efficacy for data augmentation from GPR to SVM. (a) Probability density comparison showing that GPR augmentation (solid blue) provide a smoother, more continuous distribution of bevel lengths compared to the jagged, multi-modal distribution of SMOTE (dashed red). (b) Comparison between LASSO

feature selection, highlighting complexity of data. (c) SVM performance comparison on the original test set. The data augmentation method yield a modest improvement in mean accuracy (RMSE from 1.24 to 1.17 mm) and coefficient of determination (R^2: 0.72 to 0.75), with reduced standard deviation, indicating improved model stability.

7.3.3. SVM Scalability

The necessity of using a Support Vector Machine (SVM) in conjunction with a simpler polynomial baseline is justified by the learning curve analysis in Figure 66:

- RMSE Trajectory (Figure 66a): The baseline linear/polynomial model (yellow) exhibits a "saturation effect," where the validation error plateaus after approximately 250 samples. In contrast, the Student SVM (orange) continues to learn, achieving a final error reduction of 0.6 mm.
- Explained variance (R^2) (Figure 66b): A divergence point is observed at 250 samples. Beyond this volume, the SVM leverages the additional data to improve generalisation, securing a final performance gain of in over the baseline. This confirms that the non-linear capacity of the SVM is required to fully exploit the information within the compressed ultrasonic dataset.

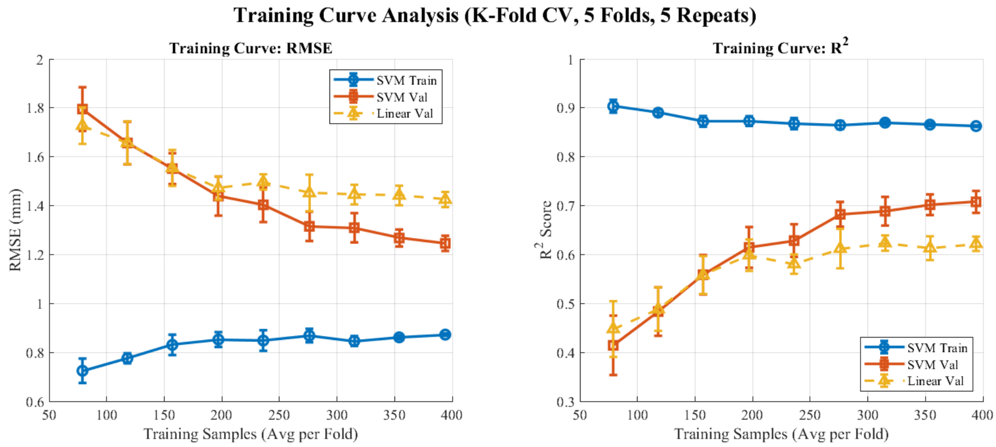

Figure 66. Learning curve analysis (5-fold cross-validation) comparing the scalability of the Student SVM against the baseline polynomial model. (a) RMSE trajectory showing the "saturation effect": the polynomial model (yellow) plateaus after 250 samples, whereas the Student SVM (orange) continues to reduce error, achieving a final advantage of ~ 0.2 mm. (b) R^2 learning performance showing that Student SVM generalizes better with larger data volumes, diverging from the baseline after 250 samples to secure a performance gain of ~ 0.08.

The persistent gap in the performance between training and validation for the SVM highlights that while the SVM can capture the local non-linearities in the dataset, the severe overfitting on the training set indicates lack of generalisation capabilities. Furthermore, the performance of the linear model is close to that of the SVM in the validation set, highlighting that there are noticeable global trends in the dataset, even if they cannot fully capture the variance. As such, in Section 7.3.4, they will be combined to capture both local non-linearities and global trends.

7.3.4. Ensemble Performance & Bias Correction

Figure 67a displays the prediction scatter plot for the final Stacked Ensemble, combining the predictions of the SVM with a polynomial ridge regression model, using a logistic regression meta-learner. The model achieves high precision for Long Bevels (>13.15 mm) but shows increased variance (heteroscedasticity) for Short Bevels (< 6.08 mm), likely due to the reduced signal-to-noise ratio in shallower geometries. The final meta-learner, which was trained on out-of-fold predictions with 5-fold validation, is presented in:

$$\widehat{y_{\mathrm{Stacked}}} = 0.681 \cdot f_{\mathrm{SVM}}(x) + 0.364 \cdot f_{\mathrm{Poly}}(x)$$

, where $\widehat{y_{\mathrm{Stacked}}}$ are the predicted values of the stacked ensemble, x are the selected features from section 7.3.1, $f_{\mathrm{SVM}}(x)$is the regression function of the SVM, and $f_{\mathrm{Poly}}(x)$is the regression function of the polynomial model. The coefficients were extracted by training the logistic regression meta learner using out-of-fold prediction. This model was extracted using 5-fold validation and calculating the mean factor.

The internal mechanism of the Stacked Ensemble is revealed via Individual Conditional Expectation (ICE) analysis (Figure 67b). ICE analysis is an explainable AI technique that shows how a machine learning model's prediction changes when keeping all but one features static, and evaluating response while varying a single feature [230]. The ensemble (bottom left) successfully integrates the behaviours of its constituents: it retains the non-linear sensitivity and local interactions of the SVM (top left) while utilising the Polynomial Ridge component (top right) to regularise predictions. This regularisation effect (bottom right) is most pronounced at the edges of the feature space (MeanStdUT), where the ensemble explicitly dampens the aggressive predictions of the SVM.

The result of this stacking strategy is a significant correction in systematic error, as shown in Figure 68, using qualitative analysis of residual distribution to evaluate homoscedasticity, which describes the spread of the residuals across all values of independent variables:

- Bias Correction: The single optimal GBT model (Figure 68a) exhibits a distinct "funnel" shape with a positive slope, indicating a systematic bias where larger bevels are consistently under-predicted.
- Homoscedasticity: The Stacked Ensemble (Figure 68b) eliminates this linear bias, achieving a uniform (homoscedastic) distribution of residuals centred on zero.

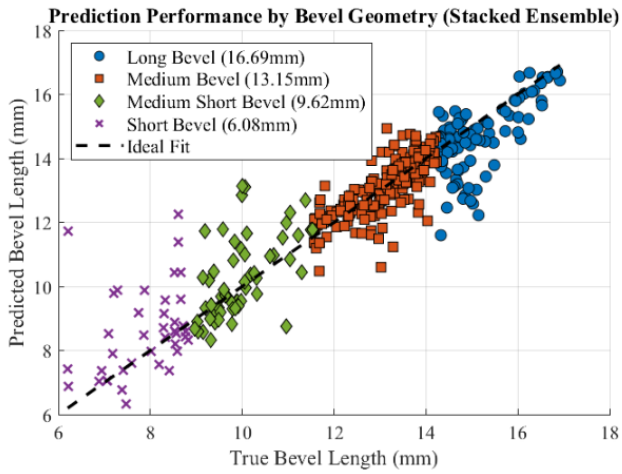

a.

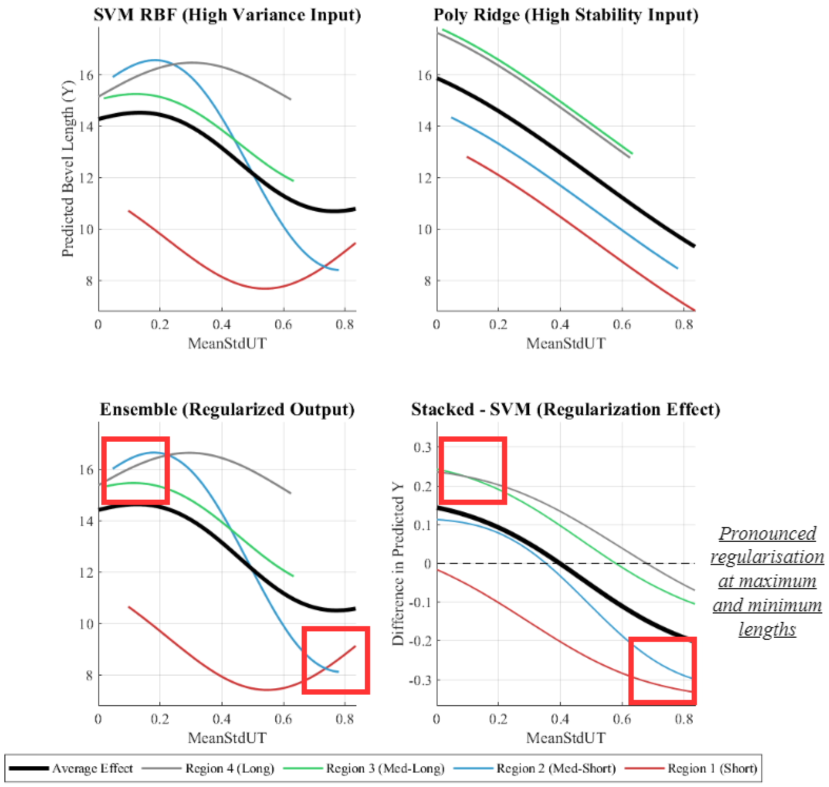

b.

Figure 67. Evaluation of the Stacked Ensemble's predictive performance and internal regularization mechanism. (a) Prediction vs. Reality scatter plot categorized by bevel geometry. The model demonstrates high precision for larger bevels (> 13.15 mm, blue/orange), but exhibits increased variance (heteroscedasticity) for smaller bevels (purple/ green). (b) ICE analysis decomposing the ensemble logic. The final ensemble (bottom left) balances the non-linear sensitivity of the SVM (top left) with the structural stability of the polynomial ridge (top right). The regularization effect (bottom right) explicitly quantifies how the ensemble dampens the SVM's aggressive predictions at the edges of the feature space for MeanStdUT.

An important consideration, as shown in Figure 68, is the change in the y-scale. For the GBT, more bias for the larger bevels is achieved. However, there is tighter cluster around the y=0 axis when compared to the result of the proposed pipeline, where less systematic bias is present. This reveals an important trade-off between performance and generalisability, as will be discussed in Section 7.3.5. To minimize the amount of outliers in the 10.0 to 14.0 mm range, there are two potential solutions for future work. The first will be to expand the initial dataset with more samples in this range, by machining a new sample with incremental steps in this range. The second, as revealed in Chapter 5, will be repeating the experimentation with different robotic parameters. As discussed in Chapter 5, 9.63 mm corresponds to a transitional zone between the linear and sector scan modality, which is reflected by the number of outliers in the 9.5 – 10.0 mm range.

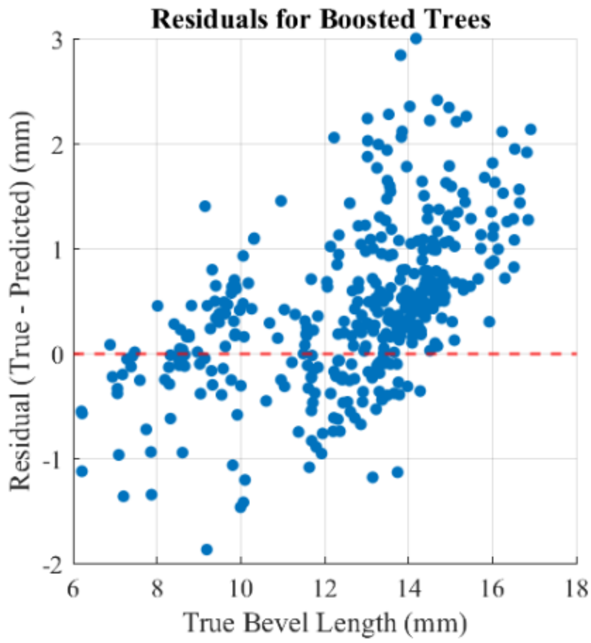

a.

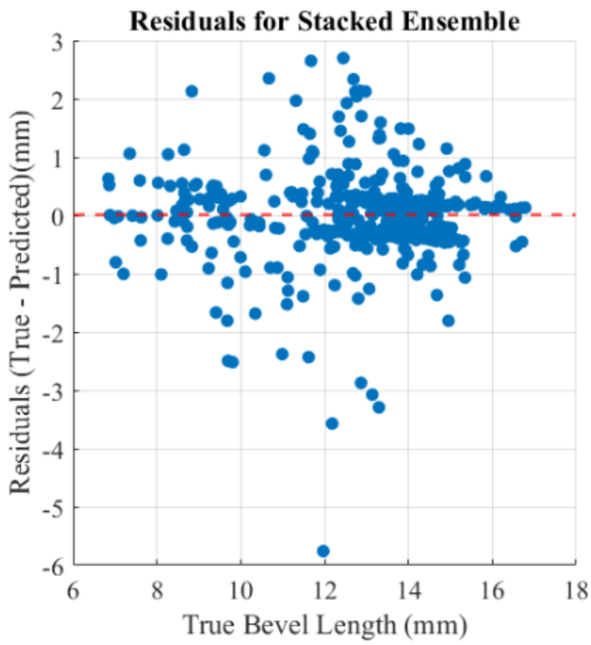

b.

Figure 68. Residual analysis comparing error structures. (a) The Boosted Trees model exhibits significant systematic bias for bevels >10 mm. The positive slope indicates the model consistently under-predicts larger values. (b) The Stacked Ensemble successfully eliminates this linear bias, achieving a homoscedastic (uniform) distribution centred on zero across the full range, though distinctive outliers remain in the 12 – 14 m region.

7.3.5 Overall Performance Benchmarking

Table 16 summarises the performance of the proposed pipeline against baseline methods. It can be observed that the LASSO model has the lowest performance (RMSE of 1.586 mm), which is expected due to highly non-linear nature with local interactions for the dataset. The GBT feature selection with 12 features exhibits increased performance, while overfitting, as shown by the gap in explained variance between training (0.88) and validation (0.7). The distilled SVM achieves the marginally best explained fold variance (R^2 of 0.75) and lowest error (RMSE of 1.172), while reducing the generalisation gap from 0.18 to 0.11. For the final stage, the stacked ensemble has minimal performance loss of 0.026 mm, while achieving the lowest generalisation gap by a factor of 10 between training and validation (0.01). This gradual descent of the gap in explained variance highlights the granular improvement in performance, simultaneously simplifying from initial model architecture, while maintaining low estimation error. In the context of geometry estimation, the minimal gap between training and fold performance indicates that with similar datasets, this approach can be expanded to different geometries, due to strong generalisation capabilities.

Model	CV-RMSE (mm)	CV-R^2	Training- R^2	Notes
LASSO	1.586	0.55	N/A	Baseline linear
GBT Feature Selection	1.193	0.70	0.88	Best single model pre-distillation
SVM	1.172	0.75	0.86	Best simple model
Stacked Ensemble (Final)	1.198	0.74	0.75	Most stable, lowest variance

Table 16. Comparative performance metrics across the pipeline. While the distilled SVM yields the highest predictive accuracy (CV-R2: 0.75), the stacked ensemble demonstrates superior generalization. Note the negligible gap between the ensemble's training (0.75) and cross-validation (0.74), confirming it as the most robust model with minimal overfitting compared to the GBT.

7.4 Discussion

7.4.1 Regression of bevel geometry

Using the proposed ML pipeline, high metrological accuracy and explained variance of up to 75% can be achieved. The ablation study confirmed that twelve features were sufficient to reach peak performance, after which redundant inputs degraded model accuracy. From an industrial and compliance perspective, however, the absolute measurement deviation provides a more meaningful indicator of performance than statistical fit indices such as R^2. The observed mean absolute error within ±1.2 mm; inside weld preparation tolerances [231];demonstrates that the regression output is both statistically consistent and metrologically compliant. This framing aligns with established measurement practice, where results are expressed as a value plus uncertainty [232], ensuring that model predictions can be validated against traceable, auditable bounds. Thus, while R^2quantifies generalisation capability under variable geometry, the decisive benchmark for deployment in robotic fabrication remains the maintenance of error within compliance tolerances.

The most influential regression features; mean standard deviation of ultrasonic signal, mean energy, and standard deviation of energy; indicate that geometry is most reliably expressed through the arrangement and stability of the ultrasonic response. Timing-related features such as compression time also gained importance, indicating that complex or poorly coupled geometries impose higher computational loads that indirectly encode information about bevel state.

The residual histogram demonstrates the industrial relevance of these results. Most predictions fall within ±1.2 mm of the ground truth, well within tolerances used during fit-up and weld preparation. Outliers are less frequent, showing that the regression framework is not only statistically robust but also operationally reliable. By filtering the feature set down to the most informative descriptors, the final ensemble model remains compact.

7.4.2 Broader implications, limitations, and future work

The regression results show that bevel length can be estimated in real-time from compressed ultrasonic data using a compact set of features. The practical significance for weld inspection workflows is clear. Real-time geometric estimation enables more accurate fit-up, reduces distortion. The lightweight computation (~250 ms per frame for compression and orientation, and 7.46μs for inference) was achieved on a consumer laptop device, highlighting the relatively low computational power requirements.

Moreover, the compact feature set (twelve for regression) simplifies retraining across different geometries. The integration of this framework with robotic welding control systems presents a clear pathway toward closed-loop, self-correcting fabrication. In such architectures, real-time ultrasonic feedback could dynamically adjust weld parameters; such as torch speed, voltage, or filler rate; based on the measurement of joint geometry for the detection of LOSWF.

There are, however, limitations. The present study was conducted on a stepped machined specimen that, while representative, does not capture the full diversity of industrial geometries. Larger datasets spanning multiple weld types, materials, and coupling conditions will be required to fully assess generalisation. Furthermore, the effect of thermal gradient on positioning accuracy and measurement, as described in [233], would need to be studied.

At the same time, the pipeline provides a general method for ML deployment in domains characterised by data scarcity, heteroskedastic noise, and strong physical priors; a regime common across NDT and structural integrity assessment. Many inspection tasks face similar challenges: limited defect samples, geometry-dependent signal variability. The combination of physics-aligned feature engineering, and regression proved here offers a reusable template for regression and estimation problems in ultrasonic inspection, radiography, structural health monitoring, and robotic metrology.

7.5 Conclusion

The presented framework demonstrates proof-of-concept for automated bevel estimation in 16mm, 90° joint configurations. Extension to variable thicknesses, materials, and joint angles is planned for future work and will require geometry-specific retraining. By combining physics-informed feature engineering with regression models for feature selection and data augmentation, the framework consistently achieves bevel length predictions within ±1–2 mm; well inside practical weld preparation tolerances. The lightweight computational requirements and low inference latency support real-time deployment alongside robotic manipulators, enabling continuous geometric feedback during fit-up and welding. Overall, this work proves that accurate bevel geometry estimation is achievable from compressed ultrasonic measurements, providing a practical step toward reliable, accurate, closed-loop NDT and welding automation.

8. Conclusion

8.1 Synthesis of Research Findings

The overarching objective of this thesis was to bridge the gap between autonomous robotic welding and volumetric ultrasonic inspection to support the digital transformation of the UK manufacturing sector. By integrating phased array ultrasonic imaging directly into the manufacturing workflow, this research has moved beyond traditional post-process inspection towards a proactive, “arc-on” quality assurance paradigm.

The experimental evidence presented in this work confirms that ultrasonic imaging is not merely a diagnostic tool but a critical feedback sensor for autonomous systems. In Chapter 4, it was established that the presence of a molten pool during active GTAW welding creates a binary acoustic condition, establishing contribution a). Specifically, proper sidewall fusion results in the absorption of longitudinal ultrasonic waves into the melt, while a LOSWF defect maintains signal stability, providing a clear, real-time proxy for joint integrity. This discovery simplifies the complex problem of in-process monitoring into an interpretable signal dropout pattern that can be leveraged for rapid fusion quality assessment.

Furthermore, the transition from static monitoring to robotic deployment necessitated a rigorous characterisation of mechanical uncertainty. The research successfully decoupled robot-induced positional errors; such as roll, lateral offset and coupling force; from the ultrasonic measurement itself, as shown in Chapter 5. This established contribution b). A fundamental transition zone was identified at a bevel length of approximately 9.62 mm, which dictates the optimal selection of scanning modalities: linear scans for wider, shallow geometries and sector scans for narrower, deeper features. By treating geometry and robotic pose as coupled variables, the robot was effectively transformed from a passive probe carrier into a high-precision metrological instrument.

Finally, the computational frameworks developed in the latter half of the thesis addressed the big data challenge of FMC, in Chapters 6 and 7. By achieving data compression rates exceeding 88% while maintaining sub-second execution times, this work proves that high-resolution volumetric imaging is compatible with the low-latency requirements of real-time robotic control, establishing contribution c). The subsequent ML architecture demonstrated that bevel geometry can be inferred within a 1.2 mm accuracy; falling directly within industrial compliance tolerances; directly at the point of acquisition. This established contribution d). Together, these findings establish a robust foundation for a closed-loop, self-correcting manufacturing environment.

8.2 Industrial Implications and Impact

By enabling the detection of critical defects like LOSWF at the point of deposition; rather than days or weeks later during post-weld inspection; this system drastically reduces the need for expensive excavation and repair work. In safety-critical sectors such as shipbuilding and nuclear manufacturing, where repair costs can escalate to 2-3 times the original fabrication expense, the ability to confirm fusion quality in real-time represents a transformative economic advantage.

Furthermore, the metrological rigor established in this works supports the manufacturing of large-scale infrastructure, such as the Type 31 frigates from Babcock and the Type 26 frigates at BAE Systems or renewable energy wind turbines. The machine learning and error-characterisation frameworks ensure that robotic systems can maintain sub-millimetre measurement precision during inspection. By achieving bevel length estimations within 1.2 mm, the system meets ISO 13920 weld preparation tolerances, providing the reliable and accurate quality assurance required for sovereign defence and net-zero energy projects.

Finally, the computational efficiency of the proposed pipeline allows advanced NDE to be deployed on portable edge platforms or mobile robotic crawlers. This democratisation of high-resolution imaging means that SMEs and larger fabricators alike can adopt “Industry 4“ standards without the need for prohibitive resources. By bridging the gap between sensing and robotic actuation, this research moves the industry closer to fully autonomous, self-diagnosing fabrication systems that can compensate for the diminishing availability of traditional skilled labor.

8.3 Limitations and Future Work

While the research presented in this thesis demonstrates a robust framework for autonomous weld monitoring and geometry estimation, several limitations remain that provide ground for future investigation. Acknowledging these constraints is essential for the transition from a laboratory environment to a fully unconstrained industrial setting.

8.3.1 Environmental and Material Constraints

The primary limitation encountered during “arc-on” monitoring was the influence of extreme thermal gradients on ultrasonic signal stability. Although this work successfully identified signal dropout patterns as a proxy for fusion, the high-temperature environment can introduce acoustic velocity shifts and signal attenuation that may degrade the monitoring window in complex multi-pass scenarios. Furthermore, while the system was validated on S275 carbon steel, further research is required to evaluate its performance on highly attenuative or anisotropic materials, such as austenitic stainless steels or nickel-based alloys, where grain structures scattering may interfere with the detection of subtle fusion defects.

8.3.2 Geometric Generalisation

A limitation of this thesis is the limited geometry variation for the assessment of Chapters 5, 6 and 7. The geometry estimation and machine learning models were primarily validated using a 90° V-joint surrogate and mock narrow-gap samples. While these represented a wide range of bevel lengths (1.69 mm to 16.69 mm) and thicknesses (up to 120 mm), industrial applications often involve more complex profiles, such as double-V or J-groove joints. These geometries introduce multiple internal reflections and mode conversions that may require more sophisticated signal separation techniques or the use of multi-modal TFM imaging to distinguish between root reflections and genuine structural echoes.

8.3.3 Future Research Directions: Closed-Loop Autonomy

Looking ahead, the logical progression of this work is the development of a fully autonomous tandem robotic system where real-time ultrasonic feedback directly drives welding process adaptation. In such a system, the trailing PAUT robot would continuously feed geometric and fusion data back to the lead welding robot to adjust parameters; such as wire feed speed, travel speed, or torch oscillation; in situ. Furthermore, the computational pipeline could be enhanced by porting the current MATLAB-based architecture to C++/CUDA to achieve even lower latencies, supporting high-frequency scanning at rates exceeding 100 Hz. Integrating ultrasonic data with complementary sensors, such as laser scanners or infrared thermography, would provide multi-modal monitoring of the weld, enhancing sensor redundancy. Finally, analytical and Finite Element Analysis simulation methods could be developed, to accurately describe the strong coupling effects between robotic trajectory, ultrasonic coverage, and effect of thermal gradient on measurement, which were out with the scope of this thesis, which relied on experimental data.

8.4 Final Concluding Statement

The research conducted in this thesis represents a contribution in the integration of volumetric sensing and robotic automation for industrial manufacturing. By successfully demonstrating that phased array ultrasonics can be utilized for real-time monitoring of LOSWF, quantifying the mechanical uncertainties of robotic delivery, and developing a high-speed machine learning framework for geometric inference, this work addresses some primary barriers to autonomous quality assurance. The work established here prove that high-resolution ultrasonic data can be compressed, processed, and interpreted within the latency requirements of industrial robotics, all while maintaining the metrological rigor required by safety-critical standards.

As the global manufacturing landscape continues to grapple with labor shortages and increasing structural complexity, the shift toward “intelligent” fabrication systems becomes imperative. This thesis provides the foundational tools necessary for that shift, offering a pathway toward intelligent welding based on volumetric feedback.

Ultimately, this work contributes to the development of more resilient, productive, and reliable manufacturing infrastructures for the modern era.

References

[1] 'UK Manufacturing: The Facts 2025 | Make UK'. Accessed: Feb. 27, 2026. [Online]. Available: https://www.makeuk.org/insights/reports/uk-manufacturing-facts-2025

[2] L. Jack, 'Why 2025's Industrial Strategy must close Britain's manufacturing robotics gap', The National Robotarium. Accessed: Feb. 27, 2026. [Online]. Available: https://thenationalrobotarium.com/why-2025s-industrial-strategy-must-close-britains-manufacturing-robotics-gap/

[3] 'Red tape to be slashed for British robotics and defence innovators', GOV.UK. Accessed: Feb. 27, 2026. [Online]. Available: https://www.gov.uk/government/news/red-tape-to-be-slashed-for-british-robotics-and-defence-innovators

[4] 'How Robotics and Automation Can Improve UK Productivity', The MTC. Accessed: Feb. 27, 2026. [Online]. Available: https://www.the-mtc.org/insights/challenges-change-how-automation-transforming-uk-manufacturing-mike-wilson-chief

[5] 'Type 31 - Babcock International Group'. Accessed: Mar. 13, 2026. [Online]. Available: https://www.babcockinternational.com/what-we-do/product/design-develop-and-manufacture/type-31/

[6] 'Construction of new state of the art shipbuilding facility underway in Glasgow', BAE Systems. Accessed: Feb. 27, 2026. [Online]. Available: https://www.baesystems.com

[7] 'Strategic Defence Review 2025 – Making Britain Safer: secure at home, strong abroad'.

[8] 'Chinese firm to build UK's largest wind turbine factory in Scotland | AJ Bell'. Accessed: Feb. 27, 2026. [Online]. Available: https://www.ajbell.co.uk/news/articles/chinese-firm-build-uks-largest-wind-turbine-factory-scotland

[9] I. Stewart, N. Burnett, and T. Hewitt, 'The UK's plans and progress to reach net zero by 2050', Feb. 2026, Accessed: Feb. 27, 2026. [Online]. Available: https://commonslibrary.parliament.uk/research-briefings/cbp-9888/

[10] 'Welding's quiet revolution: how smart skills and tech will power Britain's building', The Manufacturer. Accessed: Feb. 27, 2026. [Online]. Available: https://www.themanufacturer.com/articles/weldings-quiet-revolution-how-smart-skills-and-tech-will-power-britains-building/

[11] 'Robot Welding and Labour Shortages: Why Automation Is Becoming a Necessity'. Accessed: Feb. 27, 2026. [Online]. Available: https://www.yaskawa.co.uk/header-meta/news-events/article/robot-welding-and-labour-shortages-why-automation-is-becoming-a-necessity_n22981

[12] 'The Rise of Robotics in UK Manufacturing: A 2024 Perspective | Automate UK'. Accessed: Jun. 02, 2026. [Online]. Available: https://www.automate-uk.com/news-publications/the-rise-of-robotics-in-uk-manufacturing-a-2024-perspective/

[13] 'Robotic Arc Welding'. Accessed: Feb. 27, 2026. [Online]. Available: https://www.twi-global.com/technical-knowledge/job-knowledge/robotic-arc-welding-135.aspx

[14] Z. Jin, H. Li, and H. Gao, 'An intelligent weld control strategy based on reinforcement learning approach', *Int. J. Adv. Manuf. Technol.*, vol. 100, no. 9, pp. 2163–2175, Feb. 2019, doi: 10.1007/s00170-018-2864-2.

[15] M. Vasilev *et al.*, ‘Sensor-Enabled Multi-Robot System for Automated Welding and In-Process Ultrasonic NDE’, *Sensors*, vol. 21, no. 15, p. 5077, Jul. 2021, doi: 10.3390/s21155077.

[16] ‘GtR’. Accessed: Feb. 27, 2026. [Online]. Available: https://gtr.ukri.org/projects?ref=10054861

[17] S. Kou, ‘Fusion Welding Processes’, in *Welding Metallurgy*, John Wiley & Sons, Ltd, 2002, pp. 1–36. doi: 10.1002/0471434027.ch1.

[18] J. F. Lancaster, ‘6 - Fusion welding processes and their thermal effects’, in *Metallurgy of Welding (Sixth Edition)*, J. F. Lancaster, Ed., Woodhead Publishing, 1999, pp. 128–168. doi: 10.1533/9781845694869.128.

[19] D. Stergiopoulos, *Welding Processes and Equipment*. Elefsina, 2020.

[20] C. Loukas *et al.*, ‘A cost-function driven adaptive welding framework for multi-pass robotic welding’, *J. Manuf. Process.*, vol. 67, pp. 545–561, Jul. 2021, doi: 10.1016/j.jmapro.2021.05.004.

[21] British Standards Institution, ‘BS EN ISO 6520-1:2007 Welding and allied processes. Classification of geometric imperfections in metallic materials. Fusion welding’.

[22] E. Nicolson, E. Mohseni, D. Lines, K. M. M. Tant, G. Pierce, and C. N. MacLeod, ‘Towards an in-process ultrasonic phased array inspection method for narrow-gap welds’, *NDT E Int.*, vol. 144, p. 103074, Jun. 2024, doi: 10.1016/j.ndteint.2024.103074.

[23] G. Rihar and M. Uran, ‘Lack of Fusion Characterisation of Indications’, *Weld. World*, vol. 50, no. 1, pp. 35–39, Jan. 2006, doi: 10.1007/BF03266513.

[24] British Standards Institution, ‘BS 7910:2019 Guide to methods for assessing the acceptability of flaws in metallic structures’.

[25] British Standards Institution, ‘BS EN ISO 5817:2023 Welding. Fusion-welded joints in steel, nickel, titanium and their alloys (beam welding excluded). Quality levels for imperfections’. 2023.

[26] American Welding Society, *AWS D1.1 - Structural Welding Code - Steel*, 17th Edition. ANSI.

[27] U. Sreedhar, C. V. Krishnamurthy, K. Balasubramaniam, V. D. Raghupathy, and S. Ravisankar, ‘Automatic defect identification using thermal image analysis for online weld quality monitoring’, *J. Mater. Process. Technol.*, vol. 212, no. 7, pp. 1557–1566, Jul. 2012, doi: 10.1016/j.jmatprotec.2012.03.002.

[28] V. Balasubramaniam, M. Menaka, M. Vasudevan, and B. Raj, ‘Thermography for online detection of incomplete penetration and penetration depth estimation’, in *New Zealand*, Auckland, New Zealand, 2006.

[29] ASTM, ‘ASTM E749-01 Standard Practice for Acoustic Emission Monitoring During Continuous Welding’. ASTM International, Aug. 16, 2017.

[30] M. G. Droubi, N. H. Faisal, F. Orr, J. A. Steel, and M. El-Shaib, ‘Acoustic emission method for defect detection and identification in carbon steel welded joints’, *J. Constr. Steel Res.*, vol. 134, pp. 28–37, Jul. 2017, doi: 10.1016/j.jcsr.2017.03.012.

[31] K. He, X. Liu, Q. Yang, and Y. Chen, ‘An extraction method of welding crack acoustic emission signal using harmonic analysis’, *Measurement*, vol. 103, pp. 311–320, Jun. 2017, doi: 10.1016/j.measurement.2017.02.026.

[32] N. Godin, P. Reynaud, and G. Fantozzi, 'Challenges and Limitations in the Identification of Acoustic Emission Signature of Damage Mechanisms in Composites Materials', *Appl. Sci.*, vol. 8, no. 8, p. 1267, Aug. 2018, doi: 10.3390/app8081267.

[33] British Standards Institution, 'BS EN ISO 17636-1:2022 Non-destructive testing of welds. Radiographic testing. X- and gamma-ray techniques with film'. BSI.

[34] M. Shaloo, M. Schnall, T. Klein, N. Huber, and B. Reitinger, 'A Review of Non-Destructive Testing (NDT) Techniques for Defect Detection: Application to Fusion Welding and Future Wire Arc Additive Manufacturing Processes', *Materials*, vol. 15, no. 10, p. 3697, May 2022, doi: 10.3390/ma15103697.

[35] E. E. Ghandourah *et al.*, 'Evaluation of Welding Imperfections with X-ray Computed Laminography for NDT Inspection of Carbon Steel Plates', *J. Nondestruct. Eval.*, vol. 42, no. 3, p. 77, Aug. 2023, doi: 10.1007/s10921-023-00989-z.

[36] E. A. Foster *et al.*, 'Automated Real-Time Eddy Current Array Inspection of Nuclear Assets', *Sensors*, vol. 22, no. 16, p. 6036, Jan. 2022, doi: 10.3390/s22166036.

[37] V. Tunukovic *et al.*, 'Automated robotic system for dual ultrasonic and eddy current array integration and data fusion in wire arc additive manufacturing material inspection', *NDT E Int.*, vol. 160, p. 103665, May 2026, doi: 10.1016/j.ndteint.2026.103665.

[38] J. Blitz, 'Fundamental theory', in *Electrical and Magnetic Methods of Non-destructive Testing*, J. Blitz, Ed., Dordrecht: Springer Netherlands, 1997, pp. 13–42. doi: 10.1007/978-94-011-5818-3_2.

[39] D. Chauveau, 'Review of NDT and process monitoring techniques usable to produce high-quality parts by welding or additive manufacturing', *Weld. World*, vol. 62, no. 5, pp. 1097–1118, Sep. 2018, doi: 10.1007/s40194-018-0609-3.

[40] N. E. Sweeney *et al.*, 'In-process phased array ultrasonic weld pool monitoring', *NDT E Int.*, vol. 137, p. 102850, Jul. 2023, doi: 10.1016/j.ndteint.2023.102850.

[41] J. Krautkrämer and H. Krautkrämer, *Ultrasonic Testing of Materials*. Berlin, Heidelberg: Springer, 1990. doi: 10.1007/978-3-662-10680-8.

[42] J. L. Rose, *Ultrasonic Guided Waves in Solid Media*. Cambridge: Cambridge University Press, 2014. doi: 10.1017/CBO9781107273610.

[43] 'Ultrasound. Theory of ultrasonic waves propagation'. Accessed: Mar. 09, 2026. [Online]. Available: https://about-motors.com/ultrasound/theory/

[44] F. E. Stanke and G. S. Kino, 'A unified theory for elastic wave propagation in polycrystalline materials', *J. Acoust. Soc. Am.*, vol. 75, no. 3, pp. 665–681, Mar. 1984, doi: 10.1121/1.390577.

[45] M.-A. Ploix, P. Guy, B. Chassignole, J. Moysan, G. Corneloup, and R. E. Guerjouma, 'Measurement of ultrasonic scattering attenuation in austenitic stainless steel welds: Realistic input data for NDT numerical modeling', *Ultrasonics*, vol. 54, no. 7, pp. 1729–1736, Sep. 2014, doi: 10.1016/j.ultras.2014.04.005.

[46] L. W. Schmerr Jr., 'Time Delay Laws (2-D)', in *Fundamentals of Ultrasonic Phased Arrays*, L. W. Schmerr Jr., Ed., Cham: Springer International Publishing, 2015, pp. 99–111. doi: 10.1007/978-3-319-07272-2_5.

[47] B. W. Drinkwater and P. D. Wilcox, 'Ultrasonic arrays for non-destructive evaluation: A review', *NDT E Int.*, vol. 39, no. 7, pp. 525–541, Oct. 2006, doi: 10.1016/j.ndteint.2006.03.006.

[48] A. Ilovitsh, T. Ilovitsh, J. Foiret, D. N. Stephens, and K. W. Ferrara, 'Simultaneous Axial Multifocal Imaging Using a Single Acoustical Transmission: A Practical Implementation', *IEEE Trans. Ultrason. Ferroelectr. Freq. Control*, vol. 66, no. 2, pp. 273–284, Feb. 2019, doi: 10.1109/TUFFC.2018.2885080.

[49] 'Phased Array Ultrasonic Testing (PAUT) | Eddyfi'. Accessed: Jun. 04, 2026. [Online]. Available: https://www.eddyfi.com/en/technology/phased-array-ultrasonic-testing-paut

[50] M. Khelil, J.-H. Thomas, L. Simon, R. El Guerjouma, and M. Boudraa, 'Characterization of Structural Noise Patterns and Echo Separation in the Time-Frequency Plane for Austenitic Stainless Steels', *J. Nondestruct. Eval.*, vol. 36, no. 2, p. 31, Apr. 2017, doi: 10.1007/s10921-017-0409-5.

[51] C. Holmes, B. W. Drinkwater, and P. D. Wilcox, 'Post-processing of the full matrix of ultrasonic transmit–receive array data for non-destructive evaluation', *NDT E Int.*, vol. 38, no. 8, pp. 701–711, Dec. 2005, doi: 10.1016/j.ndteint.2005.04.002.

[52] J. Zhang, B. W. Drinkwater, P. D. Wilcox, and A. J. Hunter, 'Defect detection using ultrasonic arrays: The multi-mode total focusing method', *NDT E Int.*, vol. 43, no. 2, pp. 123–133, Mar. 2010, doi: 10.1016/j.ndteint.2009.10.001.

[53] E. Nicolson, E. Mohseni, Sumana, D. Lines, G. Pierce, and C. N. MacLeod, 'Dual-tandem phased array method for imaging of near-vertical defects in narrow-gap welds', *NDT E Int.*, vol. 135, p. 102808, Apr. 2023, doi: 10.1016/j.ndteint.2023.102808.

[54] A. J. Hunter, B. W. Drinkwater, and P. D. Wilcox, 'The wavenumber algorithm for full-matrix imaging using an ultrasonic array', *IEEE Trans. Ultrason. Ferroelectr. Freq. Control*, vol. 55, no. 11, pp. 2450–2462, Nov. 2008, doi: 10.1109/TUFFC.952.

[55] A. V. Oppenheim, A. S. Willsky, and S. H. Nawab, *Signals & systems (2nd ed.)*. USA: Prentice-Hall, Inc., 1996.

[56] L. Marple, 'Computing the discrete-time "analytic" signal via FFT', *IEEE Trans. Signal Process.*, vol. 47, no. 9, pp. 2600–2603, Sep. 1999, doi: 10.1109/78.782222.

[57] A. Prakash, N. Jothilakshmi, and P. P. Nanekar, 'Ultrasonic Simulation Studies for Sizing of Planar Flaws in Thick Carbon Steel Weld', 2015.

[58] M. Gene, 'Ultrasonic Examination: Part 2'. Accessed: Jun. 05, 2026. [Online]. Available: https://www.twi-global.com/technical-knowledge/job-knowledge/ultrasonic-examination-part-2-128.aspx

[59] British Standards Institution, 'BS EN ISO 19825:2017 Non-destructive Testing of Welds - Phased Array Ultrasonic Testing (PAUT) - Acceptance Levels'. London, 2017.

[60] T. Ye, C. Guo, J. Xu, and L. Bai, 'Adaptive TFM imaging with multi-stage channel optimization for enhanced defect characterization in coarse-grained materials', *Ultrasonics*, vol. 164, p. 108022, Aug. 2026, doi: 10.1016/j.ultras.2026.108022.

[61] C. Guo, Y. Ding, H. Cui, J. Xu, and L. Bai, 'Ultrasonic characterization of defects in polycrystalline materials based on TFM image reconstruction using denoising diffusion probabilistic models', *Mech. Syst. Signal Process.*, vol. 224, p. 111997, Feb. 2025, doi: 10.1016/j.ymssp.2024.111997.

[62] M. G. Silk and B. H. Liddington, 'Defect Sizing using an ultrasonic time-delay approach', pp. 33–36, 1975.

[63] G. Baskaran, K. Balasubramaniam, and C. Lakshmana Rao, 'Shear-wave time of flight diffraction (S-TOFD) technique', *NDT E Int.*, vol. 39, no. 6, pp. 458–467, Sep. 2006, doi: 10.1016/j.ndteint.2006.01.003.

[64] Bernoullies, Accessed: Mar. 09, 2026. [PNG]. Available: https://commons.wikimedia.org/w/index.php?curid=16647556

[65] 'Defect Sizing in Pipeline Welds – What Can We Really Achieve?' Accessed: Mar. 07, 2026. [Online]. Available: https://ims.evidentscientific.com/en/applications/defect-sizing-pipe-welds

[66] British Standards Institution, 'BS EN ISO 10863:2020 Non-destructive Testing of Welds - Ultrasonic Testing - Use of Time-of-Flight Diffraction Technique (TOFD)'. BSI, London, 2020.

[67] British Standards Institution, 'BS EN ISO 15626:2018 Non-destructive Testing of Welds - Time-of-Flight Diffraction Technique (TOFD) - Acceptance Levels'. BSI, London, 2018.

[68] B. Gauthier, G. Painchaud-April, A. Le Duff, and P. Bélanger, 'Towards an Alternative to Time of Flight Diffraction Using Instantaneous Phase Coherence Imaging for Characterization of Crack-Like Defects', *Sensors*, vol. 21, no. 3, p. 730, Jan. 2021, doi: 10.3390/s21030730.

[69] B. Wu, B. Deng, M. Zhao, and Y. Huang, 'Crack sizing in welded T-joint using an enhanced ultrasonic TOFD approach by a sparse representation framework', *Measurement*, vol. 258, p. 119517, Jan. 2026, doi: 10.1016/j.measurement.2025.119517.

[70] A. Das, A. Dutta, A. Mukherjee, and S. K. Pal, 'Gen-ToFD: A class-aware generative framework for time-of-flight diffraction data augmentation and enhanced weld defect classification', *J. Manuf. Process.*, vol. 157, pp. 670–686, Jan. 2026, doi: 10.1016/j.jmapro.2025.12.019.

[71] H. Sun, P. Ramuhalli, and R. E. Jacob, 'Machine learning for ultrasonic nondestructive examination of welding defects: A systematic review', *Ultrasonics*, vol. 127, p. 106854, Jan. 2023, doi: 10.1016/j.ultras.2022.106854.

[72] T. Latête, B. Gauthier, and P. Belanger, 'Towards using convolutional neural network to locate, identify and size defects in phased array ultrasonic testing', *Ultrasonics*, vol. 115, p. 106436, Aug. 2021, doi: 10.1016/j.ultras.2021.106436.

[73] C. Mineo, S. G. Pierce, P. I. Nicholson, and I. Cooper, 'Robotic path planning for non-destructive testing – A custom MATLAB toolbox approach', *Robot. Comput.-Integr. Manuf.*, vol. 37, pp. 1–12, Feb. 2016, doi: 10.1016/j.rcim.2015.05.003.

[74] M. Vasilev *et al.*, 'Sensor-Enabled Multi-Robot System for Automated Welding and In-Process Ultrasonic NDE', *Sensors*, vol. 21, no. 15, p. 5077, Jan. 2021, doi: 10.3390/s21155077.

[75] Y. Javadi *et al.*, 'High-temperature in-process inspection followed by 96-h robotic inspection of intentionally manufactured hydrogen crack in multi-pass robotic welding', *Int. J. Press. Vessels Pip.*, vol. 189, p. 104288, Feb. 2021, doi: 10.1016/j.ijpvp.2020.104288.

[76] Y. Wu, P. D. Wilcox, and A. J. Croxford, 'Robotic inspection of fastener holes with hybrid visual and ultrasonic motion control', *J. Manuf. Syst.*, vol. 83, pp. 770–783, Dec. 2025, doi: 10.1016/j.jmsy.2025.11.003.

[77] X. Sun *et al.*, 'A dual-resolution acoustic-sensing robot for autonomous in-pipe inspection', *Tunn. Undergr. Space Technol.*, vol. 168, p. 107133, Feb. 2026, doi: 10.1016/j.tust.2025.107133.

[78] X. Sun, A. R. K. Towlson, Q. Kong, J. Zhang, A. J. Croxford, and B. W. Drinkwater, 'A multi-view ultrasonic imaging solution for buried sewer pipe inspection', *Ultrasonics*, vol. 156, p. 107762, Dec. 2025, doi: 10.1016/j.ultras.2025.107762.

[79] A. Nubiola and I. A. Bonev, ‘Absolute calibration of an ABB IRB 1600 robot using a laser tracker’, *Robot. Comput.-Integr. Manuf.*, vol. 29, no. 1, pp. 236–245, Feb. 2013, doi: 10.1016/j.rcim.2012.06.004.

[80] M. Morozov *et al.*, ‘Assessing the accuracy of industrial robots through metrology for the enhancement of automated non-destructive testing’, in *2016 IEEE International Conference on Multisensor Fusion and Integration for Intelligent Systems (MFI)*, Sep. 2016, pp. 335–340. doi: 10.1109/MFI.2016.7849510.

[81] O. Kedilioglu, M. Nikol, J. Walter, and J. Franke, ‘Correlation Analysis of Factors Influencing the Motion Planning Accuracy of Articulated Robots’, in *2023 9th International Conference on Automation, Robotics and Applications (ICARA)*, Feb. 2023, pp. 97–101. doi: 10.1109/ICARA56516.2023.10125613.

[82] N. A. Theissen, T. Laspas, and A. Archenti, ‘Closed-force-loop elastostatic calibration of serial articulated robots’, *Robot. Comput.-Integr. Manuf.*, vol. 57, pp. 86–91, Jun. 2019, doi: 10.1016/j.rcim.2018.07.007.

[83] M. Tabatabaeipour *et al.*, ‘Mitigating RGB-D camera errors for robust ultrasonic inspections using a force-torque sensor’, *Nondestruct. Test. Eval.*, vol. 40, no. 6, pp. 2738–2759, Jun. 2025, doi: 10.1080/10589759.2024.2386618.

[84] C. Cadot, J.-F. Saillant, and B. Dulmet, ‘Method for Acoustic Characterization of Materials in Temperature’.

[85] ‘ULTEM’, Plastics International. Accessed: Jun. 03, 2026. [Online]. Available: https://www.plasticsintl.com/products/ult1-062-s/

[86] ‘Rexolite 1422 – High-Performance Plastic Sheet and Rod’, Polymer Plastics Company, LC. Accessed: Jun. 03, 2026. [Online]. Available: https://www.polymerplastics.com/rexolite-high-performance-plastic.html

[87] R. K. W. Vithanage *et al.*, ‘A Phased Array Ultrasound Roller Probe for Automated in-Process/Interpass Inspection of Multipass Welds’, *IEEE Trans. Ind. Electron.*, vol. 68, no. 12, pp. 12781–12790, Dec. 2021, doi: 10.1109/TIE.2020.3042112.

[88] C. M. Bishop, *Pattern recognition and machine learning*, vol. 4. Springer New York, 2006.

[89] T. Hastie, R. Tibshirani, and J. Friedman, ‘Basis Expansions and Regularization’, in *The Elements of Statistical Learning: Data Mining, Inference, and Prediction*, T. Hastie, R. Tibshirani, and J. Friedman, Eds, New York, NY: Springer, 2009, pp. 139–189. doi: 10.1007/978-0-387-84858-7_5.

[90] L. Breiman, ‘Random Forests’, *Mach. Learn.*, vol. 45, no. 1, pp. 5–32, Oct. 2001, doi: 10.1023/A:1010933404324.

[91] J. H. Friedman, ‘Greedy function approximation: A gradient boosting machine.’, *Ann. Stat.*, vol. 29, no. 5, pp. 1189–1232, Oct. 2001, doi: 10.1214/aos/1013203451.

[92] T. Chen and C. Guestrin, ‘XGBoost: A Scalable Tree Boosting System’, in *Proceedings of the 22nd ACM SIGKDD International Conference on Knowledge Discovery and Data Mining*, in KDD ’16. New York, NY, USA: Association for Computing Machinery, Aug. 2016, pp. 785–794. doi: 10.1145/2939672.2939785.

[93] P. Kowalek, H. Loch-Olszewska, and J. Szwabiński, ‘Classification of diffusion modes in single-particle tracking data: Feature-based versus deep-learning approach’, *Phys. Rev. E*, vol. 100, no. 3, p. 032410, Sep. 2019, doi: 10.1103/PhysRevE.100.032410.

[94] C. Cortes and V. Vapnik, ‘Support-vector networks’, *Mach. Learn.*, vol. 20, no. 3, pp. 273–297, Sep. 1995, doi: 10.1007/BF00994018.

[95] A. J. Smola and B. Schölkopf, ‘A tutorial on support vector regression’, *Stat. Comput.*, vol. 14, no. 3, pp. 199–222, Aug. 2004, doi: 10.1023/B:STCO.0000035301.49549.88.

[96] S. K. Lahiri and K. C. Ghanta, ‘The Support Vector Regression with the parameter tuning assisted by a differential evolution technique: Study of the critical velocity of a slurry flow in a pipeline’, *Chem. Ind. Chem. Eng. Q.*, vol. 14, no. 3, pp. 191–203, 2008.

[97] C. E. Rasmussen, ‘Gaussian Processes in Machine Learning’, in *Advanced Lectures on Machine Learning: ML Summer Schools 2003, Canberra, Australia, February 2 - 14, 2003, Tübingen, Germany, August 4 - 16, 2003, Revised Lectures*, O. Bousquet, U. von Luxburg, and G. Rätsch, Eds, Berlin, Heidelberg: Springer, 2004, pp. 63–71. doi: 10.1007/978-3-540-28650-9_4.

[98] F. Leclercq, ‘Bayesian optimization for likelihood-free cosmological inference’, *Phys. Rev. D*, vol. 98, no. 6, p. 063511, Sep. 2018, doi: 10.1103/PhysRevD.98.063511.

[99] B. Zdaniuk, ‘Ordinary Least-Squares (OLS) Model’, in *Encyclopedia of Quality of Life and Well-Being Research*, Springer, Cham, 2023, pp. 4867–4869. doi: 10.1007/978-3-031-17299-1_2008.

[100] G. C. McDonald, ‘Ridge regression’, *WIREs Comput. Stat.*, vol. 1, no. 1, pp. 93–100, 2009, doi: 10.1002/wics.14.

[101] R. Tibshirani, ‘Regression Shrinkage and Selection Via the Lasso’, *J. R. Stat. Soc. Ser. B Methodol.*, vol. 58, no. 1, pp. 267–288, Jan. 1996, doi: 10.1111/j.2517-6161.1996.tb02080.x.

[102] ‘KUKA KR10 R1100’. May 06, 2019.

[103] ‘KUKA.RobotSensorInterface’, KUKA UK. Accessed: Mar. 13, 2026. [Online]. Available: https://www.kuka.com/en-gb/products/robotics-system/software/hub-technologies/kuka_robotsensorinterface

[104] PEAK-NDT, ‘PEAK NDT LTPA’.

[105] ‘KUKA KR 10 R1100-2’. Accessed: Jun. 04, 2026. [Online]. Available: https://my.kuka.com/s/product/kr-10-r11002/01t5800000416jgAAA?language=en_US&tab=Details

[106] C. S. Wiesner and G. R. Razmjoo, ‘Applications of Structural Integrity Assessments for the Offshore Industry’, in *Methods for the Assessment of the Structural Integrity of Components and Structures*, CRC Press, 2004.

[107] R. Kumar, ‘Defects Associated with Welding Techniques and Their Detection Methods’, in *Advanced Welding Techniques*, CRC Press, 2024.

[108] K. A. Macdonald and C. Russell, ‘Design and Welding Challenges in the Infield Flowlines of the Encana Deep Panuke Development’, presented at the 2010 8th International Pipeline Conference, American Society of Mechanical Engineers Digital Collection, Apr. 2011, pp. 719–734. doi: 10.1115/IPC2010-31626.

[109] V. R. Rathod and R. S. Anand, ‘A Comparative Study of Different Segmentation Techniques for Detection of Flaws in NDE Weld Images’, *J. Nondestruct. Eval.*, vol. 31, no. 1, pp. 1–16, Mar. 2012, doi: 10.1007/s10921-011-0116-6.

[110] Y. Javadi *et al.*, ‘In-process calibration of a non-destructive testing system used for in-process inspection of multi-pass welding’, *Mater. Des.*, vol. 195, p. 108981, Oct. 2020, doi: 10.1016/j.matdes.2020.108981.

[111] P. Kah, M. Shrestha, E. Hiltunen, and J. Martikainen, 'Robotic arc welding sensors and programming in industrial applications', *Int. J. Mech. Mater. Eng.*, vol. 10, no. 1, p. 13, Jul. 2015, doi: 10.1186/s40712-015-0042-y.

[112] T. de A. Prado, H. L. Moura, T. A. R. Passarin, G. A. Guarneri, G. P. Pires, and D. R. Pipa, 'A straightforward method to evaluate the directivity function of ultrasound imaging systems', *NDT E Int.*, vol. 119, p. 102402, Apr. 2021, doi: 10.1016/j.ndteint.2021.102402.

[113] Y. Kim, S. Cho, and I. K. Park, 'Analysis of Flaw Detection Sensitivity of Phased Array Ultrasonics in Austenitic Steel Welds According to Inspection Conditions', *Sensors*, vol. 21, no. 1, p. 242, Jan. 2021, doi: 10.3390/s21010242.

[114] C. MacLeod and Y. Javadi, 'Chapter 12 - Advanced nondestructive evaluation for welded joints', in *Welding of Metallic Materials*, F. Khoshnaw, Ed., Elsevier, 2023, pp. 431–461. doi: 10.1016/B978-0-323-90552-7.00017-1.

[115] S. Kumar, M. Menaka, and B. Venkatraman, 'Performance comparison of phased array transducers for inspection of dissimilar welds on nuclear reactor components', *Ann. Nucl. Energy*, vol. 162, p. 108482, Nov. 2021, doi: 10.1016/j.anucene.2021.108482.

[116] C. Li *et al.*, 'Study on Phased Array Ultrasonic Testing Techniques for Austenitic Stainless Steel Butt Welds', *J. Fusion Energy*, vol. 44, no. 1, p. 13, Feb. 2025, doi: 10.1007/s10894-025-00475-6.

[117] B. Cassels, L.-K. Shark, S. J. Mein, A. Nixon, T. Barber, and R. Turner, 'Robust principal component analysis of ultrasonic sectorial scans for defect detection in weld inspection', in *Multimodal Sensing: Technologies and Applications*, SPIE, Jun. 2019, pp. 112–128. doi: 10.1117/12.2527622.

[118] E. Mirmahdi, D. Afshari, and M. Karimi Ivanaki, 'A Review of Ultrasonic Testing Applications in Spot Welding: Defect Evaluation in Experimental and Simulation Results', *Trans. Indian Inst. Met.*, vol. 76, no. 6, pp. 1381–1392, Jun. 2023, doi: 10.1007/s12666-022-02738-8.

[119] Y. Fu, J. Wu, Z. Liu, R. Wang, B. Jiang, and W. Wen, 'Phased array ultrasonic test of vertical defect on butt-joint weld of CFETR vacuum vessel port stub', *Fusion Eng. Des.*, vol. 141, pp. 1–8, Apr. 2019, doi: 10.1016/j.fusengdes.2019.02.010.

[120] H. Shi, M. Ebrahimi, P. Zhou, K. Shao, and J. Li, 'Ultrasonic and phased-array inspection in titanium-based alloys: A review', *Proc. Inst. Mech. Eng. Part E J. Process Mech. Eng.*, vol. 237, no. 2, pp. 511–530, Apr. 2023, doi: 10.1177/09544089221114253.

[121] R. Zimermann *et al.*, 'Collaborative Robotic Wire + Arc Additive Manufacture and Sensor-Enabled In-Process Ultrasonic Non-Destructive Evaluation', *Sensors*, vol. 22, no. 11, p. 4203, May 2022, doi: 10.3390/s22114203.

[122] H. He *et al.*, 'Open-source software architecture for multi-robot Wire Arc Additive Manufacturing (WAAM)', *Appl. Eng. Sci.*, vol. 22, p. 100204, Jun. 2025, doi: 10.1016/j.apples.2025.100204.

[123] A. Mohamed, C. Loukas, M. Vasilev, N. Sweeney, G. Dobie, and C. Macleod, 'Ultrasonic-driven adaptive control of robotic plasma arc cutting for bevel applications', *Int. J. Adv. Manuf. Technol.*, vol. 137, no. 7, pp. 3783–3797, Apr. 2025, doi: 10.1007/s00170-025-15331-2.

[124] G. H. Kim *et al.*, 'Qualification of phased array ultrasonic examination on T-joint weld of austenitic stainless steel for ITER vacuum vessel', *Fusion Eng. Des.*, vol. 109–111, pp. 1099–1103, Nov. 2016, doi: 10.1016/j.fusengdes.2016.01.015.

[125] L. Morgan, 'Testing defects in automated ultrasonic testing and radiographic testing', *Insight - Non-Destr. Test. Cond. Monit.*, vol. 60, no. 11, pp. 606–612, Nov. 2018, doi: 10.1784/insi.2018.60.11.606.

[126] M. Consonni, C. F. Wee, and C. Schneider, 'Manufacturing of welded joints with realistic defects', *Insight - Non-Destr. Test. Cond. Monit.*, vol. 54, no. 2, pp. 76–81, Feb. 2012, doi: 10.1784/insi.2012.54.2.76.

[127] 'ISO 13588:2019 Non-destructive testing of welds — Ultrasonic testing — Use of automated phased array technology'. Accessed: Feb. 09, 2026. [Online]. Available: https://www.iso.org/standard/72747.html

[128] A. Gilmour *et al.*, 'Robotic Ultrasonic Inspection of Large and Complex Structural Assets', *Ructural Health Monit. 2023 Proc. 14th Int. Workshop Struct. Health Monit.*, pp. 2099–2106, Sep. 2023.

[129] G. Dobie, W. Galbraith, C. MacLeod, R. Summan, G. Pierce, and A. Gachagan, 'Automatic ultrasonic robotic array', in *2013 IEEE International Ultrasonics Symposium (IUS)*, Jul. 2013, pp. 1861–1864. doi: 10.1109/ULTSYM.2013.0474.

[130] V. Papadimitriou, I. Roditis, P. Chatzakos, and D. Liaptsis, 'An adaptable and self-calibrating service robotic scanner for ultrasonic inspection of nuclear nozzle-vessel welds', in *2012 2nd International Conference on Applied Robotics for the Power Industry (CARPI)*, Sep. 2012, pp. 133–138. doi: 10.1109/CARPI.2012.6473363.

[131] A. Gilmour *et al.*, 'Using Phased Array Ultrasound to Localize Probes During the Inspection of Welds', *IEEE Open J. Instrum. Meas.*, vol. 2, pp. 1–10, 2023, doi: 10.1109/OJIM.2023.3327484.

[132] M. Zhang, M. Sutcliffe, D. Carswell, and Q. Yang, 'Robotic path planning using NDT ultrasonic data for autonomous inspection', *Int. J. Metrol. Qual. Eng.*, vol. 14, p. 16, 2023, doi: 10.1051/ijmqe/2023013.

[133] J. D. Achenbach, 'Modeling for quantitative non-destructive evaluation', *Ultrasonics*, vol. 40, no. 1, pp. 1–10, May 2002, doi: 10.1016/S0041-624X(02)00083-5.

[134] W.-J. Baek and T. Kröger, 'Safety Evaluation of Robot Systems via Uncertainty Quantification', in *2023 IEEE International Conference on Robotics and Automation (ICRA)*, May 2023, pp. 10532–10538. doi: 10.1109/ICRA48891.2023.10160598.

[135] F. von Drigalski *et al.*, 'Precise Multi-Modal In-Hand Pose Estimation using Low-Precision Sensors for Robotic Assembly', in *2021 IEEE International Conference on Robotics and Automation (ICRA)*, May 2021, pp. 968–974. doi: 10.1109/ICRA48506.2021.9561222.

[136] A. Stolt, 'Robotic Assembly and Contact Force Control', Licentiate Thesis, Department of Automatic Control, Lund Institute of Technology, Lund University, 2012.

[137] C. A. Duggan, K. C. Wolfe, B. Woosley, M. Kobilarov, and J. Moore, 'Uncertainty-Aware Planning for Heterogeneous Robot Teams using Dynamic Topological Graphs and Mixed-Integer Programming', in *2025 IEEE 21st International Conference on Automation Science and Engineering (CASE)*, Aug. 2025, pp. 1646–1653. doi: 10.1109/CASE58245.2025.11164089.

[138] L. Nardi and C. Stachniss, 'Uncertainty-Aware Path Planning for Navigation on Road Networks Using Augmented MDPs', in *2019 International Conference on Robotics and Automation (ICRA)*, May 2019, pp. 5780–5786. doi: 10.1109/ICRA.2019.8794121.

[139] H. Liao, Y. Chen, B. Hu, and S. Behdad, ‘Optimization-Based Disassembly Sequence Planning Under Uncertainty for Human–Robot Collaboration’, *J. Mech. Des.*, vol. 145, no. 022001, Nov. 2022, doi: 10.1115/1.4055901.

[140] C. Papachristos, F. Mascarich, S. Khattak, T. Dang, and K. Alexis, ‘Localization uncertainty-aware autonomous exploration and mapping with aerial robots using receding horizon path-planning’, *Auton. Robots*, vol. 43, no. 8, pp. 2131–2161, Dec. 2019, doi: 10.1007/s10514-019-09864-1.

[141] R. J. Pyle, R. R. Hughes, A. A. S. Ali, and P. D. Wilcox, ‘Uncertainty Quantification for Deep Learning in Ultrasonic Crack Characterization’, *IEEE Trans. Ultrason. Ferroelectr. Freq. Control*, vol. 69, no. 7, pp. 2339–2351, Jul. 2022, doi: 10.1109/TUFFC.2022.3176926.

[142] J. Nagawkar and L. Leifsson, ‘Efficient Global Sensitivity Analysis of Model-Based Ultrasonic Nondestructive Testing Systems Using Machine Learning and Sobol’ Indices’, *J. Nondestruct. Eval. Diagn. Progn. Eng. Syst.*, vol. 4, no. 041008, Jun. 2021, doi: 10.1115/1.4051100.

[143] H. Sun, P. Ramuhalli, and R. Meyer, ‘An Assessment of Machine Learning Applied to Ultrasonic Nondestructive Evaluation’, ORNL/SPR--2023/3245, 2320378, Dec. 2023. doi: 10.2172/2320378.

[144] S. De, B. S. M. Ebna Hai, A. Doostan, and M. Bause, ‘Prediction of Ultrasonic Guided Wave Propagation in Fluid–Structure and Their Interface under Uncertainty Using Machine Learning’, *J. Eng. Mech.*, vol. 148, no. 3, p. 04021161, Mar. 2022, doi: 10.1061/(ASCE)EM.1943-7889.0002038.

[145] T. Leach *et al.*, ‘Adaptive compensation for in-process ultrasonic cladding inspection’, *NDT E Int.*, vol. 158, p. 103571, Mar. 2026, doi: 10.1016/j.ndteint.2025.103571.

[146] A. Dimakos *et al.*, ‘Evaluation of signal disturbance and recovery in phased array ultrasonic inspection during welding’, *Weld. World*, Nov. 2025, doi: 10.1007/s40194-025-02256-3.

[147] Y. Zhang, X. Lv, L. Xu, H. Jing, and Y. Han, ‘A segmentation planning method based on the change rate of cross-sectional area of single V-groove for robotic multi-pass welding in intersecting pipe-pipe joint’, *Int. J. Adv. Manuf. Technol.*, vol. 101, no. 1, pp. 23–38, Mar. 2019, doi: 10.1007/s00170-018-2932-7.

[148] ‘BS EN ISO 2400:2025 - Non-destructive testing. Ultrasonic testing. Specification for standard block No. 1’. BSI. Accessed: Feb. 09, 2026. [Online]. Available: https://knowledge.bsigroup.com/products/non-destructive-testing-ultrasonic-testing-specification-for-standard-block-no-2

[149] ATI Industrial Automation, ‘Six-Axis Force/Torque Sensor System - Installation and Operation Manual’. ATI Industrial Automation, 2022. Accessed: Nov. 06, 2025. [Online]. Available: https://www.ati-ia.com/app_content/documents/9620-05-Transducer%20Section.pdf

[150] µicroEpsilon, ‘scanCONTROL // 2D/3D Laser profile sensors’.

[151] C.-J. Lin, H.-C. Wang, and C.-C. Wang, ‘Automatic Calibration of Tool Center Point for Six Degree of Freedom Robot’, *Actuators*, vol. 12, no. 3, p. 107, Mar. 2023, doi: 10.3390/act12030107.

[152] P. Wilcox, ‘Multi-frame Full Matrix Capture (MFMC) HDF5 Structure Specification, Version 2.0.0’.

[153] E07 Committee, *Guide for Evaluating Performance Characteristics of Phased-Array Ultrasonic Testing Instruments and Systems*. doi: 10.1520/E2491-23.

[154] BSI, 'BS EN ISO 19675:2024 Non-destructive testing. Ultrasonic testing. Specification for a calibration block for phased array testing (PAUT).' Dec. 31, 2024. Accessed: Jan. 13, 2026. [Online]. Available: https://knowledge.bsigroup.com/products/non-destructive-testing-ultrasonic-testing-specification-for-a-calibration-block-for-phased-array-testing-paut-1

[155] A. Narwadkar and S. Bhosle, 'Optimization of MIG Welding Parameters to Control the Angular Distortion in Fe410WA Steel', *Mater. Manuf. Process.*, vol. 31, no. 16, pp. 2158–2164, Dec. 2016, doi: 10.1080/10426914.2015.1127939.

[156] A. K. Mondal, A. Lohit, P. Biswas, S. Bag, and M. Das, 'Prediction of weld-induced distortion of large structure using equivalent load technique', *Proc. Inst. Mech. Eng. Part B J. Eng. Manuf.*, vol. 232, no. 3, pp. 499–512, Feb. 2018, doi: 10.1177/0954405416646309.

[157] R. Xiao, Y. Xu, F. Xu, Z. Hou, H. Zhang, and S. Chen, 'LSFP-Tracker: An Autonomous Laser Stripe Feature Point Extraction Algorithm Based on Siamese Network for Robotic Welding Seam Tracking', *IEEE Trans. Ind. Electron.*, vol. 71, no. 1, pp. 1037–1048, Jan. 2024, doi: 10.1109/TIE.2023.3243265.

[158] Z. Yin, X. Ma, X. Zhen, W. Li, and W. Cheng, 'Welding Seam Detection and Tracking Based on Laser Vision for Robotic Arc Welding', *J. Phys. Conf. Ser.*, vol. 1650, no. 2, p. 022030, Oct. 2020, doi: 10.1088/1742-6596/1650/2/022030.

[159] Z. Jia, T. Wang, J. He, L. Li, and K. Wu, 'Real-time spatial intersecting seam tracking based on laser vision stereo sensor', *Measurement*, vol. 149, p. 106987, Jan. 2020, doi: 10.1016/j.measurement.2019.106987.

[160] H. Hu, J. Du, C. Ye, and X. Li, 'Ultrasonic Phased Array Sparse-TFM Imaging Based on Sparse Array Optimization and New Edge-Directed Interpolation', *Sensors*, vol. 18, no. 6, p. 1830, Jun. 2018, doi: 10.3390/s18061830.

[161] Y. Pan, W. Tao, R. Yu, and A. He, 'Fast Total Focusing Method Based On Elliptical Arc Scanning algorithm and OpenCL Acceleration', in *2024 6th International Conference on Intelligent Control, Measurement and Signal Processing (ICMSP)*, Nov. 2024, pp. 702–705. doi: 10.1109/ICMSP64464.2024.10866281.

[162] B. Yu, Y. Mei, H. Jin, E. Wu, and K. Yang, 'Ultrasonic phased array total focusing method based on sparse deconvolution', *Proc. Meet. Acoust.*, vol. 35, no. 1, p. 055007, Nov. 2019, doi: 10.1121/2.0001105.

[163] J. K. Han, V.-K. Wong, D. B. K. Lim, P. T. Christopher Subhodayam, P. Luo, and K. Yao, 'Environmental Robustness and Resilience of Direct-Write Ultrasonic Transducers Made from P(VDF-TrFE) Piezoelectric Coating', *Sensors*, vol. 23, no. 10, p. 4696, Jan. 2023, doi: 10.3390/s23104696.

[164] E. Nicolson, E. Mohseni, D. Lines, K. M. M. Tant, G. Pierce, and C. N. MacLeod, 'Towards an in-process ultrasonic phased array inspection method for narrow-gap welds', *NDT E Int.*, vol. 144, p. 103074, Jun. 2024, doi: 10.1016/j.ndteint.2024.103074.

[165] L. S. S. Pillarisetti and S. Anandamurugan, 'Ultrasonic Inspection of Weld Defects Using Total Focusing Method', in *Advances in Non-destructive Evaluation*, C. K. Mukhopadhyay and R. Mulaveesala, Eds, Singapore: Springer, 2021, pp. 187–202. doi: 10.1007/978-981-16-0186-6_19.

[166] Z. Zhao, L. Liu, W. Liu, D. Teng, Y. Xiang, and F.-Z. Xuan, 'Discretized tensor-based model of total focusing method: A sparse regularization approach for enhanced ultrasonic phased array imaging', *NDT E Int.*, vol. 141, p. 102987, Jan. 2024, doi: 10.1016/j.ndteint.2023.102987.

[167] D. O. Dolmatov and V. Y. Zhvyrblya, 'Optimal Design of Sparse Matrix Phased Array Using Simulated Annealing for Volumetric Ultrasonic Imaging with Total Focusing Method', *Sensors*, vol. 24, no. 6, p. 1856, Jan. 2024, doi: 10.3390/s24061856.

[168] Q. Xu, H. Wang, G. Tian, X. Ma, B. Hu, and J. Chu, 'Compressive sensing of ultrasonic array data with full matrix capture in nozzle welds inspection', *Ultrasonics*, vol. 134, p. 107085, Sep. 2023, doi: 10.1016/j.ultras.2023.107085.

[169] M. Lewandowski, P. Karwat, P. Jarosik, J. Rozbicki, M. Walczak, and H. Smach, 'A High-Speed Ultrasound Full-Matrix Capture Acquisition System for Robotic Weld Inspection', *E-J. Nondestruct. Test.*, vol. 28, no. 08, Aug. 2023, doi: 10.58286/28163.

[170] J. K. Van Velsor, O. M. Malinowski, S. A. Riccardella, L. Velandia, and R. Kania, 'Modeling of Advanced Ultrasonic Testing Methods for Improved Characterization of Pipeline Damage', presented at the 2020 13th International Pipeline Conference, American Society of Mechanical Engineers Digital Collection, Jan. 2021. doi: 10.1115/IPC2020-9605.

[171] L. P. Piedade, G. Painchaud-April, A. Le Duff, and P. Bélanger, 'Compressive Sensing Strategy on Sparse Array to Accelerate Ultrasonic TFM Imaging', *IEEE Trans. Ultrason. Ferroelectr. Freq. Control*, vol. 70, no. 6, pp. 538–550, Jun. 2023, doi: 10.1109/TUFFC.2023.3266719.

[172] Y. Na *et al.*, 'Advances of Machine Learning in Phased Array Ultrasonic Non-Destructive Testing: A Review', *AI*, vol. 6, no. 6, p. 124, Jun. 2025, doi: 10.3390/ai6060124.

[173] R. Zimermann *et al.*, 'Collaborative Robotic Wire + Arc Additive Manufacture and Sensor-Enabled In-Process Ultrasonic Non-Destructive Evaluation', *Sensors*, vol. 22, no. 11, p. 4203, Jan. 2022, doi: 10.3390/s22114203.

[174] M. Bertovic, B. Fahlbruch, and C. Mueller, 'Human Factors Perspective on the Reliability of NDT in Nuclear Applications', *Mater. Test.*, vol. 55, no. 4, pp. 243–253, Apr. 2013, doi: 10.3139/120.110431.

[175] C. Mineo, S. G. Pierce, B. Wright, I. Cooper, and P. I. Nicholson, 'PAUT inspection of complex-shaped composite materials through six DOFs robotic manipulators', *Insight - Non-Destr. Test. Cond. Monit.*, vol. 57, no. 3, pp. 161–166, Mar. 2015, doi: 10.1784/insi.2014.57.3.161.

[176] G. Cardoso and J. Saniie, 'Data compression and noise suppression of ultrasonic NDE signals using wavelets', in *IEEE Symposium on Ultrasonics, 2003*, Oct. 2003, pp. 250-253 Vol.1. doi: 10.1109/ULTSYM.2003.1293400.

[177] G.-M. Zhang, T. Olofsson, and T. Stepinski, 'Ultrasonic NDE image compression by transform and subband coding', *NDT E Int.*, vol. 37, no. 4, pp. 325–333, Jun. 2004, doi: 10.1016/j.ndteint.2003.10.007.

[178] N. Molinier, G. Painchaud-April, A. Le Duff, M. Toews, and P. Bélanger, 'Ultrasonic imaging using conditional generative adversarial networks', *Ultrasonics*, vol. 133, p. 107015, Aug. 2023, doi: 10.1016/j.ultras.2023.107015.

[179] B. Wang and J. Saniie, 'Massive Ultrasonic Data Compression Using Wavelet Packet Transformation Optimized by Convolutional Autoencoders', *IEEE Trans. Neural Netw.*

Learn. Syst., vol. 34, no. 3, pp. 1395–1405, Mar. 2023, doi: 10.1109/TNNLS.2021.3105367.

[180] Z. Bai, S. Chen, Q. Xiao, L. Jia, Y. Zhao, and Z. Zeng, 'Compressive sensing of phased array ultrasonic signal in defect detection: Simulation study and experimental verification', *Struct. Health Monit.*, vol. 17, no. 3, pp. 434–449, May 2018, doi: 10.1177/1475921717701462.

[181] P. Govindan and J. Saniie, 'Processing algorithms for three-dimensional data compression of ultrasonic radio frequency signals', *IET Signal Process.*, vol. 9, no. 3, pp. 267–276, 2015, doi: 10.1049/iet-spr.2014.0186.

[182] J. Saniie, P. Govindan, B. Wang, X. Zhang, Y. Lu, and E. Oruklu, 'Machine Learning and Modeling of Ultrasonic Signals for High-Fidelity Data Compression', in *2022 IEEE International Ultrasonics Symposium (IUS)*, Oct. 2022, pp. 1–9. doi: 10.1109/IUS54386.2022.9957732.

[183] C. Fan, L. Yang, Y. Chen, and Y. Zhao, 'Ultrasonic time-reversal-based imaging for rapid non-destructive evaluation', *Insight - Non-Destr. Test. Cond. Monit.*, vol. 60, no. 11, pp. 613–618, Nov. 2018, doi: 10.1784/insi.2018.60.11.613.

[184] N. E. Sweeney *et al.*, 'In-process phased array ultrasonic weld pool monitoring', *NDT E Int.*, vol. 137, p. 102850, Jul. 2023, doi: 10.1016/j.ndteint.2023.102850.

[185] N. Dalal and B. Triggs, 'Histograms of oriented gradients for human detection', in *2005 IEEE Computer Society Conference on Computer Vision and Pattern Recognition (CVPR'05)*, Jun. 2005, pp. 886–893 vol. 1. doi: 10.1109/CVPR.2005.177.

[186] P. Asadi, M. Gindy, M. Alvarez, and A. Asadi, 'A computer vision based rebar detection chain for automatic processing of concrete bridge deck GPR data', *Autom. Constr.*, vol. 112, p. 103106, Apr. 2020, doi: 10.1016/j.autcon.2020.103106.

[187] A. Velichko and P. D. Wilcox, 'An analytical comparison of ultrasonic array imaging algorithms', *J. Acoust. Soc. Am.*, vol. 127, no. 4, pp. 2377–2384, Apr. 2010, doi: 10.1121/1.3308470.

[188] P. O. Hoyer, 'Non-negative Matrix Factorization with Sparseness Constraints', *J Mach Learn Res*, vol. 5, pp. 1457–1469, Dec. 2004.

[189] L. P. Piedade, G. Painchaud-April, A. Le Duff, and P. Bélanger, 'Minimum transmission events for fast ultrasonic TFM imaging: A comparative study', *NDT E Int.*, vol. 128, p. 102627, Jun. 2022, doi: 10.1016/j.ndteint.2022.102627.

[190] M. Zhang, M. Sutcliffe, D. Carswell, and Q. Yang, 'Robotic path planning using NDT ultrasonic data for autonomous inspection', *Int. J. Metrol. Qual. Eng.*, vol. 14, p. 16, 2023, doi: 10.1051/ijmqe/2023013.

[191] B. Lepage and G. Painchaud-April, 'Acoustic Path Filtering for Improved Multimode Total Focusing Method Inspection', vol. 81, no. 2, Feb. 2023, doi: 10.32548/2023.me-04279.

[192] M. Brankovic, E. Gildin, R. L. Gibson, and M. E. Everett, 'A Machine Learning-Based Seismic Data Compression and Interpretation Using a Novel Shifted-Matrix Decomposition Algorithm', *Appl. Sci.*, vol. 11, no. 11, p. 4874, Jan. 2021, doi: 10.3390/app11114874.

[193] A. Biber, R. Sharma, and U. Reisgen, 'Robotic welding system for adaptive process control in gas metal arc welding', *Weld. World*, vol. 68, no. 9, pp. 2311–2320, Sep. 2024, doi: 10.1007/s40194-024-01756-y.

[194] P. Wang, J. Kershaw, M. Russell, J. Zhang, Y. Zhang, and R. X. Gao, 'Data-driven process characterization and adaptive control in robotic arc welding', *CIRP Ann.*, vol. 71, no. 1, pp. 45–48, Jan. 2022, doi: 10.1016/j.cirp.2022.04.046.

[195] C. Loukas *et al.*, 'A cost-function driven adaptive welding framework for multi-pass robotic welding', *J. Manuf. Process.*, vol. 67, pp. 545–561, Jul. 2021, doi: 10.1016/j.jmapro.2021.05.004.

[196] J. Zeng *et al.*, 'A Vision-Aided 3D Path Teaching Method before Narrow Butt Joint Welding', *Sensors*, vol. 17, no. 5, p. 1099, May 2017, doi: 10.3390/s17051099.

[197] M. Li, J. Huang, L. Xue, and R. Zhang, 'A guidance system for robotic welding based on an improved YOLOv5 algorithm with a RealSense depth camera', *Sci. Rep.*, vol. 13, no. 1, p. 21299, Dec. 2023, doi: 10.1038/s41598-023-48318-8.

[198] P. Kiddee, Z. Fang, and M. Tan, 'An automated weld seam tracking system for thick plate using cross mark structured light', *Int. J. Adv. Manuf. Technol.*, vol. 87, no. 9, pp. 3589–3603, Dec. 2016, doi: 10.1007/s00170-016-8729-7.

[199] H. N. Mohd Shah, M. Sulaiman, and A. Z. Shukor, 'Autonomous detection and identification of weld seam path shape position', *Int. J. Adv. Manuf. Technol.*, vol. 92, no. 9, pp. 3739–3747, Oct. 2017, doi: 10.1007/s00170-017-0380-4.

[200] Q.-Q. Wu *et al.*, 'A study on the modified Hough algorithm for image processing in weld seam tracking', *J. Mech. Sci. Technol.*, vol. 29, no. 11, pp. 4859–4865, Nov. 2015, doi: 10.1007/s12206-015-1033-x.

[201] B. Xue *et al.*, 'A Vision Based Detection Method for Narrow Butt Joints and a Robotic Seam Tracking System', *Sensors*, vol. 19, no. 5, p. 1144, Jan. 2019, doi: 10.3390/s19051144.

[202] X. Gao, L. Mo, D. You, and Z. Li, 'Tight butt joint weld detection based on optical flow and particle filtering of magneto-optical imaging', *Mech. Syst. Signal Process.*, vol. 96, pp. 16–30, Nov. 2017, doi: 10.1016/j.ymssp.2017.04.001.

[203] Y. Xu *et al.*, 'Welding seam tracking in robotic gas metal arc welding', *J. Mater. Process. Technol.*, vol. 248, pp. 18–30, Oct. 2017, doi: 10.1016/j.jmatprotec.2017.04.025.

[204] Y. Zou, Y. Wang, W. Zhou, and X. Chen, 'Real-time seam tracking control system based on line laser visions', *Opt. Laser Technol.*, vol. 103, pp. 182–192, Jul. 2018, doi: 10.1016/j.optlastec.2018.01.010.

[205] Y. Ding, W. Huang, and R. Kovacevic, 'An on-line shape-matching weld seam tracking system', *Robot. Comput.-Integr. Manuf.*, vol. 42, pp. 103–112, Dec. 2016, doi: 10.1016/j.rcim.2016.05.012.

[206] H. Wang, Y. Rong, S. Xiang, J. Xu, Y. Peng, and Y. Huang, '3D curve weld seam path and posture planning based on line laser sensors', *Robot. Comput.-Integr. Manuf.*, vol. 94, p. 102985, Aug. 2025, doi: 10.1016/j.rcim.2025.102985.

[207] K. Zhang, M. Yan, T. Huang, J. Zheng, and Z. Li, '3D reconstruction of complex spatial weld seam for autonomous welding by laser structured light scanning', *J. Manuf. Process.*, vol. 39, pp. 200–207, Mar. 2019, doi: 10.1016/j.jmapro.2019.02.010.

[208] C. Loukas *et al.*, 'Transforming Industrial Manipulators via Kinesthetic Guidance for Automated Inspection of Complex Geometries', *Sensors*, vol. 23, no. 7, p. 3757, Jan. 2023, doi: 10.3390/s23073757.

[209] H. Bordekar, N. Cersullo, M. Brysch, J. Philipp, and C. Hühne, 'eXplainable artificial intelligence for automatic defect detection in additively manufactured parts using CT scan

analysis', *J. Intell. Manuf.*, vol. 36, no. 2, pp. 957–974, Feb. 2025, doi: 10.1007/s10845-023-02272-4.

[210] B. Milcke, P. Dinglinger, and J. Holtmann, 'Exploring the Role of Explainable AI in the Development and Qualification of Aircraft Quality Assurance Processes: A Case Study', in *Explainable Artificial Intelligence*, L. Longo, S. Lapuschkin, and C. Seifert, Eds, Cham: Springer Nature Switzerland, 2024, pp. 331–352. doi: 10.1007/978-3-031-63803-9_18.

[211] D. Zhang, R. Watson, C. MacLeod, G. Dobie, W. Galbraith, and G. Pierce, 'Implementation and evaluation of an autonomous airborne ultrasound inspection system', *Nondestruct. Test. Eval.*, vol. 37, no. 1, pp. 1–21, Jan. 2022, doi: 10.1080/10589759.2021.1889546.

[212] L. Cilia, C. A. Griffiths, A. Rees, and J. Thompson, 'Integration of an Ultrasonic Sensor within a Robotic End Effector for Application within Railway Track Flaw Detection', *Appl. Sci.*, vol. 14, no. 3, p. 1164, Jan. 2024, doi: 10.3390/app14031164.

[213] A. Gilmour *et al.*, 'Using Phased Array Ultrasound to Localize Probes During the Inspection of Welds', *IEEE Open J. Instrum. Meas.*, vol. 2, pp. 1–10, 2023, doi: 10.1109/OJIM.2023.3327484.

[214] M. Bertovic, 'A human factors perspective on the use of automated aids in the evaluation of NDT data', *AIP Conf. Proc.*, vol. 1706, no. 1, p. 020003, Feb. 2016, doi: 10.1063/1.4940449.

[215] V. Tunukovic *et al.*, 'Human-machine collaborative automation strategies for ultrasonic phased array data analysis of carbon fibre reinforced plastics', *NDT E Int.*, vol. 154, p. 103392, Sep. 2025, doi: 10.1016/j.ndteint.2025.103392.

[216] S. Zhang and Y. Zhang, 'Automated weld defect segmentation from phased array ultrasonic data based on U-net architecture', *NDT E Int.*, vol. 146, p. 103165, Sep. 2024, doi: 10.1016/j.ndteint.2024.103165.

[217] E. Provencal and L. Laperrière, 'WeldNet: From 3D phased-array ultrasound scans to 3D geometrical models of welds and defects', *CIRP Ann.*, vol. 71, no. 1, pp. 445–448, Jan. 2022, doi: 10.1016/j.cirp.2022.04.033.

[218] E. Provencal and L. Laperrière, 'Identification of weld geometry from ultrasound scan data using deep learning', *Procedia CIRP*, vol. 104, pp. 122–127, Jan. 2021, doi: 10.1016/j.procir.2021.11.021.

[219] S. Niu and V. Srivastava, 'Simulation trained CNN for accurate embedded crack length, location, and orientation prediction from ultrasound measurements', *Int. J. Solids Struct.*, vol. 242, p. 111521, May 2022, doi: 10.1016/j.ijsolstr.2022.111521.

[220] R. J. Pyle, R. R. Hughes, and P. D. Wilcox, 'Interpretable and Explainable Machine Learning for Ultrasonic Defect Sizing', *IEEE Trans. Ultrason. Ferroelectr. Freq. Control*, vol. 70, no. 4, pp. 277–290, Apr. 2023, doi: 10.1109/TUFFC.2023.3248968.

[221] R. Miorelli, S. Robert, P. Calmon, and S. Le Berre, 'Use of deep learning and data augmentation by physics-based modelling for crack characterisation from multimodal ultrasonic TFM images', *Nondestruct. Test. Eval.*, vol. 0, no. 0, pp. 1–23, Nov. 2024, doi: 10.1080/10589759.2024.2428374.

[222] R. J. Pyle, R. R. Hughes, A. A. S. Ali, and P. D. Wilcox, 'Uncertainty Quantification for Deep Learning in Ultrasonic Crack Characterization', *IEEE Trans. Ultrason. Ferroelectr. Freq. Control*, vol. 69, no. 7, pp. 2339–2351, Jul. 2022, doi: 10.1109/TUFFC.2022.3176926.

[223] R. J. Pyle, R. L. T. Bevan, R. R. Hughes, R. K. Rachev, A. A. S. Ali, and P. D. Wilcox, ‘Deep Learning for Ultrasonic Crack Characterization in NDE’, *IEEE Trans. Ultrason. Ferroelectr. Freq. Control*, vol. 68, no. 5, pp. 1854–1865, May 2021, doi: 10.1109/TUFFC.2020.3045847.

[224] L. Wen, X. Li, L. Gao, and Y. Zhang, ‘A New Convolutional Neural Network-Based Data-Driven Fault Diagnosis Method’, *IEEE Trans. Ind. Electron.*, vol. 65, no. 7, pp. 5990–5998, Jul. 2018, doi: 10.1109/TIE.2017.2774777.

[225] K. Simonyan and A. Zisserman, ‘Very Deep Convolutional Networks for Large-Scale Image Recognition’, Apr. 10, 2015, *arXiv*: arXiv:1409.1556. doi: 10.48550/arXiv.1409.1556.

[226] A. Dimakos *et al.*, ‘Ultrasonic phased array measurement & compression for in-process weld bevel estimation’, *Ultrasonics*, vol. 164, p. 108025, Aug. 2026, doi: 10.1016/j.ultras.2026.108025.

[227] ‘Dynamic Programming | Princeton University Press’. Accessed: Jan. 26, 2026. [Online]. Available: https://press.princeton.edu/books/paperback/9780691146683/dynamic-programming

[228] N. V. Chawla, K. W. Bowyer, L. O. Hall, and W. P. Kegelmeyer, ‘SMOTE: Synthetic Minority Over-sampling Technique’, *J. Artif. Intell. Res.*, vol. 16, pp. 321–357, Jun. 2002, doi: 10.1613/jair.953.

[229] P. Branco, L. Torgo, and R. P. Ribeiro, ‘SMOGN: a Pre-processing Approach for Imbalanced Regression’, in *Proceedings of the First International Workshop on Learning with Imbalanced Domains: Theory and Applications*, PMLR, Oct. 2017, pp. 36–50. Accessed: Jan. 26, 2026. [Online]. Available: https://proceedings.mlr.press/v74/branco17a.html

[230] A. Goldstein, A. Kapelner, J. Bleich, and E. Pitkin, ‘Peeking Inside the Black Box: Visualizing Statistical Learning With Plots of Individual Conditional Expectation’, *J. Comput. Graph. Stat.*, vol. 24, no. 1, pp. 44–65, Jan. 2015, doi: 10.1080/10618600.2014.907095.

[231] ‘ISO 13920:2023’, ISO. Accessed: Oct. 18, 2025. [Online]. Available: https://www.iso.org/standard/86032.html

[232] S. Kosarevsky and V. Latypov, ‘Practical Procedure for Position Tolerance Uncertainty Determination via Monte-Carlo Error Propagation’, *Meas. Sci. Rev.*, vol. 12, no. 1, pp. 1–7, Jan. 2012, doi: 10.2478/v10048-012-0001-1.

[233] E. A. Foster *et al.*, ‘Thermal compensation of ultrasonic transmit and receive data for steel welded plates at the point of manufacture’, *NDT E Int.*, vol. 137, p. 102812, Jul. 2023, doi: 10.1016/j.ndteint.2023.102812.

Appendix

A. Process Parameters and Bead Size

Wire Feed Speed (mm/min)	Travel Speed (mm/min)	Current (A)	Measured Cross Section	Bead Height (mm)	Bead Width (mm)	Cross Section
456.67	111.00	166.00	31.4565	1.34	7.5	0.4039296
563.33	111.00	166.00	36.0576	1.6	7.2	0.5024
670.00	111.00	166.00	45.5728	2.08	7	0.671780571
456.67	127.00	166.00	29.15595	1.35	6.9	0.442330435
563.33	127.00	166.00	34.5865	1.7	6.5	0.591286154
670.00	127.00	166.00	35.1186	1.7	6.6	0.582327273
456.67	95.00	166.00	47.6073	1.95	7.8	0.5652
563.33	95.00	166.00	48.8906	2.2	7.1	0.700529577
670.00	95.00	166.00	53.7108	2.2	7.8	0.637661538
456.67	111.00	182.00	31.926	1.2	8.5	0.319171765
563.33	111.00	182.00	55.088	2	8.8	0.513818182
670.00	111.00	182.00	58.67185	2.3	8.15	0.638017178
456.67	127.00	182.00	36.1828	1.7	6.8	0.5652
563.33	127.00	182.00	49.30063	1.9	8.29	0.518156815
670.00	127.00	182.00	44.982795	1.65	8.71	0.428280138
456.67	95.00	182.00	46.011	1.5	9.8	0.346040816
563.33	95.00	182.00	58.2806	1.9	9.8	0.438318367
670.00	95.00	182.00	70.9258	2.2	10.3	0.48288932
456.67	111.00	198.00	48.1707	1.5	10.26	0.330526316

563.33	111.00	198.00	39.02484	1.2	10.39	0.261112608
670.00	111.00	198.00	51.5824	1.6	10.3	0.351192233
456.67	127.00	198.00	53.21	1.7	10	0.384336
563.33	127.00	198.00	42.3176	1.3	10.4	0.2826
670.00	127.00	198.00	48.9532	1.7	9.2	0.417756522
456.67	95.00	198.00	52.584	1.6	10.5	0.344502857
563.33	95.00	198.00	56.29305	1.65	10.9	0.342231193
670.00	95.00	198.00	58.14288	1.8	10.32	0.394325581
777	95	166	54.15526	2.05	8.44	0.549127962
777	111	166	42.672855	1.83	7.45	0.55533745
777	127	166	38.0608	1.9	6.4	0.671175
777	95	182	66.65022	2.1	10.14	0.468213018
777	111	182	50.0174	1.7	9.4	0.408868085
777	127	182	47.576	1.9	8	0.53694
777	95	192	69.6738	2.1	10.6	0.44789434
777	111	192	65.9491	2.15	9.8	0.495991837
777	127	192	51.1442	1.9	8.6	0.49947907
884	95	166	55.43856	2.16	8.2	0.595527805
884	111	166	53.836	2.15	8	0.60759
884	127	166	44.78404	1.96	7.3	0.607009315
884	95	182	71.799696	2.43	9.44	0.581964407
884	111	182	71.21376	2.37	9.6	0.558135
884	127	182	57.592	2	9.2	0.491478261
884	95	192	83.0076	2.4	11.05	0.491033484
884	111	192	71.63005	2.3	9.95	0.522596985
884	127	192	64.80665	2.05	10.1	0.458875248

B. Reference Geometry